RICE UNIVERSITY

Optical Contrast Agents to Visualize Molecular Expression in Breast Cancer

by

Robert James Langsner

A THESIS SUBMITTED
IN PARTIAL FULFILLMENT OF THE
REQUIREMENTS FOR THE DEGREE

Doctor of Philosophy

APPROVED, THESIS COMMITTEE

Rebekah Drezek, PhD, Chair
Professor Bioengineering and Electrical and Computer Engineering

Tomasz Tkaczyk, PhD
Assistant Professor Bioengineering and Electrical and Computer Engineering

Stephan Link, PhD
Assistant Professor Chemistry and Electrical and Computer Engineering

HOUSTON, TEXAS
April 2013

Abstract

Optical Contrast Agents to Visualize Molecular Expression in Breast Cancer

by

Robert James Langsner

Breast cancer is the second leading cause of death of women in the United States. Improvements in screening technology have increased the breast cancer incidence rate, as smaller lesions are being detected. Due to the small size of lesions, patients can choose to receive breast conservation therapy (BCT) rather than a modified radical mastectomy. Even though the breast retains cosmesis after BCT, there is an increased risk of the patient having residual microscopic disease, known as positive margins. Patients with positive margins receive increased radiation and have an increased chance of second surgery. Pathology with hematoxylin and eosin (H&E) remains the gold standard for diagnosing margin status in patients. Intraoperative pathology has been shown to reduce the rate of positive margins in BCT. However, a minority of surgery centers have intraoperative pathology centers, limiting the number of patients that receive this standard of care.

The expression profiles of surface receptors such as ErbB2 (HER2-positive) and epidermal growth factor receptor (EGFR) provide information about the aggressiveness of a particular tumor. Recent research has shown that there was elevated EGFR expression in patients with a local recurrence even though the biopsies were assessed to be disease free using standard H&E. If the physicians had known the molecular

expression of these biopsies, a different treatment regimen or excision of more tissue might have prevented the recurrence.

This thesis investigates targeted molecular contrast agents that enhance the visualization of molecular markers such as glucose transporters (GLUTs) and growth factor receptors in tissue specimens. First, application of 2-NBDG, a fluorescent deoxy-glucose, enhances signal in cancerous tissue with a 20-minute incubation. Then, antibody functionalized silica-gold nanoshells enhance the visualization of ErbB2 overexpression in specimens with a 5-minute incubation.

To image these contrast agents in cancerous tissue, a portable, inexpensive device was developed as a tool to help physicians visualize expression of surface markers. The system visualizes absorbance from nanoshell aggregates and fluorescence in the visible and near-infrared light spectrum. This study represents the first step in the development of an intraoperative optical imaging device to enhance the visualization of molecular markers overexpressed in cancerous cells.

Acknowledgments

Graduate school is a long adventure that I definitely would not have been able to complete on my own, and I have many people to thank for helping me get through it all. First, I would like to thank my advisor, Rebekah Drezek, for her mentorship and providing me with the opportunity to complete research in her lab. Not only did she provide me with expert guidance for five years, but she also allowed me to explore other opportunities through outside internships that gave me the chance to have different experiences and help further my career. I would also like to thank Dr. Tomasz Tkaczyk and Dr. Stephan Link for serving as my committee members. I also thank Drs. Ethan Cohen and Michael Cuchiara for providing valuable mentorship to me and offering me the opportunities to perform research outside of my dissertation.

I also would like to thank all of the members of the Drezek lab that I have shared office and lab space with. I would especially like to thank Drs. Lissett Bickford and Nastassja Lewinski for their mentorship when I was a young graduate student and for teaching me numerous techniques. I would also like to thank Joe Young for showing me my first nanoparticle synthesis and conjugation. I would also like to thank JP Mattos, Liz Figueroa, and Adam Lin for their collaboration on my projects and keeping things goofy, fun, and weird in lab. I would also like to thank Germain Agollah of Nanospectra for providing me with nanoshells for my experiments, Allen Chen for editorial assistance, and Kenn Dunner Jr. of the High Resolution Electron Microscopy Facility at UTMDACC for help with TEM.

The social aspect of Rice kept me sane and happy when I was not in lab, and for that support I have the whole Valhalla community to thank. Specifically, Dr. Brent

Carey who initially convinced me that being a manager was a good idea; Dr. David Fortunato who thought that letting me be a manager was a good idea, and Erica Levorson who for thought that managing the bar with me was a good idea. I would also like to acknowledge Dr. Joe Hoffman, Clark Needham, and Allan Henslee for their support and friendship from our Med-Into-Grad years through now. As well, Goldy Thach for distracting me on google chat on a daily basis.

This thesis would not have been possible without the strong familial support that I have received from my brother, Patrick Reuther; sister, Dr. Mary Langsner; and mother, Margaret Slattery. Without their love and care, I do not think I would have lasted 6 months in school. Finally, I dedicate this thesis to my father, Robert Langsner, who always showed great patience and wisdom when teaching me, especially with physics. I miss him every day.

Table of Contents

List of Figures

Abbreviations

BCT	Breast Conservation Therapy
MRM	Modified Radical Mastectomy
H&E	Hematoxylin and Eosin
EGF(R)	Epidermal Growth Factor (Receptor)
HER2	Human Epidermal Growth Factor Receptor 2
GLUT(s)	Glucose Transporter(s)
^{18}FDG	Fluoro Deoxy-Glucose
PET	Positron Emission Tomography
AuNP(s)	Gold Nanoparticle(s)
U.S.	United States
DCIS	Ductal Carcinoma in Situ
NST	No Special Type
IDC	Invasive Ductal Carcinoma
ILC	Invasive Lobular Carcinoma
CT	Computed Tomography
MRI	Magnetic Resonance Imaging
ER	Estrogen Receptor
PR	Progesterone Receptor
TN	Triple Negative
DNA	Deoxyribonucleic Acid
VEGF(R)	Vascular Enothelial Growth Factor (Receptor)
APBI	Accelerated Partial Breast Irradiation
WGL	Wire-Guided Localization
IOUS	Intra-operative Ultrasound
CAL	Cryoprobe-assisted localization
FSA	Frozen Section Analysis
IOPTC	Intra-operative Touch Prep Cytology
MDACC	M.D. Anderson Cancer Center

ROLL	Radio Guided Occult Lesion Localization
NIR(F)	Near-Infrared (Fluorescence)
ICG	Indocyanine Green
DOI	Diffuse Optical Imaging
NS	Nanoshells
LED	Light Emitting Diode
NP(s)	Nanoparticle(s)
FDA	Food and Drug Administration
SLN	Solid Lipid Nanoparticles
FITC	Fluorescein Isothiocyanate
FGF	Fibroblast Growth Factor
PAMAM	Poly amidoamine
UV	Ultra-Violet
SPIONP(s)	Super-Paramagnetic Iron Oxide nNanoparticle(s)
PR	Plasmon Resonance
EPR	Enhanced Permeability and Retention Effect
PEI	Polyethyleneimine
PEG	Polyethylene Glycol
RNAi	RNA interference
ROS	Reactive Oxygen Species
QD(s)	Quantum Dot(s)
CTAB	Cetyl trimehtylammonium bromide
GI	Gastrointestinal
AuNS	Gold Nanoshell
mRNA	Messenger RNA
2-NBDG Deoxyglucose	2-(N-(7-nitrobenz-2-oxa-1,3-diazol-4-yl)Amino-2-
PBS	Phosphate Buffered Solution
DMSO	Dimethyl Sulfoxide
Glu-AuNPs	Glucose Capped Gold Nanoparticles
EDS	Energy Dispersive Spectroscopy

TEM	Transmission Electron Microscopy
FBS	Fetal Bovine Serum
BSA	Bovine Serum Albumin
ROI	Region Of Interest
(N)AUC	(Normalized) Area Under Curve
$HAuCl_4$	Chloroauric Acid
THPC	Tetrakis(hydroxymethyl)phosphonium chloride
FOV	Field Of View
STEM	Scanning Transmission Electron Microscopy
MFI	Mean Fluorescence Intensity
RCM	Reflectance Confocal Microscopy
APTES	Aminopropyltriethoxysilane
SEM	Scanning Electron Microscopy
PEG-SH	Polyethylene Glycol Thiol
CHTN	Cooperative Human Tissue Network
IRB	Institutional Review Board
IHC	Immunohistochemistry
MDM	Multi-spectral Digital Microscope
OPR	Orthoganl Polarized Reflectance Imaging
OCT	Optical Coherence Tomography
DSLR	Digital Single-Lens Reflex Camera
RGB	Red, Green, Blue
FITC	Fluorescein Isothiocyanate

Chapter 1

Introduction

Breast cancer accounted for approximately twenty-nine percent of all female cancers diagnosed in 2012 [1]. It is treated with a combination of chemotherapy, radiotherapy, and surgery. Recent advances in screening and diagnosis techniques have led to the discovery of smaller lesions [2]. One effect of this has been an increase in the number of breast conservation therapy (BCT) surgeries in place of modified radical mastectomies (MRM) [2]. Women who receive BCT have a better cosmetic outcome, which can remove some of the psychological burden that results from traumatic surgery. BCT also lowers infection risk at the wound site [3] and has similar survival rates to patients who receive MRM [4–6]. However, there are risks associated with BCT. About forty percent of breast cancers present as multi-focal disease [7], which adds complications to the surgery [8]. It is also more difficult for surgeons to detect *in situ* disease intraoperatively, leading to inadequate removal of cancerous cells, known as positive margins. A patient with positive margins receives increased radiation dosage

and will often undergo a second surgery a short time period after the first surgery [8]. A 2012 retrospective study by Jeevan et al. showed that twenty percent of women receiving BCT had a re-excision to remove residual disease with *in situ* disease accounting for nearly twice as many re-excisions as isolated cancers [8]. A second surgery involves poorer cosmesis [9] and higher psychological trauma for the patient [8,10]. Reducing the rate of positive margins will dramatically decrease the rate of second surgeries in BCT; however, it is difficult to visualize microscopic disease intraoperatively. Currently, intraoperative pathology has demonstrated lower recurrence of re-excision in patients [11,12]. However, intraoperative pathology is only available in approximately five percent of hospitals, limiting its widespread use.

Intraoperative pathology has other limitations as well. Studies by Camp and Riedl demonstrated lower rates of re-excision but not lower rates of positive margins [11,12]. A study by Vosoughhosseini et al. showed pathology using standard hematoxylin and eosin (H&E) had false negatives that would have been diagnosed if pathologists had analyzed surface expression of epidermal growth factor receptor (EGFR), a protein associated with aggressive cancers [13]. One growth factor receptor, ErbB2, is of particular importance to breast cancer, as it is over-expressed in up to twenty-five percent of breast cancers (known as HER2-positive) and is associated with particular aggressive subtypes of breast cancer [14–17]. HER2-positive tumors are a majority of high grade ductal carcinoma *in situ* (DCIS) [14], and a 2004 study by Miller et al. showed that surgeons operating on patients with HER2-positive DCIS had a more difficult time obtaining negative margins [18]. These facts demonstrate that there is a

clinical need for a method to visualize the overexpression of this surface receptor during BCT.

As HER2 is only overexpressed in twenty-five percent of breast cancers, there is a need to develop methods to visualize breast cancer subtypes with different surface receptors whose overexpression have been linked to breast cancer [19]. A 2012 study by Vermeulen et al. showed that eighty percent of invasive breast cancers express at least one of these proteins: CD44v6, GLUT1, EGFR, HER2, and IGF1-R) [19]. GLUT1 (glucose transporter 1) has demonstrated utility as a marker for cells with high metabolic activity (such as cancer). Clinically, its overexpression has been visualized through the use radio-labeled deoxy-glucose (^{18}FDG) that is visualized using positron emission tomography (PET) [20,21]. However, as this imaging modality can not be used intraoperatively, recent research has focused on the development of a fluorescent deoxy-glucose analog, 2-NBDG, [22–25]. 2-NBDG signal can be monitored through optical imaging techniques and enhances the fluorescent signal from cancerous cells to provide contrast between malignant and normal tissue. Additionally, contrast agents targeted to EGFR enhance tumor signal via fluorescence [26,27] or reflectance [28]. These are examples of methods to visualize surface receptor overexpression in breast cancer that have potential to assist surgeons identify microscopic disease intraoperatively.

This thesis discusses the use of targeted contrast agents to visualize molecular expression. First, three introduction chapters review breast cancer, the use of nanotechnology in breast cancer treatment and diagnosis, and optical imaging with breast cancer. Then, the utility of 2-NBDG as a contrast agent in cells and freshly excised cancerous tissue is explored using microscopy and a wide-field multispectral imaging

system. Next, glucose is conjugated to the surface of small diameter (~2 nm) gold nanoparticles (AuNPs) to investigate a new targeting moiety for nanoparticles. Also, anti-HER2 antibodies are functionalized to the surface of large diameter (~314 nm) silica-gold nanoshells (NS) for use as rapid diagnostic probes to visualize HER2 expression in *ex vivo* tissue specimens. Finally, an inexpensive, portable device is developed to image the enhanced contrast provided by 2-NBDG, anti-HER2 NS, and anti-EGFR fluorescent dye. The device is constructed as an instrument that surgeons can use in the surgical suite to visualize signal provided from the contrast agents in order to determine if there is presence of microscopic disease.

This thesis represents the first step in the development of an inexpensive, portable device that can be used with commercially available contrast agents to provide optical images of molecular expression of cancerous tissue. The research demonstrates that rapid incubation with targeted contrast agents can differentiate non-cancerous tissue from cancerous tissue, and the enhanced signal from the contrast agent can be visualized.

Chapter 2

Breast Cancer: Statistics, Imaging, and Treatment

2.1. Introduction

In the United States (U.S.) in 2011, there were approximately 230,480 new cases of breast cancer and nearly 39,250 deaths from breast cancer [29]. Nationally, breast cancer mortality rates have been in decline from the 1990s (2.2% per year), whereas incidence rates have been increasing (Fig. 2.1). This increase is thought to be a result of the increase in screening mammograms in the U.S [29]. In this chapter, we will discuss the types of breast cancer, the methods of treatment of breast cancer, current techniques to improve intra-operative visualization of breast cancer, and how the research in this dissertation can be applied to improve treatment of breast cancer.

2.2. Breast Cancer Characterization

Ninety-five percent of breast cancers are classified as adenocarcinomas; the other classifications include: squamous cell carcinomas, phyllodes tumors, sarcomas, and lymphomas [30]. There are two divisions of carcinomas: in situ and invasive. In situ indicates that the cancerous cells have not broken through the ducts or lobules in which the cancer has originated, and the cells are still limited by the basement membrane.

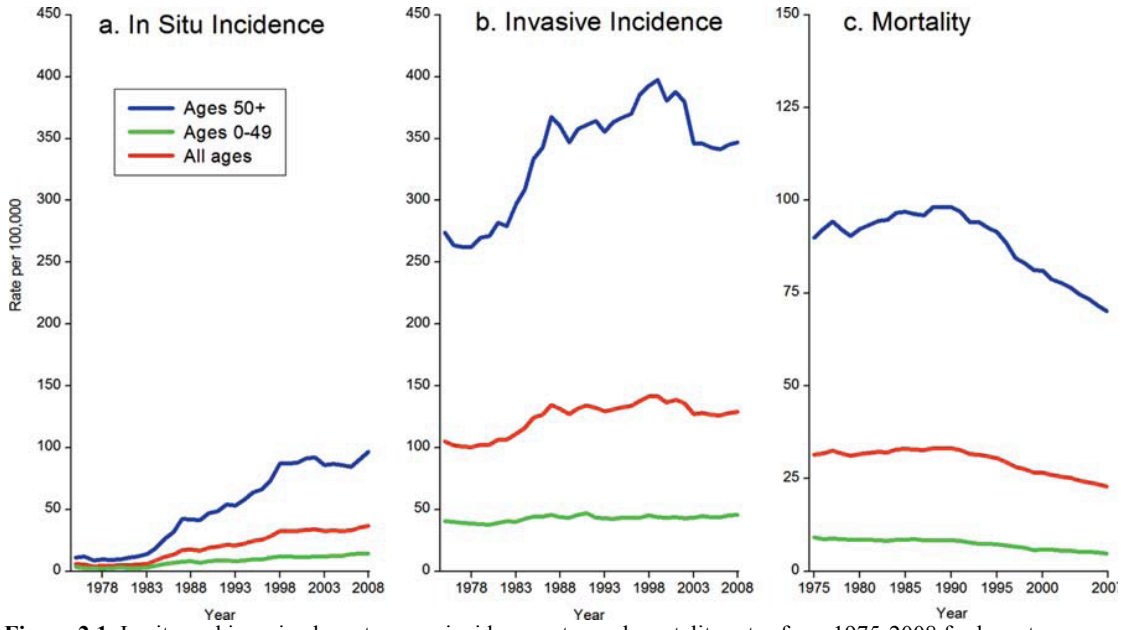

Figure 2.1. In situ and invasive breast cancer incidence rates and mortality rates from 1975-2008 for breast cancer in the United States. In situ incidence has increased as the number of screenings has increased and screening technology has improved to detect smaller lesions. Reproduced from [29].

Invasive carcinomas are classified as having penetrated the basement membrane of the duct or lobule of origin. Ductal carcinoma in situ (DCIS) is seen approximately four times more frequently (80% vs. 20%) than lobular carcinoma in situ. In situ incidences have increased recently due to improved diagnostic technology, and the increased number of screening mammograms resulting from more breast cancer awareness [29–32]. Even though in situ carcinomas have not spread beyond the duct or lobule of origin, they can

be very dangerous because the malignant cells can spread throughout the entire duct or lobule and take up a very large volume in the breast [30].

2.2.1. Types of breast cancer

There are six types of invasive carcinoma, about eighty percent of all invasive carcinomas are deemed no special type (NST), also known as invasive ductal carcinoma (IDC), which can not be classified as a specific subtype [30]. IDC have a wide variety of protein and gene expression, and there have been recent studies that have looked to classify these cancers more specifically by their expression profiles so that more specific prognoses and treatments can be accomplished. These will be explored later in the manuscript. Invasive lobular carcinoma (ILC) is the second most common breast adenocarcinoma, occurring at a rate of ten percent of all invasive carcinomas. ILC requires a different type of treatment and monitoring regiment. First ILC metastasizes to different organs than other breast cancers [30], such as the GI tract, ovaries, and uterus. Additionally, chemotherapeutic treatment of ILC is difficult to monitor using Positron Emission Tomography and Computed Tomography scans (PET/CT) because detectors have more difficult time detecting the radioactive isotopes that target the malignant tissue [33–36]. One explanation for this is the difference in cell density between cancer cell types and their respective infiltration into surrounding tissues [37,38]. Figure 2.2 demonstrates the inability of PET/CT to differentiate an ILC tumor that is easily visible with MRI, while also demonstrating the ability of PET/CT to localize IDC in a patient.

Other breast adenocarcinomas include tubular carcinoma, which accounts for six percent of invasive carcinomas and ten percent of cancers less than one cm. Ninety-five percent of these cancers will express hormone receptors and they are well-differentiated

[30]. Medullary carcinoma occurs in approximately two percent of invasive carcinomas. It is characterized by high nuclear grade and proliferation rates, yet despite these factors, it still has a better prognosis than IDC. Invasive mucinous carcinoma also occurs in

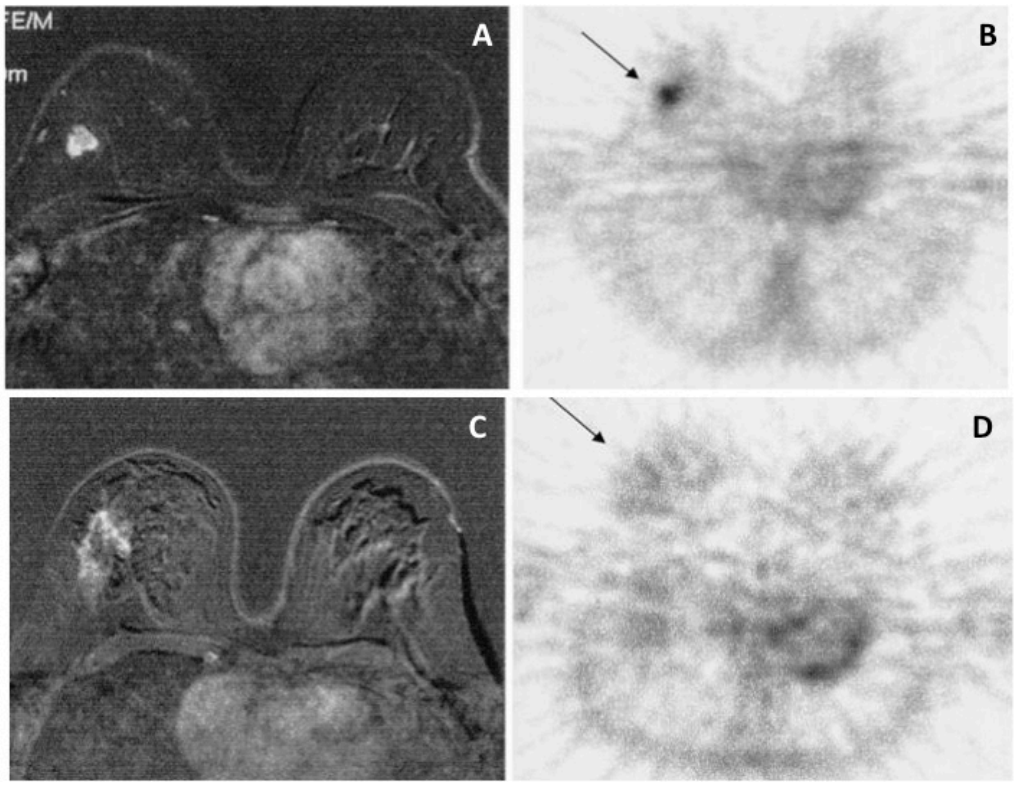

Figure 2.2. Magnetic Resonance Imaging (MRI) and PET/CT images of IDC (A&B) and ILC (C&D). Arrows delineate the respective locations of the tumor in the breast. It is very difficult to differentiate ILC in the PET/CT image, but IDC presents a very nice negative contrast. Reproduced from [34].

about two percent of invasive carcinoma and grows slowly over the course of years. It is very soft and looks like gray-blue gelatin. Two other invasive carcinomas include invasive papillary carcinoma and metaplastic carcinoma. Both of these cases are rare, totalling less than one percent of all invasive breast cancer. Disease heterogeneity and rarity make it difficult for physicians to institute patients' prognoses for these types of cancers.

There are also rare cases of stromal tumors in the breast that include benign fibroadenomas, sarcomas, and phyllodes tumors. Fibroadenoma is the most common of

benign tumors and is often presented as a palpable mass, which allows for patients to discover them with self-examination. Phyllodes tumors originate in intra-lobular stroma that are palpable, but are rarely detected in mammography [30]. Most phyllodes tumors are benign, but those that are more aggressive have been shown to over-express epidermal growth factor receptor (EGFR), a receptor whose over-expression correlates with cell proliferation [39]. Sarcomas of the breast, that present as large masses, are very rare. A final area of concern for physicians is that there is a slight risk of angiosarcoma formation (0.3-4%) in the breast after a patient receives radiation therapy to treat the primary breast cancer [30].

2.2.2. Molecular phenotypes of breast cancer

As mentioned previously, there have been studies to classify all breast carcinomas by receptor phenotype; these studies were aimed towards helping physicians determine treatment options and prognosis for patients [40,41] with a specific phenotype. Cell types have been broken into three main subtypes based on protein expression: luminal, HER2 over-expressing (HER2-positive), and basal-like. Luminal tumors are characterized by the expression of hormone receptors progesterone and estrogen (ER+/PR+) [40,41]. Tamimi further differentiates the luminal subtype into luminal A&B, where luminal A is characterized as ER+/PR+/HER2-negative and luminal B is ER+/PR+/HER2-positive [41]. HER2-positive tumors are classified as hormone receptor negative with HER2 over-expression (ER-/PR-/HER2-positive). Finally, basal-like cells are negative for all three receptors and are also known as triple-negative cancers (TN). Luminal tumors have been targeted with an anti-estrogen drug, Tamoxifen, that has demonstrated success in lowering recurrence and increasing long-term survival of

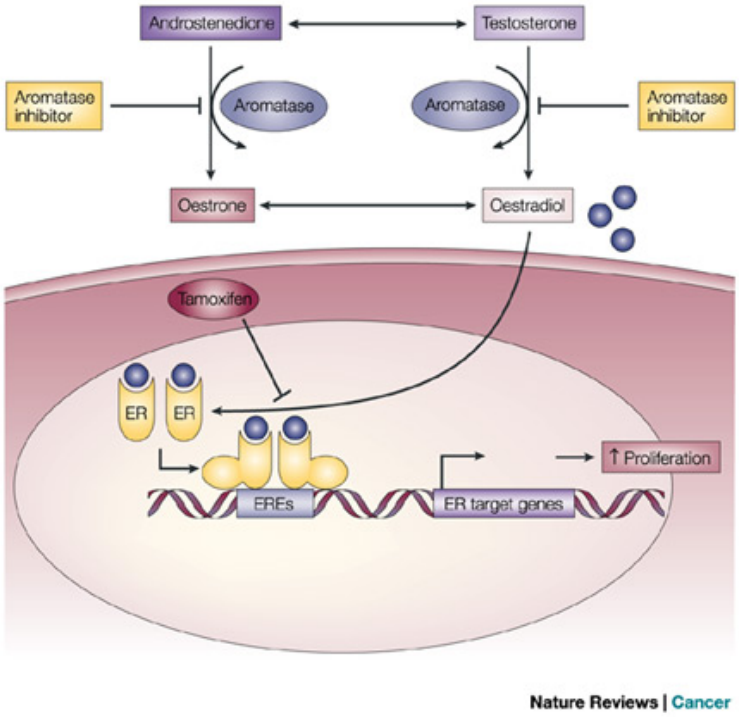

Figure 2.3. Mechanism of action of Tamoxifen, which blocks oestradiol from binding to the estrogen receptor (ER), which prevents dimerization of the receptor (ER). This stops the ER from binding to the Estrogen Receptor Elements (EREs) which then stops genes that are responsible for proliferation from being translated and transcribed. Reproduced from [43].

patients that are ER+ [42] by binding to the estrogen receptor and disallowing oestradiol from binding to the receptor (Fig. 2.3) [43]. However, tamoxifen treatment can cause endometrial cancer and cells will develop tamoxifen resistance [42]. Additionally, ER+ patients can receive oophorectomy (removal of the ovaries), to remove sources of estrogen from the body. These two treatments have been recommended as a combinatorial use to treat malignant tissue in the breast and lower the chance of recurrence by removing a source of estrogen in the body [44]. HER2+ cancers over-express the growth factor receptor ErbB2 [45]. Breast cancers of this molecular phenotype and their treatment will be discussed in greater detail in section 2.4.4. TN cancers are of major concern for physicians and patients due to the lack of receptors on the surface which does not allow for targeted therapy that is used with the other two

subtypes of cancer [46]. Lowery et al. showed that TN patients were more than likely to have a recurrence of cancer when compared to the luminal type cancers [40]. This is a result of a lack of a properly targeted therapeutic that physicians can use to treat the tumors.

2.3. Treatment of Breast Cancer

There are three major treatment methods for breast cancer patients: chemotherapy, radiation therapy, and surgery. Chemotherapy involves the administration of agents to the body that will cause damage to the malignant cells. However, these compounds are also toxic to healthy cells in the body, so physicians must balance the drugs' potential health benefits with the overall health of the patient. Chemotherapeutics can be administered pre-surgery (neoadjuvant) to reduce tumor volume before patients undergo surgery [47,48]. They can also be administered after surgery to control tumor recurrence and metastasis. The two main types of chemotherapeutic agents are small molecule therapeutic agents and biologically specific targets [49].

Small molecule agents include anthracyclines and taxanes. Anthracyclines' mechanisms of therapy include inhibiting DNA synthesis and creating free radicals in the cells that attack DNA [49]. Studies have shown that using multiple anthracyclines in combination raises the efficacy of the drugs [50], but there is cardio-toxicity associated with anthracyclines that limits the amount that can be administered to the patient [51]. Taxanes, which include the drug paclitaxel, disrupt microtubule formation and function to disrupt mitosis. Because taxanes and anthracyclines have different mechanisms (and

therefore different mechanisms of toxicity to healthy cells), combination of these therapies has proven an effective method of prolonging survival of patients [52].

Biologically specific agents are targeted at specific receptors on the surface of cancers such as ER, PR, and HER2. VEGFR (vascular endothelial growth factor receptor) is another important surface receptor in tumor health, as it stimulates angiogenesis and vasculogenesis that build blood vessels specifically for the tumor when bound with VEGF [49]. Bevacizumab is an anti-VEGFR antibody that competitively inhibits VEGF binding and prohibits vessel formation for the tumor area. As a single therapeutic, there is a very low response (9.6%) [53], but when boosted with an anthracycline, the time to disease progression in head and neck cancers more than doubles [54]. The combination of these drugs can also be used to lower toxic effect of the small molecule drug. Cameron et al. showed that lapatinib (an anti-HER2 antibody) in combination with the anthracycline capecitabine increased survival time by 11 weeks in comparison to patients treated with capecitabine alone [55]. Chemotherapeutics play an important role in patients' treatment plan and have great uses both pre and post surgery. However, cytotoxicity issues will always arise with these drugs, as they inhibit both healthy and diseased tissue.

Whole breast radiation therapy has been used for decades as a conjunction to breast conservation therapy and has reduced the rate of recurrence and increased long-term survival of patients [56,57]. However, it delivers a large amount of ionizing radiation to the breast that is dangerous and has potential long-term harmful effects. A newer technology is accelerated partial breast irradiation (APBI) that treats a smaller volume of breast, just around the area of excision and does not expose the whole breast to

ionizing radiation. However, one concern is that areas of the breast with a multi-focal tumor will not receive enough radiation and could lead to an increase in tumor recurrence [48]. There have been recent advancements to improve APBI. The first is interstitial multi-catheter brachytherapy that places multiple catheters around the lumpectomy cavity and then delivers radiation through these catheters to localize radiation delivery. The patients can be given high or low radiation dosages, and 5-year recurrence rates ranged from 0-6% [58]. Mammosite is very similar to interstitial multi-catheter brachytherapy, but in place of multiple catheters, a single balloon catheter (Figure 2.4) that is loaded

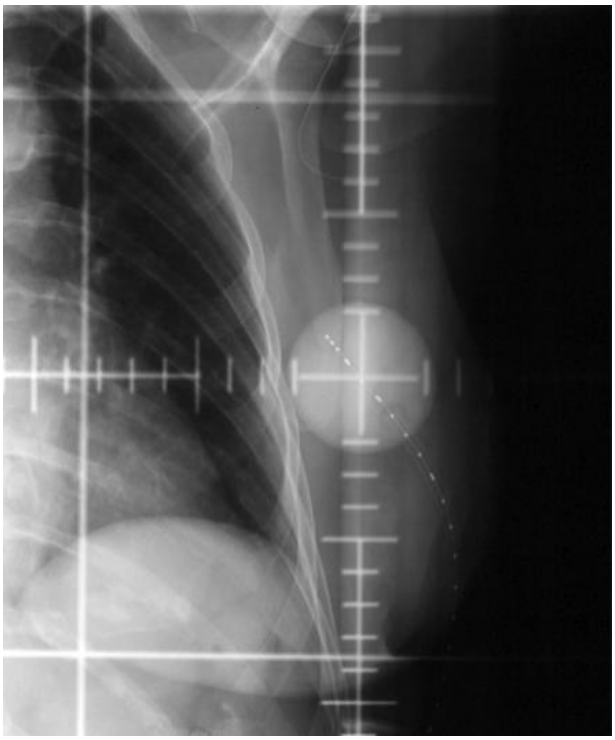

Figure 2.4. Radiograph of Mammosite balloon catheter for delivery of radiation therapy to a localized area of the breast. This catheter is located in the right breast of a patient. A radio-opaque ruler is placed over the breast with 1 cm intervals marked for sizing of the catheter. Reproduced from [59].

with saline and fills the entire tumor cavity. Radiation is delivered through this balloon twice a day. A 2008 study by Stewart et al. showed a local recurrence rate of 3.8% and good cosmetic results (>90%) after a 60-month follow up. One potential downside of Mammosite is that tumors that are in the deep breast might be too close to the heart and

deliver too high of a dose to the organ [59]. The final option for APBI delivery is using a 3-dimensional external beam to treat the tumor cavity. This requires extensive planning and modeling to ensure maximized dosage delivery to the tumor cavity because there is no catheter to deliver the radiation. Multiple studies showed no local recurrence three years after treatment [60,61]. Even though whole breast therapy is still the standard therapy for breast conservation therapy (BCT), APBI offers a new method of maintaining cosmesis and minimizing local recurrence.

Surgery remains the primary method of removing the bulk of breast cancers. There are two main surgical methods, modified radical mastectomy (MRM) and BCT. MRM involves total removal of the breast tissue [62] that lowers the chance of disease recurrence and removes the need for post-operative radiation therapy [62]. However, one major downside of MRM is the removal of the full breast, and its resulting trauma for the patient. BCT involves the surgeon removing the part of the breast with the malignant tissue and attempting to preserve as much of the breast as possible to maintain cosmesis for the patient. There is a higher chance of recurrence [4,63] with this procedure whose factors will be explored in further detail later in this section. Because of the amount of local recurrences during BCT, surgeons may remove larger volumes of breast tissue, and that has adverse effects on patient cosmesis. A new surgical specialty has developed in response to this problem, termed “onco-plastics,” which involves the use of volume replacement or reconstruction of the breast during the BCT after all malignant tissue has been removed [48]. These are very difficult surgical procedures and are the source of some controversy because it is thought that surgeons who are skilled enough to perform the plastics aspect of the surgery do not have enough knowledge of cancer as breast

cancer surgeons and vice versa [64]. Due to these complications Clough et al. developed a two-tier classification system (Clough I&II) based on the percentage of tissue being removed from the breast (Clough I <20%) that aids the surgical teams to determine the specialty of the surgical procedure [48,65]. Margenthaler defines Clough II surgeries as a surgery where two surgical specialists are present (breast and plastic) that work in tandem to complete the complicated procedure; these surgeries include radial excision lumpectomy, batwing mastopexy lumpectomy, and lumpectomy with concurrent reduction mammoplasty [48].

Technical advancements in breast cancer screening technologies have led to the detection of smaller cancerous lesions within the breast [31,66]. Due to the decreased size of the lesions, a higher number of patients are opting to undergo BCT followed by radiotherapy than the more traditional MRM [2]. Recent studies have shown that there is no difference in long-term survival rates for patients that undergo the respective treatments for early stage breast cancers [4,67–69]. While BCT is optimal for cosmesis because it preserves the original breast, many studies have shown that local recurrence occurs at a higher rate for patients receiving BCT, especially with younger patients [70–72]. Even though the rate of recurrence does not effect overall survival rate [69], patients must undergo re-excision and increased radiation dosage [2,73]. Additionally, these patients undergo stress and psychological trauma that has an additive effect on the stress already seen with initial treatment [74,75]. Most importantly, local recurrences have been associated with increased rates of metastases in patients [76,77], and these metastases due to recurrence lead to a higher mortality rate.

Many retrospective studies have been conducted to determine the factors that lead to a local recurrence after therapy [2]. These studies include patient age [78–82], tumor size[78,81,83], radiation treatment [79,80,83], and lymph node status [78,83,84]. Even though these studies found that these factors can be used as independent predictors of a local recurrence of breast cancer, tumor margin status is still thought of as the strongest predictor for recurrence [85–88].

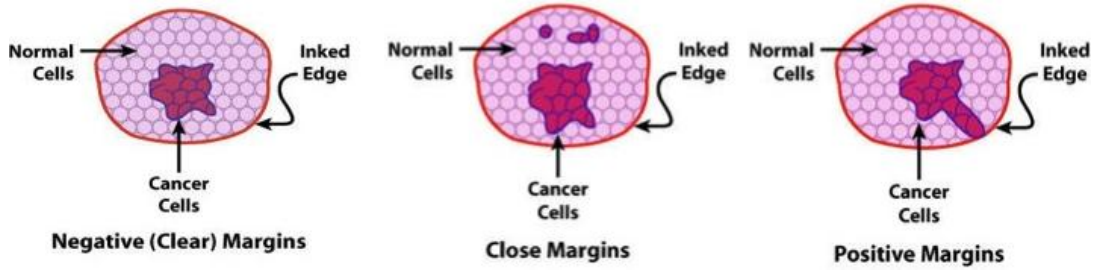

Figure 2.5 Cartoon rendering of margin status interpretation. Negative margins indicates that there are no cancerous cells in the predetermined margin width. Close margins indicated that there are cells within the margin width, but not at the edge of the resected specimen. Positive margins indicate that malignant cells are on the edge of the resected specimen. Reproduced from [95]

2.4. Tumor Margins

The tumor margin is the area around the edge of the resected tissue specimen of the patient (Fig. 2.5). Tumor margin status refers to the question of whether or not there are microscopic cancer cells located at the edge of the excised tissue specimen; a positive status indicates microscopic disease, whereas negative indicates disease free tissue. It is generally thought that if there are cancerous cells on the edge of the tissue, then the patient has an increased chance of a local recurrence due to the increased chance of cancerous cells not being removed from the body [87]. However, this is where the consensus on margin status ends, and argument begins [87]. Many studies have argued

and presented evidence as to what constitutes a proper negative margin for patients [89–93]. In particular, the argument over what is the proper distance from the edge of the tissue that must be disease free in order for the patient to have negative margins. For example, Zavagno used a distance of 3 mm whereas a panel led by Kauffman recommends that as long as there are no cells "touching ink" then the patient should be declared to have free margins, effectively a margin distance of 0 mm [91,94]. Additionally, some studies use a third diagnosis: a close margin. Close margins are defined as tissues that contain microscopic disease within the pre-determined margin width, but not at the edge of the tissue [95]. This leads to the conclusion that it is very difficult to compare studies that use different indications of negative margins; however, it is accepted that the margin status (regardless of the definition of distance) is an important predictor of local recurrence.

The distance in margin status is important in BCT because surgeons are trying to strike a balance between treating the disease while also maintaining cosmesis for the patient. Studies have shown that having a more normal breast appearance has positive psychological effects for patients who have undergone breast cancer treatment [96–98]. Increasing margin width will add to the amount of excised tissue during surgery leading to a higher difficulty of maintaining cosmesis [99] and perhaps leading to future psychological problems for a patient. In 2010, Houssami et al. performed a meta-analysis of 21 margin status studies to determine how well margin status and width correlated with local recurrence rates. The authors found that positive (or close) margins correlated positively with local recurrence and patients with a negative margin status had a lower rate of recurrence. However, the study also concluded that the increasing the tumor

margin width (ranges of different studies were 1-5 mm) did not significantly lower the rate of recurrence, especially when they considered if the patient received a radiation therapy boost [87]. However, Houssami et al. did recommend that surgeons use at least a 1 mm margin width when determining margin status in contrast to the "touching the ink" method recommended by Kaufman [87,94].

Proper margin width is debatable throughout the medical community; however, the principle of removing as much diseased tissue as possible during surgery still holds paramount to reducing local recurrence. There are numerous ways that physicians can increase the amount of diseased tissue removed by obtaining information about the tumor preoperatively [2].

2.4.1. Pre-operative imaging to improve margin status

Pre-operative imaging includes mammography, which allows the surgeon to assess the borders of a palpable tumor before the procedure begins. Additionally, physicians can determine if there are micro calcifications in the breast, an indicator of possible DCIS presence [100]. A recent study by Rauscher et al. discovered that mammography has a high sensitivity in cancerous detection (94%), however it is lacking in specificity (61%) due to the presence of islands of fibroglandular or fibrocystic tissue in the breast that are indistinguishable from malignant tissue [101,102]. In some patients, ultrasound is used to supplement mammography findings as it provides better information on size and growth patterns of tumors [2]. MRI is a newer technology that provides significant improvement in pre-operative imaging of cancerous tissue when compared to mammography and ultrasound [103], especially with DCIS (Fig. 2.6) [104]. MRI provides patients and physicians with extensive information, such as multifocality of the disease, that can help

determine if a patient should even undergo BCT [3]. A study by Houssami et al. demonstrated that MRI helped detect additional cancer in 16% of patients, leading 1.1% of patients to select a mastectomy over BCT [105]. Even though MRI can help direct patients away from a surgery in order to decrease the chance of local recurrence, its preoperative use does not have a significant impact on margin status or local recurrence [106,107]. This is likely due to intra-operative MRI not being available [108].

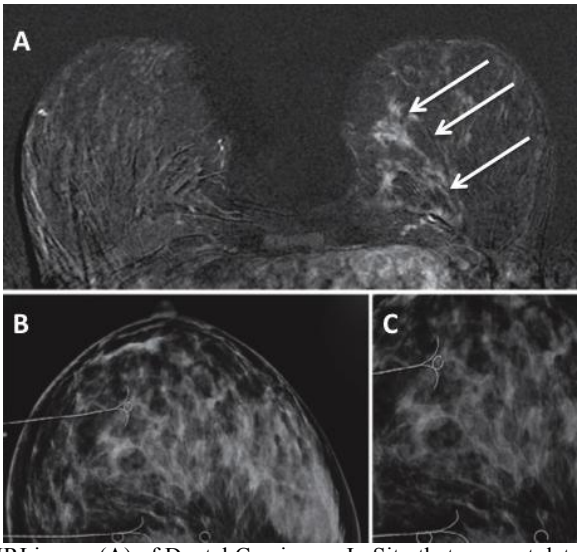

Figure 2.6. Pre-operative MRI image (A) of Ductal Carcinoma In Situ that was not detected with mammographical screening. B&C demonstrate zoomed in pre-operative mammographical views of the same breast with clips localizing the tumor. Notice the lack of contrast in the mammography, demonstrating the efficacy of MRI in delineating DCIS. Clips were placed with MRI. Reproduced from [104].

2.4.2. Current intra-operative visualization of breast cancer

Due to limitations of implementing pre-operative techniques intra-operatively and their minimal effect on overall margin status and local recurrence, methods of peri-operative tumor localization have been developed to improve resection of tissue. For twenty years the standard for intra-operative localization was wire-guided localization (WGL). WGL involves a pre-operative procedure in which a wire is placed in the tumor

under the guidance of ultrasound, X-ray, or mammography. The surgeon would then use the wire's location during surgery to help extract diseased tissue. There were many problems with this procedure;the wire tended to move between procedure and surgery, the wire did not provide 3-dimensional information for the tumor (making edges of the tumor difficult to locate), and it was very uncomfortable for the patient [2,109]. Recent studies also demonstrate that WGL was ineffective, with 21-43% of patients diagnosed with positive margins [110–112] after surgeries implementing WGL. A newer technique is intra-operative ultrasound (IOUS) guided excision that uses ultrasound in the surgical suite to guide resection of both palpable and non-palpable tumors. Several studies have shown that positive margin rates for this technology range from 3 to 11% [113–116], with Rahusen's study directly comparing IOUS to WGL and showing a much better sensitivity (11% positive margins for IOUS compared to 45% for WGL) [115]. However, IOUS cannot detect the micro-calcifications that are associated with ductal carcinoma in situ (DCIS), which limits the usefulness of the technique. X-ray radiography of the excised tissue is another intra-operative technique to improve patients' margin status. However, this technique has very low sensitivity and is limited to detection of tumors without calcification [117]. Cryoprobe-assisted localization (CAL) is another methodology that is helpful in resection of non-palpable tumors. An ultrasound helps guide a cryoprobe into the tumor, which then freezes the tumor into a detectable sphere that is easier to find and remove. Tafra et al. found that there was no significant difference between CAL and WGL in reducing the amount of positive margins or rates of re-excision; however, there was a significant reduction in excised tissue volume which improved cosmesis [118]. Even though these techniques have shown promise as an intra-

operative technique for margin detection, each has its limitations and each is a supplement to surgery. They have also yet to replace the gold standard for peri-operative margin detection: intra-operative pathology.

Intra-operative pathology involves the use of an on-site pathological team that slices, stains, and analyzes the resected specimen while the patient is still under anesthesia. The pathological team stains the various edges of the tissue to give spatial orientation of the tissue (Fig. 2.7) in order that the physician can tell the physical location of malignant tissue with regards to the edge of the resected specimen. Next, the tissue or cells are stained for hematoxylin and eosin (H&E) [119]. A pathologist then reads and analyzes the samples and informs the surgeon where there is still microscopic disease present. The surgical team will then decide whether to proceed with a re-excision. Hematoxylin is a blue stain that stains DNA in the nucleus, and eosin is a pink dye that stains other cellular structures. There are two different methods of intra-operative pathology, frozen section analysis (FSA) and intra-operative touch prep cytology (IOPTC).

Figure 2.7. Inked breast specimen indicating spatial orientation of the resected specimen. Green area is thought to be area of tumor. Tissue will be frozen, sliced, and stained for H&E. An on-site pathologist will then indicate where cancerous cells are present. Reproduced from [85].

FSA involves freezing, slicing, staining, and a pathologist analyzing samples to determine the presence of malignant cells. The pathologist will work with the surgeon while the patient is under anesthesia, and the team of physicians will determine whether or not the surgeon needs to remove more tissue from the patient. This process adds an average of 30 minutes to each surgery [12]. While there is risk with holding the patient under anesthesia for an extended amount of time, the benefits outweigh the risks because this procedure decreases the chance that patients will have to undergo a second surgery (and subsequently go under more anesthesia) and increased radiation dosage. Since 1994, M.D. Anderson Cancer Center (MDACC), a leading cancer research institution, has been performing FSA during BCT. In a 2007 article published by Cabioglu et al., the authors evaluated the effectiveness of the FSA procedure at the institution and found that the overall accuracy of the procedure was 87.4% [71]. Studies by Camp, Riedl, and Olson showed that 24-27% of patients undergoing lumpectomy had additional tissue resected after FSA [11,12,120] during the same surgery, however Camp and Riedl's studies did

not show an overall improvement in local recurrence [11,12]. Additionally, studies have shown that FSA has high specificity but a lower and more inconsistent sensitivity rate [71,120,121]. Pleijhuis et al. concludes that while FSA lowers the need for a second excision, it does not reliably improve negative margin rates [2].

IOPTC has been promoted as an alternative to FSA because of its speed, simplicity, and relative low cost [122,123]. Its process involves placing a glass slide at the edge of the tissue. Surface characteristics of the cancerous cells will allow them to stick to the slide, whereas the benign mammary cells do not. The cancerous cells are then stained with using H&E, or other cellular stains [124,125], and margin status is determined. A study by Weinberg et al. showed that IOPTC significantly lowered recurrence rates (2.8% vs. 8.8%) when compared to all other margin assessment procedures [126]; however this study did not differentiate between patients who received intra-operative pathology or had permanent analysis performed post-operatively. Additionally, IOPTC is adequate for determining if there are malignant cells on the edge of the tissue, but does not give any indication if there are cells within the margin width, and pathologists will not be able to determine margins [2,71]. Additionally, there may be scarring, cell damage, and artifacts on the edge of the resected tissue as a result of the cauterization that the surgeon has to perform when the specimen is removed [89].

While both FSA and IOPTC are promising techniques, they have limitations. Firstly, they require an on-site pathological team consisting of technicians and a pathologist. This is not feasible in many community hospitals due to costs and number of physicians (currently, <5% of hospitals offer this service) [127–129]. There is a vast unmet need for surgeons to be able to visualize tissue peri-operatively without the use of

a full pathological team. Techniques continue to evolve to aid surgeons in determining margin status. We are now going to discuss some future techniques that range in stages of development, from taking part in clinical trials to still being developed on the bench-top.

2.4.3. Future intra-operative imaging devices

One device that has been developed for use in a clinical setting is the MarginProbe™ from Dune Medical Devices. The device is a spectroscope that measures the response of cells when interacting with broad range of radiofrequencies [85]. The device has a detection volume of about 38.5 mm^3 that uses an algorithm to compare signal reflected from tissue to previously recorded signal from tissue (Fig. 2.8). It gives the surgeon a simple readout of negative or positive using this algorithm. Recently it received a pre-market approval from the food and drug administration for clinical use in the United States. The sensitivity of the device over a range of margin widths averaged 67% sensitivity and a specificity of 68% [85]. Another study by Allweis et al. demonstrated that the MarginProbe™ was effective at lowering rates of a second surgery (12.6% to 18.6%) that was not statistically significant. Additionally, the volume of excised tissue for the device was higher than that of the control group, which may have skewed the results in the device's favor [130]. Even though the device is not as effective as other options, it does show that there is potential for development of an intra-operative tool for surgeons to use as a supplement to already existing technologies.

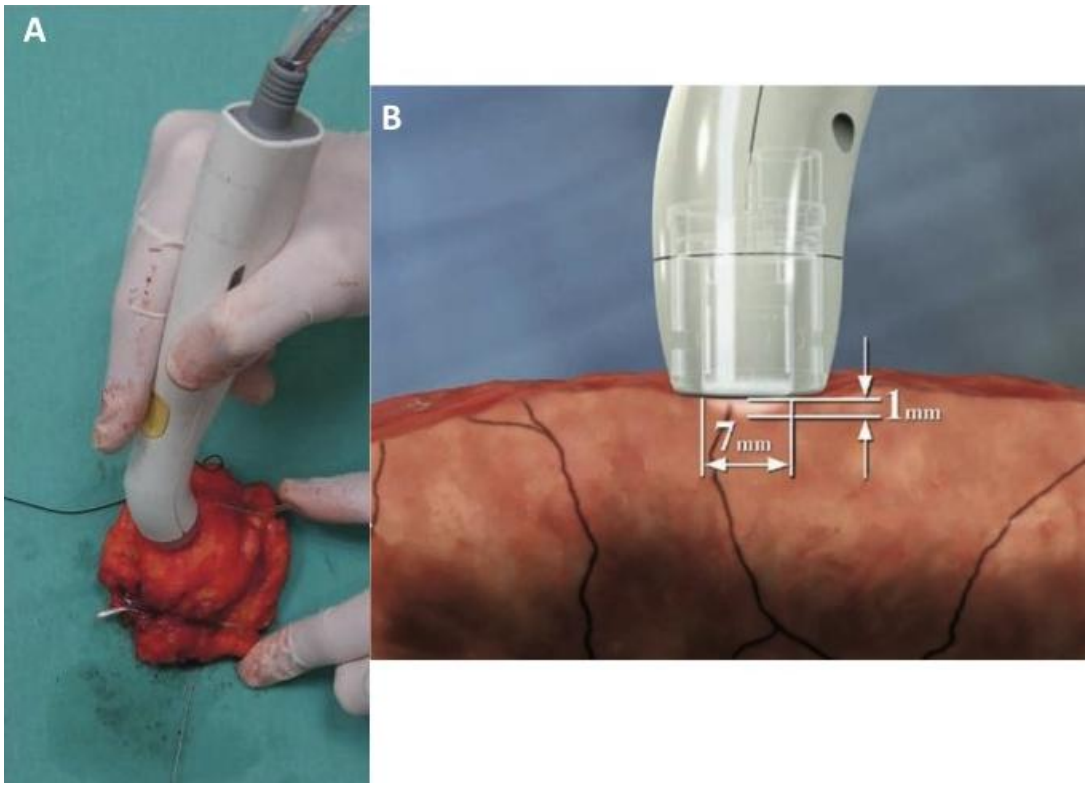

Figure 2.8. Examination of gross tumor specimen (A) of the MarginProbe™ intra-operative margin assessment device. (B) shows the effective volume of examination of the assessment device on the resected specimen. Reproduced from [85].

PET has been used for imaging malignant breast tissue for many years [20,33,131], especially as a noninvasive method of monitoring chemotherapeutic response [132]. PET uses a radio-labeled glucose analog, ^{18}F-FDG, that accumulates in areas of high metabolism, such as malignancies [21]. PET has a high sensitivity value in detection of large lesions (>1 cm) [33,133,134] but its specificity is low due to accumulation in non-malignant cells that are associated with infection and inflammation [135]. In addition to the sensitivity and specificity concerns of PET, it originally was not a good candidate for intra-operative imaging because the device was large and not practical for a surgical suite. However, recent technological developments have enabled hand-held PET probes in colorectal [136], renal [136], ovarian [137], and breast cancer [138]. The handheld probes are a very nice proof of concept; however, for BCT

implementation, there is still the issue that PET cannot detect lesions under 1 cm, and with recent screening technologies being able to detect lesions even smaller than that, the handheld probe would not be useful during BCT because as it could not detect something below its resolution limit. Additionally, the use of a radio labeled tracer in the surgical suite not only has safety implications for the patient but for the entire surgical staff [139], and repeated exposures may have long-term carcinogenic effects on medical personnel.

Another radio labeled visualization technology is radio guided occult lesion localization (ROLL). This technology is described as a theranostic device that can both visualize and resect the desired tissue from the patient. ROLL is similar to WGL in that it uses a pre-operative procedure to inject a non-targeted radioisotope into the tumor. During the surgery, a handheld gamma probe locates the isotope in the tumor and guides excision. As with WGL, the placement of the isotope is paramount to maintain specificity and sensitivity. Studies have shown correct placement of the radiotracer in 95-100% of cases [110,112,140–142]. This technique shows approximately the same clinical success as WGL. 20% of patients in the study by Sarlos et al. had positive margins post-operatively [140], and surgeons were able to detect the lesions at a rate of 98%. Even though, ROLL achieved the same clinical results as WGL, it was found to be more comforting for the patients and an easier technique for surgeons to perform [142]. Even though ROLL seems to be an alternative to WGL; however, surgeons have yet to see an improvement in re-excision rates for this technique, which likely means that the limitations seen with both technologies are probably from the pre-operative placement and the imaging device used to implant the radiotracer or wire.

The next evolution of imaging breast cancer is the use of optical imaging with targeted contrast agents and autofluorescent signal of tissue. Currently, near-infrared fluorescence (NIRF) has shown strong development and progress as a clinically relevant breast cancer imaging modality [2]; however, most clinically relevant trials have been limited to mapping sentinel lymph nodes with indocyanine green (ICG) [143–146] and not breast malignancies [147]. NIRF is considered a candidate for optical imaging of breast cancer as it has resolution down to 10 μm, higher penetration depth than light in the visual range, and autofluorescence of molecules in this wavelength is reduced [146–148]. Even though NIRF has shown great potential in cancer studies, it is limited to the use of contrast agents that must be injected into the patient, and there are cytotoxicity issues involved with the agents inside the patient, particularly at the levels needed to differentiate tissue [148]. However, NIRF contrast agents can still be used on excised tissue, which would allow physicians to use the contrast agents' positive aspects while minimizing their negative impact. This possibility will be discussed in chapter 4.

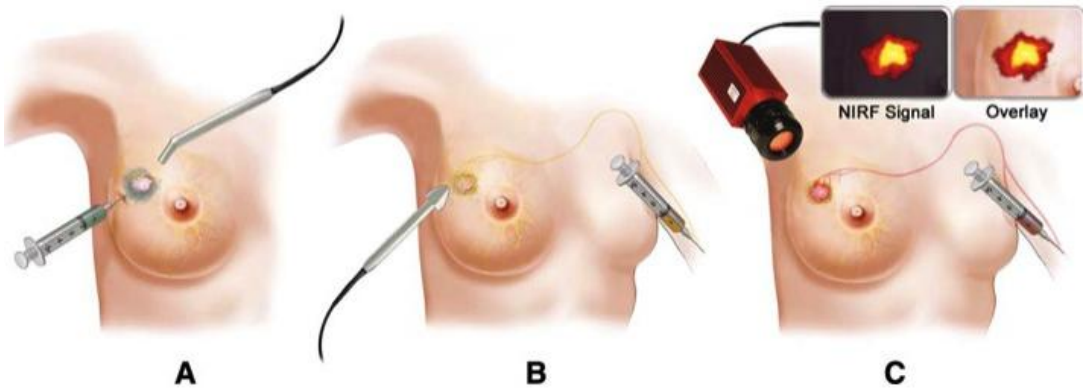

Figure 2.9. Future intra-operative *in vivo* methods to visualize cancerous tissue during BCT. (A) Radio-guided occult lesions localization (ROLL). (B) Handheld positron emission tomography (PET), (C) Near-infrared fluorescence (NIRF) Reproduced from [2].

Other imaging modalities use the endogenous signal differences between cancerous and non-cancerous tissue to attempt to differentiate tissues without contrast

agents. These signal differences arise from a difference in oxygenation of blood, hemoglobin content, and cell density [149–151]. One of the most successful of these technologies is Diffuse Optical Imaging (DOI). DOI has been used to measure the absorption of a broad spectrum of NIR light that is directed into specimen. Due to the presence of absorbers such as deoxy-hemoglobin, hemoglobin, lipid, and water, light will propagate through a tissue in different time lengths. These lengths can be measured, and correlated to the presence of specific absorbing molecules that characterize malignant or benign tissue [152]. Figure 2.10 shows a DOI image corresponding to the amount of oxygenated hemoglobin that is present in IDC in a patient. The data corresponds well to the MRI image delineating the tumor. This data can be combined with other imaging modalities such as mammography, and a quantitative 3-dimensional map of the breast can be created. Additionally, a study by Kurkredi et al. demonstrated tumor only spectra (650-1000 nm range) in 22 cancerous patients versus 43 normal patients [153]. However, those studies were not used to study margin status, and reconstructing an image intra-operatively would be very difficult. Wilke et al. developed a spectroscopic imaging

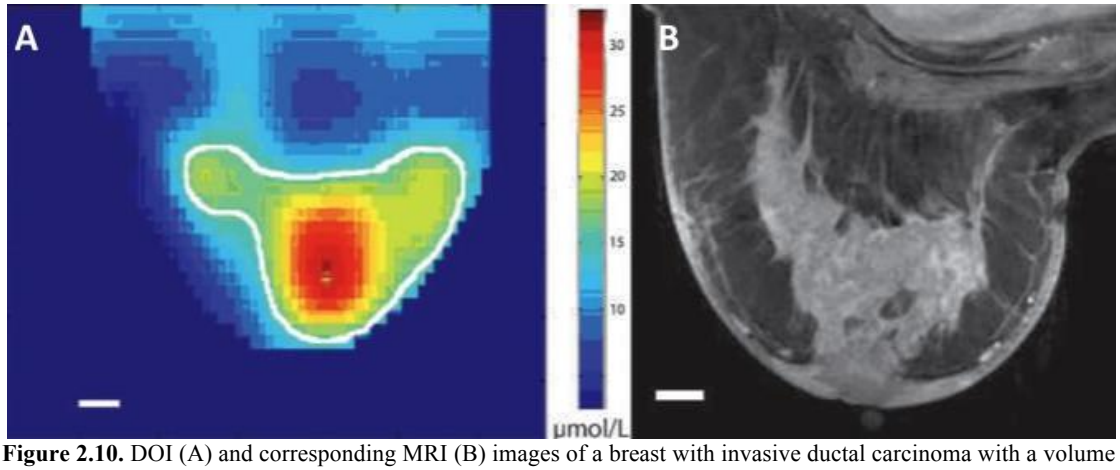

Figure 2.10. DOI (A) and corresponding MRI (B) images of a breast with invasive ductal carcinoma with a volume of 5.5 X 6.5 X 7.5 cm. Color map of DOI image shows areas of high oxygenated Hemoglobin that correspond very well to area of tumor. Reproduced from [151].

device that measured β-carotene scattering coefficient in negative, close, and positive margins. The increased coefficient is due to decreased adipose tissue and higher cell density [149]. Though this study showed success, (identified 79% of positive tissues correctly), there was decreased accuracy with patients who received neoadjuvant therapy which affected physiologic and metabolic parameters that were used in their algorithm [149]; this device shows great potential for intra-operative margin assessment.

Many technologies have been developed to help physicians visualize diseased tissue intra-operatively. Whether it is pre-operative procedures, radiolabeled tracers, or using endogenous tissue differences, there are a number of methods to delineate malignant tissue. As previously stated, less than 5% of BCT are completed with the use of intra-operative pathology assessment [127]. The overall goal of this project has been to develop a method of differentiating malignant breast tissue that has the potential to be used in a portable, inexpensive, and rapid manner, with minimal processing performed on the tissue to maximize speed and minimize time that a patient is under anesthesia. Our aim is the construction of a system that can be used intra-operatively without the added cost and time of extra technicians or pathological staff. This system would enable the surgical team to take whole tissue at the margin area, add a targeted contrast agent, and visualize malignant tissue during surgery. Previous work has demonstrated the efficacy of using antibody targeted silica-gold nanoshells (NS) as a visual contrast agent in cells [154,155], tissue slices [129], and even as a theranostic [156]. These studies have demonstrated that NS can be used in an efficient and rapid (<5 minutes) manner to differentiate cells that can be visualized using a variety of optical imaging techniques. However, these studies were performed on cell lines or tissues that needed to be sliced to

obtain images. Tissue slicing requires an element of time, equipment, and personnel that would add to the cost and complications of the surgical procedure.

Additionally, these studies used expensive imaging equipment, and with exception of the Bickford et al. study from 2010 that utilized a Lucid VivaScope 2500 (Fig. 2.11) [129], images were acquired with modalities that do not readily translate to the clinic. There remains a vast unmet need to further research into developing methods of imaging whole tissue rapidly with a portable and inexpensive system used in conjunction with targeted contrast agents.

2.4.4. Importance of visualization of the over-expression of HER2 receptor

Our previous research has used silica-gold NS linked to the anti-HER2 antibody that attaches to HER2 on the surface of cells, and we can use this targeting mechanism to visualize over-expression of HER2 in malignant cells. HER2 is an EGFR that is part of the ErbB family [39], a group of four tyrosine kinase receptors expressed on the surfaces of cells in various levels. When expressed in proper levels, the receptors have a role in cell growth, proliferation, and differentiation; however, abnormal expression levels are

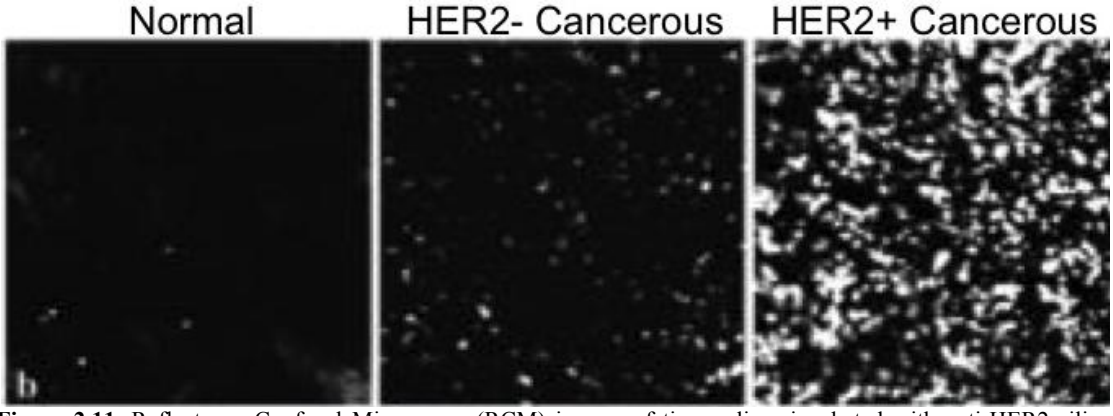

Figure 2.11. Reflectance Confocal Microscopy (RCM) images of tissue slices incubated with anti-HER2 silica gold Nanoshells. Images show that HER2+ tissue had much higher signal due to the presence of the antibody targeted nanoshells. Reproduced from [ref 129].

apparent in malignancies of a variety of organs, not only breast, and lead to uncontrolled cell growth [14]. The other three receptors include HER3 and HER4, and the commonly known EGFR. The HER2 receptor is most commonly associated with breast cancer because it is found in 25% of all breast cancers and is thought to be a more aggressive subtype of cancer [14–17] that is associated with less favorable clinical outcomes. Even though tumors that are HER2-positive are considered to be a more dangerous subtype, the over-expression of the receptor has made it easier for targeted therapy using a monoclonal antibody against the receptor, either trastuzumab [157,158] or lapatinib [159,160]. This has also led to research in targeting the HER2 receptor for contrast agents, such as silica-gold NS [154–156] that can help physicians visualize HER2 status in tissues and cells.

Visualization of growth factor receptors at the margin status could be more important for pathologists than previously thought. As mentioned previously, cells at the tumor margin are stained for H&E, and pathologists use these slides to determine disease extent and margin status. This helps the team of physicians determine the course of action for post-operative treatment of the patient. However, a recent study of oral squamous cell carcinoma by Vosoughhosseini et al. demonstrated that there were cells that over-expressed EGFR in the samples that were deemed to be negative margins by normal H&E [13]. This is significant because patients who are declared cancer free, are, in fact, not, which is a possible explanation for local recurrence when patients are declared to have negative margins. Additionally, a false-negative leads to a different post-operative treatment regimen that could possibly allow the cancer to proliferate at a higher rate than if the proper diagnosis was made. Another growth factor, VEGF, has been studied as a

possible marker of local recurrence. With only three published studies, no conclusive evidence has yet to be established. Moran et al. found that in only a specific sub-group of patients with local relapse, was VEGF an independent indicator; however when performing multi-variate analysis with that same group, they were not able to reach statistical significance [161]. Linderholm et al. found that VEGF status contributed to overall survival but did not mention VEGF as a predictor of local recurrence [162]. A study by Manders et al. concluded that VEGF contributed to reducing the effectiveness of radiotherapy in patients with negative lymph node status [163]. These studies indicate that physicians are delving deeper into receptor phenotype as indicators for all aspects of the treatment of breast cancer and that there is much to be gained from knowing these phenotypes.

Lowery et al. states that knowledge of the molecular phenotypes in breast cancer will not only help drive treatment decisions that will optimize patient care, but will offer valuable insight into prognosis [40]. Recent reviews that have studied the relationship of tumor expression and results such as margin status and local recurrence [18,39,45]. Tse et al. found that high EGFR expression was implicated in the pathogensis of phyllodes tumors [39]. Wang et al. concluded that DCIS patients that were HER2-positive had a higher rate of recurrence than patients that were hormone receptor positive [45]. Additionally, in a retrospective study of 143 patients by Miller et al., 27% of patients with a positive margin were HER2-positive versus 15% of patients with a negative margin (p-value 0.04) [18]. DCIS was of particular importance to these studies due to the increased incidence and smaller lesions that are a result of the improved screening technologies. Over-expression of HER2 occurs in up to 50% of lower grade DCIS;

however, 50-100% of higher grade DCIS over-express the receptor [14]. Wang et al. found that patients that were ER-/PR- but HER2-positive had a higher rate of recurrence than patients that were ER+/PR+ and HER2-negative [45]. A 2004 study by Miller et al. states that in DCIS patients with HER2-positive status it is more difficult for surgeons to reach negative margins on patients with these characteristics than other types, including invasive carcinomas that were HER2-positive [18]. In 2011, Munirah et al. found that a higher percentage of HER2-positive patients had positive lymph nodes (regardless of estrogen receptor status), indicating the aggressiveness of the subtype [164]; a 2006 study by Kim et al. showed that HER2-positive cancers were the most frequent subtype found in distant metastases [165].

Due to the increasing incidence of DCIS [166,167], the increased number of DCIS patients choosing BCT over mastectomy for DCIS [14], the increased prevalence of HER2-positive tissue in DCIS [41], and increased chances of local recurrence with HER2-positive DCIS [168,169] there is a need for a method not to identify cancerous tissue at the margins, but HER2-positive cells at the margin during BCT for DCIS. As stated previously, Vosoughhosseini et al. demonstrated that normal H&E might not be good enough to identify all cancerous cells at the margin [13], and a method to identify HER2-positive cells rapidly and intra-operatively gives physicians another tool to ensure negative margins are achieved during excision.

Our aim is to use these targeted contrast agents to differentiate tissue that over-expresses HER2-positive tissue from HER2-negative tissue optically. An imaging system that combines proper optical set-up to visualize an agent with high luminescence, such as silica-gold NS, could be an invaluable tool for surgeons intra-operatively as they

attempt to achieve negative margins that have been difficult to achieve in HER2-positive cancers [18]. As demonstrated with earlier research, our targeted nanoshells have shown measurable results in differentiating individual HER2-positive cells from noncancerous cells because an average of 1500 nanoshells were bound to each HER2-positive cell [155]. This is important because studies deem patients to be HER2-positive when there is strong immunohistochemical staining in greater than 10 [41,165] – 20% [170] of the cells being examined. During an intra-operative procedure where cells will be visually detected, such a small percentage of cells might be difficult to detect optically. The optical properties of silica-gold NS offer vast potential for use as an intra-operative contrast agent. Additionally, the use of a NIR fluorescent dye (IRDye) that targets EGFR has potential for use. Using NIR LEDs and white light imaging, we hypothesize that we can visualize both the IRDye fluorescence and the scattering and absorbance of anti-HER2 to detect HER2-positive cells and tissues.

In the proceeding chapters, we will discuss the increased use of nanotechnology as a theranostic, the utility of optical imaging for cancer diagnostics, and how our research will combine the use of optical imaging and nanotechnology to provide a new method to visualize cancerous tissue intraoperatively.

Chapter 3

Nanoparticle Use in Cancer Treatment and Diagnosis

3.1. Introduction

The previous chapter presented a review of breast cancer from the different subtypes to intra-operative imaging options. In this chapter, we will explore nanotechnology and overview the current use of nanoparticles (NPs) in treating cancer through improved diagnostic and therapeutic applications. Nanotechnology in medicine has been in use for approximately thirty years [171,172], with different NP materials offering various clinical uses. For example, iron oxide NPs are used as contrast agents in MRI because of their magnetic properties [173,174]. Dendrimers are branched polymers whose size can be controlled by the number of polymer generations [171]. The physicochemical properties of dendrimers have been utilized for photodynamic therapy [175] and gene delivery [176]. Liposomes are nanostructures with a core of water (and

drug) surrounded by a lipid bilayer [177]. The first NP approved for human use by the FDA is a liposome that encapsulates the anti-cancer drug doxorubicin. Studies demonstrated that encapsulating doxorubicin in these liposomes not only decreased cardiotoxicity of the drug, but also improved the accumulation efficiency of the drug in breast cancer [178,179]. In addition to particle type, other factors such as size, surface charge, and targeting mechanisms also have an effect on particle efficiency and uptake in both *in vitro* and *in vivo* studies. This chapter will explore the classes of NPs and the evolution of NPs that has resulted from increased study and understanding of the interactions between NPs and the biological environment into which they are introduced.

3.2. Classification of Nanoparticles in Cancer Treatment

In the introduction, we introduced three different NPs that are used in breast cancer treatment. This section will explore those NPs and other formulations in depth. From a materials standpoint, NPs can be classified into two categories: "flexible" particles that are made of polymers or liposomes and particles that are composed of inorganic material [177].

3.2.1. Flexible nanoparticles

Most flexible NPs are in the size range of 30 to 100 nm and have an advantage over inorganic particles, as they are composed of materials that have natural interactions with the cell membrane. These characteristics help inorganic NPs penetrate the cell membrane more easily than inorganic NPs. Correspondingly, this can increase the amount of drug delivered to the inside of a target cell.

The second NP to be approved by the FDA for use in cancer therapy was Abraxane®, a 130 nm diameter conjugate of Taxol® to albumin [171,177]. Albumin can solubilize Taxol® as efficiently as Cremophor EL®; however albumin does not have the same toxic side effects that are a result of using Cremophor EL® [171,177]. In addition to increased solubility, there was an increase in intratumoral accumulation with these particles. Desai et al. hypothesizes this is due to the caveolin-1 transport mechanism that naturally occurs in cells that express the gp60 receptor, and this system actively transports the bioconjugate into the cells after albumin binding [180]. Miele et al. and Hawkins et al. both suggest that the overexpression of osteonectin, a matrix glycoprotein that shares the same binding sequence as gp60, in breast and prostate cancers leads to high accumulation of Abraxane® in these tumors [181,182].

Solid lipid nanoparticles (SLN) were introduced in 1995 by Müller et al. [183]; they can be optimized to carry either lipophilic or hydrophilic drugs depending on the method of NP production [177]. Additionally, SLN have controlled release mechanisms that allow the NPs to exhibit versatility in drug administration (oral or otherwise) [177]. SLN can protect their encapsulated drugs from degradation [184] with low systemic toxicity [185], but they handle a low volume of drugs [184]. While SLN have dramatically decreased toxicity of standard chemotherapeutic drugs, there is a lack of targeted SLN mechanisms that can increase targeting *in vivo*.

Dendrimers are promising agents for breast cancer treatment as researchers can easily control the particles' molecular weight and structure [186]. Their unique chemical and physical makeup allows for binding and packaging of an array of chemicals: from contrast agents, to targeting ligands, to therapeutic compounds [177]. They can either

physically encapsulate drugs inside their spherical structure or act as drug-dendrimer complexes [171,177]. This diversity in application is evidenced by two studies released by the Baker group. In the first study, researchers conjugated both fluorescein isothiocyanate (FITC) and fibroblast growth factor-1 (FGF-1) to the same dendrimer, poly amidoamine (PAMAM), to visualize the cellular trafficking of FGF-1 time (Fig. 3.1) [187]. In the second study, Choi et al. demonstrated that the same generation PAMAM dendrimer could be conjugated to doxorubicin and folic acid to function as a targeted drug delivery agent. This compound was then excited with ultra-violet (UV) light and the drug was released in a controlled manner [188]. Even though dendrimers have shown great pre-clinical promise as agents in the treatment of cancer, only one has entered clinical trials, the VivaGel™ microbicide [171], a treatment for HIV. The lack of clinical progress may be because the dendrimer itself can be cytotoxic to the host or because the drugs encapsulated within the NP are released very rapidly upon entry into the host [171,177].

3.2.2. Inorganic nanoparticles

The other main class of NPs is the inorganic NP that is composed of one or more inorganic compounds such as gold, iron, or silica. Super-paramagnetic iron oxide nanoparticles (SPIONPs) are currently the most popular type of NP as they offer a multi-modal particle whose iron core can be imaged via T_2 weighted MRI [171,177,189]. Researchers have also been able to conjugate contrast agents, drugs, or siRNA to its surface [190,191]. A study by Yu et al. demonstrated that SPIONPS labeled with both doxorubicin and Cy5.5 could be used as a multi-modal contrast agent that also delivered a therapeutic drug to the target [192].

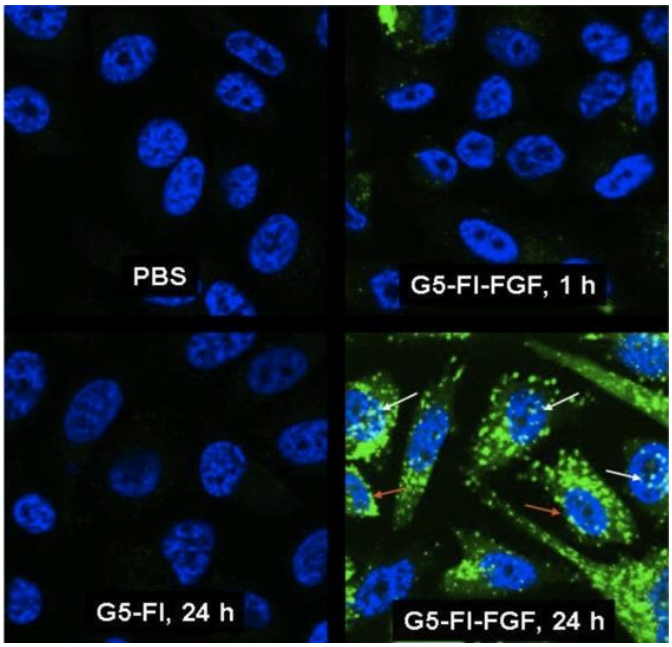

Figure 3.1 G5-FTIC-FGF complexes incubated with MCF7 cancer cells at 1 and 24 hr timepoints. Controls of cells without NP incubation and cells incubated with non-targeted NPs demonstrate specificity of complex. Different time points show that complexes can be tracked as NPs enter cell via cell internalization mechanisms due to FGF interaction with the cell line. Reproduced from [187].

Treatment of cancer using gold-based NPs (AuNPs) has increased in the past decade. AuNPs are popular because they are non-toxic, a variety of molecules can be functionalized to their surface, and they exhibit strong plasmon resonance (PR) properties [193–195]. PR is the oscillation of electrons along the surface of the particle upon interaction with an electric field [196], and the PR of AuNPs is manifested in their strong absorption or scattering capabilities [195]. The PR wavelength of a particle is dependent upon the physical characteristic of the AuNP such as size [197,198], shape [199], and surface chemistry. The PR wavelength can be tuned to achieve scattering of the incident light at wavelengths from the visible to NIR [200]. Both Sokolov and El-Sayed et al. have demonstrated enhanced molecular targeting of AuNPs by conjugating an anti-EGFR antibody to the surface of AuNPs and visualizing the particles via reflectance [201] or transmission [200] (Fig. 3.2).

Due to their electron dense structure and non-toxic effects, AuNPs have also demonstrated utility as contrast agents and therapeutics in CT and X-ray systems. Hainfeld et al. demonstrated increased CT contrast in a mouse breast cancer model by injecting 1.9 nm diameter AuNPs intravenously. The small size of the NPs allowed for clearance of the particles in 24 hours, demonstrating the safety of the particles [202]. Kim et al. injected 30 nm AuNPs conjugated to polyethylene glycol (PEG) and

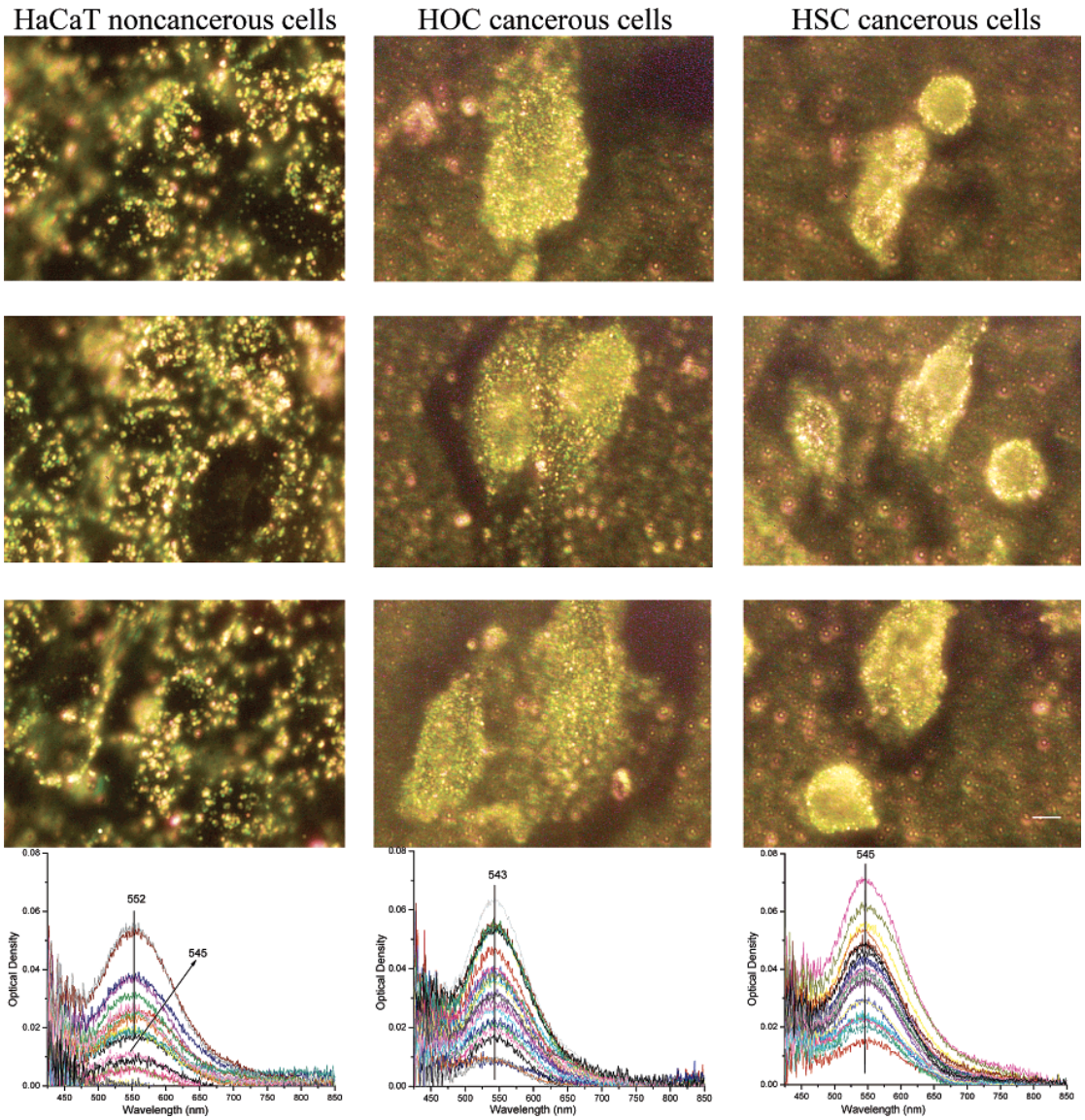

Figure 3.2 Representative scattering images and absorption spectra of anti-EGFR AuNPs incubated with noncancerous and two malignant oral cell lines. Representative spectra from 23 cells in each condition is shown. Peaks for cancerous cells are shown to be at 543 and 545 nm respectively, where as non-cancerous HaCaT have a peak at 552 nm. Reproduced from [200].

demonstrated increased contrast with no increased cytotoxicity in a rat hepatoma model [203]. A study by Geng et al. showed decreased proliferation in ovarian cancer cells due to the increased presence of glucose-capped AuNPs inside the cells interacting with X-rays [204]. Another study by Zhang et al. demonstrated increased cytotoxicity in prostate cancer cells due to the combination of glucose-covered AuNPs and X-ray radiation (Fig. 3.3) [205]. AuNPs have also been used as delivery agents for gene transfection as ammonium groups functionalized to the particles' surface can bind plasmid DNA and protect the DNA from digestive enzymes such as DNAse I [206].

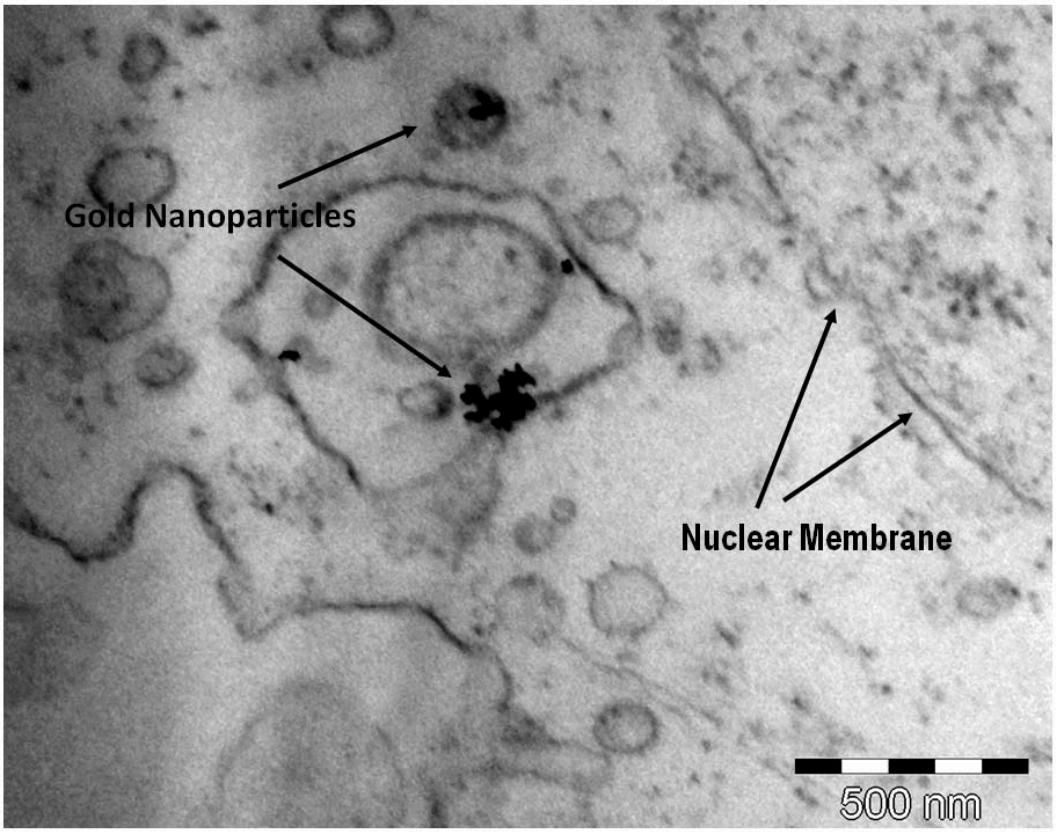

Figure 3.3 Thioglucose capped AuNPs localized to the interior of Du-145 prostate carcinoma cell. High-resolution TEM images show aggregates of AuNPs in vesicles in the cytoplasm near the cell membrane. Reproduced from [205].

The studies mentioned previously were examples of NPs composed solely of one material. Another class of NP is termed a nanoshell (NS), which consists of a core of one

type of material (usually silica) with metal functionalized to the surface of the core. Silica-gold NS are generally the most common form of NS whose size can be designed for diagnostic, therapeutic, or theranostic approaches. Oldenburg et aldemonstrated that the thickness of the gold shell on the same size core can shift the plasmon resonance of the structure so that a particle can be tuned to scatter or absorb a specific light wavelength (Fig. 3.4) [207]. These particles have demonstrated efficiency as photothermal agents that accumulate in tumors via the enhanced permeability and retention effect (EPR) [208–210]. Once in the tumors, an NIR laser illuminates the tumor (and subsequently, the NS). Depending on the size of the NS, it will either scatter the incident light for imaging purposes or absorb the energy of the laser and convert that laser to heat to cause tumor death via hyperthermia [211]. NS can also be functionalized with a targeting antibody such as HER2 for both visualization [128,129,154] and therapy [156,212,213] to improve the specificity of the particles. There are a variety of types of nanotechnology available for the treatment of breast cancer, from use as a delivery vesicle for highly toxic chemotherapy drugs to contrast agents for MRI. However, recent research has been

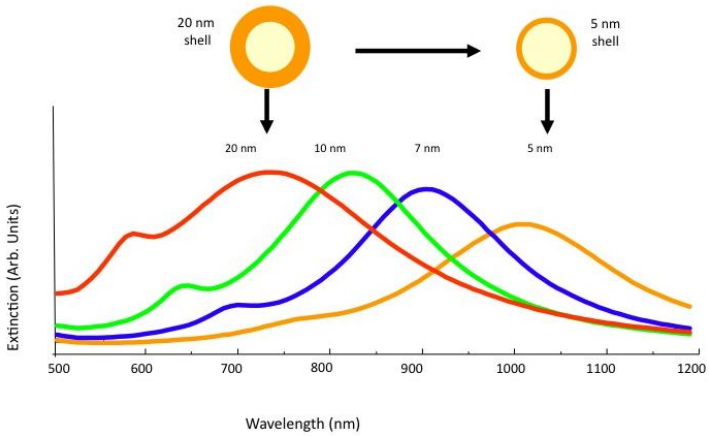

Figure 3.4 Extinction spectra of silica-gold NS changes as the thickness of gold shell is varied. Reproduced from [207].

trending towards making an "all-in-one" particle that will act as both the contrast agent and as a therapeutic. These particles are called theranostics and have shown high potential for future clinical use.

3.2.3. Theranostic nanoparticles

Earlier in this chapter, we alluded to the use of multi-use NPs such as multi-modal contrast agents and theranostic NPs. This section will review the increase of theranostics-based research in the past decade and catalog the most recent developments published. The multi-modal NP is still in its infancy, as the term theranostics was first used in literature in 2002 [214]. However, a SCOPUS search reveals that the number of published articles has risen steadily over the past decade to 191 in 2012 (480 total). A comprehensive review by Jokerst and Gambhir separates theranostics into five classes [215]. Types I and II are NPs used in conjunction with surgery; surgeons use the contrast provided by the diagnostic aspect of the theranostic to delineate the cancerous tissue. Type I has intrinsic contrast (like an SPIONP) whereas type II is functionalized with an imaging agent such as a fluorophore [215]. Types III and IV are liposomes [216] or quantum dots [217] that act as drug carriers. These classes of NPs can accumulate in tumors in a variety of manners such as EPR or via more specific receptors such as EGFR [218]; once again, the difference between the classes of particles is that they can be imaged via endogenous contrast or a secondary agent attached to the particle. Class V theranostics are particles that respond to stimuli such as magnetic field [219] or NIR light [211] to cause hyperthermia in targeted cells or release of therapeutics. These particles can also respond to external stimuli such as a magnetic field or ultrasound waves to facilitate more active targeting of the NPs to the tumor site. A study by Chertok et al.

demonstrated the use of an applied external magnetic field to polyethyleneimine (PEI) coated iron oxide NPs to improve delivery of the particles to an intra-cranial brain tumor [220]. Watson et al. demonstrated that ultrasound could be used to enhance the delivery of therapeutic NPs to tumor phenotypes with limited vascularization and loose cell-cell adhesion sites by lowering pressure inside the tumor [221].

Significant hurdles such as cytotoxicity and biodistribtion still remain before theranostics enter widespread clinical use. Theranostics also require different dosages of therapeutic and diagnostic agent to be effective; this affects the dose and, subsequently, systemic toxicity of the NP. Cole et al. also reports that embolisms in blood vessels can occur with iron oxide NPs as a result of an incorrect angle of applied magnetic field [222].

Despite challenges and limited knowledge of the nano-bio interactions of the particles, clinical translation of theranostic research has risen at a dramatic rate, resulting in five different particle formulations undergoing human clinical trials [215]. As scientists become more familiar with how the properties of theranostic NPs (and all NPs) affect their biodistribution and circulation time, these particles will likely become more effective in the treatment of cancer. In the next section, we will discuss the different characteristics of NPs and how these properties affect NP circulation time and interaction with a host's defense system. Additionally, we will discuss modifications to NP surfaces, such as addition of a targeting ligand, to improve targeting efficacy.

3.3. Effect of Different Nanoparticle Characteristics on Biological Interactions

As mentioned above, when NPs are introduced into a host's system the shape, size, and surface charge of the particle affect the interaction of the particle with components such as serum proteins in the blood [223]. When designing NPs for cancer treatment, researchers must optimize their agent's characteristics to insure it remains in the body long enough for its intended use and maintains low toxicity for the host. This section will review how NP characteristics affect particle behavior when introduced into a biological environment.

3.3.1. Effect of surface charge

NPs with a neutral surface charge have a much longer circulation half-life than charged particles [172,223]. Serum proteins like immunoglobulin and metal-binding proteins interact with a charged particle instantaneously form a layer of proteins coating the surface called the hard corona [224,225]. The addition of the proteins to the surface can affect the properties of the NPs and cause them to aggregate, which will affect the distribution of the particles [223]. Additionally, the type of proteins that adsorb will affect particle distribution. For example, if opsonins adsorb onto the surface, NPs are tagged for immediate consumption by macrophages [226]. If antibodies adsorb onto the surface, the complement system is activated, and the particles will be consumed by receptor mediated phagocytosis [227]. In *in vitro* studies, positively charged NPs have a higher uptake, which could be a result of the slightly negative charge of the cell membrane [228,229]. Additionally, a negatively charged bound NP can cause gelation in the fluid membrane of the lipid bilayer [172]. The medium in which the NPs are being

introduced to the cells must be considered, as the protein composition will affect the protein corona. This is seen *in vivo*, so any reaction by the cells to the NPs could be due to the particular proteins that are adsorbed onto the particle surface and not necessarily the charge of the particle that was introduced to the cell.

To combat rapid adsorption, a strategy of stabilizing the particles with a layer of PEG (also known as PEGylation) has been adopted for all types of particles. PEG prevents rapid protein adsorption and has been shown to increase the blood half-life of particles [172,230,231]; however, a majority of the particles are still found in RES organs after an extended period of time [230]. The thickness of the PEG layer can be controlled by the molecular weight of the PEG [232] with increasing layer thickness increasing the blood half life of the same size AuNP [232]. However, the PEG layer will affect overall diameter, which has a very significant effect on biodistribution, including tumor accumulation [232,233]. Additionally, even though a longer PEG chain length adds further stability for the particle, it limits the ability to functionalize targeted ligands to the particle (Fig 3.5) [234].

Even though PEG is the most common mechanism for prolonging blood half-life, other compounds have been used. Almeida et al. offer a very thorough review of the biodistribution of SPIONPs with different coatings [223]. A brief summary will beprovided here. Dextran (an anti-thrombotic) and its variants have been researched with various degrees of success. For example, Bourinett et al. reported on SPIONPs coated with a low molecular weight dextran and injected three separate times to have a blood half-life of 97, 208, and 222 minutes respectively [235], with approximately 11% of the injected dose being found in the liver. Whereas Lawaczeck et al. coated SPIONPs with

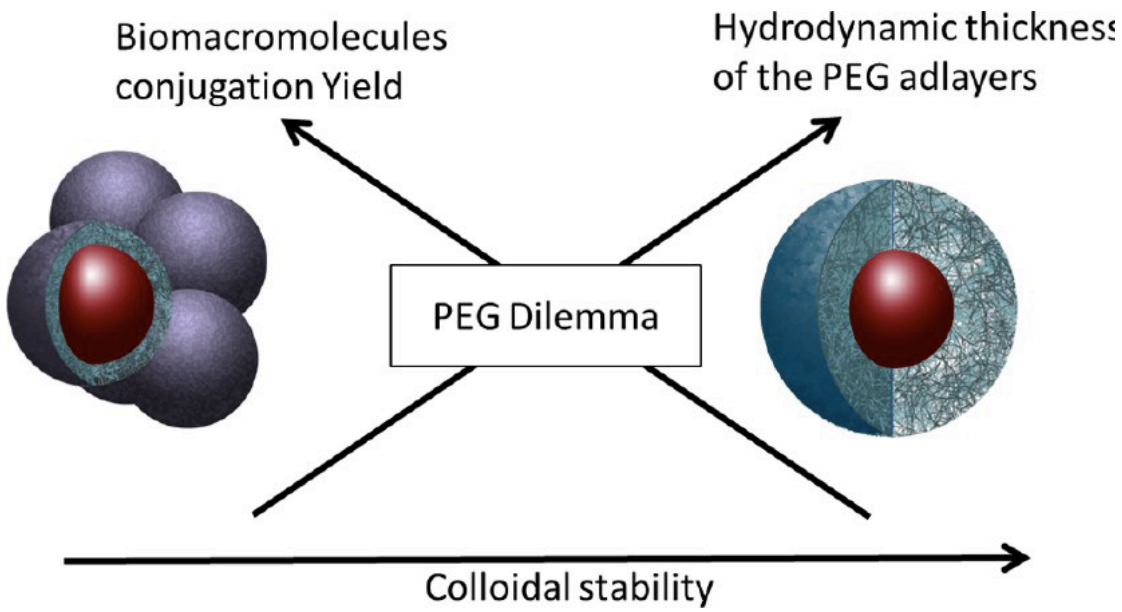

Figure 3.5 Illustration displaying the "PEG dilemma," where increasing PEG thickness increases blood biocompatibility of a particle but also limits the number of biomolecules that can be attached to the surface of the PEGylated particle. Reproduced from [234].

low molecular weight carobxydextran in two phases with a clearance time of 2.2 and 41 minutes respectively [236] with approximately 80% of the injected dose found in the liver. In contrast, Chen et al. reported on the coating of SPIONPs with a copolymer of anti-thrombotic polysiloxane and amphiphilic polyethylene oxide that was able to lower the amount of iron in spleen and liver significantly when compared to dextran coated NPs [237]. In addition to the surface charge having an effect on the fate of NPs, ligands and molecules bound to the surface also can affect systemic distribution and intracellular localization of NPs. In the next section, we will explore how ligands bound to the surface can affect NP fate.

3.3.2. Surface-bound ligands' effect on nanoparticle fate

Targeting ligands such as antibodies against cell surface receptors have been functionalized to NP surfaces to improve the targeting ability above the EPR effect. A study by Choi et al. showed that active targeting of AuNPs with transferrin did not

improve the amount of particles that accumulated in the tumor. However, it did improve the intra-cellular localization of the AuNPs, as the particles were identified inside endosomes of cells that overexpressed the transferrin receptor [238]. A 2012 study by Kievit et al. demonstrated the efficacy of HER2 targeted SPIONPs versus NPs functionalized with a non-specific IgG antibody in a breast cancer murine model (Fig. 3.6) [239]. In addition to providing enhanced specificity, surface ligands can also improve circulation time of AuNPs. Goel et al. demonstrated that AuNPs with PEG and tumor necrosis factor (TNF-α) had a longer circulation and slower uptake by the RES organs; however this was only a temporary effect as gold levels in the liver were similar at 24 hours [240]. Currently, there is one targeted theranostic in clinical trial, a melanoma treatment that targets the transferrin receptor and delivers RNAi [215].

Several studies have demonstrated the binding efficacy of anti-HER2 targeted nanoshells for diagnostic [128,129,155,241] and therapeutic [156] uses. Carpin et al. demonstrated the utility of anti-HER2 funcionalized therapeutic NS in photothermal ablation of a Herceptin resistant HER2-positive cell [156]. NPs are good carriers for ligands because the curvature of the surface can increase the overall density of the antibodies on the surface, leading to increased affinity. Jiang et al. demonstrated that 10 nm particles with anti-HER2 had two orders of magnitude better binding affinity then Herceptin in solution with even higher affinity on larger particles [242]. However, Jiang et al. also showed that even though larger particles had a higher binding affinity than smaller particles they did not necessarily have a stronger impact on the activation of downstream enzymes, as particles with 40-50 nm diameter had the greatest effect when compared to sizes in the 2-100 nm range [242].

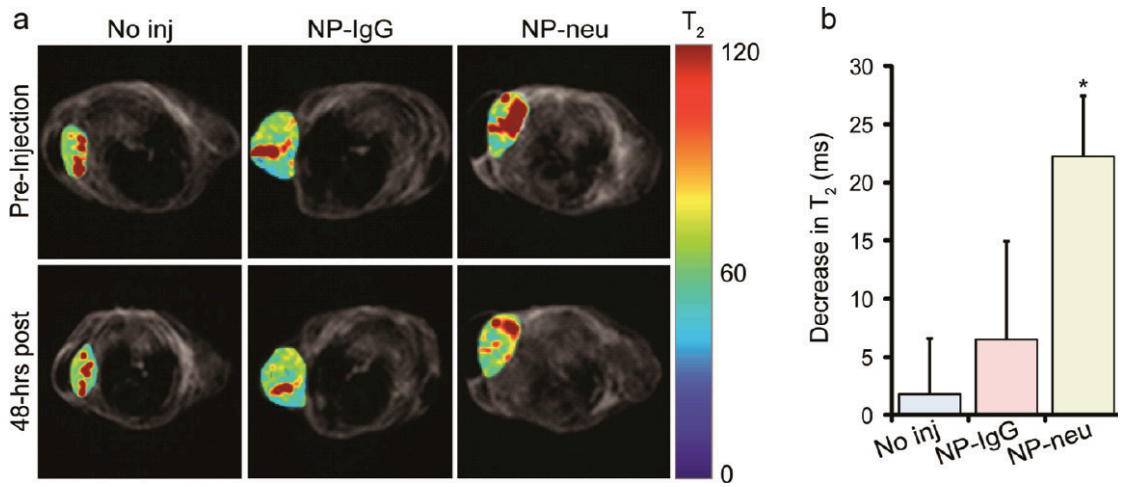

Figure 3.6 (A) MRI images of a HER2-positive tumor implanted in a mouse. Images display T_2 color maps of tumors pre and post injection. (B) Graph representing the decrease in relaxation signal from the tumors after injection of non-targeted and targeted SPIONPs. Reproduced from [239].

NPs with targeting ligands are likely internalized by receptor mediated endocytosis, but the intracellular fate of these particles is still relatively unknown [172] See et al. suggest that Cathepsin L in the endosomes cleaves the ligands from the nanostructure [243], which could lead to removal of the particle from the cell [172]. They can also remain in the cell and be passed to daughter cells through mitosis [244]. The only direct conclusion about intracellular particle fate is that it is size and cell dependent [245]. Additionally, some NPs are engineered to leave the endosomal system so they can interact with subcellular organelles. For exampled, once inside cells, silver NPs can disrupt mitochondrial function leading to reactive oxygen species (ROS) that induce cytotoxic effects [246]. As well, Kang et al. attached nuclear targeting sequences to the surface of AuNPs to direct the particles into the nucleus to cause apoptosis in a cancer cell line [247].

Targeted surface ligands can play an important role in the distribution, accumulation, and intracellular fate of NPs. Researchers have been able to tune a particle behave in a specific manner when encountering a specific environment. As this field

grows, researchers will be able to optimize particle design to achieve even higher target specificity and desired therapeutic effect. In the next section, we will discuss how particle size and shape affect the interaction between a NP and its environment.

3.3.3. Effect of size and shape on nanoparticle fate

The cellular uptake of NPs when introduced to cells has a strong dependence on overall diameter of the particle. This is likely due to the thermodynamics of the membrane wrapping process [172] and the number of surface ligands bound by the particle. For example, small (2 nm) NPs have high curvature, which requires more energy for membrane wrapping. This indicates that multiple particles need to bind in the same area to cause a large enough free energy change to induce endocytosis. Additionally, the small amount of ligands attached to a NP surface lower the ability of that particle to interact with its targeted surface receptor. In contrast, a large 100 nm particle holds a greater number of surface ligands, decreasing overall uptake because one particle can bind too many receptors and limit binding of other particles [172]. NPs with a range of 30-50 nm are able to bind enough receptors to induce endocytosis individually while not exhausting the receptors on the surface. However, for each cell and receptor type, the optimal diameter is different due to different protein expression levels for each cell line.

Size also has a significant effect on cytotoxicity and intracellular fate of particular particles. For example, Pan et al. demonstrated that small (<2 nm) AuNPs were more cytotoxic than 15 nm particles [248] with different size small AuNPs (1.2 & 1.4 nm) inducing cell death via different mechanisms. The 1.2 nm clusters had slower cytotoxicity with an equal number of cells being apoptotic or necrotic; whereas the 1.4

nm NPs caused necrotic death very rapidly [248]. A second study by Pan et al. found that these 1.4 nm particles cause intracellular creation of ROS and damage to the mitochondrial membrane leading to rapid necrosis [249]. Additionally, surface charge of these small particles needs to be factored as studies by Goodman and Arvizo et al. showed that positively charged AuNPs were more cytotoxic than neutral or negatively charged particles, which is likely due to the positively charged AuNPs depolarizing the cell membrane and causing a calcium influx into the cell [250,251].

In vivo distribution of NPs is also very size dependent. For example, Choi et al. found that QDs $\leq$ 5.5 nm in diameter were cleared through the urine because they were able to pass through pores in the kidney [252]. The researchers were able to show that after 4 hours, half of the injected dose of particles had been excreted from rats [252]. However, the majority of particles developed for clinical applications are larger than 5.5 nm and a high percentage of the injected dose resides in the liver and spleen and can remain there for up to 8 months [253].

For larger particles, biodistribution is still important as researchers aim to design particles that are non-toxic to the spleen and liver and also accumulate in tumors. Two studies by De Jong and Sonavane et al. showed that smaller AuNPs (10 and 15 nm diameter, respectively) had a much wider distribution than larger particles used in the studies, with both groups observing particle presence in the brain [254,255]. A study by Hirn et al. found this same size dependent distribution of particles found in the liver (less of the smaller particles detected in liver) but not in the spleen after 24 hours [256]. The researchers posit that smaller particles have higher “diffusional displacement” that limits the binding ability of receptors in the liver; this could help explain why smaller particles

are more widespread in the body. Furthering this research, a 2011 study by Zhang et al. studied the systemic cytotoxicity and distribution of 5, 10, 30, and 60 nm PEGylated AuNPs and found widespread distribution in the smaller particles (Fig. 3.7) [257]. However, the researchers found that toxicity of the particles did not follow a trend as the 10 and 60 nm particles were found to be toxic to the liver and kidney, but the 5 and 30 nm AuNPs were not, warranting further investigation [257]. Size is significant in both *in vitro* and *in vivo* distribution and intracellular fate of NPs. It is an important factor in the design and optimization of a particle for treatment of cancer.

The final parameter that ties directly to size is the shape of the NP. Throughout this chapter, we have been only discussing NPs that are spherical in shape. However, there are nanostructures other than spheres that have been fabricated and the work using these particles warrants mention in this section. The most common non-spherical shape is a nanorod, which is cylindrical in shape with two different axes. A study by Gratton et al. showed that nanorods had higher cellular uptake than spheres at sizes greater than 100 nm [258]; however at sizes below 100 nm there is higher uptake of spherical particles [259]. Another study by Chithrani et al. speculates it is more difficult for cells to endocytose nanorods because the membrane must wrap around the entire length of the nanorod as the surface receptors are only located along the ends of the particle [260]. For *in vivo* biodistribution assays, reports conflict whether spherical AuNPs or nanorods have wider distribution [223]. A study by Arnida et al. showed that PEGylated 10 X 45 nm nanorods had a longer blood half-life compared to 50 nm PEGylated AuNPs [261]; however, Sun et al. demonstrated that bare 30 X 80 nm nanorods had a higher accumulation in the liver than 40 nm AuNPs [262]. These studies are too different to

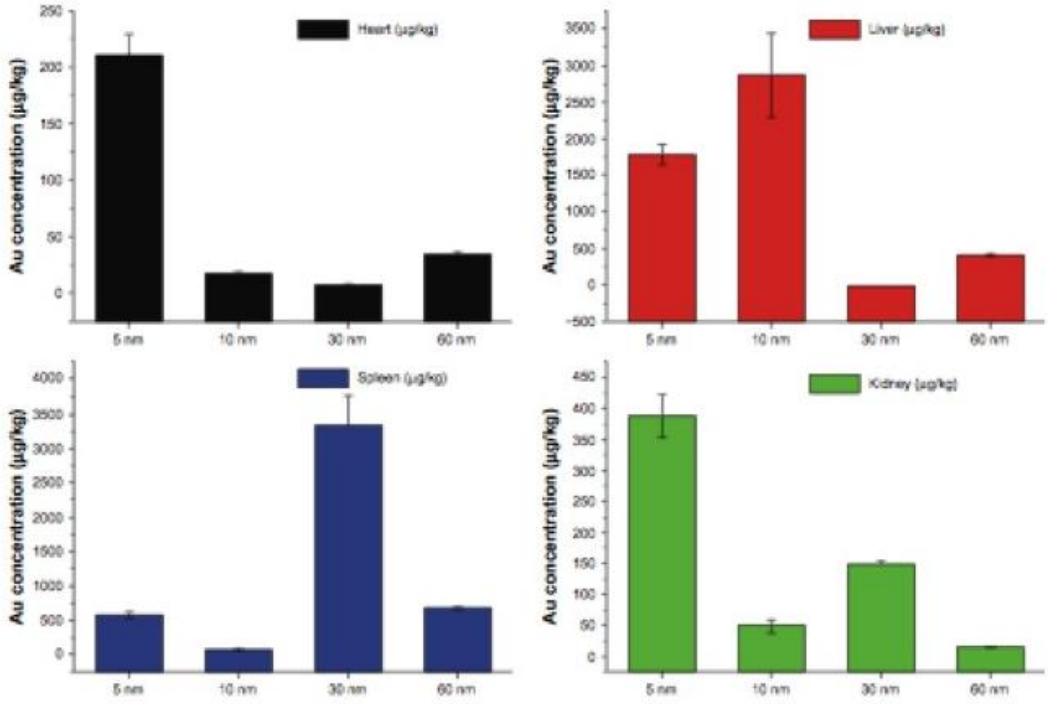

Figure 3.7 Tissue distributions for various sizes of PEGylated AuNPs. Smaller NPs (5 nm) show widespread distribution to organs whereas larger particles are not as widely distributed. Graph displays the role that size plays in particle distribution. Reproduced from [257].

draw any significant conclusions, and much more research needs to be completed before a meaningful conclusion can be reached on biodistribution differences between the different nanostructures.

The nanourchin, whose structure resembles a sea urchin, has been synthesized by Yu and Bakr [263,264]; the spikes of the "urchin" increase the electromagnetic field of a particle, which is helpful for imaging [265]. In a study by Hutter et al. nanourchins that were capped with cetyl trimethylammonium bromide (CTAB) were non-toxic to a microglial cell line *in vitro*. *In vivo* studies revealed that the structures were preferentially taken up by glial cells and not neurons [265]. This study did not investigate biodistribution or intracellular fate, and there is still further research to be completed on this shape.

Differing sizes and shapes can change the properties of a nanomaterial such as increased local plasmon resonance and enhanced raman scattering [266]. However, for these specialized structures to be translated to clinical relevance, more characterization of these particles needs to be done. Assays from simple *in vitro* cytotoxicity to *in vivo* distribution assays will need to be performed for each new structure. As researchers improve the ability to control size and shape at the nanoscale, new particles will continue to be synthesized and will contribute to our knowledge of how size and shape effect the fate of particles.

3.4. Conclusion

There are a large number of NPs being designed, optimized, synthesized, and characterized for use in biomedical applications. Each type of particle has its own unique use and characteristics that can be used in the treatment of cancer. Depending on the final goal of treatment, researchers can choose from any number of parameters to optimize the use of a particle. In this chapter, we explored some of the more common NPs and the factors that affect their behavior in cells and animals. We explored the different core materials, how their surfaces interact with biological systems, how targeting ligands affect their ability to differentiate cancer, and how their size has an effect on distribution in animals and cells.

In this thesis, we discuss the development of biodmedical applications of two types of particles. In chapter 5, we will discuss the use of 2 nm gold colloid capped with glucose for use as a targeting agent in cancer cells with high metabolism. We will explore the ability of this particle to penetrate the cell membrane in different cell lines,

compare the targeting ligand to other ligands, and examine its mechanism of entry. We also demonstrate the use of large (314 nm diameter) silica-gold NS with targeted ligands to differentiate HER2-positive cancerous tissue from HER2-negative tissue. We will optimize these structures for use in tissue as diagnostic agents and then explore the methods with which NS can be visualized in tissue.

Chapter 4

Background on Optical Imaging and Contrast Agents

4.1. Introduction

In the previous chapter, we discussed the use of nanoparticles in both the treatment and diagnosis of cancer. This chapter continues with the use of other types of targeted contrast agents such as fluorophores and quantum dots. This chapter will also relate the use of these agents in optical imaging and catalog the recent refinements in optical imaging technology that have improved visualization of malignant tissue.

As cancer treatment has progressed over the past century, therapeutics have evolved from broad chemotherapeutic agents that kill both healthy and diseased cells to agents that are more specific for molecules that correlate with malignant tissue development [267], thus halting cancer spread and sparing healthy tissues from cytotoxicity. Therapeutic compounds such as lapatinib and bevacizumab, which target

growth factor receptors that are overexpressed, are prime examples of molecularly targeted therapeutics that have proven effective [49,53]. Unfortunately, these successes in molecularly-targeted therapeutics have not transitioned to vast improvements in molecularly targeted diagnostics [267]. However, molecular imaging allows clinicians to visualize an almost infinite array of information by choosing the proper target, targeting agent and imaging technique [268]. Molecular imaging can be used to feature each molecular step that neoplastic tissue undergoes until it becomes malignant tissue [267,269]. Depending on cancer type and stage, molecular imaging can be used to visualize gene expression [270,271], angiogenesis markers (i.e. integrin $\alpha_v\beta_3$) [272,273], and metabolic activity [274,275]. Molecular imaging can also offer the ability to detect cancerous tissue earlier in its development by increasing contrast in tissues to help increase sensitivity and specificity. This early detection is paramount as it has been shown that early detection in breast cancer correlates with a higher survival rate for patients [276]. Molecular imaging also locates multiple biomarkers on a single sample, allowing physicians to use the molecular profile of the tissue to tailor specific molecular therapeutics [267].

One goal of this project is to take advantage of the variety of biomarkers that can be screened using molecular imaging by combining the specificity of molecular targeting with the ease and low cost of optical imaging to create an optical molecular imaging platform. Our aim is that this system will be fast, inexpensive, and highly specific for malignant tissue. We hope to accomplish this by finding specific optical contrast agents that target neoplastic tissue and using known optical imaging techniques. The purpose of this chapter is to explore optical imaging technologies and contrast agents that have vast

potential to be used to target malignant tissue in a clinical setting, with a focus on breast cancer.

4.2. Optical Imaging Background

Optical imaging has taken great strides in providing new methods of molecular imaging. It has the ability to provide a variety of data from sub-cellular to macroscopic images [267,277]. It offers fast, high lateral resolution, and inexpensive options for imaging a range of disease states, such as hypoxia, hemoglobin levels, and metabolic state [277–279]. Optical imaging is generally thought to involve the analysis of visual or NIR light (i.e. scattering, absorption, or fluorescence) and its interactions with normal and malignant tissue. [277].

Optical imaging has shown limitations in clinical practice, however, because of the lack of penetration depth of the wavelength used to interrogate target tissues. The lack of penetration depth is due to the presence of water, collagen, and other extracellular components that all have different indices of refraction [280,281]. This heterogeneity in tissue and indices causes light to scatter randomly as it travels through the tissue [281], lowering the utility of optical imaging. Additionally, light in the visual range (400-650 nm) is absorbed by the skin at almost two orders of magnitude greater than NIR light (see Fig. 4.1) [282,283]. The NIR range (700-1000 nm) has become known as the “optical window” due to the penetration depth of the illumination light into the tissue of interest. This has been exploited for techniques such as diffuse optical imaging and optical coherence tomography [284,285]. We will now review some of the current optical

imaging technologies that have been used to visualize molecular profiles and expression of neoplastic tissue.

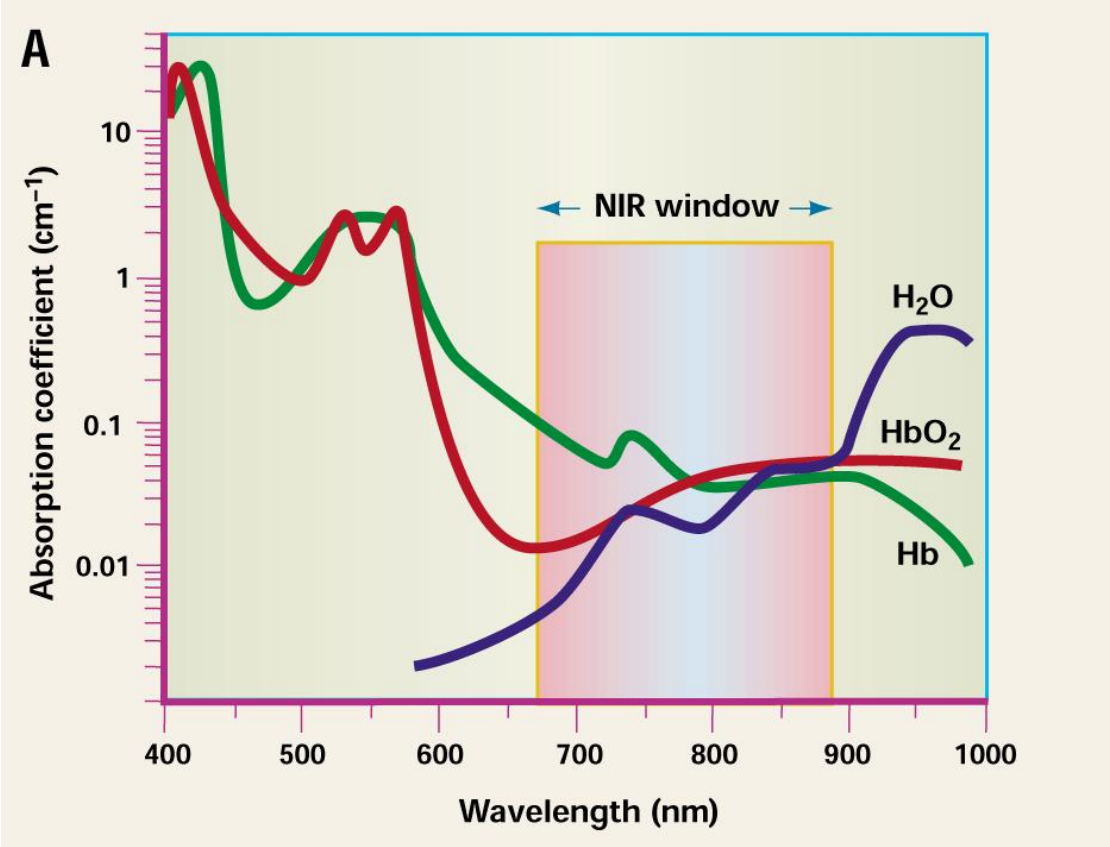

Figure 4.1 Absoprtion values for deoxygenated and oxygenated hemoglobin and water showing the NIR window that is optimal for optical imaging because of the minimal interaction of light with these chromophores. Reproducd from [283].

4.3. Optical Imaging Using Endogenous Tissue Signal

As discussed briefly in Chapter 2, imaging systems, such as MRI, use energy to interrogate tissue and detect lesions based off of the tissue's interactions with the excitation energy. Optical imaging systems are mainly focused on the use of visual/NIR light and its interactions with the breast to detect changes in absorption and scattering of this illumination signal [286]. Increased absorption in the NIR corresponds to an

increased level of oxy- and deoxy-hemoglobin that is indicative of angiogenesis [287], a hallmark of cancer [288]. In three separate 2005 studies by Floery et al., Tromberg et al., and Zhu et al., malignant lesions are detected using optical imaging of the breast [289–291]. Example absorption spectrum from one of these studies is presented in Figure 4.2. However, even though these papers showed the promise of optical imaging, it has been suggested that these technologies are not sensitive enough to be used as method of detection like mammography [286,292]. This is due to oxygen levels in the breast being affected by factors such as a patient's age [293], menstrual cycle phase [294,295], or even type of cancer [296]. It has been suggested that the optimal use of this technology is to monitor tumor response for chemotherapy because it can use the patient's baseline lipid and hemoglobin levels to specifically follow tumor size as shown by Enfield et al. [297]. This could serve as safer alternative than PET/CT, which uses ionizing radiation that might have long-term adverse effects on the patient [132,298,299].

Optical imaging has also been used to measure autofluorescent signal changes of neoplastic tissue in organ sites that can be accessed without invasive surgery. These areas include the oral cavity [300–302], the cervix [303], and the lung [304], where the illumination and detection is accomplished with the use of an endoscope. These devices operate under the principle that malignant tissue loses autofluorescent signal under white-light imaging [267] and appear dark where normal tissue is white. Even though there has been recent FDA approval of autofluorescent imaging devices in oral, gastrointestinal (GI), and pulmonary systems to visualize neoplastic areas, these devices have a low specificity because inflammatory response has the same effect on the autofluorescent signal that is seen with malignancies. This causes many benign areas that

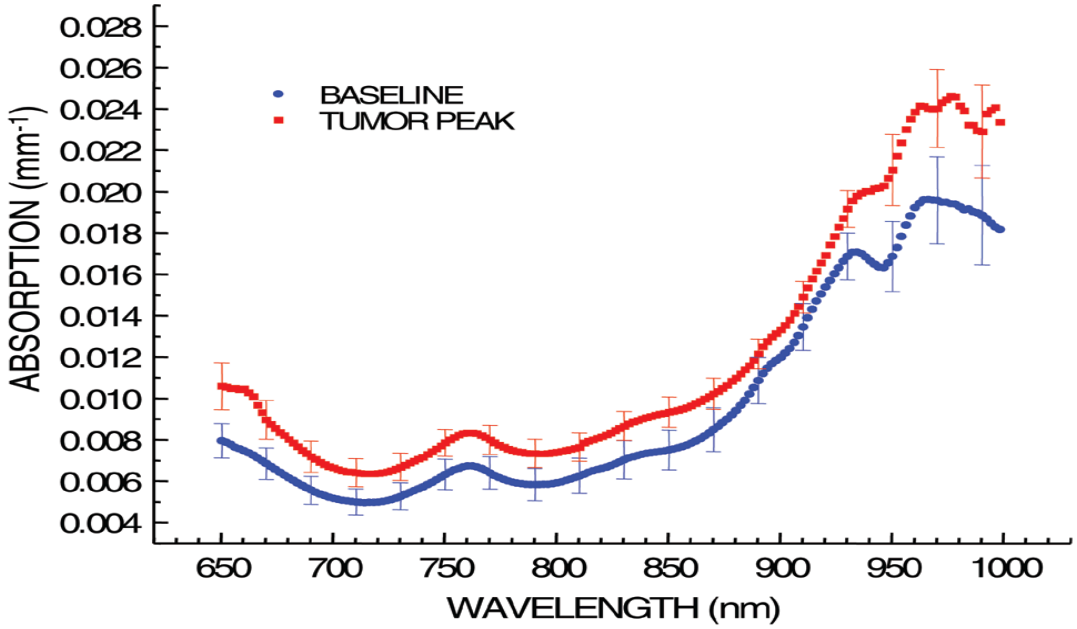

Figure 4.2 Average absorption spectra of 13 tumors (red) and normal (tissue). Increased absorption in the 650-850 nm indicates higher hemoglobin concnentration and increased signal in the 950-1000 nm range indicates increased water content in the tissue. Reproduced from [290].

are areas of inflammation to be mistaken for cancerous areas [305–308]. To improve specificity of optical imaging, there has been a large portion of research dedicated towards using contrast agents that can identify neoplastic cells by targeting specific biomarkers.

In the previous chapter, we discussed nanoparticles that behaved as contrast agents because they were conjugated to antibodies that targeted specific biomarkers such as HER2. In the next section, we will explore other targeted contrast agents that have been used in optical imaging to improve disease visualization.

4.4. Targeted Contrast Agents for Optical Imaging

Molecular imaging with contrast agents can be thought of as a three-piece system that needs all pieces present to work. The first piece is the biomarker (molecular target)

that is characteristic of malignant cells and located on the cell membrane or inside the targeted cell. The biomarker that researchers choose to target is site, organ, and cancer type specific. The second piece is the optical agent that will be visualized and provide the contrast that is necessary to differentiate the malignant and benign tissue. Optical agents include fluorophores, quantum dots, and nanoparticles. Each agent has advantages and disadvantages and will be explored later in this chapter. The third and most important piece is the targeting molecule that is the linker between the optical agent and the biomarker so that the specific marker can be visualized. In most cases the linker is chemically attached to the optical agent on one end and the targeting moiety for the specific biomarker on the other end. An example of a targeting moiety attached to an optical agent is seen in the paper by Loo et al., in which the authors described attaching an anti-HER2 antibody to the surface of the same theranostic gold nanoshell (AuNS) as described by Carpin et al. [156,309]. Using an OPSS-PEG-NHS linker, the Fc region of the antibody was conjugated to the PEG with the NHS functional and then self-assembled onto the surface of the NP through the Au-S dative bonds. These targeting moieties will be explored in further detail in this chapter.

4.4.1. Biomarkers

It would be ideal if the biomarkers were only present in the neoplastic cells; however, most biomarkers are present on each membrane, so most molecular contrast agents are targeted against the overexpression of a specific biomarker, such as HER2. For example, Carpin et al. demonstrate that there is still expression of HER2 on the surface of a HER2-negative epithelial breast line. The MCF10A (HER2-negative) cell lines expresses an average 2.43×10^4 HER2 binding sites per cell, but the HER2-positive

SkBr3 cancer cell line expresses 2.19 X 10^6 sites per cell. This large expression difference led to an increased targeting efficiency of a theranostic particle in SkBr3 cells that led to enhanced contrast and therapeutic effect from the nanoparticles [156].

In addition to surface markers, the overexpression of different glucose transporters (GLUTs) in the cell membrane has been used to differentiate breast cancer in both cell lines and *ex vivo* tissue [22–24]. Due to the increased metabolic rate of the disease, a high number of cancers overexpress GLUTs to increase the amount of available energy for the cancer to grow. Different cancers overexpress different GLUTs and these GLUTs are specific for the different types of glucose they transport. For example, GLUT1 transporter allows for the common D-glucose to pass though the membrane where as GLUT5 is a commonly known as the fructose transporter [310,311]. A final biomarker that has been targeted for use with molecular contrast agents is the expression of specific mRNA molecules that are translated into proteins such as survivin that help cancer cells overcome apoptosis [312].

4.4.2. Optical agents

In the previous chapter we discussed the use of nanoparticles as optical agents for disease visualization; however, there are two other agents that are much smaller in size that are frequently used in optical imaging: fluorophores and QDs. Fluorophores are organic dyes that, when interacting with a photon, promote an electron from a lower energy orbital to a higher energy orbital (called absorption), when the electron returns to the ground state, a photon is emitted. Generally, this photon has less energy than the excitation photon so the wavelength of light emitted will be longer [313]. Specific fluorophores have different absorption and fluorescence maximums and researchers need

to ensure that their optical imaging set-up is optimized to excite and visualize the fluorophore of interest. Some specific examples of fluorophores used in optical imaging of cancer include Alexa Fluor® and cyanine dyes that were used to visualize the overexpression of EGFR [314,315] in oral and breast cancers. Fluorophores have many advantages in that they are low-cost and can easily be conjugated to targeting molecules [267]. These properties allow fluorophore based contrast agents to be manufactured with high fidelity. The small diameter of most of these molecules (<1 nm) also improves the ability of the contrast agent to penetrate the cell membrane or pass through transporters, as is seen with 2-NBDG. However, there are challenges with fluorophores: they photobleach over time when excited, and there are limited agents with approval for use in humans. A very significant problem with fluorophores is that the majority of dyes emit in the visual wavelength range, limiting enhanced contrast to epithelial layer of the tissue of interest. There are studies that have focused on the use NIR fluorophores because of minimized light absorption in this range using both targeted [316] and non-specific agents [317]. We point to a comprehensive review by Luo et al. that thoroughly examines NIR dyes that are being used for cancer visualization [279]. The largest hurdle to overcome with the use of fluorophores is that the fluorophores emit the same signal no matter if they are attached to the desired biomarker or not, so if there is not a proper method of removing unbound contrast agent, then there will be a high signal from areas where the specific biomarker is not present, leading to a much lower specificity for the contrast agent.

QDs are semiconductor crystals whose diameter varies in size from 2-10 nm, whose optical properties vary with size and core composition (see Fig. 4.3) [318]. QDs

are very useful optical agents because their semiconductor material ensures minimal photobleaching, their optical properties can be tuned to have a very broad absorption spectrum but very narrow emission peak, and they have a higher quantum yield than fluorophores. This allows for different QDs to be targeted against various biomarkers used in one sample because of the minimal spectral overlap between different QDs' emission profiles [319]. Even though QDs have superior optical properties, their use is very limited because the cadmium that makes up the majority of QD cores is toxic to humans and animals at very low concentrations [320]. Due to the high toxicity concerns, the only *in vivo* studies performed with QDs has been limited to mice [253,321] and rats [322]. There have been recent studies that have used rare earth based nanocrystals as a more biocompatible alternative to cadmium based QDs. Kumar and Setua et al. synthesized Ytterbium based nanocrystals that were combined with fluorescent and magnetic elements (Eu^{3+} and GD^{3+}) to create multimodal imaging agents that have been used to image cancer cells *in vitro* with no toxicity [323,324]. However, there have yet to be further studies published on the use of these QDs in *in vivo* studies.

The use of nanoparticles as targeting agents was discussed in the previous chapter and will not be discussed here. However another contrast agent warrants further discourse is proflavine. Proflavine is a DNA intercalator that binds reversibly to DNA with a strong absorption peak at 445 nm [325]. Muldoon et al. showed that, when used in

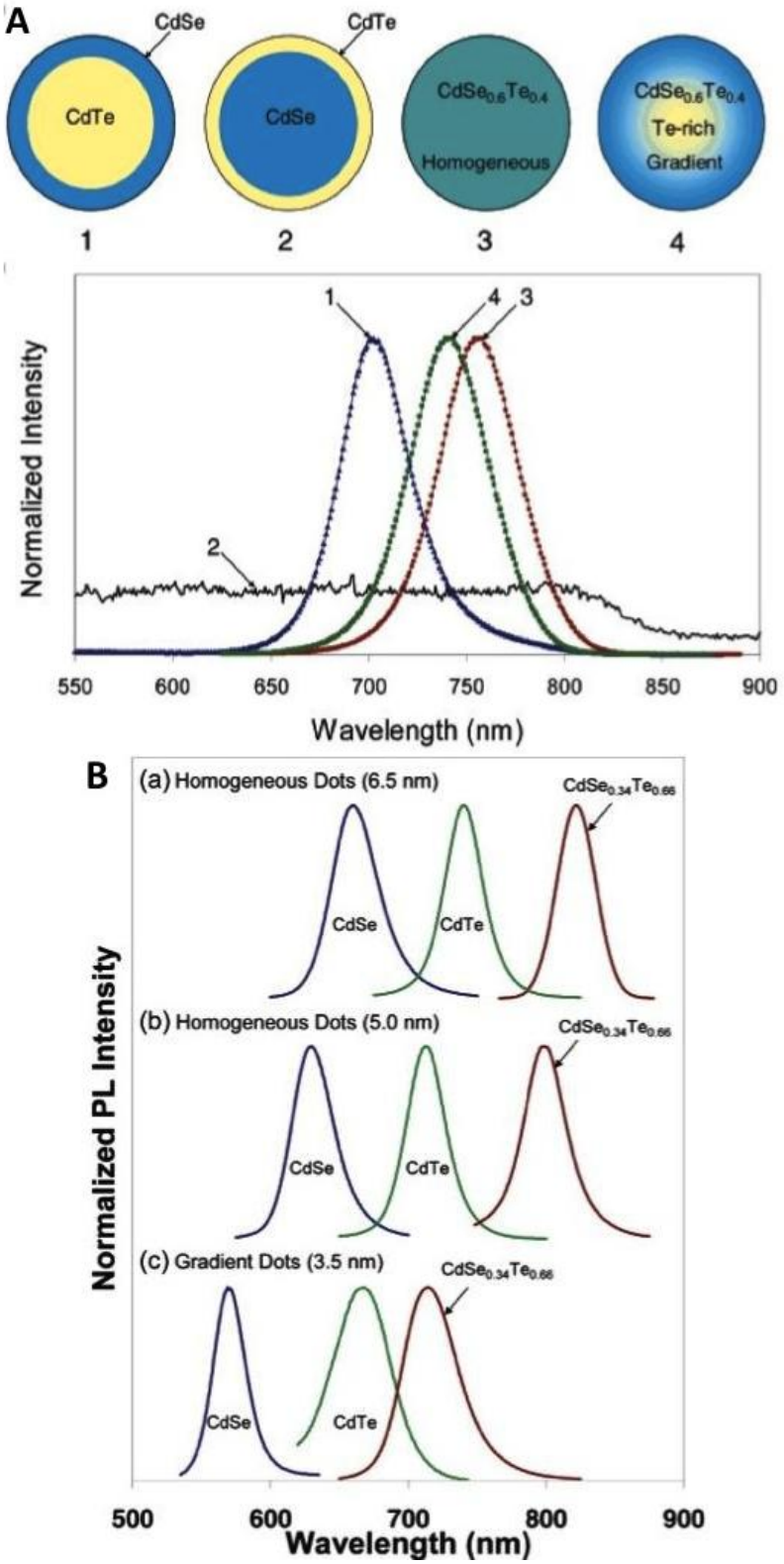

Figure 4.3 (A) Chemical makeup of different core-shell combinations of cadmium QDs and corresponding fluorescence emission spectra each combination. Results show the spectral shifts that are a result of core and shell composition. (B) Fluorescence emission spectra of different combination of QDs with different particle diameters showing both spectral changes due to chemical composition and overall diameter. Reproduced from [318].

combination with a high-resolution micro-endoscope, proflavine could be used to visualize the spatial distribution and density of nuclei in highly suspicious areas in the oral mucosa [326]. The researchers were able to visualize the nucleus and use an algorithm to calculate the ratio of nucleus to cytoplasm to differentiate patients with moderate dysplasia to cancer [326]. Proflavine has seen use in clinics as a form of protection from infection for newborns' umbilici [327] and has seen use in exploratory GI surgeries [328,329]. However, very few groups outside of Dr. Richards-Kortum's research group have explored its use as contrast agent for the diagnosis of dysplasia.

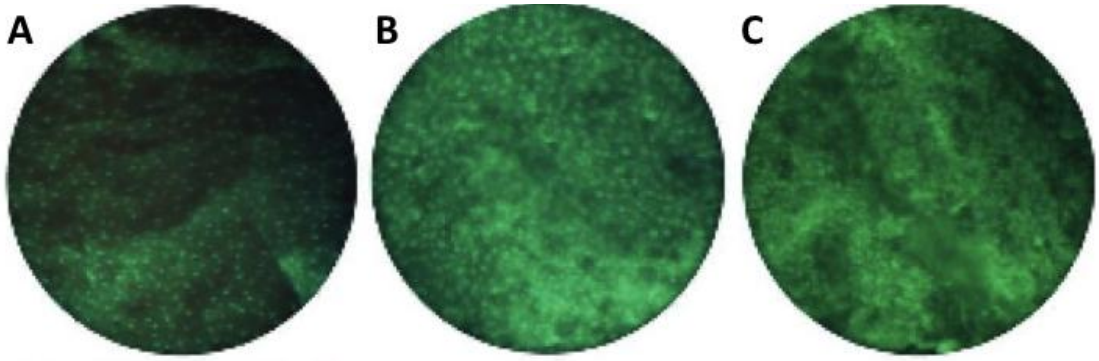

Figure 4.4 High resolution microendoscope images of proflavine accumulation in (A) normal squamous mucosa (B) moderate dysplasia, and (C) invasive squamous cell carcinoma. The higher signal from B&C indicates an increased amount of DNA present. These images were then used to calculate DNA to cytoplasm ratios and compared to histopathological results. Reproduced from [326].

The final optical agent that is important in optical imaging is the use of a fluorescence quencher with a fluorophore that helps indicate the presence of a specific mRNA molecule or a specific peptide sequence from a target protein. These are known as smart probes or molecular beacons. These probes are conformed so that when they are unfolded there is an absorbing (or quenching) molecule on one end and a fluorescent molecule on the other end. The two molecules are linked linearly via a specific mRNA sequence that is designed so that the molecule will naturally conform to bring the donor and quenching molecule in close proximity to each other. If the targeted sequence is not

present and the fluorophore is undergoing fluorescence it will transfer its energy to the quenching molecule and no signal will be seen. However, in the presence of the mRNA sequence, the molecule will unfold which moves the quenching molecule away from the fluorophore whose signal can now be visualized. Another example of these moieties are fluorescent smart probes in which the quencher and donor are linked by a specific peptide sequence that is cleaved in the presence of specific proteases like caspase-1. These optical agents are much more specific than normal fluorophores because their signal is only seen when the quencher is no longer near the fluorophore, allowing for specific sequences to be delineated and raising the target to background ratio to a much higher level than with normal fluorophores.

4.4.3. Targeting moiety

As discussed before, targeting moieties are the molecules that are used to link the optical agent to the biomarker of interest. These molecules can range in size from sub nanometer to 10s of nm [267]. There are a wide variety of agents that are used as targeting moieties for cancer visualization. Choosing the proper moiety is dependent upon desired biomarker and ease of functionalization to optical agent. Small moieties such as glucose and fructose are chosen because they can target the overexpression of GLUTs that is frequently seen in cancer cells. Generally, small moieties such as glucose are paired with a fluorophore as a contrast agent because the small size of the fluorophores does not interfere with the ability of glucose to pass through the GLUTs. Additionally, the functionalized fluorophore attached to the glucose prevents the glucose from undergoing glycolysis past the first glycolytic step [25]. Other targeting moieties that are used to visualize overexpression are growth factors such as EGF and VEGF. The

overexpression of the surface receptors for these growth factors is seen in malignant cells and the binding of growth factors leads to downstream signaling in cells that promote certain hallmarks of cancer such as uncontrolled growth, cell survival, and increased vascularization [330–333]. As the location of these receptors is on the surface of cells, growth factors can be paired with a variety of optical agents because researchers do not have to worry about transporting the optical agent across the cell membrane. For example, EGF has been functionalized with fluorophores [314], QDs [334], and AuNPs [201] for visualization of EGFR on the surfaces of cancer cells.

Another targeting strategy is the use of antibodies against surface receptors like VEGFR and EGFR to visualize their overexpression [128,335]. Antibodies paired with fluorescent optical agents have demonstrated very high specificity in both *in vitro* and *in vivo* studies [336,337] with a very high signal to background ratio. One major disadvantage of antibodies is that their size prevents from penetrating tissues and that has a potential to limit their use both *in vivo* and *ex vivo* [338]. Additionally, antibodies might induce an immune response in the host's body, which is thought to be due to the presence of murine antibody regions in the antibodies [339]. To combat these, researchers have engineered antibody fragments [340], chimeric antibodies [341], and humanized antibodies [342,343] to improve specificity and reduce immune response. Using antibodies as a targeting moiety has high potential for clinical use because of the ability to engineer very specific antibodies and the theranostic potential of using a therapeutic antibody conjugated to an optical agent.

The final two moieties are specific for use with smart probes (molecular beacons). As discussed earlier, these moieties are constructed so that they are turned off when the

specific molecular target or enzyme is not present and there is fluorescent signal when it is. The molecular beacon moiety is known as a nucleic acid aptamer with a specific complementary RNA (or DNA) sequence that is modified to a variety of targets including nucleic acids and proteins [344–346]. The aptamers are generally 25 nucleotides long with the middle 15 nucleotides acting as the complementary probe for the sequence [347]. The 5 nucleotides on each side of the target sequence are complementary to each other and attached to the two fluorescent molecules (donor and quencher). When in the presence of the target sequence, the unbound complementary sequence will bind to its target which forces the aptamer to unfold and fluoresce, signaling the presence of the target nucleotide sequence. One restraint of using molecular beacons is that they must be able to enter the cell to detect the sequence of interest. Therefore, ensuring delivery of the probe is of utmost importance. The other moiety that is used with fluorescent donor and quencher molecules is an enzyme cleavable peptide sequence with two fluorescent probes attached to each end of the sequence. These specific sequences are cleaved by specific proteases, such as caspase-1, an indicator of apoptosis [348]. These probes can be used to interrogate the protein expression of neoplastic areas and probe for upregulation (or down-regulation) of proteins that are characteristic of malignant cells, such as cathepsin protease [349]. While there are some very promising results, using cleavable peptides has two downsides: uptake of the peptides into cells is slow and there are also specificity issues due to the presence of other cleaving enzymes that can cleave the target sequence [267].

4.4.4. Delivery of contrast agents

The final hurdle researchers must overcome when considering the use of a contrast agent is the delivery of that contrast agent to the specific site. For some epithelial contrast agents, delivery is done topically and can be easily accomplished by exposure of the agent to the surface of interest. However, there are two factors that limit topical agent delivery. First, the surface must be easily accessible, so only areas such as the oral cavity, skin, or resected specimens can be targeted with topical agents. Second, the agent needs to be able to penetrate the epithelial surface, or else only a small layer of cells will interact with the agent. This limits the use of the agent to specific cell types and locations. Research by Van de ven et al. described the application of an anti-EGFR fluorophore diluted in Triton-X100 that allowed for penetration of the contrast agent to approximately 400 μm from the surface of malignant tissue, whereas agent diluted in PBS or DMSO did not penetrate the surface (Fig. 4.5) [350]. However, even using a permeation agent such as Triton-X 100 has limited penetration depth, which restricts the use of topical contrast agents to very specialized instances.

Systemic injection of contrast agents intravenously is the other method for delivery of contrast agents. Systemic injection can increase the likelihood of agent penetration and accumulation in desired tumor tissue through the enhanced permeation and retention effect. However, larger doses of injected agent are used for systemic injection, which can involve toxicity issues. Nanoparticle based contrast agents tend to have much higher accumulation in the spleen and liver [233] because their presence can induce an immune response in the host [223,226]. Nanoparticle fate is due to many different factors: size, shape, surface charge, and nanoparticle material are just a few of

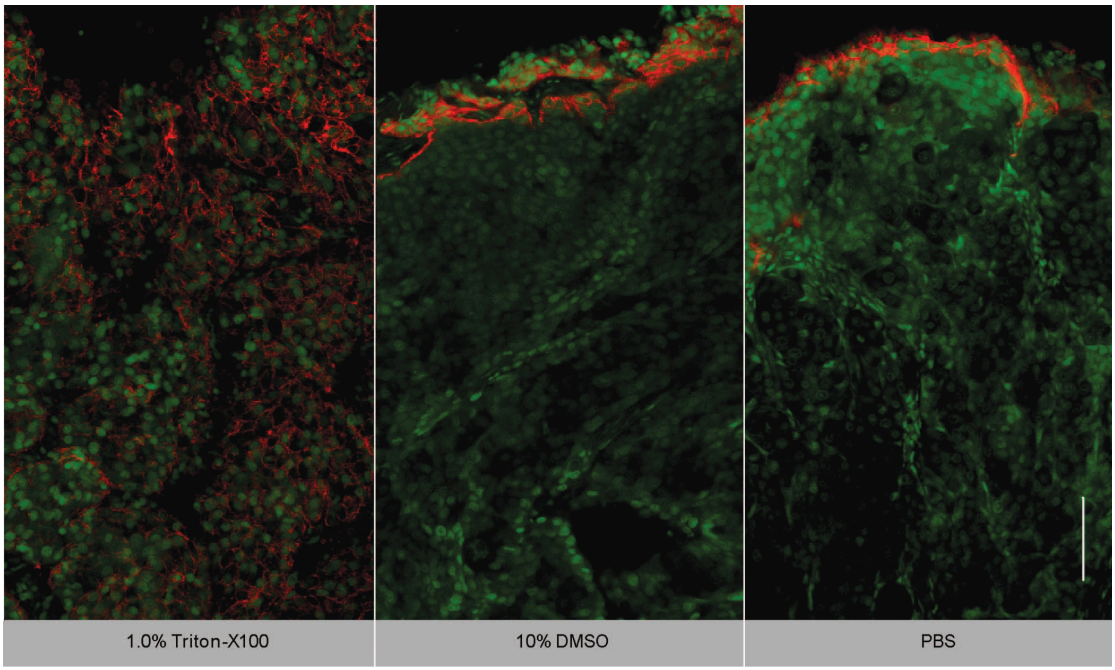

Figure 4.5 Fluorescent images of tumor tissues sliced so that the top of the image is the surface of the tissue that interacted with the contrast agents. Images display an anti-EGFR fluorophore (red) that has been diluted with Triton-X100, DMSO, and PBS. Acriflavine is counter stained in green to give tissue morphology. Images show the penetration of the anti-EGFR molecule to areas below the surface. In contrast to the other two images that had different dilution compositions so little to no penetration. Scale bar = 100 μm. Reproduced from [350].

the considerations researchers must consider when picking a nanomaterial, and we point to a review by Almeida et al. as a more thorough exploration of these factors and how they affect the biodistribution of nanoparticles [223]. However, one can apply the same reasoning to the factors that affect systemic delivery of nanoparticles to contrasts agent that are delivered systemically.

In addition to avoiding an immune response, agents must also be able to accumulate in tissue of interest while minimizing non-specific binding in other areas of the body. Once an agent reaches the targeted cell (via topical or injection) it must also penetrate the cell membrane and perhaps the nuclear membrane if the agent is targeting DNA expression. There is not one correct method for agent delivery; determining the delivery method is based on biomarker, target, and optical agent, amplifying the factors that must be considered.

4.5. Conclusion

Optical imaging is a new field that has great potential in helping researchers and clinicians visualize and delineate cancerous cells from non-cancerous cells. There are different approaches to optical imaging, from using endogenous signal of patients' tissues to using a systematically injected contrast agent that can penetrate the cell membrane and interact with a specific nucleic acid. Optical imaging is a promising tool that can help in both clinical and basic research. Choosing the proper target organ, proper target cancer type, and type of optical imaging will have a tremendous impact on a researcher's success.

The goal of this thesis is to use two contrast agents in conjunction with an inexpensive imaging camera to provide surgeons with a tool to visualize microscopic disease presence, macroscopically. We aim to use a fluorescent-based contrast agent, 2-NBDG, that targets the overexpression of GLUT1 seen in breast cancers, and an anti-HER2 targeted silica-gold NS that targets the overexpression of HER2 that is seen in 25-30% of breast cancers. The goal of this work is to combine two agents that have shown the ability to differentiate cancer cells in less than 10 minutes as an optical imaging tool for breast cancer surgeons intraoperatively. Using two contrast agents will help increase the specificity of the agents as there will be two different enhanced signals that need to be present in order to confirm the presence of HER2-positive cancer cells. In the next two chapters, we will discuss how we have used these contrast agents separately to differentiate and visualize tissue in resected cancerous specimens. Then, in the final chapter we will discuss the visualization of these agents (and IRDye) with a portable, inexpensive camera.

Chapter 5

Glucose to Enhance Targeting of Fluorescence and Scatter Based Contrast Agents

5.1. Introduction

As discussed previously, there is an unmet need for physicians to visualize malignant tissue intraoperatively. The combined use of optical imaging and contrast agents has the potential to allow surgeons to visualize microscopic disease during surgery. In this chapter, we demonstrate the use of the fluorescent contrast agent 2-NBDG to differentiate cancerous cell lines from non-cancerous cell lines. We then expand upon this research by demonstrating that there is increased signal from 2-NBDG in freshly excised cancerous tissue when compared to benign tissue. Finally, we translate the use of glucose with a fluorescent contrast agent to its use as a targeting moiety for

*Partially adapted from: Langsner, R J, L P Middleton, J Sun, F Meric-Bernstam, K K Hunt, R A Drezek, and T K Yu. 2011. "Wide-field imaging of fluorescent deoxy-glucose in ex vivo malignant and normal breast tissue." *Biomed Opt Express* 2 (6): 1514-1523.

small diameter (~2 nm) gold nanoparticles (AuNPs). We demonstrate the mechanism of entry of glucose-capped AuNPs and demonstrate the specificity of glucose to enhance contrast in *in vitro* experiments.

5.2. Background

In many tertiary care centers, appropriate facilities and staff exist to allow assessment of margin status intraoperatively. Surgeons in these centers have the opportunity to remove more tissue during the same procedure to achieve negative margins if the initial resection margin is positive. However, many hospitals and smaller surgery suites in the general community (>95%) [127] do not have pathology support services to allow for intraoperative margin assessment, and thus the margin status is not known until several days after the surgery [129].

Positron Emission Tomography (PET) is currently being used in clinics to stage breast cancer and monitor response to therapy [20,33,351]. PET utilizes a positron emitter analogue of glucose, 2-(fluorine-18)-(fluoro-2-deoxyglucose) (^{18}FDG) to monitor *in vivo* glucose uptake. PET leverages the higher metabolic state, higher expression of glucose transporters (GLUTs), and lower expression of glucose-6-phosphatase of malignant cells to image the high level of ^{18}FDG uptake in cancerous cells, distinguishing them from non-cancerous cells [352–357]. 2-[N-(7-nitrobenz-2-oxa-1, 3-diazol-4-yl)amino]-2-deoxy-d-glucose (2-NBDG) is a fluorescent glucose analogue that undergoes a similar pathway of uptake and metabolism to ^{18}FDG and accumulates preferentially in malignant cells [25,358]. In preclinical imaging studies, 2-NBDG accumulation was shown to be higher in cancerous cells than in normal cells [25,359]. Nitin et al. have

demonstrated the use of 2-NBDG to enhance fluorescent molecular imaging of oral neoplasia [359].

In this study, we perform an important proof of principle study that demonstrates that topical application of 2-NBDG can be used as an optical contrast agent to help differentiate cancerous tissue using a wide-field imaging system. First, we demonstrate the cellular localization of the contrast agent in the cytoplasm of cancerous cells *in vitro*. Then, we imaged fresh human breast tissue acquired from surgical specimens and stained them with 2-NBDG. We establish that the 2-NBDG signal in tissue can be visualized using a wide-field camera and filters to create multispectral images of tissue. These multispectral images can then be analyzed both qualitatively and semi-quantitatively by using the area under the curve metric of the spectral profile of the tissues. Our analysis demonstrates that 2-NBDG preferentially enhances the fluorescent signal of malignant tissue. Future steps will be to develop a simpler and more portable wide-field optical system that uses 2-NBDG and can be applied to assist in the detection of cancerous tissue at the time of surgery.

Additionally, we follow the same principle of using glucose to target cells with increased metabolism by conjugating thioglucose to the surface of small diameter (~2 nm) gold colloid that is made in the lab or purchased commercially. As discussed in chapter 3, AuNPs have excellent plasmon resonance properties that allow for increased scattering of incident light. Successful conjugation of thioglucose to the surface of the particles (glu-AuNPs) was confirmed using Energy Dispersive Spectroscopy (EDS). Next, different surface coatings (citrate, glucose, or bare) of AuNPs show different effects on the targeting of the particles. Cells treated with glu-AuNPs have an increased

scattering signal from inside the cells, indicating preferential cellular uptake. We also demonstrate the difference between cancerous and non-cancerous cell lines by observing changes in the cellular uptake of the NPs. To accomplish this, the AuNPs were localized in the cytoplasm and the nucleus using Transmission Electron Microscopy (TEM) and EDS. Finally, we attempt to elucidate the mechanism of entry of these particles in the cells by using competitive inhibition and endocytosis inhibition studies.

5.3. Materials and Methods

5.3.1. Cell lines

The SK-BR-3 and MCF10A cell lines were obtained from the American Type Culture Collection (Manassas, VA). The SK-BR-3 cells were maintained in McCoys Modified Solution 5A supplemented with 10% fetal bovine serum (FBS) and 3% penicillin/streptomycin. The MCF10A cell line was maintained using a Mammary Epithelial Basal Medium Kit (Lonza) supplemented with standard growth factors. Both cell lines were grown at 37°C and 5% CO_2.

5.3.2. 2-NBDG characterization

2-NBDG was acquired from Invitrogen in powdered form and was re-suspended in 1X DPBS (Gibco) to a final concentration of 194 μM. The pH of the solution was 7.4. Aliquots of the fluorophore were kept frozen at -20°C in black centrifuge tubes until needed. Before receipt of the tissue, the aliquots were thawed in a 37°C water bath and kept at that temperature until being added to the specimens. To evaluate variability in the imaging system between testing days, 1 ml of 194 μM 2-NBDG was pipetted into a

quartz cuvette and placed in the same position in the imaging system and imaged under the same conditions for four consecutive days. The spectra of each day was acquired and compared to determine the system's stability between testing days.

5.3.3. Cellular staining with 2-NBDG

1 X 10^5 cells in fresh medium were plated onto glass chamber slides with removable plastic wells. After 48 hr, when the cells were in their log growth phase, the medium was removed and PBS with 1% bovine serum albumin (BSA) was added to the wells for 20 minutes at 37°C to starve the cells (cell medium alone was used as a control). The PBS-BSA was then aspirated and 2-NBDG was added to the wells for 20 minutes at 37°C in darkness. The 2-NBDG was then aspirated; the cells were placed on ice, and rinsed twice with cold PBS to remove any non-metabolized 2-NBDG.

5.3.4. Cellular imaging

Immediately after the cells were washed, the slides were placed on a CytoViva 150 microscope (Auburn, AL) for fluorescence and darkfield imaging. For fluorescence images, the cells were excited with light at 474-510 nm and emission from 515-555 nm was captured using a DAGE-MTI (XLMX, 152) charge-coupled device camera with 500 milliseconds (ms) integration time. For darkfield images, integration time was 1 ms.

5.3.5. Ex vivo tissue acquisition

Freshly excised human breast tissue samples were acquired from 14 patients undergoing surgical resection of suspected breast cancer at The University of Texas MD Anderson Cancer Center (MDACC) with the approval of the institutional review boards

at Rice University and MDACC. All patients gave written informed consent to participate. Each specimen was received from surgery and inked so that the pathologist could identify the *in situ* location of the specimen. The specimen was then bread loafed in 2-5 mm increments and visually inspected and palpated to determine the area of residual tumor. Leftover specimen that was not necessary for diagnosis by the surgical pathologist was used for the imaging process. A separate specimen of normal tissue away from the gross tumor was also acquired as an internal control for each patient. For one patient (#2), a single specimen was obtained with gross palpable tumor at one end and normal appearing tissue at the other end. Typically, the tissues were processed for imaging within 60 minutes of resection.

5.3.6. Ex vivo tissue sampling

Upon receipt of the tissue, autofluorescent images of both normal and malignant tissue were acquired using a Maestro wide-field multispectral fluorescent camera (CRi, Woburn, MA). The imaging system has a spatial resolution of 25 μm/pixel and the field of view for each image acquired was 4.9 X 3.7 cm. The tissue samples were excited with filtered light (445-490 nm) and the emitted light was filtered (515 nm LP) before entering the camera. The exposure time for the camera was 18.56 ms. A multispectral image cube comprised of the different images at different wavelengths (520-720 nm, every 10 nm) was created using these settings. This process created a prestain image that would be used for comparison after the tissue had been stained with 2-NBDG.

After the prestain image cube was created, both normal and malignant tissue specimens were incubated topically with 2-NBDG at 37°C for 20 minutes in the dark. The remaining 2-NBDG was aspirated and the tissue samples were rinsed twice in cold

PBS on ice in the dark for 10 minutes. The samples were placed under the wide-field camera in approximately the same positions as the prestain images. The tissues were subsequently imaged under the same conditions described above, and a poststain multispectral cube was created.

After imaging, the tissue samples were fixed in formalin for 24 hr, placed into 70% ethanol, and sent to the research pathology core laboratory at MDACC for hematoxylin-and-eosin (H&E) staining. Both the control and sample tissue slides were then reviewed by a breast pathologist (L.M.), who provided a histological diagnosis of the tissue. Pictures of the slides were taken at a 40X magnification using an Olympus DP70 camera (Center Valley, PA).

5.3.7. Fluorescence spectrum acquisition and quantitative analysis

For semi-quantitative analysis of the images, a region of interest (ROI) was custom-fit along the edges of the tissues on the before and after-staining images. The fluorescence spectrum from 520-720 nm of this ROI was plotted based on the fluorescent signal calculated at every 10 nm. The intensity for each wavelength was the average intensity for each pixel in the ROI. This allowed the creation of two sets of data for each of the tissues that could be used to compare the effect of adding 2-NBDG to both of the tissues. Tissue samples from one patient (#10) had only a data set for the post stain image due to a machine malfunction that was not detected until after the tissue had been stained; however, samples from this patient were included because poststain comparisons between the cancerous and noncancerous tissues could be made.

Analyses of each tissue spectrum revealed a slight peak in the 560-600 nm range for the prestain images and a larger, more prominent peak in the same range for the

poststain images. To quantify the 2-NBDG signal from each tissue and compare the different samples, an area under the peak of each curve (AUC) was calculated by multiplying the height (fluorescent signal) of each curve at 580 nm by the width of the peak (40 nm). The area under the prestain curves was subtracted from that of the poststain curves to normalize the autofluorescence (NAUC). The average NAUC of the cancerous and normal tissue was calculated, as well, the mean of all samples was calculated. This mean was then drawn as a horizontal threshold line to help discriminate between the two groups. Statistical significance between the groups of NAUCs was determined using a two-tailed Student's t-test.

The signal differences between the pre and poststain images at each wavelength from 520-720 nm were also calculated for each set of cancerous and normal tissues for the patients. For example, the differences at 580 nm for the cancerous tissue from each patient (excluding patient #10) were placed into one group and the differences at 580 nm for the normal control tissues were also placed into a group. The two groups were then compared by using a two-tailed student's t-test; this was done for each wavelength from 520-720 nm.

5.3.8. Fluorescent imaging of tissue slices

For further confirmation of the localization of 2-NBDG in the tissues. H&E slides of invasive ductal carcinoma were viewed under darkfield fluorescence using a Qimaging Exi blue CCD. Tissue slices were excited with 474-510 nm excitation light and signal from 515-555 nm was collected. Additionally, a darkfield image of the tissue was acquired for comparison.

5.3.9. Gold colloid synthesis and thioglucose conjugation

Gold colloid synthesis began with 45 mLs of distilled H_2O rotating in a glass beaker at 800 RPM. 1 mL of 1 N KOH was then added; 1 minute later, 12 uL of THPC (Tetrakis(hydroxymethyl)phosphonium chloride) was added for 1.5 mins followed by 2 mLs of 1% $HAuCl_4$ for 2 minutes to form the colloid solution. 10 mLs of colloid solution was then combined with 10 mLs of 10 mM thioglucose or sodium citrate and spun at 800 RPM for 15 minutes. The solution was then rinsed three times using a centrifugal dialysis filter (10,000 Dalton cutoff) for 20 minutes at 2500 g. The final solution was then re-suspended to a total of 10 ml and kept at 4°C. TEM images of the particles were acquired using a JEOL 2010 TEM and carbon-copper TEM grids acquired from electron microscopy sciences (FCF-200-Cu).

5.3.10. Thioglucose binding characterization

2 nm gold colloid from Ted Pella Inc. ($1.25X\ 10^{14}$ particles/mL) were conjugated and filtered in the same method as the synthesized colloid above. However, TEM images were acquired with a JEMF-2100 Field Emission Gun Transmission Electron Microscope that is equipped with EDS to confirm the presence of gold and sulfur. Energy spectra were collected at different areas in the field of view (FOV). Electron counts at peaks corresponding to gold and sulfur were used to calculate the percentage of atoms present at each area. The percentages of each element present were then calculated using energy detected by the scanner.

5.3.11. Different surface coatings' effect on uptake

175,000 Sk-Br-3 cells were plated onto glass chamber slides and allowed to grow as previously indicated. Media was removed and 1 mL of fresh media was then added to each chamber. 500 μL of AuNPs (thioglucose, sodium citrate, or no coating) or 500 μL of media (negative control) were added to the cells for an incubation period of 20 minutes at 37°C. The cells were then rinsed in PBS and imaged on the Cytoviva™ darkfield microscope. Images were acquired with a Qimaging Exi Blue CCD. Images were acquired at different exposure times so that cellular features could be visualized.

5.3.12. Cell line specificity of glu-AuNPs

175,000 Sk-Br-3 and Mcf10A cells were plated onto separate chamber slides and allowed to grow as previously discussed. 250 μL of 0.312 μM particles conjugated with either thioglucose or sodium citrate were added to the cells for 20 minutes. After 20 minutes, the media was aspirated, the cells were rinsed quickly with PBS and then fixed with glutaraldehyde fixation buffer for 30 minutes. Buffer was then removed and the chamber slides were imaged under darkfield microscopy.

5.3.13. Localization of glu-AuNPs inside cells using TEM-EDS

75,000 Sk-Br-3 cells were plated on a 24 well plate (Corning 3527) and allowed to grow to ~75% confluency after 48 hrs. The cells were then treated with gold colloid coated with thioglucose as mentioned in previous studies. After treatment, the cells were fixed in sodium cacodylate buffer with glutaraldehyde and formaldehyde (Electron Microscopy Sciences 15949) and placed in the refrigerator for further processing. After

fixation, the samples were washed, postfixed with 1% buffered osmium tetroxide for 30 min, and stained en bloc with 1% Millipore-filtered uranyl acetate. The samples were dehydrated in increasing concentrations of ethanol, infiltrated, and embedded in LX-112 medium. The samples were polymerized in a 60° C oven for 2 days. Ultrathin sections were cut in a Leica Ultracut microtome (Leica, Deerfield, IL), stained with uranyl acetate and lead citrate in a Leica EM Stainer, and examined in a JEM 1010 transmission electron microscope (JEOL, USA, Inc., Peabody, MA) at an accelerating voltage of 80 kV. Digital images were obtained using AMT Imaging System (Advanced Microscopy Techniques Corp, Danvers, MA).

After visualizing the AuNPs in the cells, EDS was used to confirm the presence of gold inside the cell. A single cell was visualized on a JEOL TEM microscope (Jeol JEM 2100F), then, using a Scanning Transmission Electron Microscopy (STEM) EDS technique, we were able to pinpoint specific points around the cell to excite with an electron beam. The characteristic energy emitted by the sample corresponds to unique atomic structures, allowing us to detect presence of specific atoms. The amount of gold in specific areas was tabulated by measuring the height of the gold peak at 2.5 keV and comparing its height to the peak of the maximum energy level (measured at 70 counts) to calculate the amount of gold in specific intracellular areas. The areas interrogated include intranuclear, cytoplasm, and extracellular spaces. We interrogated three intranuclear, three cytoplasmic, and one extracellular area for comparison. Additionally, spectra of untreated cells were acquired. For each specific area, 5 runs were completed and averaged. For this experiment, a TEM grid from the same set of cells that is displayed in Figures 5.13 & 5.14 was analyzed. However, due to the destructive nature of the EDS

imaging process that damages the sample grids, different grids were analyzed. Additionally, the specific areas of AuNPs that are highlighted in 5.13-5.14 are not the areas analyzed for EDS. However, these cells were from the same experiment and were treated with the same glu-AuNPs.

5.3.14. Inhibition of clathrin mediated endocytosis

75,000 Sk-Br-3 cells were plated on a 4 well chamber slide (Labtek 154941) at 37° C and 5% humidity for 48 hours. After 48 hours, the clathrin mediated endocytosis inhibitor chlorpromazine hydrochloride was added to the cells at a concentration of 5 μg/ml for 2 hours without changing media. The concentration of chlorpromazine needed to inhibit endocytosis is cell-type dependent [360], so optimization studies were performed to determine the optimal concentration of chlorpromazine that inhibits endocytosis without being cytotoxic. After 2 hours, glu-AuNPs were added to the cells in the same fashion as previously described. Additionally, human transferrin tagged with Alexa Fluor 488 (Invitrogen T13342) was added at a concentration of 1 mg/ml as a marker for endocytosis. After 20 minutes, the entire media, transferrin, and glu-AuNPs mixture was aspirated and cells were fixed in cytofix buffer. After fixation, the cells were imaged on the Cytoviva darkfield microscope where images were acquire in both standard darkfield mode (exp. 5 ms) and fluorescence darkfield mode (500 ms) of the same field of view. Both sets were converted to 8-bit and contrast was adjusted to remove background signal (fluorescent images were set at a range of 44-255 and the darkfield images were set at 0-100). Next, the fluorescent and darkfield images were false colored red and blue respectively, and the images were combined.

In addition to darkfield and fluorescence images being acquired, TEM images of cells that were treated with both chlorpromazine and AuNPs were also acquired. TEM images of the cells were then acquired at various magnifications to localize the glu-AuNPs inside the cell.

5.3.15. Competitive inhibition with D-glucose

To further elucidate the mechanism of entry of the particles into cells, a competitive inhibition assay was performed with D-glucose. First, cells were plated in the same manner as previously stated and allowed to grow for 48 hours. Then, 500 μL each of AuNPs and 40 μM D-glucose were added to 500 μL of media. Additionally, D-glucose alone and glu-AuNPs alone were added to cells as controls. After 20 minutes, cells were fixed and imaged as previously described.

In addition, flow cytometry analysis was conducted to evaluate the impact of glu-AuNPs and citrate-AuNPs on the 2-NBDG signal in Sk-Br-3 cells. For this experiment, 75,000 cells were plated in 24 well plates and allowed to grow for 48 hrs. Media was then aspirated and 200 μL of 10 μM 2-NBDG was added to each well. Additionally, 200 μL of two different concentrations (20 and 40 μM, respectively) of D-glucose were added to different sets of cells as positive controls. 1.67 μM of citrate or glu-AuNPs were added to the cells with 2-NBDG for 20 minutes at 37°C. After incubation, the media was aspirated and the cells were trypsinized from the wells and fixed in cytofix buffer. Samples were analyzed in a flow cytometer (BD FACSCANTO II) and the mean fluorescence intensity (MFI) of the FITC channel was calculated for the cells. Samples were run in triplicate and the average FITC intensity for each group was compared using an ANOVA and tukey-kramer t-test.

5.4. Results

5.4.1. *In vitro* 2-NBDG results

Figure 5.1 demonstrates the cellular specificity of 2-NBDG and its ability to differentiate cancerous cells (Fig. 5.1(A)) from non-cancerous (Fig. 5.1(B)) cell lines *in vitro*. Additionally, normal darkfield images of the same field of view (not shown) were used to confirm the presence of cells in the area. The increased metabolism of cancerous cells leads to an increase in expression of GLUTs on the cell membrane. This leads to an increase in 2-NBDG uptake in malignant cells that is visualized with fluorescence microscopy. These results demonstrate an important proof of concept that allowed us to move on towards using 2-NBDG in resected tissue specimens and using glucose to target other contrast agents such as AuNPs.

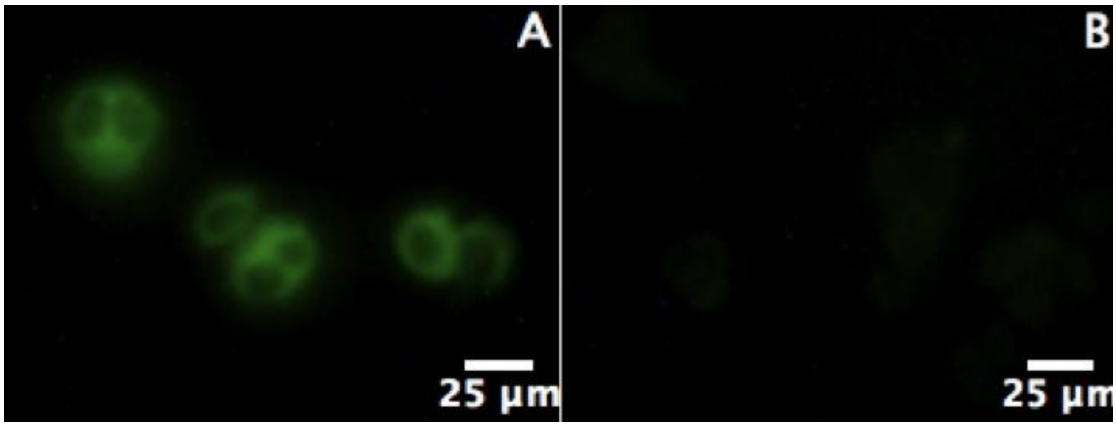

Figure 5.1 Fluorescent images of cancerous Sk-Br-3 (A) and non-cancerous Mcf10A (B) cell lines demonstrate the preferential uptake of 2-NBDG in the cancerous cell lines due to the over-expression of GLUTs in the cell membrane of the cancerous cells.

5.4.2. 2-NBDG in freshly excised breast specimens

After establishing that using glucose to target contrast agents in cancerous cell lines that over-express GLUTs, our next step was to use the fluorescent contrast agent 2-

NBDG to target and optically differentiate malignant tissue. Figure 5.2 displays the patient characteristics of the tissues that were sampled for imaging. The pathologic diagnosis of each tissue sample was confirmed by a breast pathologist in a blinded fashion. There were five tissues that contained invasive ductal carcinoma (IDC), one that contained invasive mammary carcinoma (IMC), three that contained invasive lobular carcinoma (ILC), three that contained ductal carcinoma in situ (DCIS), and two that contained no cancer cells. Of the two specimens that did not contain cancer cells, one was obtained (patient #13) from the periphery of resected breast tissue that did contain metaplastic carcinoma with both spindle cell and IDC components. The other tissue sample was from a patient (#14) who had received neoadjuvant chemotherapy and achieved a complete pathologic response. In that specimen, there was evidence of tissue repair and fibrosis.

Patient/Sample Number	Diagnosis	Nuclear Grade
1	Ductal Carcinoma in Situ	3
2	Ductal Carcinoma in Situ	3
3	Ductal Carcinoma in Situ	3
4	Invasive Ductal Carcinoma	2
5	Invasive Ductal Carcinoma	2
6	Invasive Ductal Carcinoma	2
7	Invasive Ductal Carcinoma	2
8	Invasive Ductal Carcinoma	2
9	Invasive Lobular Carcinoma	3
10	Invasive Lobular Carcinoma	3
11	Invasive Lobular Carcinoma	3
12	Invasive Mucinous Carcinoma	1
13	No Cancer Cells	N/A
14	No Cancer Cells	N/A

Figure 5.2 Tissue characteristic and grades for 14 tissues that were declared to be malignant tissue by on-site pathology.

Figure 5.3 represents the images acquired of both the malignant (IDC) and normal non-cancerous tissue before and after incubation with 2-NBDG. These two images are representative of the images analyzed from the malignant and normal tissues. The tumor specimen clearly showed brighter fluorescent signal after incubation with 2-NBDG (Fig.

5.3(B), T) as compared to its prestained image (Fig. 5.3(A), T) and the poststain image of the normal tissue (Fig. 5.3(B), N). Each tissue specimen had similarly low-levels of autofluorescence (Fig. 5.3(A)). The non-neoplastic tissue was mildly brighter after 2-NBDG incubation, which probably reflects the basal level of glucose uptake in normal tissue. Figure 5.3(C) illustrates a representative H&E stained tissue slice from the tumor specimen imaged in Figure 1B. It confirmed the presence of carcinoma in the tissue with high fluorescent signal.

Figure 5.3(D) illustrates the post stain image of a single specimen in which it was unknown whether there was presence of malignant tissue. This fluorescent image was used to slice the tissue into two different specimens, one that was believed to be cancerous and one that was non-cancerous. The presence of DCIS in the left-side aspect and normal tissue in the right-side aspect of the specimen was confirmed histologically.

The fluorescence spectra of the tissues imaged in Figure 5.3 (A&B) was calculated and is presented in Figure 5.4. The spectra are representative of the spectra seen with the other tissues. The fluorescent signal of the malignant tissue after 2-NBDG staining was on average 13.1±1.0 (average±standard error of the mean) times greater at eachwavelength than the signal calculated from the prestain image. Conversely, the fluorescence of normal breast tissue was only an average of 1.7±0.1 times greater after addition of 2-NBDG. Hence, the fluorescence increase after 2-NBDG staining of the malignant tissue was much higher than that of the normal, non-cancerous control tissue, indicating that there was increased 2-NBDG consumption in the malignant tissue relative to the normal tissue.

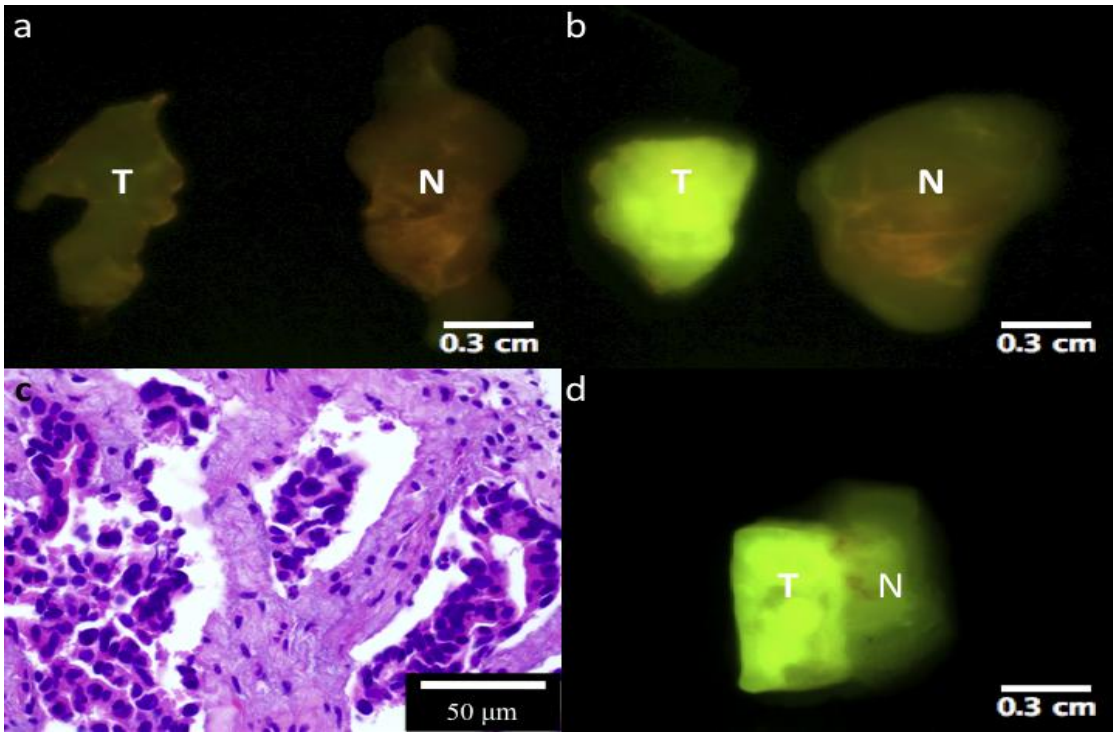

Figure 5.3 Wide-field multispectral images of invasive ductal carcinoma (T) and normal breast tissue (N) from patient #6. (a) Tissues pre 2-NBDG stain; (b) tissues post-2-NBDG stain. Tissues were excited with 445-490 nm light and images were collected after having passed through a 515 nm LP filter. (c) Tissue slice stained with hematoxylin and eosin depicts IDC. (d) One tissue slice with ductal carcinoma in situ (DCIS) and normal tissue. The left, brighter side was diagnosed as DCIS, whereas the other half was diagnosed as normal tissue.

Additionally, spectral analysis of the two different slices from Figure 5.3(D) showed that the intensity at each wavelength was 2.0±0.1 (data not shown) times greater in the malignant tissue than the normal tissue for each spectral measurement. This demonstrates that there was clear demarcation of an area of high fluorescence corresponding to DCIS and an adjacent low level of fluorescence corresponding to normal tissue.

One issue addressed was 2-NBDG variation on a day-to-day basis. Our tests showed that the intensity variability at each wavelength was less than 3.2% of the average intensity calculated for each wavelength over the 4-day period; this demonstrated the system's stability and allowed us to perform quantitative analysis of the images.

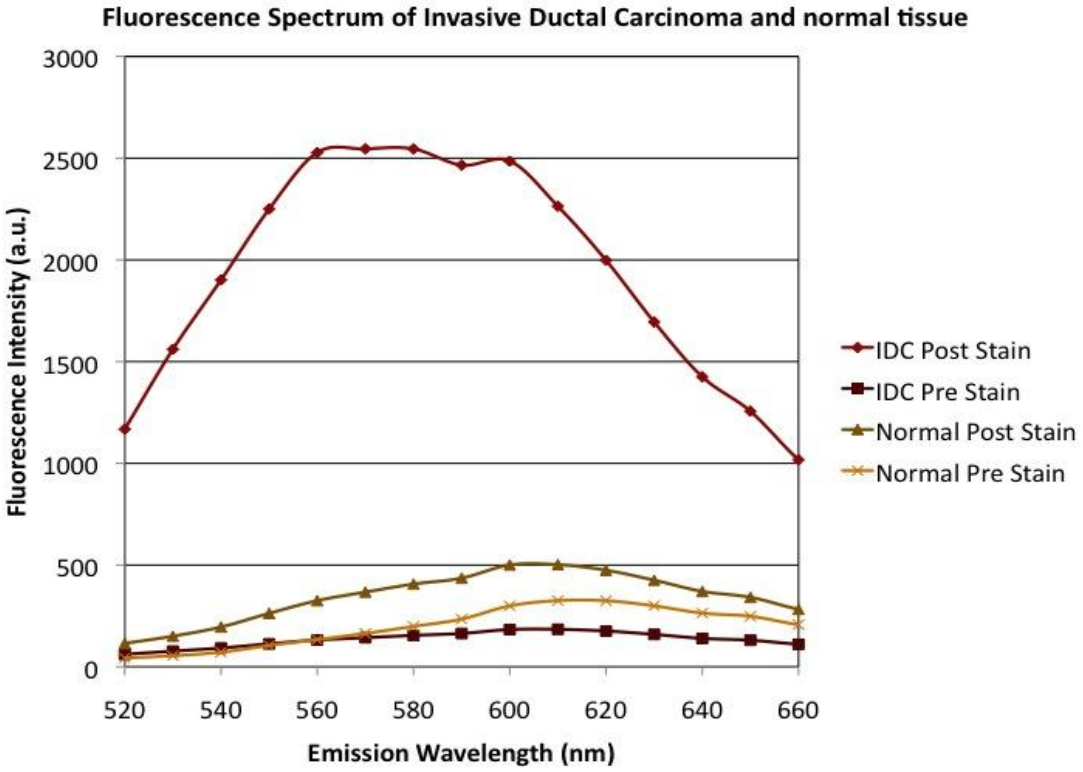

Figure 5.4 Emission spectra of multispectral cubes represented in Figure 1. Regions of interest were hand-drawn on each tissue; fluorescent signals every 10 nm from 520 to 660 nm are shown.

The fluorescent signal difference between the poststain and prestain images from all the tumor samples and normal controls were averaged separately at each wavelength and are illustrated in Figure 5.5. The difference in the intensity of fluorescence of the tumor samples was significantly higher than that of the normal controls at each wavelength from 520 to 720 nm (P<0.0001). At 580 nm (the center of the fluorescence spectrum peak ranging from 560 to 600 nm), the average intensity difference from the malignant tissues (1,878.2±169.7) was 2.7 times higher than that from the normal non-cancerous tissue (704.9±108.2).

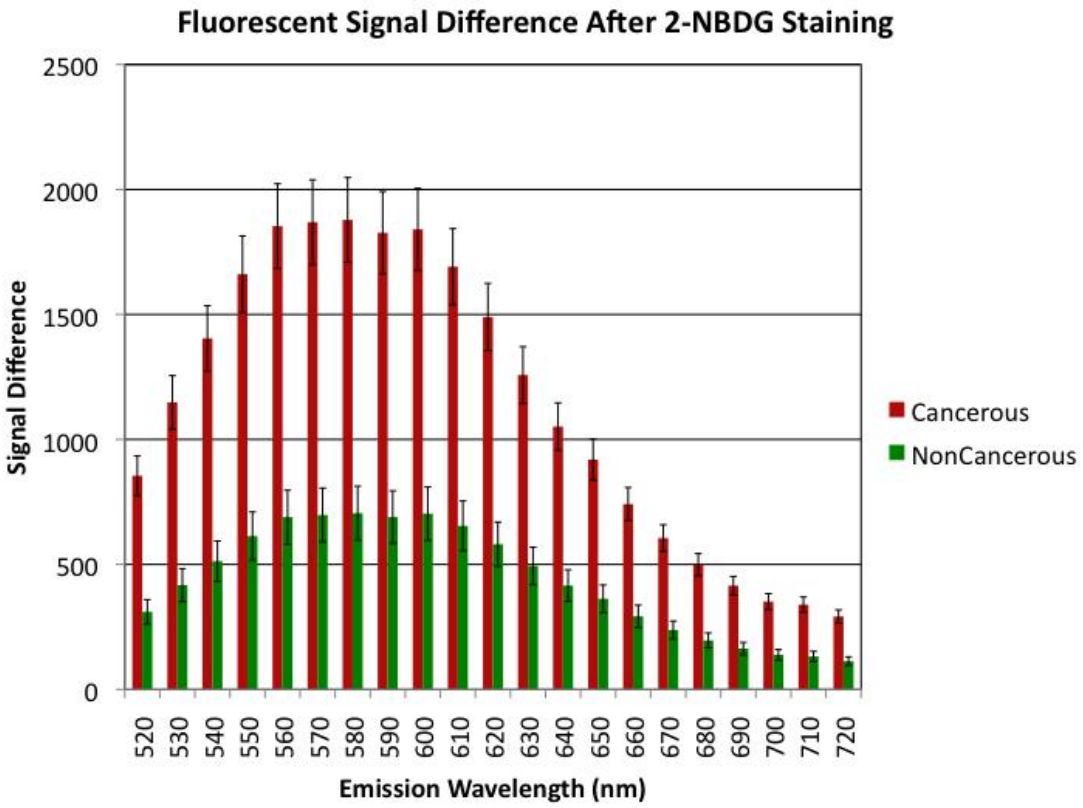

Figure 5.5 Average signal difference between the poststain and prestain images calculated at each wavelength. A *t*-test comparison between the groups at each wavelength revealed that all of the groups were statistically different ($P<0.0001$). Error bars represent standard error of the mean.

To quantitatively distinguish the fluorescence of malignant tissue from that of normal, non-cancerous tissue, the NAUC values for the 560-600 nm range of the spectra were calculated for each sample (Fig. 5.6). The mean NAUC for the tumor samples (81,670±7,142) was significantly higher than that for the control (31,170±5,411, $P<0.00001$). The difference between malignant and non-cancerous tissue for some samples (#1, #5, and #10) exceeded a factor of 2; however, other tissues (#3, #6, #7, and #8) had less than a 2-fold difference between the tissues. The small differences did not seem to be limited to a particular type of breast cancer, as IDC had both some of the largest differences and some of the smallest differences. These differences may be

attributed to each specific tissue and the part of the normal breast tissue that was provided by the pathologist.

Using the average NAUC (56,420) as a discrimination line, the NAUC values for nine of the malignant samples were above the line while the NAUC values for three were below. However, the NAUC value of all but one of the normal control samples was below the threshold.

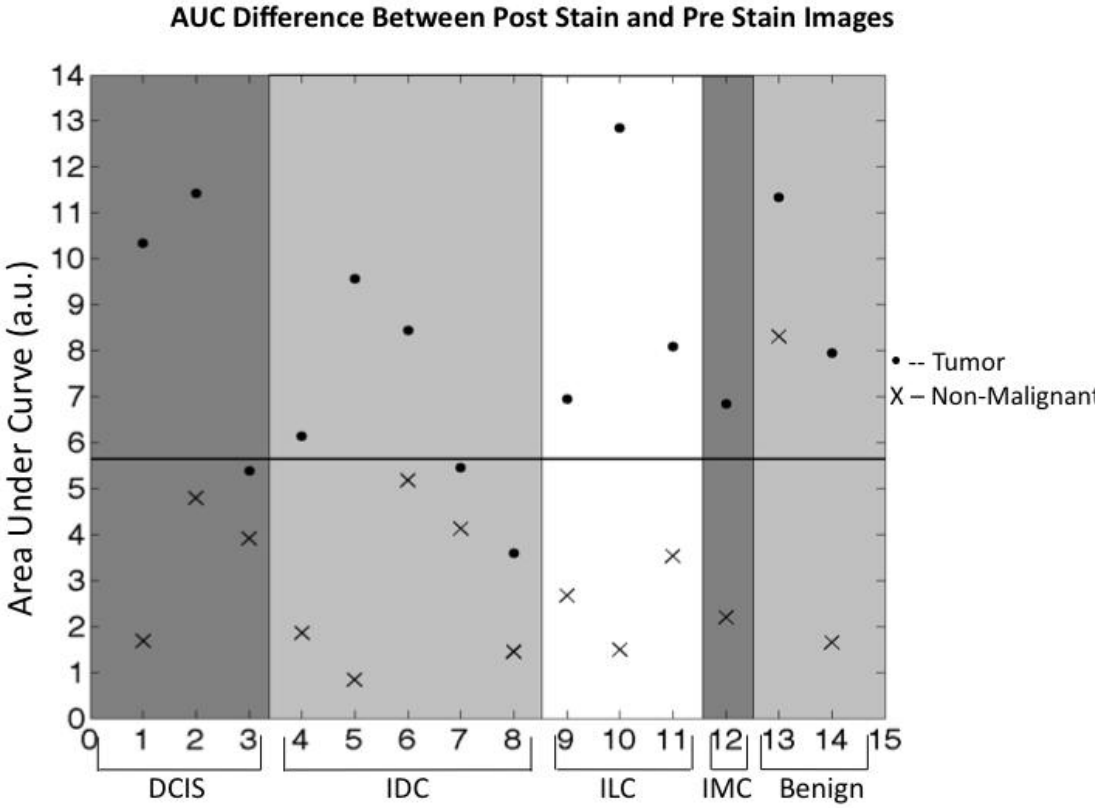

Figure 5.6 Areas under each curve for the range of 560-600 nm. Each point on the graph represents the difference in AUC between the prestain and poststain images of the tissues from each patient. Dots represent the differences for tissues considered to be cancerous at time of collection. The black line represents the average NAUC of the two groups.

Figure 5.7 demonstrates the localization of the fluorophore to the cancerous tissue cells on the H&E slide. There was concern that due to the very different tissue structures of cancerous and normal tissue that 2-NBDG accumulation could be occurring in the

extracellular matrix of the tissue and not in the cells themselves. These darkfield fluorescent images demonstrate that 2-NBDG is found in the cells of the tissue and not just the outside of the cell. Figure 5.7(A) is the darkfield fluorescence image that was acquired with the same settings for the cells from Figure 5.1 and 5.7(B) shows that there is increased signal in the tissue when in fluorescence mode due to the presence of the fluorescent contrast agent.

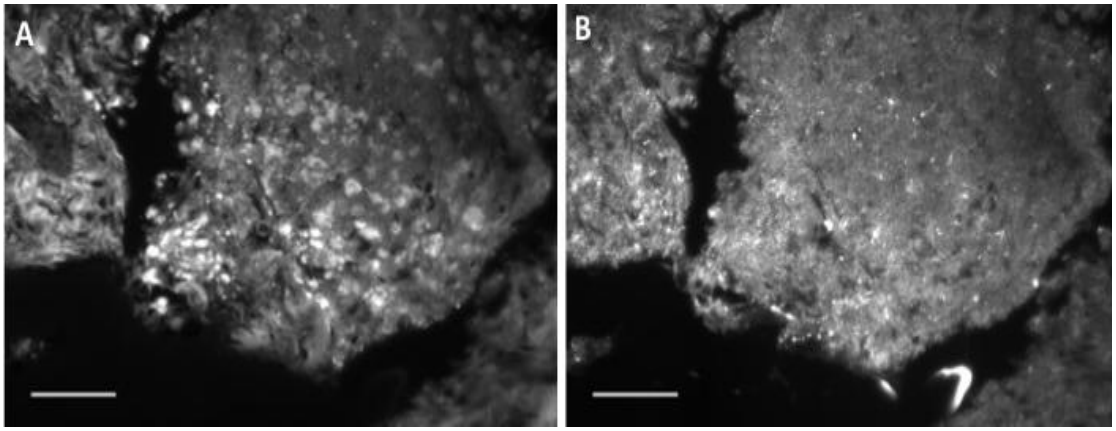

Figure 5.7 Fluorescence darkfield (a) and darkfield (b) images of hematoxylin and eosin stained invasive ductal carcinoma tissue. The increased fluorescence in the fluorescent image indicates presence of 2-NBDG in the cells and not extracellular stroma. Scale bar = 100 μm.

5.4.3. Glu-AuNPs *in vitro* results

After demonstrating the utility of glucose to target a fluorescent contrast agent, we hypothesized that we could use this same principle to target small diameter AuNPs. The following sections discuss the surface ligand specificity, cell type specificity, and mechanism of entry of glucose functionalized AuNPs.

Figure 5.8 displays TEM images of synthesized colloid after capping with thioglucose. Both figures display the same sample with a zoomed in view displayed in Figure 5.8(B). Using ImageJ, diameters of 13 AuNPs displayed in 5.8(B) were calculated to have an average diameter of 3.12 ± 0.71 nm after conjugation with

thioglucose. Additionally, Figure 5.8(A) shows that there is very even distribution of sizes of AuNPs in the sample allowing us to conclude that there are no particle aggregates.

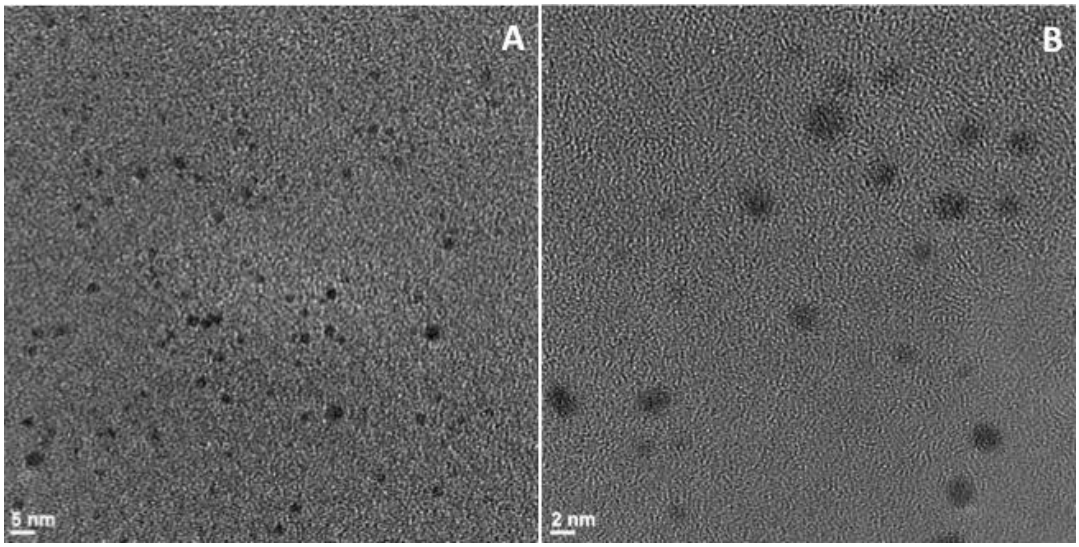

Figure 5.8 TEM images of glu-AuNPs . 5.8(A) displays the size distribution of the nanoparticles. Figure 5.8 (B) demonstrates a zoomed in view of the field of view displayed in 5.8 (A). ImageJ was used to calculate the average size of the AuNPs to be 3.12±0.71 nm.

Figure 5.9(A) displays AuNPs commercially produced from Ted Pella, Inc that have been coated with thioglucose. The average size of these AuNPs was 2.4±0.54 nm. Two spots where EDS was used to collect the relative percentage sulfur and gold atoms that were present at each point. Sulfur was calculated to show the thiol binding of thioglucose to the surface of the gold particle. Figure 5.9(B) displays the relative percentage of elements present at each spot, showing that the edge of the AuNP is where the majority of sulfur is localized, confirming the surface coating of thioglucose.

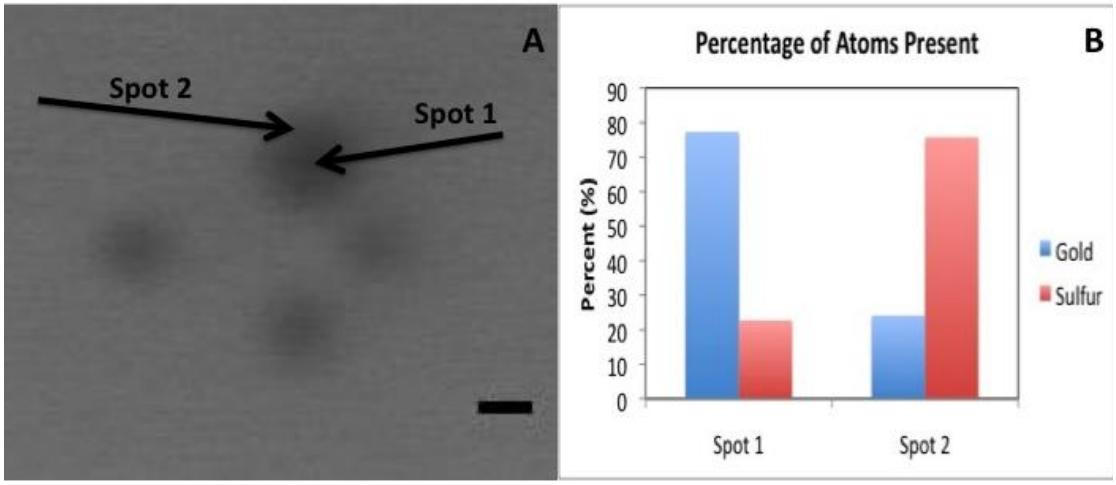

Figure 5.9 Glu-AuNPs after filtration to remove any impurities. ImageJ was used to calculate the average size of these AuNPs to be 2.4±0.54 nm. Energy Dispersion Spectroscopy (EDS) was used to calculate the relative percentage of elements present at points displayed in (A). Percentages calculated demonstrate the localization of thiol bonds of thioglucose to the surface of the AuNP. Where there was very little sulfur in the central area of the AuNP. Scale bar = 2 nm

Figure 5.10 displays representative images of Sk-Br-3 cells after incubation with AuNPs with no coating, two different coatings, and a negative control. This experiment was conducted three times. The negative control (Fig. 5.10(A)) displays cells with no scattering from inside the cell and slight signal from the cell membrane. Figure 5.10(B) displays cells that were incubated with AuNPs that had no coating. Cells incubated with citrate-AuNPs and glu-AuNPs are presented in Figure 5.10(C&D). Cells that were incubated with glu-AuNPs showed increased scattering signal from inside the cell. Scattering from the bare or citrate functionalized AuNPs was localized to the cell membrane (Fig. 5.10(B&C), which may be a function of electrostatic interactions between the membrane and the particles causing them to stick to the surface. However, we see very little scattering inside these cells.

We also examined the changes in uptake of the glu-AuNPs in cancerous versus non-cancerous breast cell lines as was shown with 2-NBDG in previous experiments. The results from Figure 5.11(A) show that Sk-Br-3 cancerous cells once again had the

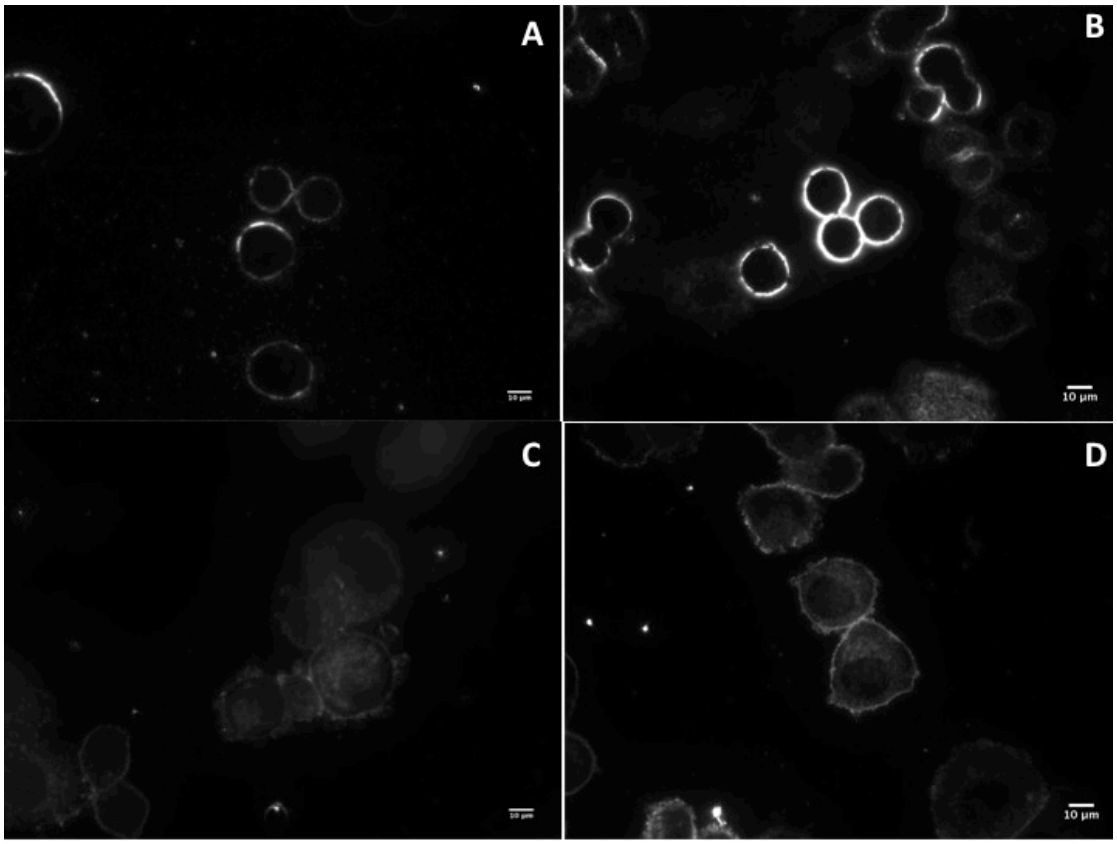

Figure 5.10 Sk-Br-3 cells incubated with (A) media only, (B) AuNPs without a surface coating, (C) citrate-AuNPs, and (D) glu-AuNPs. After a 20 minute incubation there is increased scattering signal from inside the cells of (D) that are localized to the cytoplasm of the cell. The other treatments seem to only have increased signal from the outside of the cell.

intense intracellular scattering signature that delineated the nucleus. In contrast, the normal mammary cell line (Mcf10A) had minimal scattering inside the cells,. Additionally, Figure 5.12 displays the controls of cells without treatment and cells treated with citrate AuNPs to demonstrate that the intense scattering from theperiphery of the Mcf10A cells is not due to the presence of AuNPs but is an inherent signal of the cell line. This could be due to naturally occurring extracellular structures with mismatching indices of refraction causing intense scattering profiles outside of the cells [281]. Additionally, scattering from cells treated with citrate-AuNPs is localized to the cell membrane.

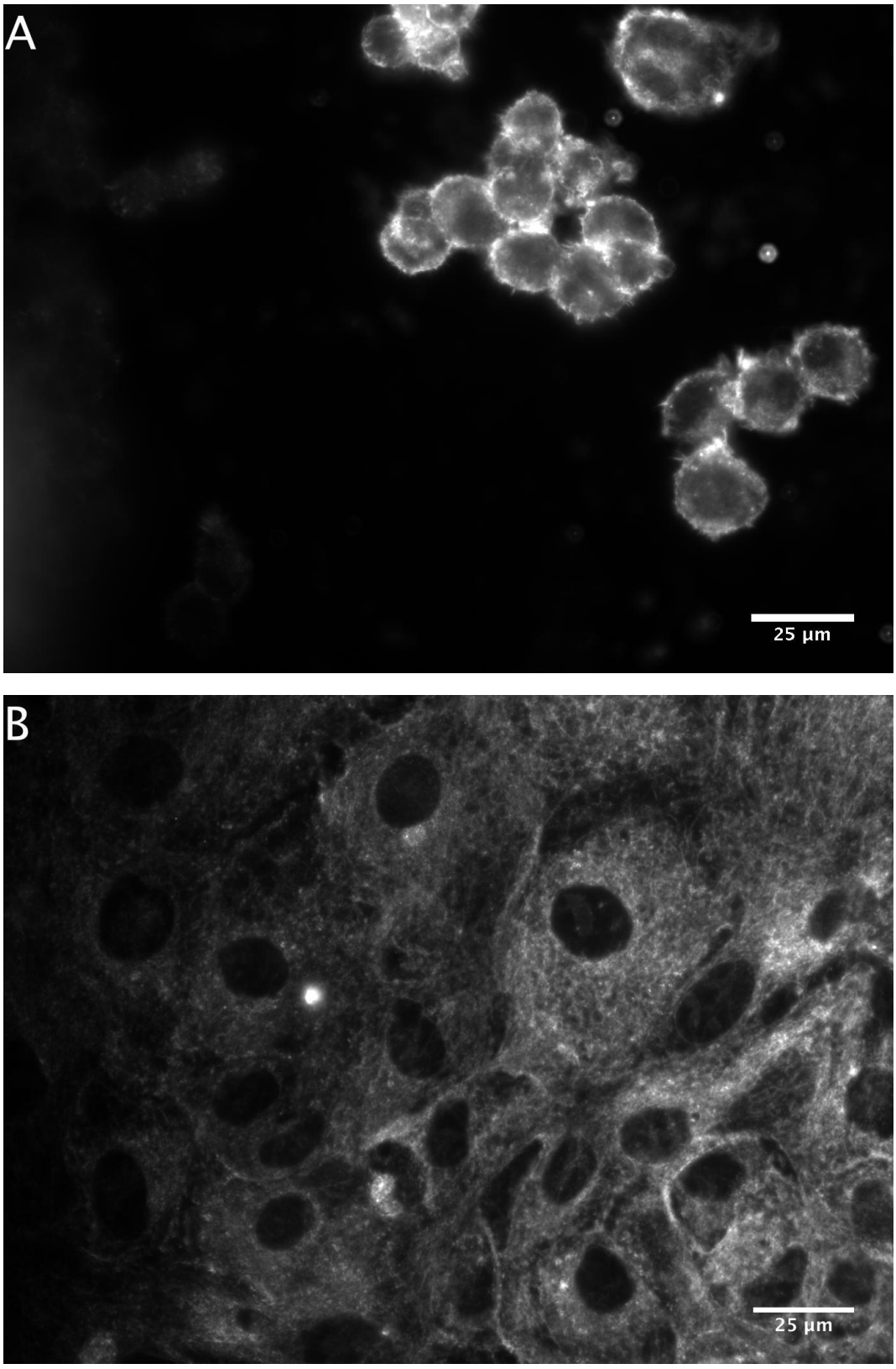

Figure 5.11 Sk-Br-3 (A) cancerous and Mcf10A (B) non-cancerous breast cell lines after treatment with glu-AuNPs. Sk-Br-3 shows a distinct scattering pattern from inside the cell membranes that is seen with previous experiments, whereas the Mcf10A line does not exhibit these characteristics.

To determine the precise intracellular location of the glu-AuNPs, TEM was performed on cell samples that had been treated with glu-AuNPs in the previously described method. TEM images of Sk-Br-3 cells that were untreated (A-C) and treated (D-H) with glu-AuNPs are shown in Figure 5.13. Three different magnifications are displayed, with circles outlining the area that is magnified in the subsequent higher magnificatiodisplayed in the row below. In the negative control (Fig. 5.13 (A-C)), there is a distinct lack of the black, electron dense areas that can be seen at the higher magnifications in the treated cells (Fig. 5.13(D-F). Upon further magnification (Fig. 5.14), we can see that these electron dense areas have a black pepper structure, which indicates presence of a large number of AuNPs. Even though the particles have accumulated inside one large area, there is very little aggregation, which can occur from drastic pH changes and protein aggregation on the surfaces of particles (Fig. 5.14).

An issue with visualizing small diameter AuNPs is the lack of electron density for individual particles to show contrast against the cytoplasm, indicating that there needs to be a high concentration of particles either from aggregation or localization inside an intracellular structure. An example of this can be seen in Figure 5.13(D) where the AuNPs are found inside an autophagosome, which is formed when a cancer cell is undergoing autophagy. Possible reasons for this phenomenon will be explored further in the discussion section. Due the small diameter of these particles, it is difficult to isolate individual particles that we hypothesized might be found in the cytoplasm. However, further exploration with EDS might allow us to pinpoint specific areas of the cell without aggregates and outside of extracellular structures to demonstrate AuNP presence. These

results confirmed the presence of glu-AuNPs within the cell, showing that the scattering profile seen inside the cells was due to the presence of the AuNPs.

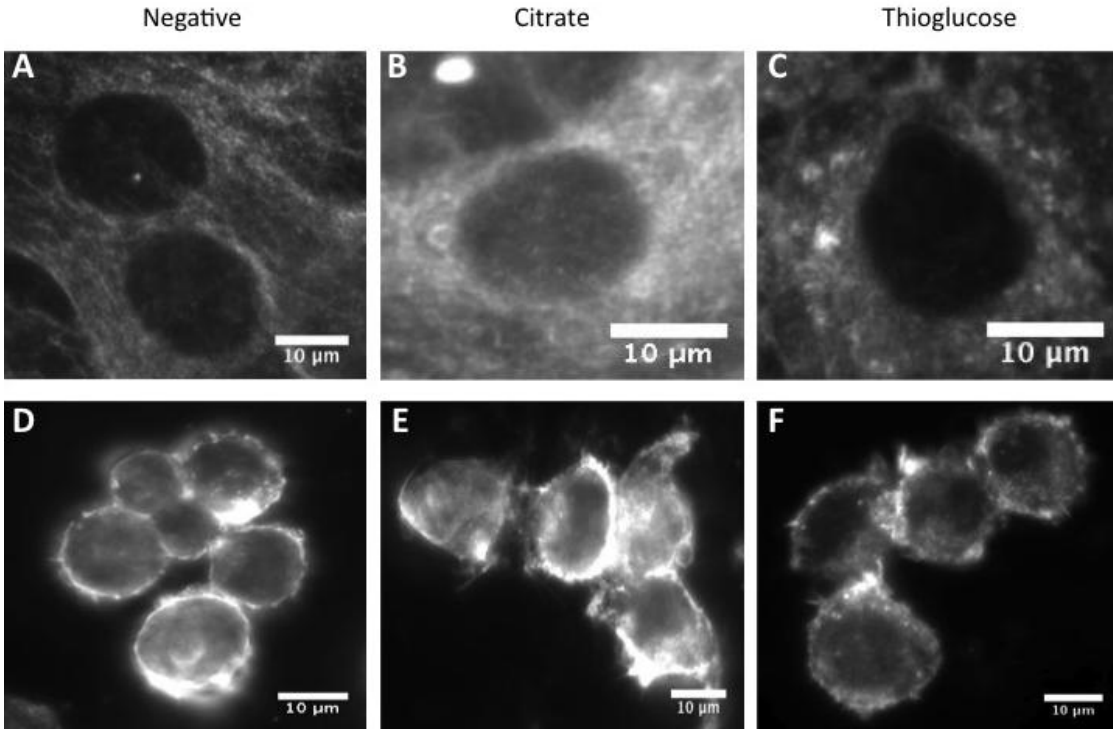

Figure 5.12 Darkfield microscopy images of normal (A-C) Mcf10A and malignant (D-F) Sk-Br-3 cell lines displaying the scattering differences that between cell lines when treated with the same targeting moiety. It is interesting to note that Mcf10A cells all have the same scattering profile, regardless of treatment, but the Sk-Br-3 cell lines have differences between treatments.

The final confirmation of the intracellular localization of glu-AuNPs was accomplished with EDS. The presence of any gold signal would confirm that there were glu-AuNPs inside the cell. A representative spectrum of a cell incubated with glu-AuNPs is presented in Figure 5.15(A), and a negative control in Figure 5.15(B). There are distinct differences in the energy spectra of each cell, with the peak at 2.5 keV indicating a high amount of gold inside the cell, with no visible peak in the same region in Figure 5.15(B). We were also able to pinpoint specific regions of interest inside the cell using this technique. Figure 5.16 shows the average signal at 2.5 keV taken at different areas inside the cell (intranuclear, cytoplasmic, and extracellular). There is a

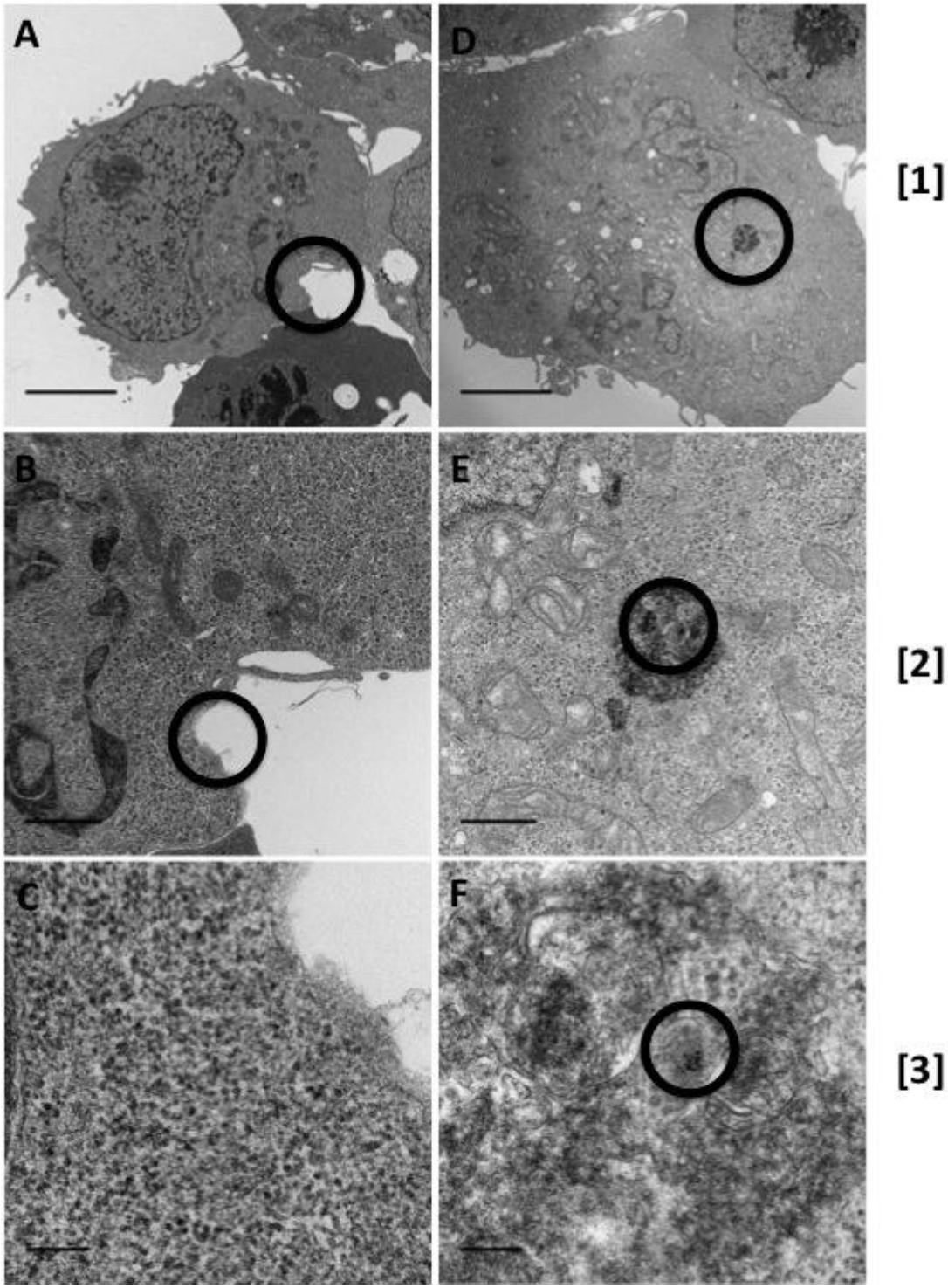

Figure 5.13 TEM images of Sk-Br-3 cells treated with glu-AuNPS (D-F) and their negative control (A-C). Various magnifications are presented for each row and black circles represent areas that are magnified for the next row of magnification. Magnifications and scale bars for each respective row: (1) 6000X, 5μm; (2) 25,000, 1 μm; (3) 100,000, 100 nm.

different amount of gold in various areas of the cell, with a higher amount of gold inside the nucleus than from inside the cytoplasm; this observation will be explored further on in the chapter. EDS is a powerful tool that has allowed us to confirm the presence of AuNPs inside Sk-Br-3 cells that have been treated with targeted AuNPs. When used in combination with TEM, we were able to confirm that there was gold inside the cell and verify the conclusions from our darkfield microscopy experiments. Our next step in studying glu-AuNPs interactions' with cells was to investigate the mechanism of entry of these particles.

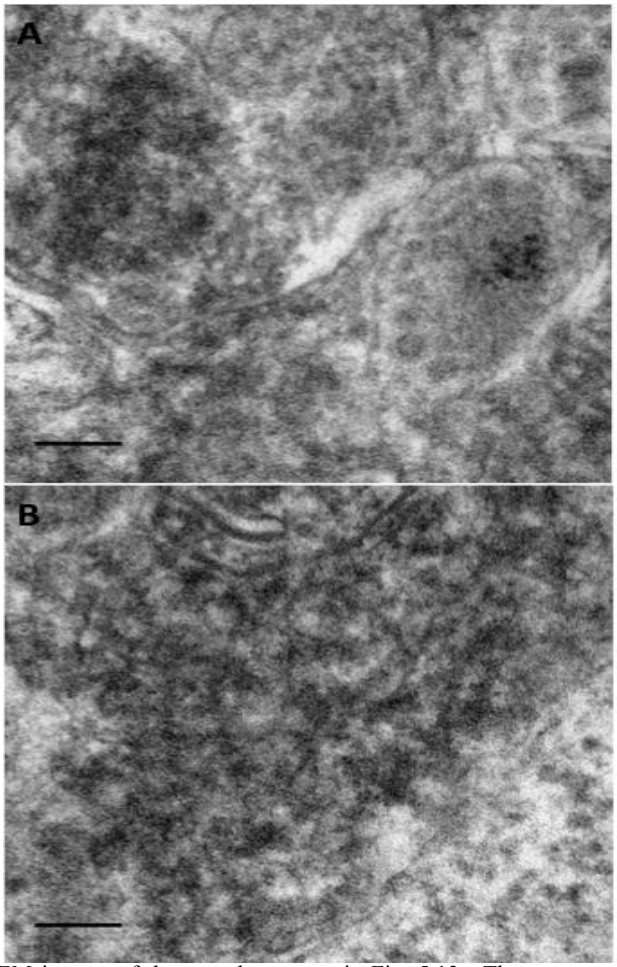

Figure 5.14 200,000X TEM images of the autophagosome in Fig. 5.13. The appearance of black pepper in the middle right and upper left of (A) are areas of the autophagosome where AuNPs have accumulated. Additionally, in (B), the AuNPs are spread out throughout the autophagosome displaying a large amount of AuNPs inside the cell. Scale bar = 100 nm.

5.4.4. Determining the mechanism of entry of glu-AuNPs

The purpose of these experiments was to determine if conjugating 2 nm AuNPs with glucose could improve targeting of the particles. Our hypothesis was that by placing glucose on the surface of these particles, we could take advantage of the increased glucose transporter expression in cancerous cells to develop a new method of targeting AuNPs. Almost all NPs are consumed by the cell via endocytosis whether it is by receptor mediated or clathrin independent mechanisms. Our hypothesis was that these particles would enter the cells via the glucose transporters and not undergo the same cellular processes that most AuNPs go through upon entering cells through endocytosis. A new mechanism of entry for particles has implications for the development of newtargeting moieties that could improve both diagnostic and therapeutic applications. Additionally, if NPs were able to enter the cell through a non-endocytotic process then physiologic phenomena such as the low pH of lysosomes, might be avoided and a fully intact particle with a specific therapeutic might be more effective.

Finally, as Nitin and O'Neil demonstrated, fluorescent glucose accumulates to 90% of maximum signal within 10 minutes of incubation, and at 20 minutes, there is maximum accumulation [25,359]. This phenomenon led us to hypothesize that targeting AuNPs with glucose might increase the speed of targeted nanoparticles entering cancerous cells. Previous studies by Kong and Feng have shown the ability of glucose-targeted AuNPs to increase radiation cytotoxicity by increasing the amount of gold inside the cell that is available for interaction X-rays. However, both of these studies use significantly larger AuNPs (10-14 nm diameter) that would be unable to enter cells via GLUTs [204,361]. Additionally, neither of these studies explore the mechanism of entry

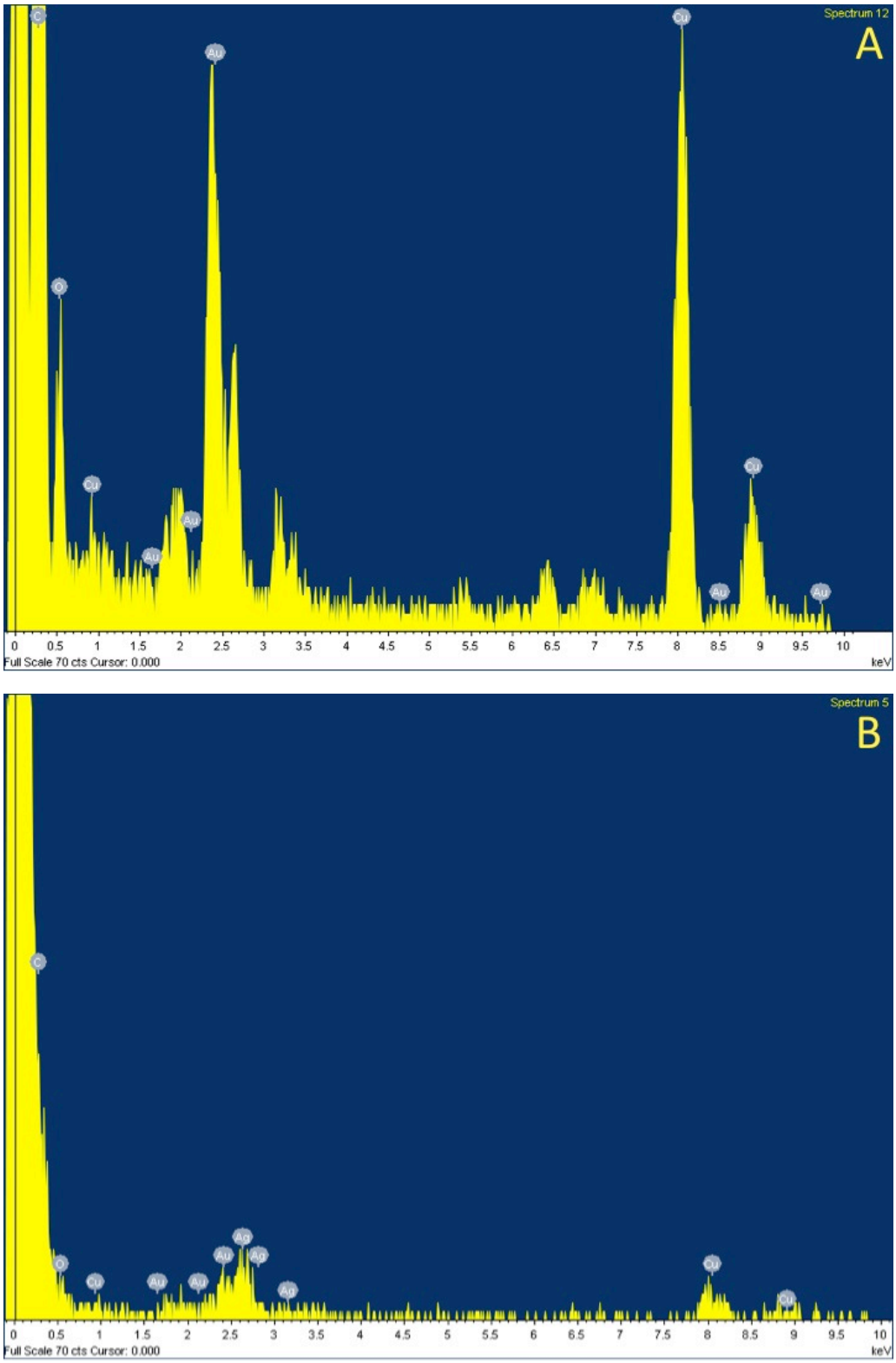

Figure 5.15 Representative electron energy spectra of Sk-Br-3 cells incubated with AuNPs (A) and cells without AuNPs (B). Peaks at the 2.5 keV confirm the presence of gold inside the cell.

of the particles into the cells, so it is unclear if the glucose helped improve intracellular localization by improving uptake through endocytosis or another method. Therefore, we aimed to show that glu-AuNPs pass through the GLUTs that are over-expressed by performing various inhibition assays. We also aimed to use smaller AuNPs because the size of the GLUT1 transporter is approximately 3.6 X 2.6 nm [362], which we believe is much too small for AuNPs as large as Kong and Feng used for their respective studies.

Our first experiment was to inhibit the clathrin-mediated endocytosis of Sk-Br-3 cells and visualize the cells under darkfield microscopy to determine if we could detect AuNPs after inhibition. The results are shown in Figure 5.17; red fluorescence is a marker for endocytosis from the protein transferrin that was conjugated to an Alexa Fluor tag. Blue fluorescence is scattering from the cells when seen in darkfield mode (same imaging setup as in Figs. 5.10-12). In Figure 5.17(A), the negative control shows

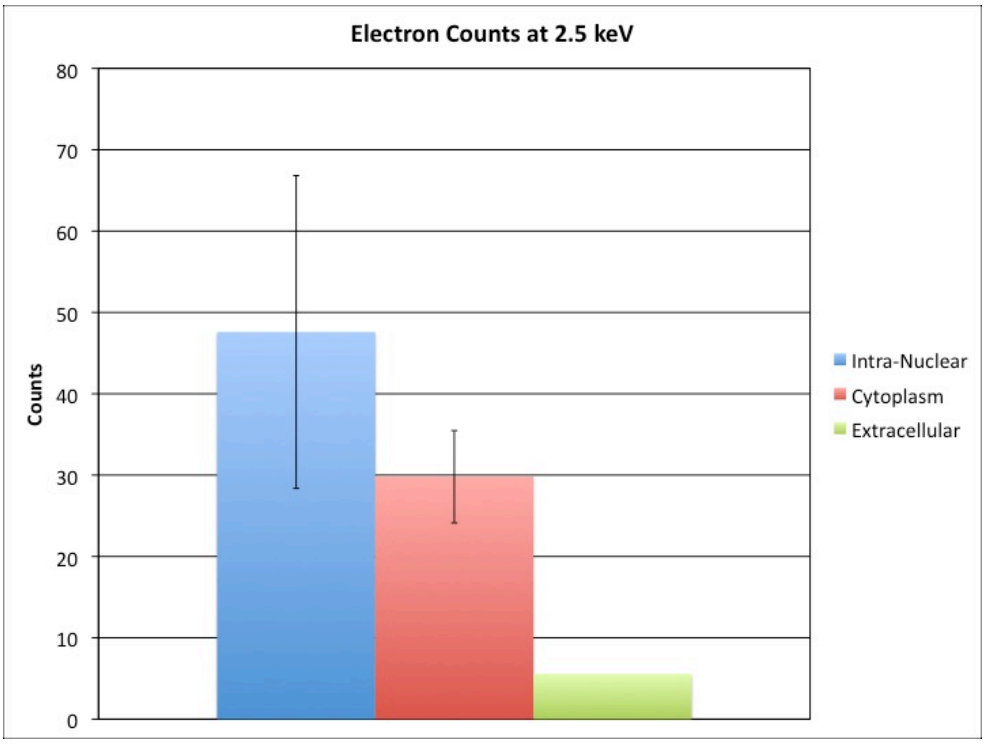

Figure 5.16 Average electron counts from specific areas inside the cell demonstrate that Glu-AuNPs are localized in different areas of the cell, even after a 20-minute incubation.

endocytotic activity and scattering on the cell membrane, as seen previously. There is very high scattering signal from inside the cells in Figure 5.17(B) shows cells that were treated with AuNPs but were not treated with chlorpromazine, with positive endocytosis signal. Finally, in Figure 5.17(C), there is no signal from transferrin, indicating that endocytosis has been inhibited; however there is still scattering from inside the cell, indicating that there is a presence of AuNPs inside the cell. The signal is much less than what is indicated in 5.17(B), but is still higher than the signal in the negative control. This indicates that even with endocytosis being inhibited, we were able to show intracellular uptake of glu-AuNPs.

Additionally, TEM images of cells that were treated with AuNPs and chlorpromazine are displayed in Figure 5.18. In the different magnifications, we once again see the accumulation of the glu-AuNPs inside an autophagosome, as shown in Figures 5.13-14, when endocytosis was not inhibited. Additionally, images in Figure 5.19 show the localization of glu-AuNPs to a large vacuole inside the cell. Similarly, in a 2011 study by Li et al., large vacuoles were found throughout cells undergoing autophagy after treatment with AuNPs [363]. Of interest, individual particles in Figure 5.19 can be discerned inside the vacuole. It is important to note that the reason these individual particles can be visualized is that there is no background signal from the cell cytoplasm. This may explain our inability to locate single particles in the cytoplasm as the 2 nm AuNPs do not have enough electron density to provide contrast with the cytoplasm. This highlights the value of acquiring EDS data to confirm the intracellular presence of AuNPs.

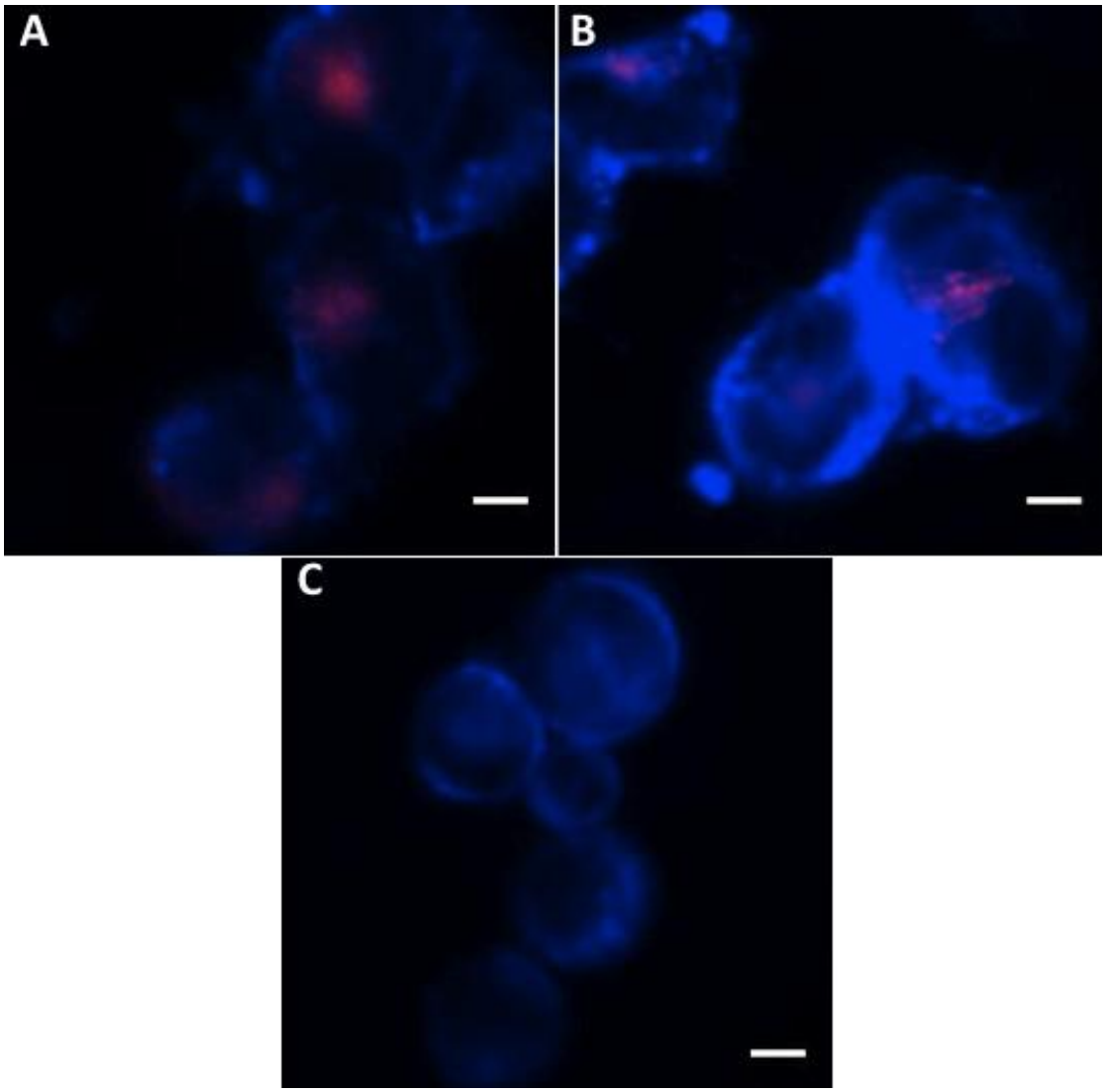

Figure 5.17 Merged images of Sk-Br-3 cells that have been treated with chlorpromazine hydrochloride (5μg/ml) a known inhibitor of clathrin mediated endocytosis. Red fluorescence is a positive marker for endocytosis whereas blue is scattering signal from the cells in darkfield microscopy. (A) Negative control of cells without AuNPs or chlorpromazine displaying positive endocytosis and minimal scattering from around the cell membrane. (B) Cells treated with glu-AuNPs but not chlorpromazine indicate strong scattering from inside the cell presumably due to glu-AuNPs and there is still positive indication for endocytosis. (C) Cells treated with both AuNPs and chlorpromazine showing scattering from inside the cell without indications of endocytosis. Scale bar = 5 μm.

Another assay to determine the mechanism of entry into the cells was a competitive inhibition assay. Both Nitin and O'Neil [25,359] demonstrated that 2-NBDG enters cells via the GLUTs by adding increasing concentrations of D-Glucose in the presence of 2-NBDG and quantifying the decreasing fluorescence from 2-NBDG. This illustrated that D-glucose was competing with 2-NBDG to enter the cells via the GLUTs

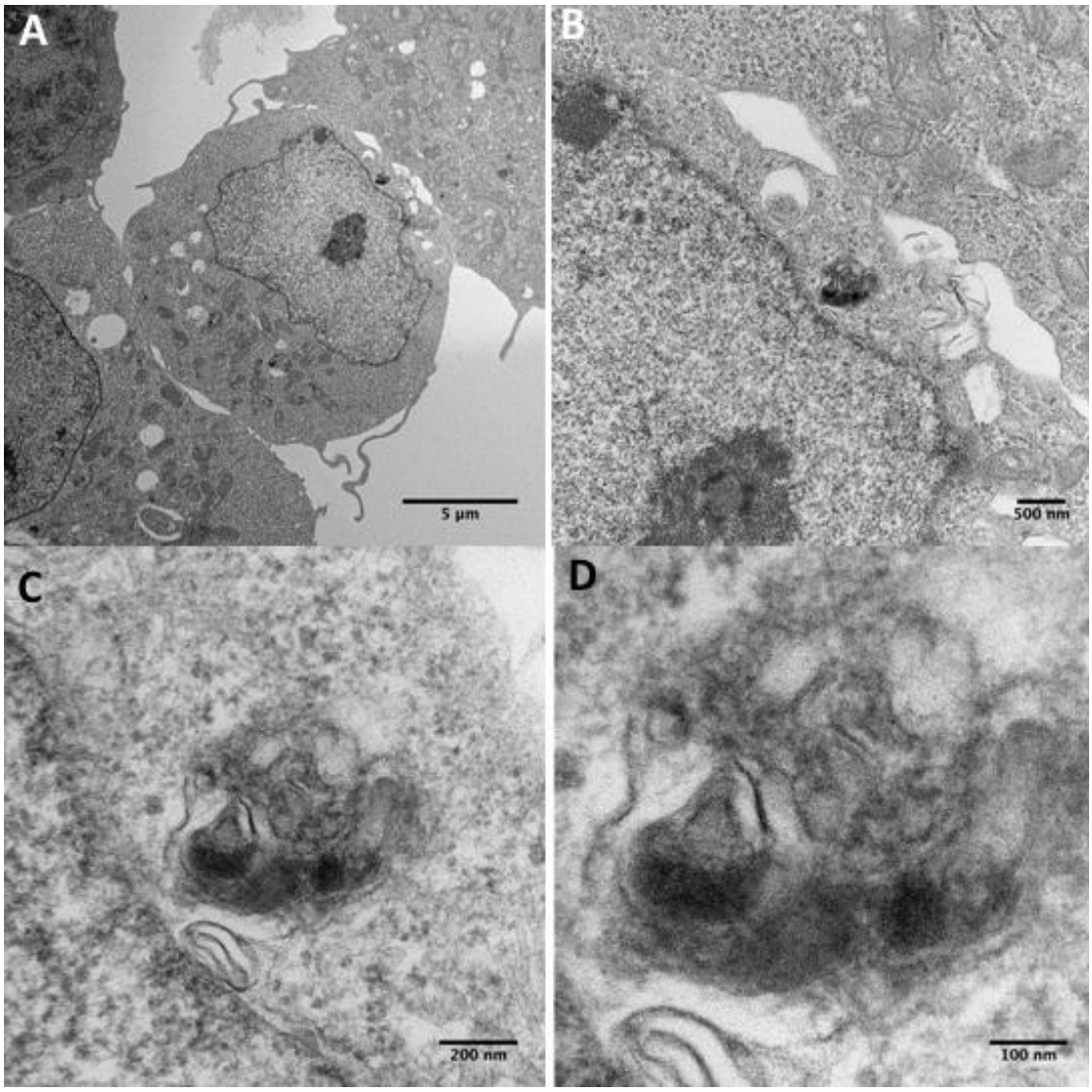

Figure 5.18 TEM images of cells treated with AuNPs and an inhibitor of clathrin mediated endocytosis. Images confirmed the presence of cells inside an autophagosome located inside the cell, indicating that the AuNPs could enter cells via another mechanism. Images were acquired at 6,000 (A), 25,000 (B), 100,000 (C), and 200,000 (D) zoom. Scales are indicated in each individual image.

and inhibiting the entry of the 2-NBDG into the cells. We replicated this assay with glu-AuNPs instead of D-glucose. Figure 5.20 shows the results of incubating cells with media only (A), D-glucose only (B), D-glucose and AuNPs (C), and AuNPs only (D). In Figure 5.20(C) the addition of D-glucose with glu-AuNPs together limited scattering signal to the cell membrane. Figure. 5.20(D) shows the increased scattering that has been previously seen. These results showed promise that a possible mechanism of entry of the glu-AuNPs into Sk-Br-3 cells was through the GLUT1 transporter.

After confirming that the addition of D-glucose affected the scattering profile of Sk-Br-3 cells incubated with glu-AuNPs, we hypothesized that the glu-AuNPs would also inhibit the entry of 2-NBDG into cells, thus lowering the 2-NBDG. This signal can be calculated using flow cytometry. Figure 5.21 displays a bar graph of average 2-NBDG

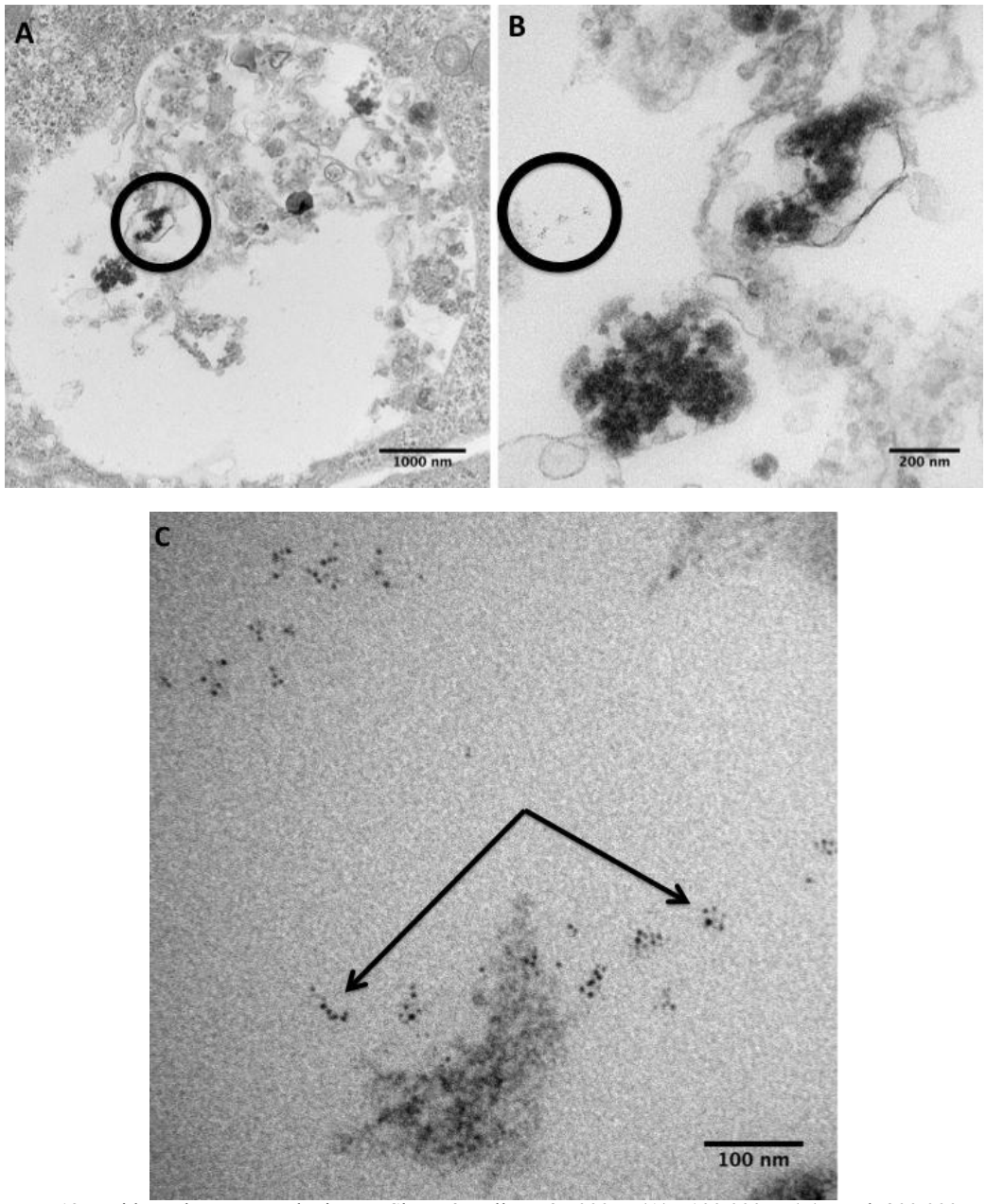

Figure 5.19 Inside a large vacuole in an Sk-Br-3 cell at 25,000X (A), 100,000X (B), and 200,000X (C) magnification. Circles show areas of interest that are magnified in the subsequent magnification. (C) Displays individual particles that are found inside the vacuole, showing that AuNPs can be identified inside the cell when the signal from the cell is not present. Large vacuoles such as these are found in autophagic cells treated with AuNPs.

signal observed in the cells after incubation with two types of AuNPs (glucose and citrate) and two concentrations of D-glucose as a positive control. From the graph, we observe that the two negative controls are significantly different than the groups incubated with 2-NBDG. We also see that treatment with either D-glucose or either AuNP lower the 2-NBDG signal; however, the only condition to significantly lower the 2-NBDG signal was the citrate covered AuNPs.

We believe that the decrease in signal from citrate AuNPs can be partially attributed to their toxicity due to their ability to cause oxidative stress and damage mitochondria [364,365]. This is further validated in studies by Pan and Turner et al. that have reported on the size-dependent cytotoxicity of AuNPs in which small (~1.4 nm

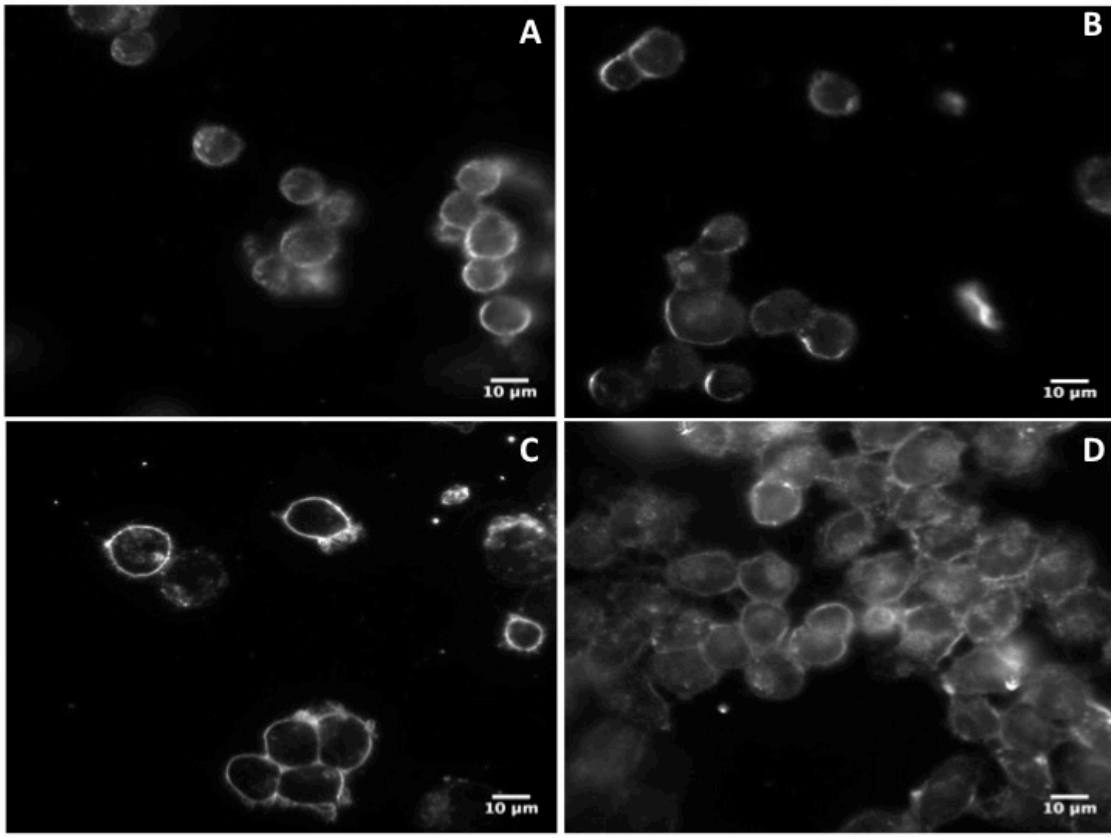

Figure 5.20 Sk-Br-3 cells after treatment with (A) media, (B) D-glucose, (C) D-glucose and AuNPs, and (D) AuNPs. Results show qualitative differences between the cell lines after incubation of only 20 minutes. Cells that are treated with AuNPs have the same scattering profile that was seen in previous experiments where as cells that were treated with both glucose and AuNPs do not have an increased scattering signal from inside the cell.

diameter particles) were much more toxic than 15 nm AuNPs functionalized with the same surface ligand [248,366]. Tsoli et al. also reported that 1.4 nm AuNPs were able to penetrate the nucleus of cells and condense DNA without a nuclear targeting sequence[367]; this may explain why we were able to detect signal from gold inside the nucleus (Fig. 5.15(B)).

Additional studies by Pan and Goodman et al. have also demonstrated that the capping agent has a significant impact on degree of cytotoxicity for small particles as their mechanism of action upon the cell is ligand dependent [249,250]. This is a possible explanation for the difference in 2-NBDG signals between citrate and glu-AuNPs. We

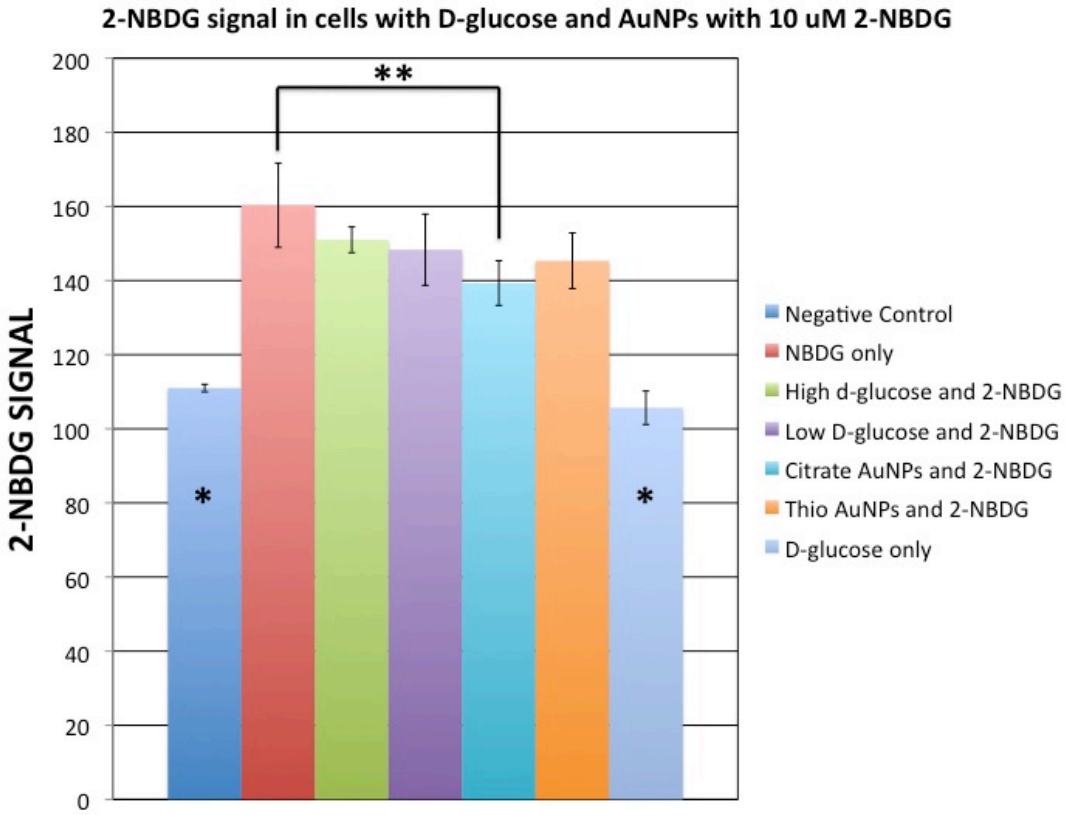

Figure 5.21 2-NBDG signal calculated on the FITC channel of a flow cytometer. Each bar graph represents MFI of 3 samples for each condition. The columns marked with * show that the negative controls fluoresced significantly less than samples stained with 2-NBDG (p-value <0.01). The two columns marked with ** indicate the only two samples whose means were statistically different from each other (p-value 0.048) This indicates that the incubation of citrate capped AuNPs had a significant effect on the signal of 2-NBDG from inside the cells compared to the other conditions.

explored the localization of citrate AuNPs using TEM and the results are presented in Figure 5.22. In Figure 5.22, we observe a very high concentration of AuNPs localized in large clumps inside and outside the nucleus. As we increase the magnification, we begin to discern the same NP structure as seen in previous experiments. However, the lower magnifications seem to indicate a number of clusters that were not seen previously. Additionally, the cells that were treated with citrate AuNPs were unhealthy and approximately half the size of healthy Sk-Br-3 cells. Cells that were incubated with serum free media and glu-AuNPs or citrate-AuNPs were also observed to have large clusters of AuNPs inside their nuclei (data not shown). These images confirm that we see localization of small diameter particles inside the nucleus, as was previously reported. This is a possible explanation for why we observed such low 2-NBDG signal from cells treated with citrate AuNPs: they may have undergone a high amount of oxidative stress due to the presence of AuNPs in the cell. The stress would lead to the cell undergoing apoptosis and therefore not consuming as much 2-NBDG as seen with the normal healthy cells.

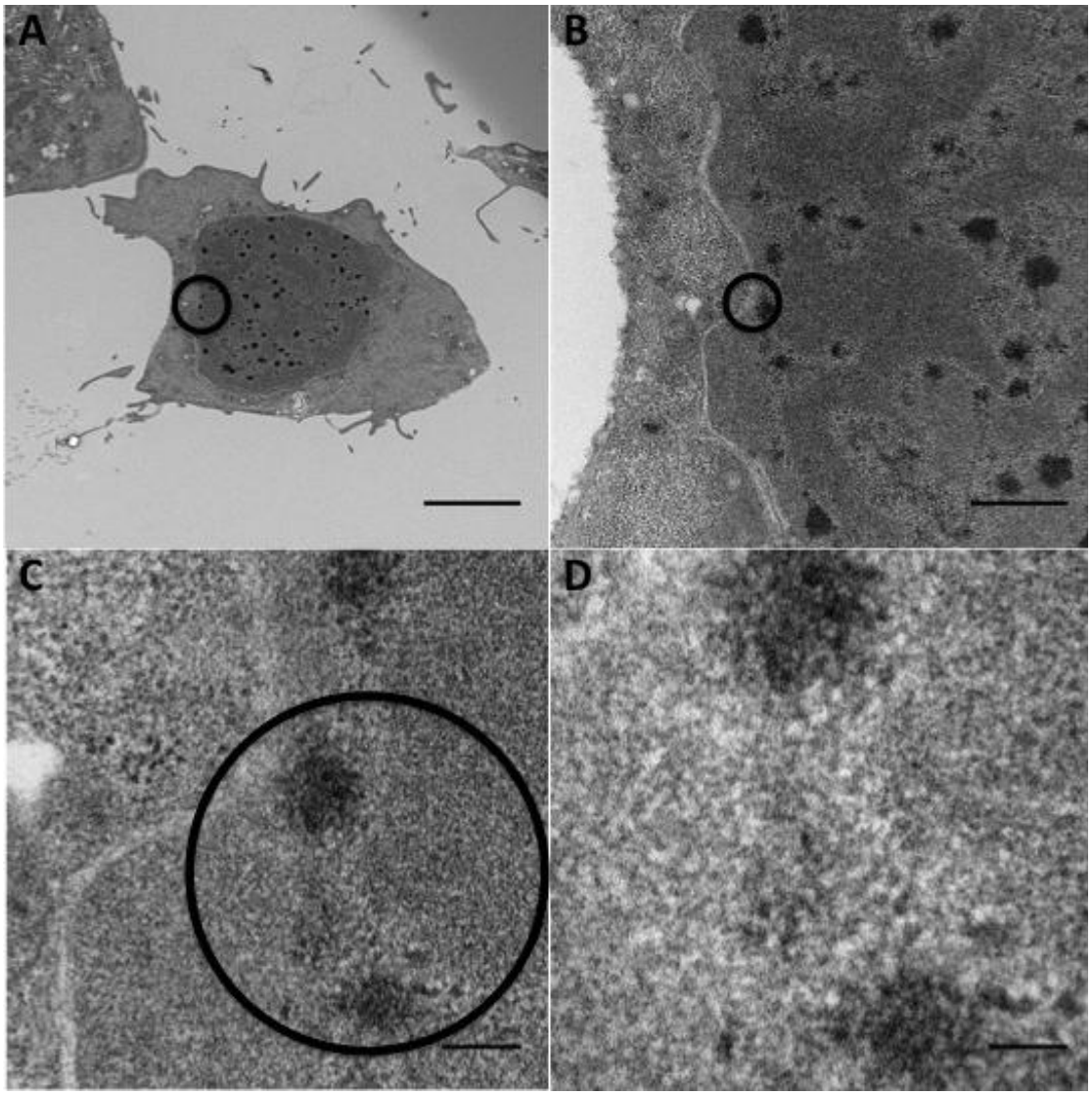

Figure 5.22 Sk-Br-3 cells incubated with 2 nm citrate capped AuNPs at 5,000X (A), 25,000X (B), 100,000X (C), and 200,000X (D). Images show large clusters of AuNPs mostly found throughout the nucleus. Higher resolution magnifications show the AuNPs that are found in previous figures (Figs. 5.13. 5.14, 5.18) Figure 5.21 (B&C) also display clusters of AuNPs outside the nuclear membrane. Scale bars: (A) 5 μm, (B) 1μm, (C) 200 nm, and (D) 100 nm.

5.5. Discussion

The presence of positive surgical margins is associated with a higher risk of local disease relapse [129,368–370]. Typically, it is recommended that patients with positive margins on final pathology undergo re-excision of the margins or intensification of

adjuvant radiation therapy [371–373], both of which carry additional risks for the patients. Therefore, intraoperative evaluation of the surgical resection margins is an important component of the patient care. A rapid method of intraoperative margin evaluation could reduce second surgeries for breast cancer patients in the general community.

Our study represents an initial step towards the development of an optical imaging strategy that would aid both pathologists and surgeons in expediting the process of margin assessment during surgery. Our study demonstrates that 2-NBDG signal in tissue specimens can be analyzed both qualitatively and semi-quantitatively and that wide-field fluorescence imaging has the ability to discern malignant from normal tissue.

Our strategy is based on the same principles that make PET scans so effective in the detection of breast cancer cells in patients. Similar to ^{18}FDG used in PET scan, 2-NBDG is a glucose analogue that is transported into cells via the GLUT1 and GLUT2 transporters [358]. It undergoes the same metabolic processes as ^{18}FDG [25]. Since cancer cells express higher levels of GLUTs and lower levels of glucuose-6-phosphatase that metabolizes the glucose than normal cells [353–357], both ^{18}FDG and 2-NBDG accumulate in the cancer cells [21]. This process allows PET imaging and fluorescent imaging of the cancer cells using nuclear ^{18}FDG and fluorescent 2-NBDG contrast agents.

Nitin et al. demonstrated that following topical placement of 2-NBDG, the fluorophore entered the cancerous cells in both tissue phantoms and excised oral neoplasia [359]; this demonstrated the ability of 2-NBDG to differentiate cancerous cells because of their high metabolic activity not because the different extracellular structures

found in cancerous tissue allow for better 2-NBDG diffusion. As well O'Neil et al. demonstrated that 2-NBDG does enter breast cancer cells and at a much higher rate than for non-cancerous cells [25].

Using 2-NBDG as a topical contrast agent, we were able to optically discriminate freshly excised breast tissue that contained cancer cells from the normal surrounding tissue using our *ex vivo* imaging system. The single specimen with DCIS and normal tissue in Figure 5.7(D) demonstrates how readily the area of tissue with cancer cells can be imaged by the fluorescence from 2-NBDG uptake compared to the adjacent normal tissue and displays the potential of imaging tissue at the margin. By quantifying the fluorescence signal through spectrum AUC, we were able to set a threshold level that identified 9 out of 12 tissues that contained cancerous cells. Hence, this strategy may be developed in the future into an automated staining and quantification system to expedite the intraoperative assessment of excised specimen of tumor margins. With further studies, this strategy could even potentially be implemented to assess cancer cells at the surgical margin *in vivo*.

Clinical studies had found ILC was associated with lower standard uptake values (SUV) [34] and a higher false-negative rate than IDC in PET imaging [21,353,374–376]. However, our study suggests that the ILC cells do accumulate glucose preferentially over normal surrounding tissue. We found all three cancerous tissues that contained ILC showed high fluorescence intensity after metabolizing 2-NBDG (Fig. 4). In fact, one had the largest NAUC. Most likely, the diffuse growth pattern of ILC does not concentrate the FDG signal high enough beyond the resolution limit of the PET imager to

generate a high SUV. However, due to the small number of samples that contained ILC, this result should be interpreted with caution.

Similar to PET imaging, high basal metabolic state of the patient is likely to influence fluorescent glucose imaging of breast cancer. This most likely contributed to the high level of fluorescence in the normal breast tissue from patient #13 (Fig. 4). It was the only normal control tissue with NAUC above the threshold level. Likewise, the tumor sample obtained from this patient also had high level of fluorescence although there were no cancer cells in the specimen. Therefore, similar to the steps implemented prior to the FDG-PET imaging in the clinics, the patients' metabolic state and glucose intake may need to be regulated to optimize the use of this strategy.

Further investigation of this strategy is required before it can be used in clinical settings. Foremost, this strategy is expected to have a minimal threshold limit of detection, and thus the minimum number of cancerous cells that can be detected by using the *ex vivo* imaging system needs to be determined. For this strategy to be clinically useful, it does not necessarily have to detect all margin tissue with cancer cells because the tissue would ultimately undergo permanent pathology review after the surgery, which would identify all cancer cells close or at the surgical margin. However, detection of cancer cells at the margin intraoperatively for some patients would spare those patients another surgical procedure for re-excision or adjuvant radiation treatment intensification.

In addition, the influence of breast cancer sub-types and treatments the patient received on the 2-NBDG uptake and imaging needs to be determined and optimized. In our study, patient #14 had received neoadjuvant chemotherapy with trastuzumab prior to her surgery. The tumor specimen from this patient had high fluorescence intensity but

did not contain cancer cells. This elevated fluorescence level could be a result of the increase in immune response and activated natural killer cells that was reported in patients with breast cancer that overexpresses the human epidermal growth factor receptor 2 (HER2) and were treated with chemotherapeutic drugs [377,378]. This is an example of the many factors that need to be considered when considering this technology's clinical use.

We also aimed to develop a new method to introduce AuNPs to cells via GLUTs. We first were able to demonstrate our ability to reliably synthesize AuNPs and characterize the binding of thioglucose onto the surface of these particles using EDS. We showed that the surface coating had an effect on the interaction of AuNPs with the cancerous Sk-Br-3 cell line, and that there was increased scattering inside the cells incubated with glu-AuNPs. Glu-AuNPs were also cell type specific as there was increased scattering inside Sk-Br-3 cells but not Mcf10A cells. This increased signal from inside the cell was also seen with 2-NBDG in earlier experiments, which led to the hypothesis that these glu-AuNPs were entering the cell through the GLUTs and not through endocytosis, as is seen with other AuNPs.

To validate this hypothesis, cells were incubated with a clathrin mediated endocytosis inhibitor and 2 nm glu-AuNPs. Our results showed that there were AuNPs internalized by the cell with and without endocytosis inhibition. These findings are consistent with a 2012 study by Moros et al. that shows 6 nm glu-SPIONPs entered cells via caveoloae/lipid raft mediated endocytosis [379]. However, the authors found that the SPIONPs were colocalized with lysosomes. This is not consistent with other literature that shows NPs internalized via caveloae/lipid rafts do not undergo lysososmal

degradation [380]. One possible explanation is that the glu-SPIONPs are taken up by autophagosomes inside the cell, which then fuse with lysosomes, leading to further degradation of the particles. This theory is supported by respective work from Li and Ma et al. that demonstrate lysosomal degradation of autophagosomes with AuNPs directly correlates with the size of AuNPs incubated within the autophagosomes [363,381] The small diameter glu-SPIONPs synthesized by Moros may enter the cells via caveolae mediated endocytosis, become consumed by autophagosomes, and consequently consumed by lysosomes, explaining the colocalization of the particles in the lysosomes. This theory is also supported by data in Figure 5.14, 5.18, and 5.19 that show glu-AuNPs inside autophagosomes and large vacuoles that are a result of the autophagy caused by AuNPs.

Even though our initial results from the endocytosis inhibition studies correlate well with the conclusions presented by Moros et al, there are still fundamental differences between the studies that do not allow us to conclude the mechanism of entry of the NPs into the cell. The particles were of different size and material property, the glucose was functionalized via different chemical linkers, and the cell lines used were different. As discussed in previous chapters, each of these factors has a large impact on intracellular fate. Due to these differences, there are further assays that need to be performed to confirm the mechanism of entry of 2 nm glu-AuNPs into Sk-Br-3 cells.

One assay involved incubating the cells with both D-glucose and glu-AuNPs to competitively inhibit the entry of the glu-AuNPs into the cell. Our initial qualitative results showed a limited amount of intracellular scattering in cells incubated with both particles and D-glucose, indicating that the glucose was successful in stopping the glu-

AuNPs from entering the cell. This is a strong indicator of some involvement between the glu-AuNPs and GLUTs. We attempted to quantify this inhibition by incubating 2-NBDG with glu-AuNPs and quantifying the reduction in 2-NBDG signal due to the presence of glu-AuNPs. Our hypothesis was that the if the glu-AuNPs were entering the cells via GLUT1, then the 2-NBDG signal would be reduced as is seen with the D-glucose inhibition performed by Nitin et al. [359]. Even though we were able to see a reduction in 2-NBDG signal (Fig. 5.21) that was similar to D-glucose inhibition, it was not significant. A possible reason for this is that the concentration of D-glucose used by Nitin et al. was much higher than the concentration of glu-AuNPs that were added to the cells. Additionally, an unexpected result from this experiment was the significant loss in 2-NBDG signal with cells incubated with citrate-AuNPs.

TEM images of cells incubated with citrate-AuNPs showed a high number of AuNPs clustered inside and outside the nucleus that was not previously seen in other experiments. The cells were also unhealthy and half the size of normal Sk-Br-3 cells, indicating cells under high stress, possibly a result of the large clusters of AuNPs in the nucleus. Previous studies have shown that cells undergoing stress down-regulate GLUT1 expression, thus decreasing glucose consumption [382]. This is a possible explanation for the significantly decreased 2-NBDG signal in cells incubated with citrate-AuNPs. However, other experiments have not shown cells undergoing high stress and this data is too preliminary for any conclusions to be made. Further experiments need to be performed to fully explore the mechanism of entry of glu-AuNPs and the cellular stress induced by 2 nm citrate-AuNPs .

5.6. Conclusion

In conclusion, this study represents the initial step towards the development of fluorescence imaging system that can improve diagnostic imaging in the clinic. Our goal was to develop a method that will optically differentiate malignant from non-cancerous tissue. Using this *ex vivo* wide-field imaging system, we were able to use a fluorescent glucose analogue and tunable light filters to create multispectral images that were analyzed to discriminate the presence of malignancy in excised tissue. We also began to explore the development of a new method of targeting small diameter AuNPs to be uptaken by cells with high metabolism. Our initial experiments showed promise in the use of glucose capped AuNPs to target GLUT1 expression in cancer cells. However, more characterization assays need to be performed to fully understand these particles and their interactions with cells. Full characterization assays include inhibition of all types of endocytosis and tracking the intracellular fate of AuNPs after entering the cell via high resolution imaging techniques.

Chapter 6

Functionalized Silica-Gold Nanoshells as a Targeting Agent for HER2-Positive Breast Cancer

6.1. Introduction

In the previous chapter, we presented the use of fluorescent deoxy-glucose as a molecularly targeted contrast agent to differentiate cancerous tissue. In this chapter, we present the use of silica-gold nanoshells functionalized with an anti-HER2 antibody to visualize the overexpression of HER2 on the surface of HER2-overexpressing cancerous tissues. As in the previous chapter, we are using whole tissue sections to better simulate the condition in which a surgical team would use these nanoshells intraoperatively. In this chapter, we will demonstrate the ability of the nanoshells to enhance contrast in HER2-positive tissue with a 5-minute incubation. We show that the nanoshells are localized to the surface of these tissues.

*Partially adapted from Lissett R. Bickford, Robert J. Langsner, Joseph Chang, Laura C. Kennedy, Germaine D. Agollah, and Rebekah Drezek, "Rapid Stereomicroscopic Imaging of HER2 Overexpression in Ex Vivo Breast Tissue Using Topically Applied Silica-Based Gold Nanoshells," Journal of Oncology, vol. 2012, Article ID 291898, 10 pages, 2012

Currently, breast cancer is the second leading cause of cancer-related deaths in women, and it accounts for approximately one-third of all cancers diagnosed in women in the United States [383]. To reduce cancer recurrence and progression, cancerous tissue must be completely eliminated, regardless of grade [384]. Surgical breast cancer therapy focuses on removing the primary tumor and identifying the possibility of metastatic disease from the evaluation of sentinel lymph nodes. Although some patients may require modified radical mastectomy, many patients with less-advanced breast cancer elect breast-conservation therapy (BCT). The presence of a positive surgical margin during these surgeries has been associated with lower rates of patient survival [385]. Due to residual cancer cells being left in many patients that undergo breast conservation therapy, as many as 40% of patients have experienced local breast cancer recurrence near the site of the original tumor [4]. Intraoperative treatment decisions are, therefore, absolutely critical.

As discussed in previous chapters, intraoperative tumor margin detection occurs primarily in specialized tertiary centers, such as The University of Texas M.D. Anderson Cancer Center (MDACC). In these centers, the resected tissue undergoes a preliminary evaluation by a pathologist while the patient remains in the operating room; if necessary, additional tissue can be removed until the pathologist determines the tumor margins are negative. In community hospitals, where greater than 95% of BCT is performed [127], pathologic analysis of excised tissue only occurs postoperatively [2]. Patients who consequently have positive tumor margins must return for surgical re-excision and receive increased doses of adjuvant radiation therapy [386,387]. Thus, the existence of positive tumor margins portends additional risks and costs to the patient. Due to the

existing limitations of current intraoperative tumor margin detection, there is an opportunity to develop superior diagnostic tools to assist in reducing the recurrence and progression of cancer due to inadequate tissue removal during primary surgery.

While histological analysis remains the gold standard for tumor margin assessment, the macroscopic evaluation of whole, non-sectioned tissue specimens may also be used to provide an intraoperative estimate of tumor margin status prior to subsequent processing. This would be an invaluable tool in hospitals without onsite pathology suites. Macroscopic visualization of questionable tissue is attractive for enhancing the sensitivity and specificity of tumor margin delineation: if the number of suspicious regions that require further microscopic processing can be reduced, surgeons and pathologists can focus their attention and resources on areas that remain inconclusive. Currently, macroscopic evaluation only occurs for breast cancer specimens that are characterized by micro-calcifications or nonpalpable masses and does not occur for palpable breast masses [71]. For nonpalpable masses that have been resected, radiographic images are used to determine the extent of the breast disease and the proximity to the resected margins. Although specimen radiography appears to increase the accuracy of tumor margin detection, limitations have been noted. For instance, micro-calcifications that appear as tumor on radiographic images may actually be areas of lymphocytic accumulation [388]. The use of contrast agents targeted to specific biomarkers associated with disease may present an opportunity to increase the sensitivity and specificity of macroscopic evaluations.

In preceding studies, we confirmed that silica-based gold nanoshells targeted to the Human Epidermal Growth Factor Receptor 2 (HER2) could be used for the rapid

contrast enhancement of both cells [155] and tissue sections [129] which overexpress HER2 biomarkers. While gold nanoshells can be conjugated to a variety of biomarkers [201,389], we have selected HER2 due to its association with increased cancer aggression, recurrence, and progression when amplified [390,391]. Amplification of this cell-surface bound tyrosine kinase receptor occurs in up to a quarter of all human breast cancer cases [392]. Importantly, using biomarkers for tumor margin detection has recently been shown to better identify patients at high risk of cancer recurrence over standard histological analysis [13].

To facilitate prompt tumor margin detection intraoperatively, the ability to assess tumor margins without physical sectioning is highly desirable as sectioning may incur significant time to the surgical procedure [2]. Thus, in this study, we advance our previous findings by examining the ability to rapidly target HER2 receptors in intact *ex vivo* human breast tissue specimens without sectioning. We first confirm the predominance of the surface targeting needed to identify the tumor margins and preferential labeling of HER2-positive tissue using two photon and hyperspectral imaging. Then, we demonstrate that anti-HER2 targeted gold nanoshells can be used as rapid diagnostic imaging agents for HER2-overexpression in intact breast tissue specimens using a standard stereomicroscope and confirm these results through reflectance confocal microscopy (RCM) and immunohistochemistry.

6.2. Materials and Methods

6.2.1. Nanoshell fabrication and antibody conjugation

Nanoshells were fabricated as formerly described [213,309,393]. Briefly, silica cores were made using the Stöber method [394], in which tetraethyl orthosilicate was reduced in the presence of ammonium hydroxide dissolved in 200 proof ethanol. The surfaces of the cores were then modified by reaction with aminopropyltriethoxysilane (APTES) to functionalize reactive amine groups on the surface. The final particles were measured by dynamic light scattering (DLS) to have an average diameter of 276 nm. Next, gold colloid (~1-3 nm diameter) was fabricated and adsorbed onto the surface of the silica cores via the amine groups to form gold nucleation sites [395]. To fully cover the surface of the silica cores, additional gold was added to these nucleation sites via a reduction reaction in which hydrogen tetrachloroaurate trihydrate ($HAuCl_4 3H_2O$) was dissolved in potassium carbonate and then reduced by formaldehyde. After the gold layer over the silica cores was formed, the spectrum of the final nanoshell solution was visualized using a UV-VIS spectrophotometer (Varian Cary 300) (Fig. 6.1).

To determine the concentration of nanoshells in solution, the absorption, scattering, and extinction coefficients were determined using Mie theory. The average nanoshell diameter, as validated by scanning electron microscopy (SEM), was 314 nm with a peak surface plasmon resonance at 840 nm. The concentration of the working nanoshell solution was approximately 2.0×10^9 particles/ml.

Nanoshells were targeted to biological HER2-antigens by linking the surfaces of the nanoshells to anti-HER2 antibodies using previously described methods [213]. Prior

to beginning experimental studies, nanoshells were incubated with an anti-HER2-linker cocktail [213] for 2 hours at 4°C. To ensure nanoparticle stability in biological media, the nanoshells were next incubated with a 1 mM polyethylene glycol-thiol solution (PEG-SH, MW = 5kD, Nektar) for 12-16 hours at 4°C. Finally, unbound antibodies and excess PEG-SH were removed from the nanoshells by centrifugation. Prior to experimental studies, the nanoshells were resuspended in antibody diluent (IHC World, pH 7.4) by gentle pipetting to a final volume of 165 μl.

The proper concentrations of PEG-SH and antibody linker were determined using an optimization assay. In these assays, we performed a parameter sweep by incubating different volumes of both antibody-linker and PEG-SH with the nanoshells. After incubation with either solution, a 10% (weight/volume) NaCl solution was added to the nanoshells to make a final concentration of 1% w/v. Excess salt in the solution can cause the nanoshells to aggregate, resulting in the loss of desired optical properties. By adding a layer of PEG to the surface, we can protect the nanoshells from the aggregation; however, the proper concentration of PEG needs to be added to ensure maximum stability. Figure 6.2(A) shows UV-VIS spectra of the nanoshells after a 25-minute incubation with NaCl.

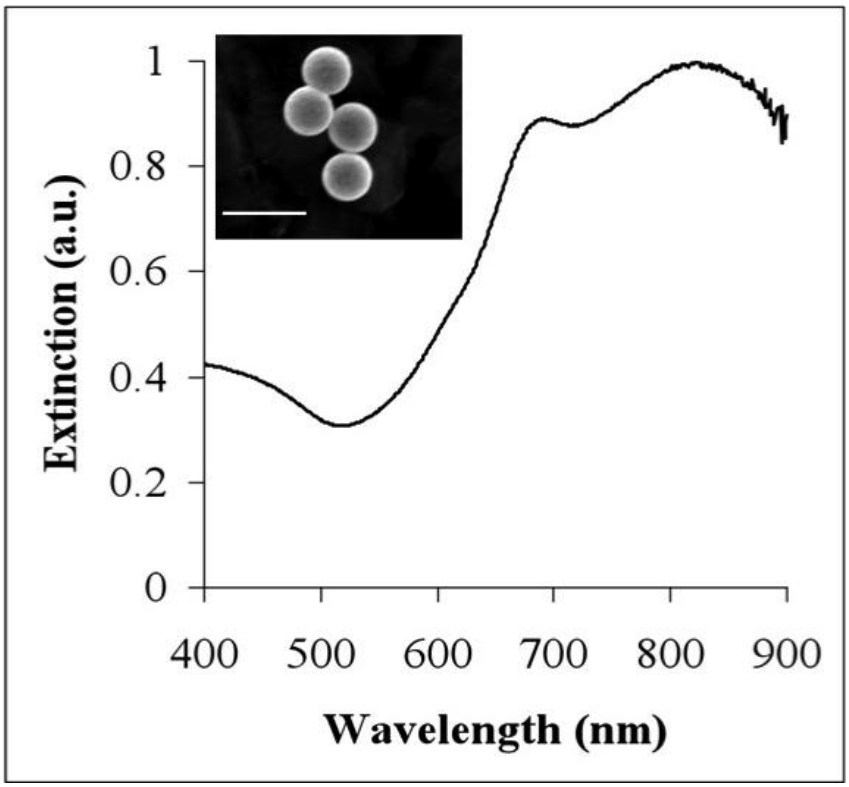

Figure 6.1 Measured extinction spectra of nanoshells with an average core diameter of 276 nm and average shell thickness of 19 nm. Insert depicts corresponding image from scanning electron microscopy. Scale bar represents 500 nm

The positive control graph represents nanoshells without NaCl that did not aggregate; the negative control was nanoshells that were not stabilized with PEG. Time points were taken at 10, 25, 45, and 60 minutes. Figure 6.2(B) shows the spectra of the nanoshells that were acquired after conjugation of different volumes of antibody-linker and 2 μl of 1 mM PEG-SH that were then incubated with salt solution at 30 minutes.

6.2.2. *Ex vivo* human breast tissue specimens

Normal and cancerous (HER2-negative and HER2-positive) breast tissue specimens were supplied by the Cooperative Human Tissue Network (CHTN) through a protocol approved by the Institutional Review Board (IRB). Tissues were designated as normal or cancerous by pathologists at the medical centers where the tissue samples were

obtained. Additionally, HER2 status was previously determined by pathologists at the respective medical centers prior to the patients undergoing any form of medical treatment.

Before use, samples were thawed briefly in a 37ºC water bath and cut on a disposable cutting board using a 5 mm punch biopsy to maintain size consistency. At least two punch biopsies were taken from each specimen for control and experimental conditions. Each cut specimen used was 5 mm in diameter with an average thickness of 1 mm. Tissue samples were subsequently incubated in pre-warmed antibody diluent for 1 minute at room temperature with gentle agitation in a 24-well plate. After pre-rinsing, the samples were incubated in either antibody diluent or the aforementioned targeted-nanoshell cocktail in polyethylene sample vials (Sigma Aldrich). The vials were placed on a nutator in an incubator at 37°C for 5 minutes. After incubation, the tissue samples were removed from the vials and rinsed 3 times in 1X PBS briefly in a 24-well plate. Samples were moved to a clean well of 1X PBS prior to imaging.

6.2.3. Two photon imaging of human breast tissue specimens

Both HER2-positive and HER2-negative cancerous samples were evaluated for surface labeling of HER2-targeted nanoshells by employing two-photon imaging of intact breast tissue specimens. Samples were placed directly on a glass coverslip (Fisher Scientific), and an additional coverslip was placed on top of the tissue in order to facilitate moderate tissue compression. For image acquisition, a Zeiss multi-photon confocal microscope (LSM 510 META NLO) was used in tandem with a Coherent Chameleon femtosecond-pulsed, mode-locked Ti:sapphire laser. This system was set to operate as formerly described [154]. Specifically, an excitation wavelength of 780 nm

and a power setting of 10% maximum excitation power were used. The collected emission

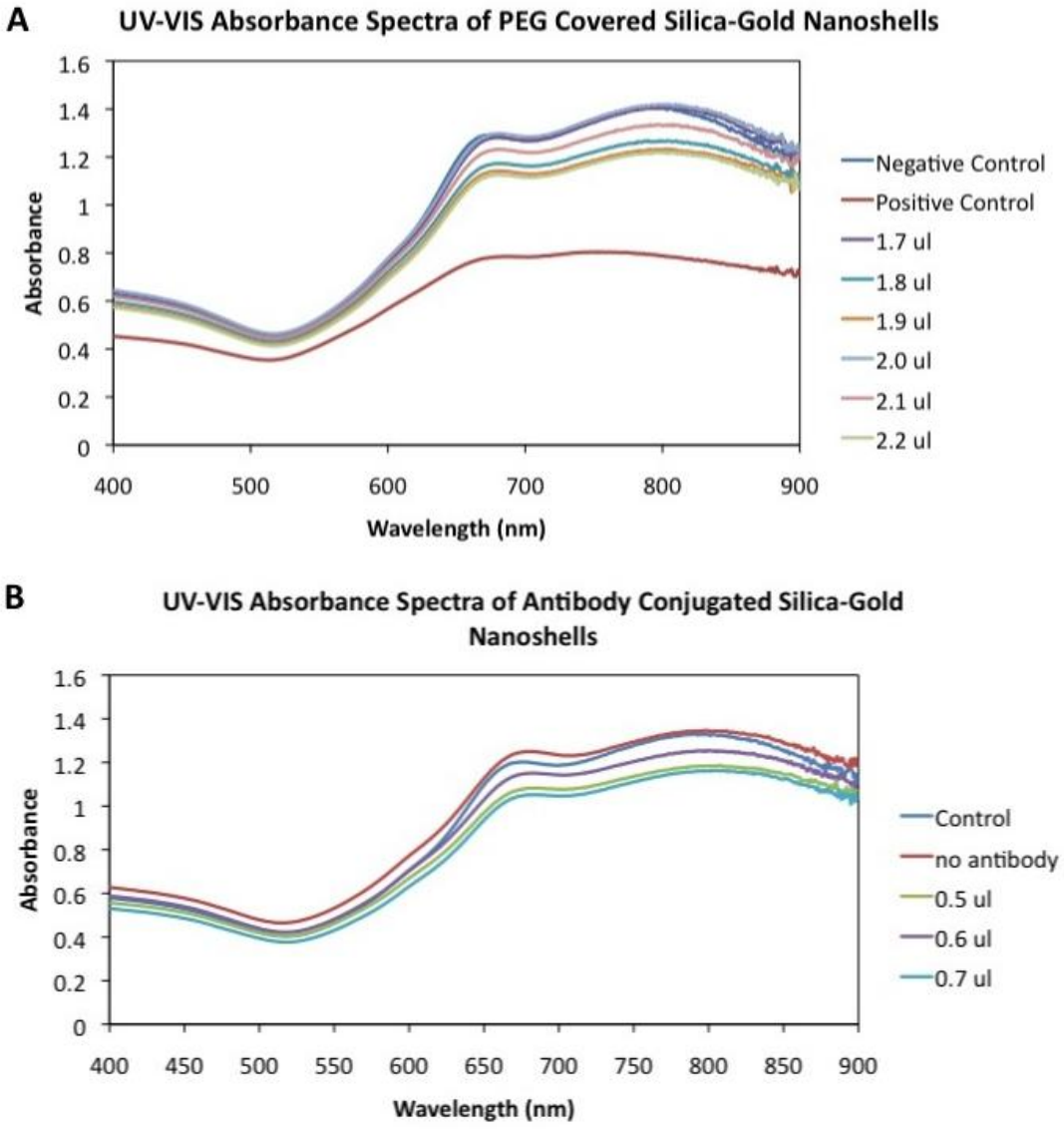

Figure 6.2 Absorbance spectra of silica-gold nanoshells after incubation with different volumes of (A) 1 mM PEG-SH or (B) PEG-Antibody. It was concluded that incubating the nanoshells with 2.0 µl of PEG-SH and 0.6 µl of antibody gave the most stable nanoshells. These concentrations were used for subsequent tissue incubations.

wavelength range was 451-697 nm. Images were collected at a magnification of 20X and a z-stack (depth) increment of 5 µm. In order to calculate the percentage of area covered by nanoshells, ImageJ image analysis software was implemented after image acquisition. Recent research has shown that ImageJ can be used to analyze signal intensity of silica-

gold nanoshells under different imaging systems [129,212]. Each pixel in the images had an intensity value in the range of 0-255. To determine the nanoshell level in each image, an intensity threshold of 30 was used to separate areas that did not have nanoshells (≤ 30) from those that did have nanoshells (> 30). The value of 30 was chosen because images of negative controls were found to have a maximum intensity of 30. The number of pixels that were above the threshold value was then used to calculate the area of each image that contained nanoshells.

6.2.4. Darkfield hyperspectral imaging of human breast tissue slices

To confirm the presence of nanoshells on the surface of the tissues, HER2-positive cancerous, HER2-negative cancerous and normal tissue samples were incubated with nanoshells as previously described. A thin layer of pathological ink was placed on the tissue surface for orientation. The tissues were embedded in OCT media (BBC chemical) and frozen rapidly over dry ice. The specimens were cut at a section thickness of 8 μm using a Leica CM1850 UV cryostat. Cancerous specimens were sectioned at −20ºC and normal specimens at −30ºC. The different temperatures were used to maintain optimal tissue morphology as recommended by Leica. Additionally, Magalhães et al. reported on the use of different temperatures to slice normal and cancerous tissue [396]. The sections were immediately placed on superfrost slides (Fisher Scientific) and allowed to dry overnight. The next day the tissue slices were imaged with a 10X objective on an Olympus microscope equipped with a Cytoviva high-resolution darkfield illuminator. Hyperspectral images of the tissue slices were taken using a hyperspectral camera that provides both spatial and spectral data for each image.

Spectral data of each field of view (FOV) was used to determine if nanoshells were present on each slice of tissue. Comparisons were made between tissue surfaces and tissue beyond the surfaces to determine the presence of nanoshells. Additionally, spectral data from tissues that were not incubated with nanoshells was used as a control. A final comparison between HER2-positive and HER2-negative cancerous tissue and normal tissue was also performed to confirm the specificity of the nanoshells for HER2-positive tissue. Data for each spectral graph was calculated by dividing the raw spectral data by the spectral profile of the illumination lamp and then normalizing the resultant spectra to its largest value.

6.2.5. Macroscopic imaging of human breast tissue specimens

Normal and HER2-positive cancerous breast tissue specimens (from patients who had and had not received neoadjuvant chemotherapy) were imaged using a Zeiss Discovery.V8 stereomicroscope equipped with a VisiLED MC1000 light source. For macroscopic imaging of breast tissue specimens, a thin plastic black stage was placed beneath a glass coverslip to enable ease of tissue placement and to provide a consistent black background among all samples. The specimens (controls and respective nanoshell-labeled counterparts) were placed alongside each other on top of the coverslip. Images were taken at both 1X and 2X magnification under the same lighting conditions.

6.2.6. Reflectance confocal microscopy imaging of human breast tissue specimens

Following widefield imaging, the aforementioned samples were prepared for microscopic analysis under RCM. For this component of the study, a Lucid VivaScope

2500 inverted confocal microscope was used. Samples were placed directly on glass slides that were modified by the addition of an adhesive 1-mm-deep, 20-mm-diameter silicon isolator (Invitrogen). To compress the tissue slightly and consistently among samples, an adhesive tissue cassette (Lucid, Inc.) was placed directly on top of the silicone isolators above the tissue specimens. Multiple images were taken at a power of 0.4 mW and at the same distance from the glass surface for both samples and controls. After reflectance imaging, the samples were prepared for histological processing.

Additionally, RCM was used to confirm the localization of the nanoshells to the surface by utilizing the confocal software to change focal planes and acquire images at various depths below the surface. After incubation with the functionalized nanoshells, the HER2-positive tissue was imaged every 3 μm at a power of 1.11 mW for each image. Finally, RCM was used to image HER2-positive tissue surfaces before and after incubation with the nanoshells. For each tissue, three images were acquired at different spatial locations on the tissue surface and the signal intensity was calculated as previously described [129]. Averages for each tissue were then calculated for pre and post incubation and then compared using a 2-tailed, paired Student's t-test.

6.2.7. Immunohistochemistry and histology

Once images were collected under both stereomicroscopy and RCM imaging systems, normal and HER2-positive cancerous samples (with and without previous neoadjuvant chemotherapy) were embedded in OCT media and sectioned to a thickness of 5 μm. Multiple sections from each specimen were prepared for either immunohistochemistry (IHC) or hematoxylin and eosin (H&E) staining. IHC for the HER2-antigen was executed using the Histostain Plus AEC Broad Spectrum Kit

(Invitrogen) per manufacturer's instructions. H&E staining was also performed per manufacturer's instructions (Sigma Aldrich) for the alcoholic Eosin Y solution. For image acquisition, a standard brightfield microscope (Zeiss Axioskop 2 equipped with a Zeiss Axiocam MRc5 color camera) was used at a magnification of 20X.

6.3. Results

6.3.1. Optimization of incubation parameters

Figure 6.2 displays representative UV-VIS absorbance spectra of the silica-gold nanoshells after conjugation with PEG (Fig. 6.2(A)) and anti-HER2 antibody (Fig. 6.2(B)). The pH level, proteins, and specific cell types present in the tissue can interact with the surface of the nanoshells to cause aggregation [223] which has significant effect on their optical properties. PEG has been used with many different particles to protect these particles to improve long-term circulation in *in vivo* models [231,397,398], which can be translated to this project by using PEG to protect the nanoshells during incubation with the tissue. Additionally, the presence of antibodies can have a significant effect on the aggregation of the particles in a biological environment [234]. With this in mind, we first optimized the volume of PEG-SH to protect the nanoshells at various incubation times with NaCl (10, 25, 45, and 60 minutes). The graph shown in Figure 6.2(A) is for the 25-minute incubation experiment. We compared the spectra of the nanoshells to two controls, nanoshells that were not incubated (negative control) and incubated with salt (positive control). The graph shows that two volumes of PEG-SH (1.7 and 2.0 μl) were very similar to the negative control; however, over the different incubation times the volume of 2.0 μl held its spectra more consistently (data not shown). Once the optimal

PEG-SH volume was determined, we performed the same experiment with the antibody-linker. Figure 6.2(B) shows that incubation with 0.6 μl of antibody produced the most stable nanoshell-linker. These steps suggested that the nanoshells would stay stable while incubating with the resected tissue specimens.

6.3.2. Distribution and penetration of gold nanoshells in intact human breast tissue

The goal of this study was to evaluate the distribution of anti-HER2-conjugated gold nanoshells on resected intact tissue specimens. For comparison, the nanoshell labeling between HER2-positive and HER2-negative tissue samples was evaluated using a two photon imaging system. As previously reported, this imaging system is capable of enhancing and capturing the luminescence signature of the gold nanoshells [154] while also collecting a stack of images taken through the depth of the tissue of interest. Figure 6.3 represents such images of HER2-positive and HER2-negative cancerous tissue samples incubated with HER2-targeted nanoshells. Each sequential increment in the z-direction represents 5 μm into the tissue. Qualitatively, the first image (taken at the surface, or at 0 μm) in Figure 6.3 demonstrates that the nanoshells preferentially label HER2-receptors on the surface of the tissue. Additionally, Figure 6.3 displays decreased signal as the focal spot from the confocal microscope penetrates further into the tissue. This is believed to result from a minimal number of nanoshells being able to penetrate the tissue in the limited incubation time, thus decreasing signal collected beyond the surface. A quantitative difference of the nanoshell signal at the surface of the HER2-positive and HER2-negative tissue was calculated. Using ImageJ imaging software, it was determined that approximately 66% of the FOV for HER2-positive tissue was covered in nanoshells

compared to 2% of the FOV of the HER2-negative tissue. This confirms the preferential labeling and visualization of HER2-positive tissue using anti-HER2 nanoshells.

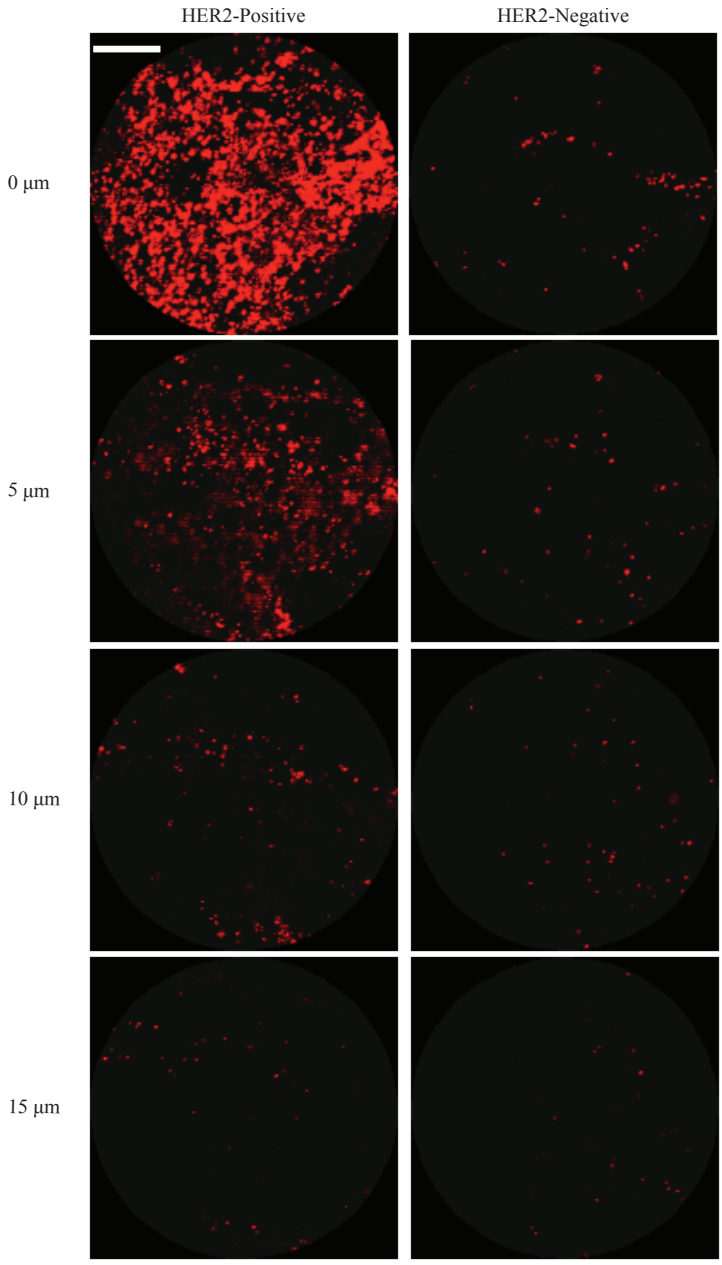

Figure 6.3 Z-stack two-photon luminescence images of HER2-positive and HER2-negative tissue incubated with HER2-targeted nanoshells for 5 minutes at 37°C. Each progressive image represents an increase in depth penetration of 5 µm. Magnification = 20X. Scale bar = 50 µm.

To further validate the surface binding of the nanoshells, hyperspectral images of different tissue sections were also acquired. Figure 6.4(A) shows a representative surface

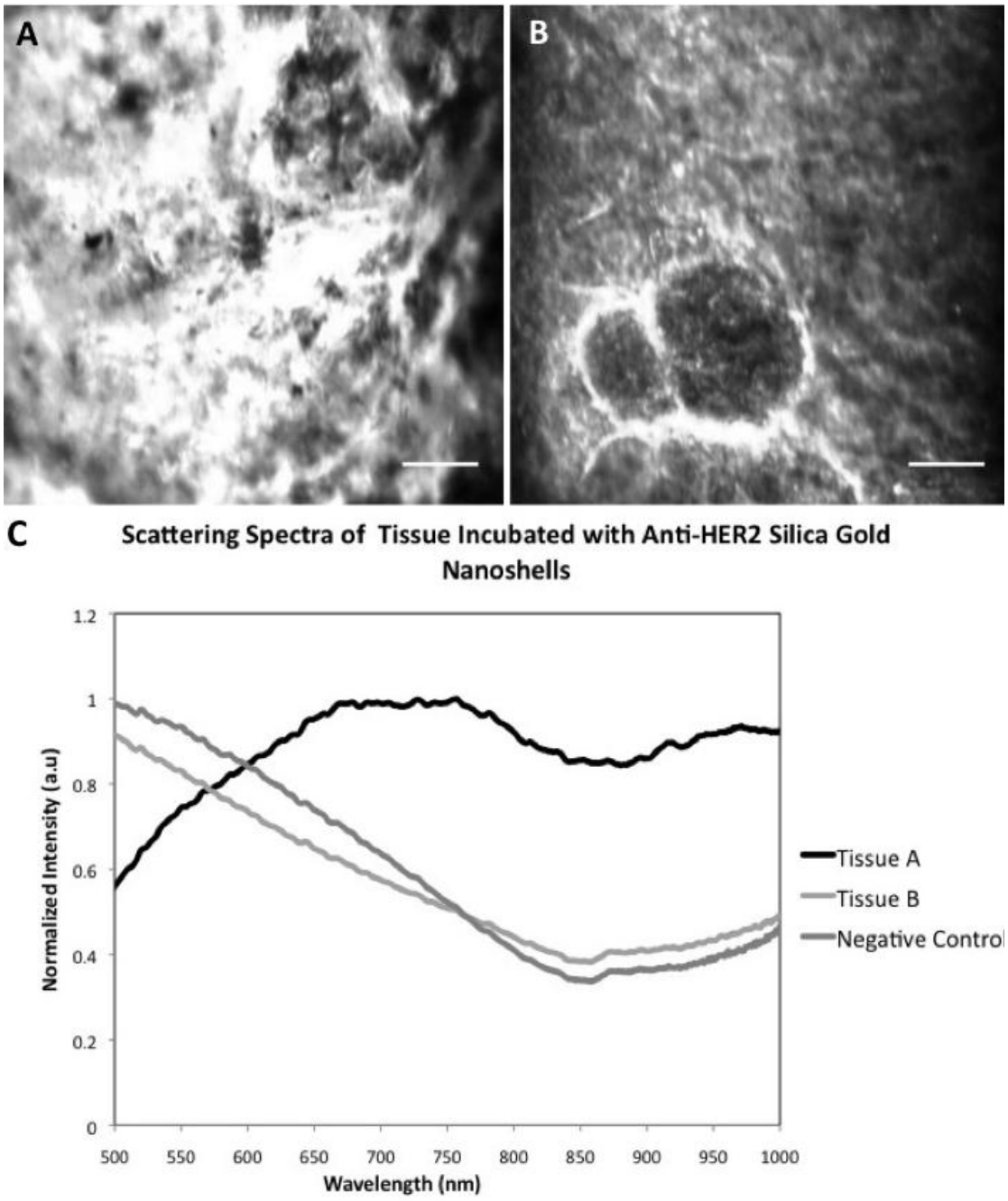

Figure 6.4 Darkfield images of HER2-positive tissue sectioned after incubation with anti-HER2 targeted silica-gold nanoshells. (A) Surface of HER2-positive tissue, (B) 24 μm beyond the surface of the same tissue. (c.) Scattering spectra of the fields of view depicted in (A) and (B). Additionally, spectra from the surface of HER2-positive tissue not incubated with silica-gold nanoshells is shown as a negative control. Scale Bar = 50μm.

of a HER2-positive tissue section after incubation with anti-HER2 nanoshells. Figure 6.4(B) illustrates tissue 24 μm beyond the surface of the same tissue. Figure 6.4(C) displays the respective spectral information of each FOV shown in (A) and (B). Additionally, the spectrum of HER2-positive tissue without nanoshells has been included as a control. As seen in this graph, the spectrum of the surface of the HER2-positive tissue incubated with anti-HER2 nanoshells is distinctive from that of the same tissue 24 μm beyond the surface. In fact, the spectrum of the tissue beyond the surface of the nanoshell-labeled specimen is very similar to the spectra of the surface of the control.

To ensure that we see this spectral data across multiple specimens, three different patients were incubated with anti-HER2 nanoshells and the spectral data of the surfaces of these tissues was acquired. Analysis revealed that these surfaces had similar spectra to each other (Fig. 6.5) and dissimilar spectra to the negative control spectra presented in Figure 6.4(C), showing that the spectral differences is due to the presence of the nanoshells on the surface of the tissues.

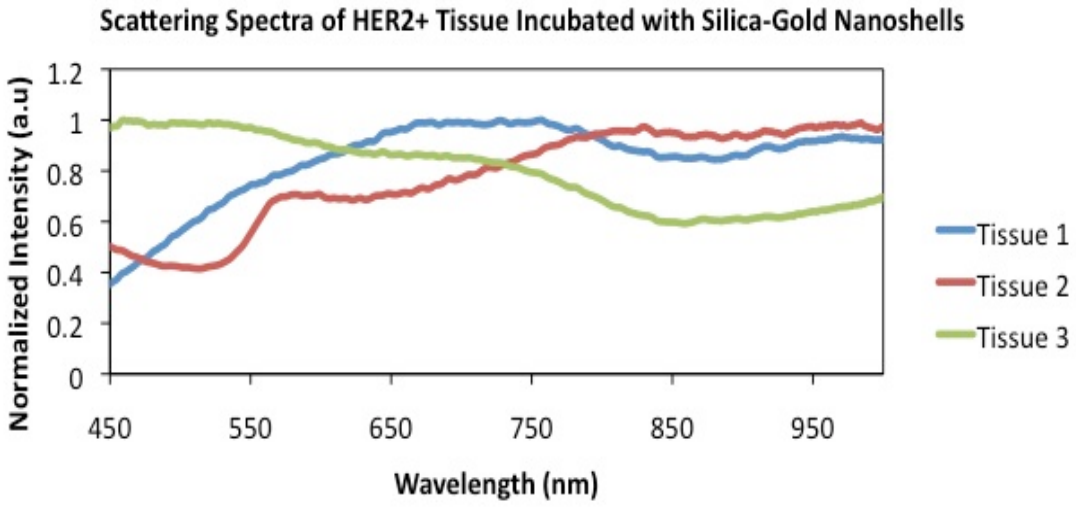

Figure 6.5 Spectra of the surface of three different HER2-positive tissues after incubation with anti-HER2 silica-gold nanoshells. All three spectra were very dissimilar to the spectrum of the negative control, demonstrating the presence of the nanoshells changes the spectral signal of the tissue.

Our final experiment to confirm surface localization of the nanoshells used RCM to acquire images of tissue incubated with nanoshells. Figure 6.6(A-C) displays images acquired of HER2-positive tissue after incubation with the nanoshells at (A) the surface, (B) 24 μm, and (C) 45 μm below the tissue surface. These images display the increased scattering signal from the surface when compared to the images from below the tissue surface. We hypothesize that this increased signal is due to the localization of silica-gold nanoshells at the surface. These results and this hypothesis are consistent with the results we observed using two-photon microscopy and darkfield microscopy (Figs. 6.3 & 6.4). Figure 6.6(D) displays the average signal intensity from six different HER2-positive tissue surfaces that were taken before and after incubation with the nanoshells. Each tissue was scanned three times and the average intensity was calculated for each tissue before and after incubation using ImageJ. The average intensity is higher for tissues after tissue incubation (59 to 45); however, variation in signal between tissues led to a non-significant difference between the groups (p-value 0.122). These results support our findings that the targeted nanoshells primarily localized to the surface of the tissue.

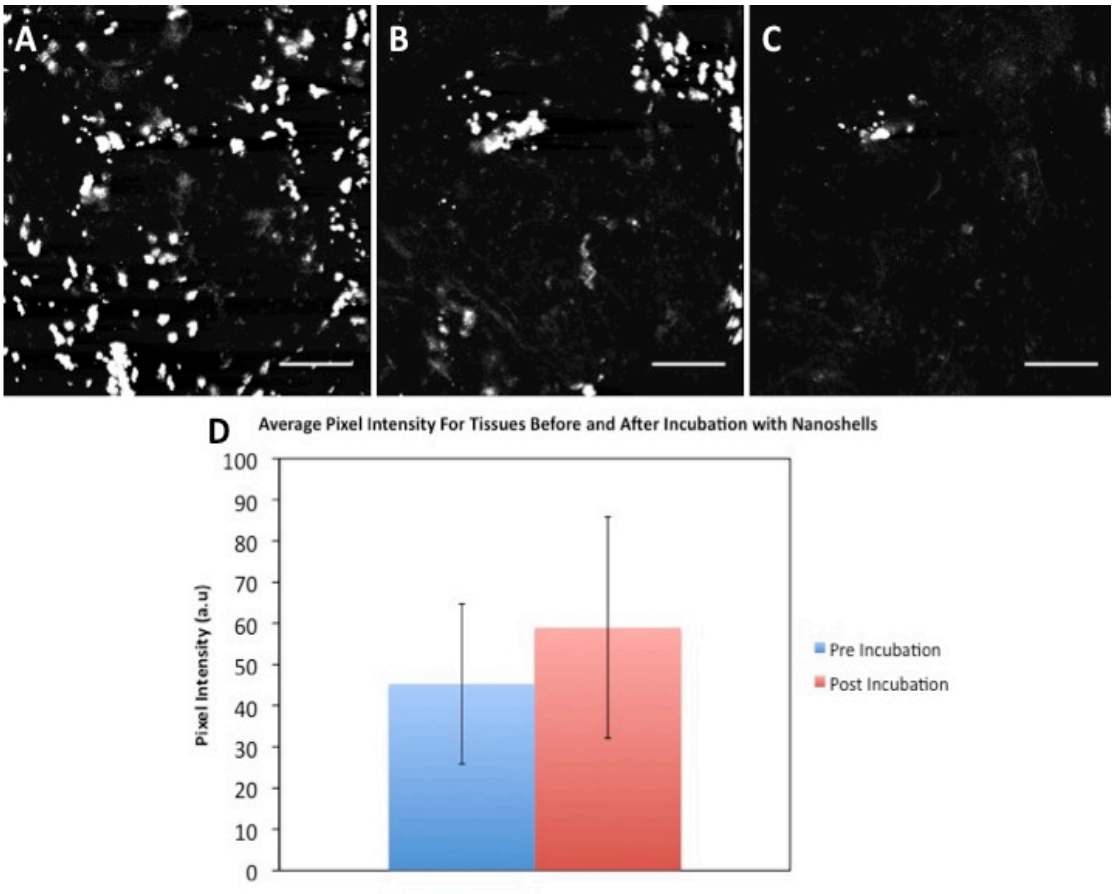

Figure 6.6 HER2-positive tissue after incubation with anti-HER targeted silica-gold nanoshells visualized using a commercially available reflectance confocal microscope at various depths (A) at the surface, (B) 24 μm below the surface, and (C) 45 μm below the surface. There is a much higher scatter signal seen at the surface when compared to both the 24 and 45 μm levels. Scale bar = 100 μm. (D) Average reflectance intensity from six HER2-positive tissues at the surface before and after incubation with silica-gold nanoshells.

6.3.3. Enhanced optical imaging of intact *ex vivo* human breast cancer tissue using gold nanoshells

Based on previous results demonstrating the preferential labeling of HER2-targeted nanoshells on the surface of intact *ex vivo* HER2-positive tissue specimens, we assessed the potential of using a standard stereomicroscope to visualize this enhanced contrast. For this component of the study, human breast tissue specimens that over-

expressed HER2 receptors at the time of patient diagnosis were evaluated and compared to normal breast tissue. Due to the ultimate goal of utilizing gold nanoshells to rapidly label tumor margins intraoperatively in diverse patient populations, we examined tissue from patients who had and had not undergone neoadjuvant chemotherapy. All tissue samples were incubated with either antibody diluent buffer or the anti-HER2-targeted nanoshells for 5 minutes at 37°C. As shown in Figure 6.7, which represents raw images taken with a stereomicroscope, intact tissue specimens incubated with antibody diluent alone showed no markings or features characteristic of nanoshells. However, tissue specimens incubated with the anti-HER2-targeted nanoshells demonstrate numerous particles on the surfaces of the tissues. Qualitatively, the HER2-positive tissue from the patient who did not undergo previous chemotherapy shows the greatest labeling with the targeted nanoshells. The HER2-positive tissue from the patient who did undergo neoadjuvant chemotherapy does demonstrate enriched nanoshell labeling when compared to normal tissue, though not to the same extent as the patient without previous chemotherapy. In contrast, the normal tissue shows the least amount of nanoshell labeling and only a few areas of nanoshells can be visually perceived.

While the degree of nanoshell labeling can be visualized without image adjustments under a standard stereomicroscope, the superior extent of this labeling can be seen more clearly after a simple contrast enhancement using imaging software (Image J). As seen in Figure 6.8(A) the nanoshells are even more discernable against the tissue background regardless of inherent tissue constituents.

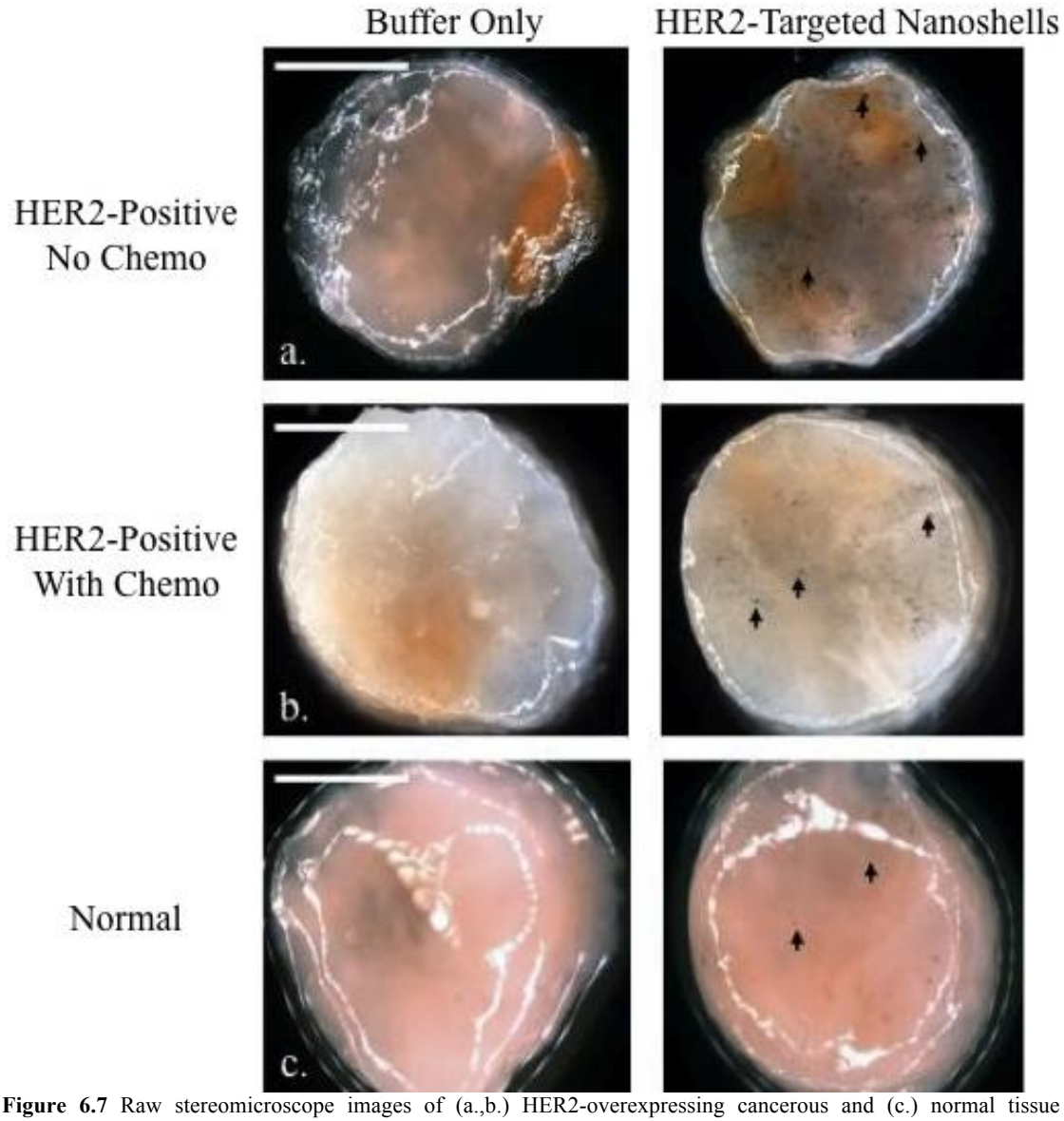

Figure 6.7 Raw stereomicroscope images of (a.,b.) HER2-overexpressing cancerous and (c.) normal tissue incubated with either buffer or HER2-targeted nanoshells for 5 minutes at 37°C. Cancerous tissue taken from a patient (a.) without chemotherapy and (b.) following neoadjuvant chemotherapy. Arrows represent nanoshells. Images taken at 2X. Scale bars = 2.5 mm

To validate the enhanced nanoshell labeling seen by macroscopic imaging, the surfaces of the same tissue samples were also imaged using RCM (Fig. 6.8(B)). Concurrent with the stereomicroscopic images, we see dramatic nanoshell surface-labeling when using targeted nanoshells with previously untreated HER2-positive tissue. For the HER2-positive sample that had formerly undergone chemotherapy, we also see

enhanced nanoshell labeling, though to a lesser degree than the untreated sample as suggested by the stereomicroscopy results. The normal breast tissue displays the least amount of surface labeling with only minimal nanoshells evident with either imaging system. Reflectance intensity measurements (data not shown) were ~2.5 to 3 times greater for both the HER2-positive tissue sample receiving chemotherapy and for the HER2-positive tissue not receiving chemotherapy when compared to the normal tissue sample.

Subsequent histological analysis shown in Figure 6.8(C) reveals that the distribution of HER2 receptors seen with nanoshell-enabled contrast corresponds to that seen with IHC against HER2. The HER2 expression seen by IHC is greater for the previously untreated HER2-positive tissue sample than for the sample that had undergone neoadjuvant chemotherapy. This is believed to be due to the effects of chemotherapy. Rasbridge *et al.* previously demonstrated that patient response to chemotherapy is highly variable, with patients previously negative for HER2-overexpression occasionally becoming positive after treatment and patients previously positive for HER2-overexpression subsequently becoming negative [399]. Although patient response to chemotherapy varies, tissues previously identified as overexpressing HER2 receptors during initial diagnosis, regardless of chemotherapy exposure, demonstrate enhanced nanoshell labeling over normal tissue. Additionally, H&E-stained sections of all tissue samples have been included (Fig. 6.8(D)) to illustrate the microscopic characteristics and differences associated with cancerous vs. non-cancerous conditions.

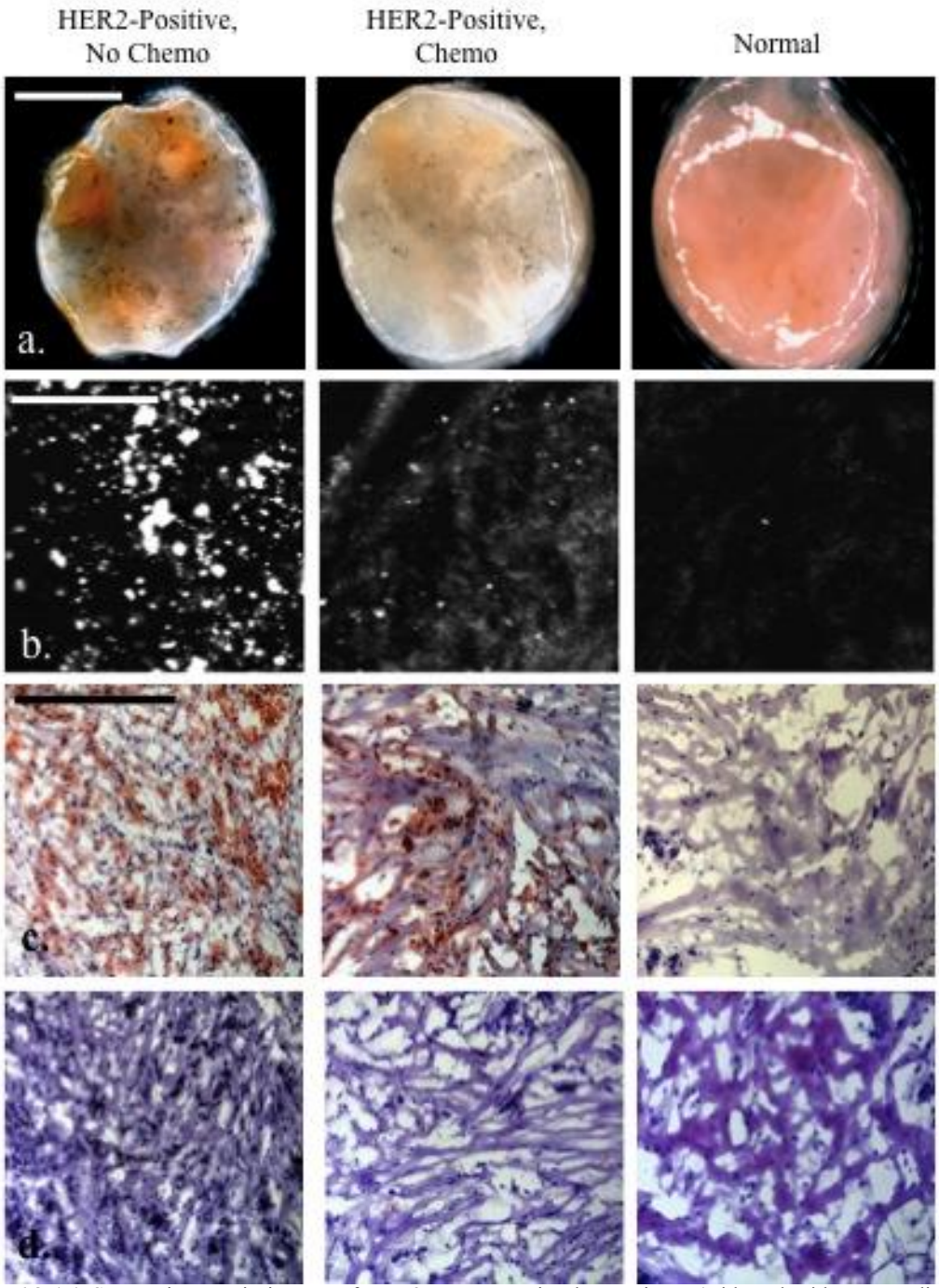

Figure 6.8 (a.) Stereomicroscopic images of HER2-overexpressing breast tissue (with and without neoadjuvant chemotherapy) and normal breast tissue incubated with HER2-targeted nanoshells for 5 minutes at 37°C after contrast enhancement. Magnification at 2X; scale bar = 2.5 mm. Arrows represent nanoshells. (b.) Respective reflectance confocal microscopy images of tissue samples from (a.). Power = 0.4 mW and scale bar = 75 μm. Respective (c.) HER2 immunohistochemistry and (d.) H&E results taken under brightfield microscopy under 20X magnification. Scale bar = 0.35 mm.

6.4. Discussion

In this study we demonstrated the ability to use targeted gold nanoshells to rapidly improve visualization of a specific biomarker (HER2) associated with disease aggression and progression in intact *ex vivo* human breast tissue and confirmed binding location via confocal and darkfield hyperspectral microscopy. By utilizing silica-gold nanoshells designed as rapid diagnostic imaging agents, surgeons and pathologists may be able to realize tumor margin status directly in the operating room after both macroscopic and microscopic assessment. While multiple methods of intraoperative tumor margin detection are currently under investigation [85,118,123,359,400], we are developing an inexpensive and portable system for rapidly analyzing *ex vivo* specimens based on the desire to enhance current methodologies without delay in clinical translation due to regulatory concerns associated with *in vivo* systems.

The ability to enhance contrast of malignancy using topically applied agents has previously been demonstrated for oral and breast tissue using fluorescently labeled deoxy-glucose and epidermal growth factor (EGF) conjugates [23,136,314] as well as cervical tissue using fluorescently labeled gold nanoparticles targeted to EGF receptors [401]. However, these studies employed incubation times ranging from 20-45 minutes, which exceeds the length of time currently needed to obtain tumor margin status using frozen section histology. Additionally, some of the aforementioned studies utilized optical clearing agents, which may be necessary for particles that target intracellular biomarkers [350,402]. Nevertheless, gold nanoshells targeted to extracellular biomarkers may offer more favorable opportunities for *ex vivo* intraoperative tumor margin detection without the need for lengthy incubation times or the use of optical clearing agents.

Recently, we verified that silica-based gold nanoshells could be used to enhance contrast of both HER2-overexpressing cells and tissue sections within 5 minutes of incubation time [129,155]. However, translating this technology towards clinical relevancy requires the ability to assess whole, un-sectioned specimens. Here, we confirm that gold nanoshells, when targeted to HER2 receptors, can be used to distinguish intact HER2-overexpressing *ex vivo* tissue from normal tissue within the same incubation time and we demonstrate that this difference can be observed macroscopically. These results are supported by microscopic imaging and immunohistochemistry against HER2.

By employing macroscopic imaging intraoperatively, clinicians may be better able to distinguish cancerous and normal breast tissue prior to further microscopic analysis and subsequent histological processing. Ultimately, this system could also be used for other diagnostic applications, for other anatomical locations, and for other biomarkers associated with disease. By facilitating fast and accurate tumor margin results intraoperatively as a supplement to current diagnostic methods, we expect to reduce the amount of time spent in surgery due to inadequate tissue removal.

In the previous two chapters, we have demonstrated the ability to differentiate tissue using two molecular contrast agents. However, these agents were visualized with imaging systems that are not expensive and/or portable. In the next chapter, we will demonstrate the combined use of these two agents (2-NBDG and anti-HER2 silica-gold nanoshells) with a low-cost, portable widefield imaging system that can be used to detect both increased metabolism and HER2 overexpression.

Chapter 7

Development of a Portable Device to Visualize Contrast Agents in Cells and *Ex Vivo* Specimens

7.1. Introduction

In the previous two chapters, the use of optical contrast agents to enhance the visualization of specific molecular markers in both *in vitro* and *ex vivo* studies was discussed. In this chapter we further these studies through the development of a portable and cost effective imaging device designed to visualize both 2-NBDG and anti-HER2 NS in cells and tissue specimens. The previous studies described in this dissertation reported the use of visualization techniques that required expensive equipment and software that could not be easily transported [23,128], or the samples required preparation to localize the NS [128]. The RCM described in chapter 6, was the only device designed specifically for clinical use; however, this instrument was designed to work in the NIR

spectrum and is unable to visualize multiple contrast agents in tissue. In this chapter, we describe the design, development, and characterization of a low cost portable imaging system to visualize 2-NBDG and anti-HER2 silica-gold nanoshells in cell lines and excised tissue.

7.2. Background

As discussed earlier, optical imaging can improve cancer diagnostics via minimal acquisition time and high lateral resolution. The addition of contrast agents can increase the specificity of optical imaging by improving contrast between cancerous and normal cells due to differences in molecular expression. We have already demonstrated the enhanced specificity of both 2-NBDG and anti-HER2 NS in separate studies, and we aim to combine their properties to demonstrate the ability of multi-wavelength imaging to visualize cancerous tissue. Multi-wavelength NIRF imaging has been demonstrated *in vivo* in two studies by Baeten and Montet et al. [403,404]. In the study by Baerten et al., the authors used enzyme-cleavable fluorophores to indicate protease activity and vascularization of tumors. The authors were able to use the intensity values from these two measurements to correlate cathepsin expression with tumor size. Another multi-wavelength imaging system, the multi-spectral digital microscope (MDM), was developed by Roblyer et al. [301,405]. This device uses white light, orthogonal polarized reflectance (OPR) imaging, and multiple visible range wavelengths for visualization of neoplasia in the oral cavity [301] or molecularly targeted NPs in tissue phantoms [405]. The multiple wavelength approach provided the researchers with information on the best

wavelength for interrogating the autofluorescent changes that are consistent with neoplastic tissue [406]

In addition to multiple wavelength imaging, there has been a shift towards the combination of wide-field imaging followed by high resolution probes to interrogate areas of interest [406,407]. Another study by Lam et al. demonstrated the utility of using an endoscope to obtain wide-field autofluorescent images of the bronchi, followed by high resolution optical coherence tomography (OCT) of suspicious lesions to differentiate invasive carcinoma from carcinoma *in situ* based on the thickness of the epithelial layer [408]. A recent study by Patel et al. demonstrated the use of wide-field imaging followed by confocal fluorescence to visualize specific areas of breast cancer on histopathological slides [409]. In this study, slides were incubated with methylene blue (MB) and accumulated preferentially in malignant areas after 10 minutes. Wide-field images of the tissue were first acquired followed by fluorescence imaging at high-resolution. The researchers were able to separate the malignant from normal cells on the slices by the increased fluorescent signal in the cancerous areas [409].

Most multi-modal and multi-wavelength imaging systems still rely on endogenous contrast or contrast provided by non-specific contrast agents such as MB. Additionally, there is little work reported on the use of multiple specific contrast agents in one sample to enhance specificity. In a study by Xie et al., the authors used two IRdyes, 2-DG (deoxyglucose) and EGF for visualization of tumors in a murine model [27]. However, in this study, the authors used contrast agents in separate animals. As the optical agent for the biomarkers was the same (IRDye), they would have been unable to resolve the differences between the contrast agents in one animal. Additionally, the

authors used the Maestro© system that is both non-portable and costly. This study is the first to approach using multiple molecularly specific contrast agents, and the authors were able to show for their particular model that the EGF dye had higher signal than the DG dye. However, this result will vary due to the varied expression of molecular markers, especially across breast cancer subtypes [19]. A recent study by Vermeulen et al. demonstrated that increasing the number of interrogated biomarkers improved the detection of cancer on immunohistochemical slides [19]. Detection of multiple markers in one sample is also important due to the heterogeneity of expression levels in one tumor [410–412]. The device presented in this chapter aims to use multiple contrast agents as the heterogeneity in expression profiles could lead to the system obtaining a false negative if only one contrast agent is used.

In this chapter, we aim to develop a method to visualize multiple molecular contrast agents that are used to visualize HER2-positives cells and tissue. The ultimate goal of this research is to develop a system that can be translated for use in the clinic as an *ex vivo* imaging device that provides surgeons with rapid results regarding the molecular expression of GLUT1 and HER2. Our previous experiments have shown that the expression of these proteins can be imaged using 2-NBDG and anti-HER2 NS in a rapid manner (20 and 5 minutes, respectively) [23,128]. We further this research by designing, fabricating, and characterizing a portable, inexpensive imaging designed to visualize 2-NBDG fluorescence and anti-HER2 NS. We show that the device can visualize 2-NBDG and anti-HER2 NS in the cancerous Sk-Br-3 cell line. Additionally, we present data characterizing the performance of the system in visualizing the contrast agents in *ex vivo* tissue.

7.3. Materials and Methods

7.3.1. Design of imaging system

The system was designed to visualize and illuminate 2-NBDG fluorescence and NS scattering without displacing the tissue or camera to capture a composite image of both fluorescence and scattering. Preliminary studies demonstrated that 360° illumination of tissues with NS was necessary because the varying height in the tissue blocked illumination light when there was a single illumination source. This led to the design of placing three separate illumination sources placed on the diameter of a circle at an angle of 120° from each other and all facing the center of the circle (Fig. 7.1(A)). We chose the use of high-power LEDs as our illumination sources as they have low cost and specific wavelengths are available for our contrast agents. LEDs were purchased from Marubeni Corporation (FL-470-06, FL760-03-80)). Additionally, we placed excitation filters in front of the LEDs to control the wavelength of light interacting with the tissue (Fig. 7.1(B)). Short-pass (SP) 500 and 800 nm filters were purchased from Thor and Chroma (FES0500, E800sp). Once the filters and LED circuits were assembled, the two parts were placed together and held together with a set screw to create one modular piece in which the holes for the LED attachments are lined up with the excitation filters (Fig. 7.1(C)). The aperture at the top of the device was designed to match the outer diameter of the filters that attach to the lens of the camera (58 mm).

As we are using our system to visualize two different contrast agents, two different circuits were designed and are controlled through an On-Off-On switch. Each

circuit was soldered so that the LEDs were connected in series with a 12V battery (GP 23-AE 12V) as the voltage source and a resistor so that the LEDs would not burn out.

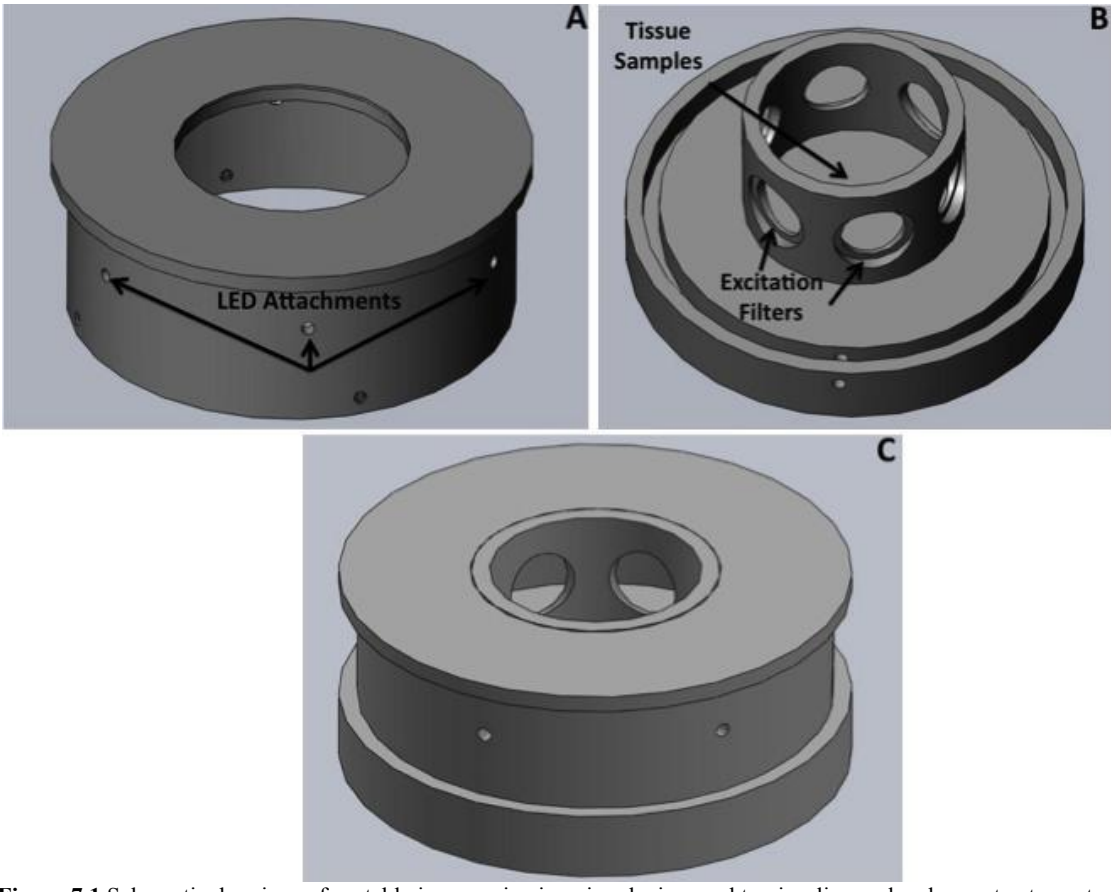

Figure 7.1 Schematic drawings of portable inexpensive imaging device used to visualize molecular contrast agents in cells and tissue. (A) Schematic of the outside cover in which the LEDs are attached and pointed towards the center of the device. (B) Base attachment of the device displaying placement of tissue samples and excitation filters. (C) Assembled device with holes for LED attachments lined up with large holes for excitation filters.

To capture tissue signal, a camera was attached to the device so that the lens of the camera was perpendicular to the tissue in order to capture the side scattering of the NS. Camera selection is an important design parameter as our aim was to visualize signal in both the visible and NIR wavelengths, our system required a device to detect both signals. RGB (red, green blue) sensors in digital cameras have the ability to sense in the NIR; as a result, most cameras have an internal IR blocking filter so that the sensors do not detect IR light and translate it to a color. Removal of the IR filter would allow for

sensing of both NIR and visual light from NS and 2-NBDG given that the proper emission filter was placed in front of the camera lens. In addition to their versatility in sensing, digital cameras are also relatively inexpensive, another important design parameter for the system. A digital single-lens reflex camera (DSLR) with the NIR filter removed was purchased from LDP LLC for $1,095.00 (Xnite Canon450D Rebel Xsi). Additionally, a variable zoom lens from Canon was purchased for $199.00 (EF-S 18-55 mm, F/3.5-5.6 IS II). Multiple 58 mm lens filters were purchased to help further characterize the ability of the system including a 500-550 nm bandpass (BP) and two LP filters (720 and 780 nm). Additionally, the BP filter transmits light above 800 nm. The cost of the filters ranged between $70-$145.

The system was fabricated with black delrin using a variety of machinist tools, including a mill, lathe, and a CNC (computer numerical control) mill. Threaded holes were tapped so screws could be used to attach the machined pieces. An optical post was attached to the top of the system to anchor the DSLR during image acquisition to minimize camera movement. Finally, a one-inch diameter circle was etched into the center of the tissue specimen area as a scaling reference. With all components attached (Fig. 7.2), the system weighs 8.2 lbs and has a foot-space of 55.25 in^2.

7.3.2. Characterization of system

There are three imaging modes for this system. In white light imaging, the LEDs are not turned on and there is no emission filter; the only illumination is from

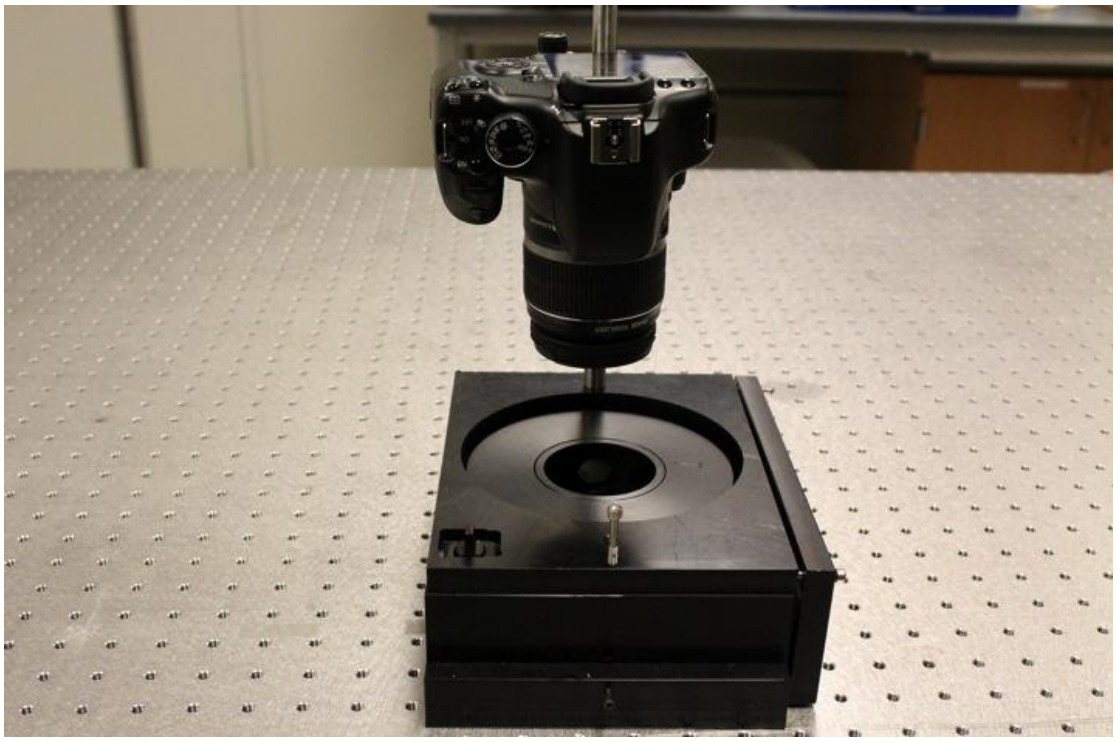

Figure 7.2 Side view of fully assembled imaging device. An optical pole was attached to the top of the device for camera stabilization and adjustable height. An on-off-on witch allows for easy control of the two circuits.

the overhead lights in the room. When the term "blue light imaging" is used, we refer to the setup used to image 2-NBDG: blue LEDs illuminated with a BP 525 emission filter for the lens. For "NIR imaging", the NIR LEDs were illuminated and a LP720 emission filter is used (unless otherwise noted). The overhead lights were turned off during the latter two imaging modes so that no background signal is captured by the camera

Preliminary experiments demonstrated the importance of camera settings such ISO speed, aperture size, and exposure time. These preliminary studies led us to use the same aperture size (f/5.6) and ISO setting (800) for all experiments presented in this chapter. Different exposure times were used for all three imaging modes and for different lighting settings. These different settings will be indicated in the materials and methods section. However, any quantitative analysis performed between images was performed with images acquired at the same exposure. Additionally, an optical power

meter (Newport Optics) was placed in the system during different days to confirm that illumination power did not decrease between days. We did not see any measurable change between days. However, as a precaution, any quantitative analysis was performed between samples that were acquired during the same experiment so that any difference between experiments did not affect the analysis.

To demonstrate the ability of the system to visualize NS and quantify signal intensity changes with the number of particles, 1 mL of a serial dilution (2 $X10^9$ particles to 31.25 X 10^6 particles per mL) of NS was placed in a quartz cuvette in the same orientation in the imaging device. Images were acquired in the NIR imaging mode at an exposure time of 10 ms. After image acquisition, ImageJ was used to draw a ROI around the NS area and the average intensity for each concentration was calculated and plotted in Figure 7.3(A). Additionally, a serial dilution of 2-NBDG (156 mM to 15.6 nM) was characterized in the blue light imaging settings at an exposure time of 1 s and is displayed in Figure 7.3(B).

7.3.3. Performance of system *in vitro*

To demonstrate the ability of the system to visualize both contrast agents, the Sk-Br-3 cell line was chosen as previous experiments have demonstrated increased contrast with both optical agents. Cells were incubated with 2-NBDG only, anti-HER2 NS only, or both contrast agents (along with a negative control). NS were incubated with antibodies and PEG-SH in the same ratios as previously described [128]. Briefly, 2.25 mLs of NS (at a concentration of 2.0 X 10^9 particles/mL) were incubated with 3 μL of antibody-PEG-linker and 237 μL of deionized (DI) water at 4°C. After 2 hours, 10 μL of 1mM PEG-SH was added to stabilize the particles. Particles were then centrifuged at

2500 RPM for 5 minutes and resuspended in 500 µL of antibody buffer. 2-NBDG was diluted to a concentration of 500 µM in 1X PBS.

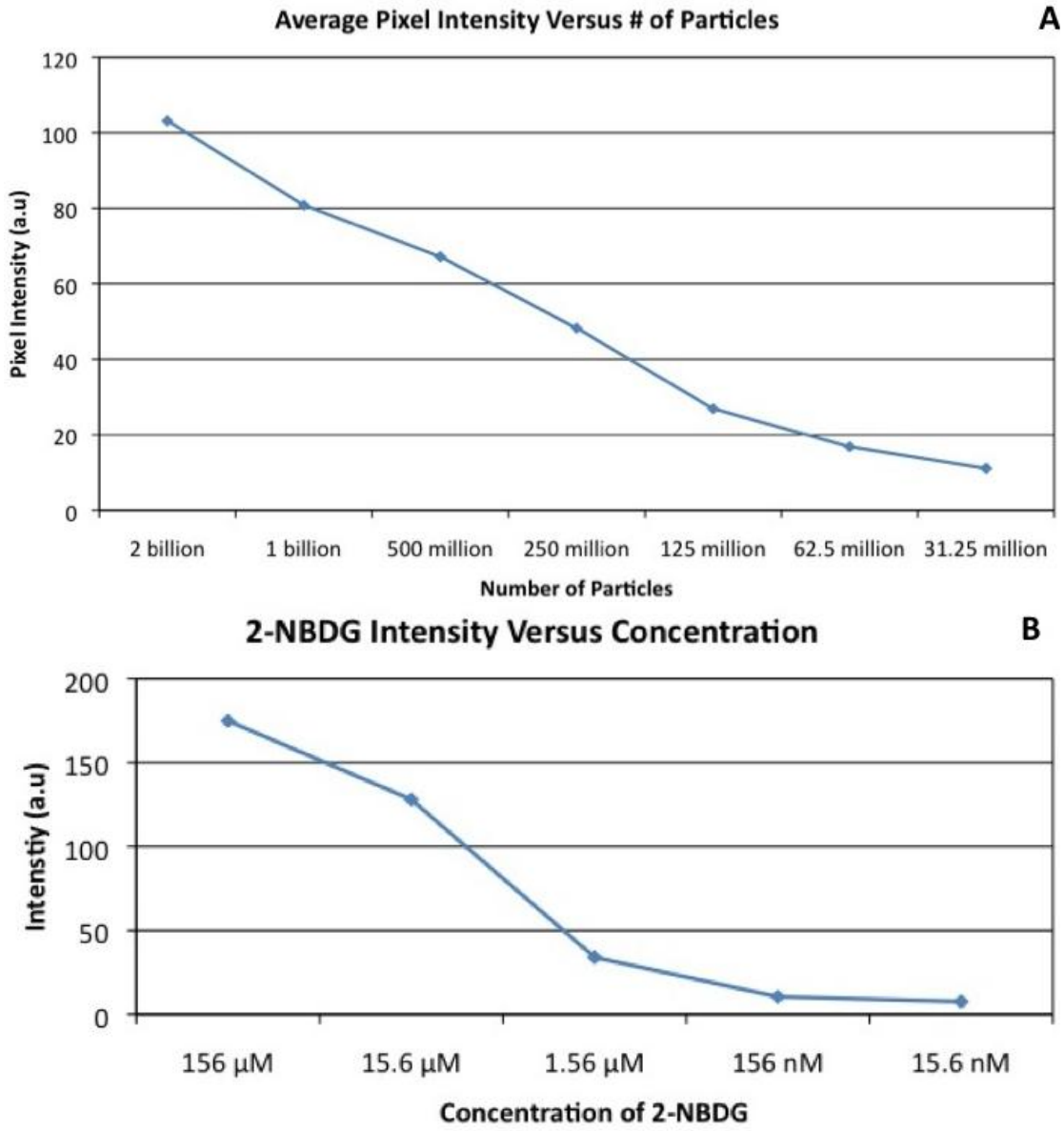

Figure 7.3 Pixel intensity versus number of silica-gold NS (A) and concentration of 2-NBDG (B).

Sk-Br-3 cells were grown at 37°C and 5% CO_2 until reaching confluency. Trypsin was added to the cells to detach from the flask and centrifuged into a pellet at 120g for 3 minutes. Supernatant was aspirated and cells were resuspended in 1X PBS to a

concentration of 1.77 X 10^6 cells/ml. 150,000 cells were added to a flat bottom centrifuge tube (Fisher 05-406-16) and 500 μL of contrast agent was added to the cells and 1X PBS was added to each centrifuge tube so each tube had a total volume of 1 mL. Samples were then placed in a rotating hybridization chamber (VWR 23050 TV) for 20 minutes. Samples were then centrifuged to remove any unbound 2-NBDG or NS and fixation buffer (Enzo ADI-950-011) was added to the cells for 20 minutes.

Cells were then transferred to coverslips and placed into the center of the device, and white light, blue light, and NIR images were acquired at exposure times of 5 ms, 6 s, and 66.6 ms respectively. Results for each wavelength of imaging are shown in Figure 7.4. As the signal in the 2-NBDG only (Fig. 7.4(D)) image was faint, the images were further processed into respective RGB channels and contrast for the green channel was enhanced to demonstrate the higher 2-NBDG signal in cells with 2-NBDG versus cells with NS only. These resulting images are displayed in Figure 7.5.

7.3.4. 2-NBDG in *ex vivo* specimens

All tissue used in this chapter was supplied by the CHTN in an IRB approved protocol as described in the previous chapter. To characterize the ability of the system to differentiate 2-NBDG signal from autofluorescent signal in tissue, a HER2-positive IDC was incubated with 1.56 mM 2-NBDG for 10 minutes at 37°C. Pre and post incubation images were acquired in both white light and blue light settings at an exposure time of 100 ms and 1 s respectively. Resulting images are displayed in Figure 7.6. To quantify the difference between the blue light images, ROIs were drawn around the tissues and average intensities were calculated for both the RGB composite and green channel image.

7.3.5. Anti-HER2 NS in *ex vivo* specimens

The same HER2-positive tissue was also incubated with anti-HER2 NS after the 2-NBDG. Pre and post incubation images with NIR LEDs, 780 LP filter and an exposure time of 1 ms are shown in Figure 7.6(C&F). 1 ms was chosen as the exposure time as this was the lowest exposure setting in which there was no endogenous signal from the tissue in the pre incubation image.

As shown in Figure 7.6, there is very little signal from the tissue in both pre and post incubation NIR images, due to the low exposure. Using a different HER2-positive tissue, we varied the exposure time for both pre and post incubation from 10 to 50 ms to visualize the NS more effectively (Figure 7.7). However, increasing exposure also increased the signal from the tissue, and it became difficult to differentiate the signal from the tissue and the NS.

To reduce the signal from the tissue and increase contrast between the NS and tissue, the tissue was incubated with glycerol for 10 minutes at 37°C. Glycerol is known as an optical clearing agent that reduces scattering of tissue through dehydration [281,413–415] or reversible disassociation of collagen fibers in the extracellular matrix [280,415,416]. Pre and post incubation images were acquired in the NIR imaging setup with a LP 780 filter at an exposure time of 20 ms (Fig. (7.8(A&B)). To demonstrate enhanced signal in tissue with NS after glycerol incubation, a different HER2-positive tissue was incubated with glycerol for 10 minutes at 37°C, followed by a 5 minute incubation with anti-HER2 NS at 37°C, and results are presented in Figure 7.8(C&D).

7.3.6. Application of FITC-functionalized NS to co-localize NS in tissue

As we were unable to demonstrate enhanced signal in tissue after glycerol and NS incubation (Fig. 7.8), we chose to examine if the NS were present in tissue using PEG functionalized with FITC so that the NS could be localized using the blue light imaging settings. In this experiment, HER2-negative tissue from the same patient was incubated with non-targeted NS functionalized with FITC-PEG or PEG for 10 minutes at 37°C. Tissues were not rinsed, as we did not want to remove the NS that were bound by electrostatic interactions. Pre and post incubation images and side-by-side images were acquired at an exposure of 1 s and 40 ms (Blue light and NIR). Representative images are displayed in Figure 7.9(A&B); the blue light images were split into RGB components and the average intensity of the green channel for each tissue was calculated with a hand-drawn ROI.

After establishing that FITC-PEG NS could be visualized in the blue light imaging settings of our system, we aimed to use targeted anti-HER2 NS that were backfilled with FITC-PEG on HER2-positive tissue. 2.25 mLs of silica-gold NS were incubated with 2.4 μL of anti-HER2-PEG linker and 189.6 μL of DI water for 2 hours at 4°C. Following incubation 8 μL of 1 mM FITC-PEG-SH were incubated with the NS overnight. NS were then centrifuged at 2500 RPM for 5 minutes and supernatant was aspirated. Finally, the NS were re-suspended in 165 μL of antibody diluent buffer. HER2-positive tissue was thawed at 37°C in PBS and pre incubation images were taken in white light, blue light, and NIR imaging settings (with a LP 720 filter). Exposure times for imaging were 66.6 ms, 1 s, and 10 ms respectively. Tissues were then incubated for 10 minutes in 99.9% glycerol and images were acquired under the same

conditions. Next, 165 μL of NS were incubated with the tissue for 10 minutes at 37°C. Post incubation images were acquired. Blue imaging pictures were processed in ImageJ to visualize signal from the FITC particles. Images were split into RGB components and the contrast in the green channel was enhanced by 0.05%.

7.3.7. Application of NIR fluorescent dye

Anti-EGFR IRDye 800CW was purchased from LI-COR Biosciences (926-08446) and resuspended in 1.5 mLs of 1X PBS to a final concentration of 133.3 mM. HER2-positive tissue was incubated with 99.9% glycerol for 10 minutes at 37°C and pre incubation images were acquired in the NIR setting with a LP500 filter at an exposure time of 5 s. Tissue was then incubated 165 μL NIR dye (or PBS) for 10 minutes at 37°C. Post incubation images were acquired at the same imaging settings.

7.4. Results

Our results show that we were able to design, build, and characterize a portable system to image multiple contrast agents in resected tissue specimens. Concentration versus intensity graphs are shown for silica-gold NS and 2-NBDG in Figure 7.3. Both graphs show that pixel intensity decreases logarithmically with the decreasing concentration, demonstrating the concentration dependence of the device.

7.4.1. Performance of system *in vitro*

Figure 7.4 demonstrates the ability of our system to capture both 2-NBDG and NS signal in separate imaging settings.. Images of SK-Br-3 cells incubated with contrast

agents are presented in Figure 7.4. Cells with 2-NBDG only (A,D&G), anti-HER2 NS only (B,E,&H), and both contrast agents (C,F,&I). are presented. In the blue light imaging mode, there is faint green signal in cells incubated with 2-NBDG only that is not seen in the NS only cells. However, this green signal is very strong in cells incubated with both NS and 2-NBDG. Also, the cells with 2-NBDG have no signal in the NIR imaging setting, which was expected as there were no NS present. Cells incubated with NS only had no signal in the blue light imaging, which was consistent with the negative control. There is signal from the cells in the NIR imaging that is also seen in the cells incubated with both 2-NBDG and NS.

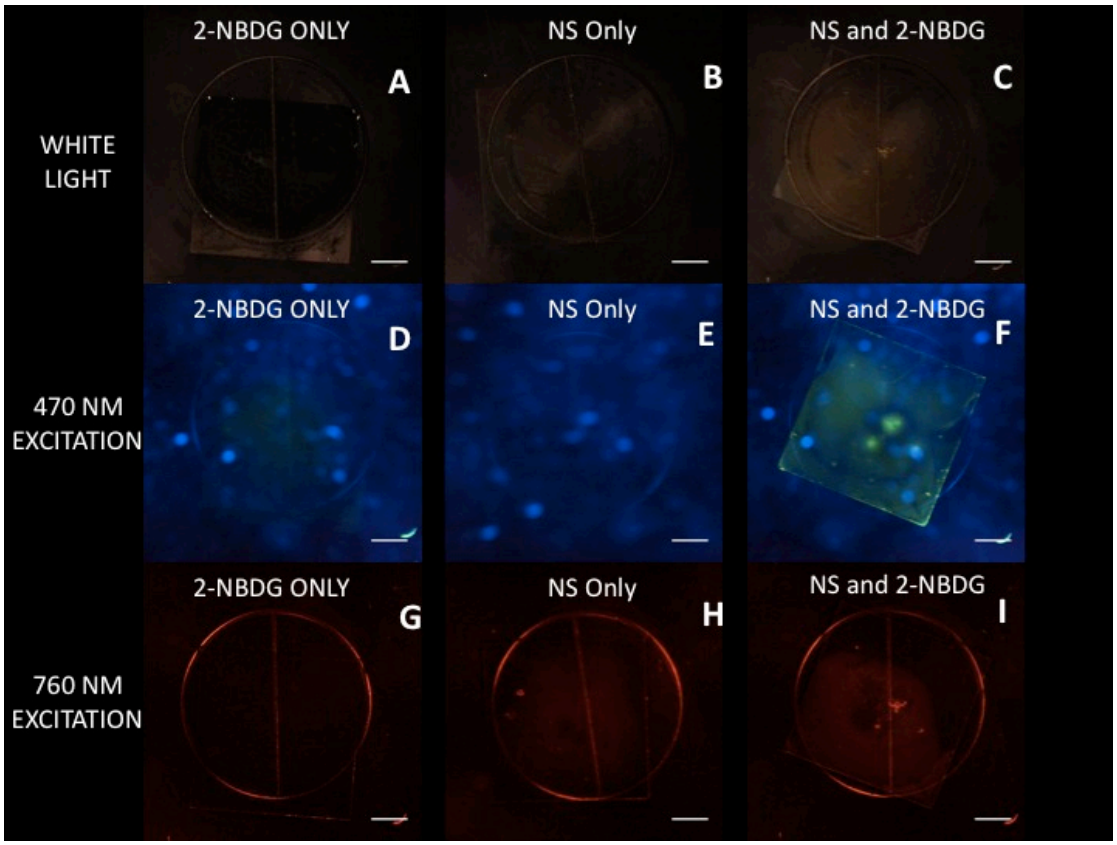

Figure 7.4 Images acquired with Sk-Br-3 cells incubated with 2-NBDG only (A,D&G), anti-HER2 NS only (B,E,&H), and both contrast agents (C,F,&I). Green signal from 2-NBDG is seen in both D&F but not in cells incubated with NS only. Additionally, for cells in NIR imaging settings (G-I), there is no signal from cells incubated with 2-NBDG only, but cells incubated with NS only had similar signal to cells incubated with both contrast agents. Cells with no signal (Fig. 7.3(E&G)) had the same signal as negative control cells. Scale bar = 5 mm.

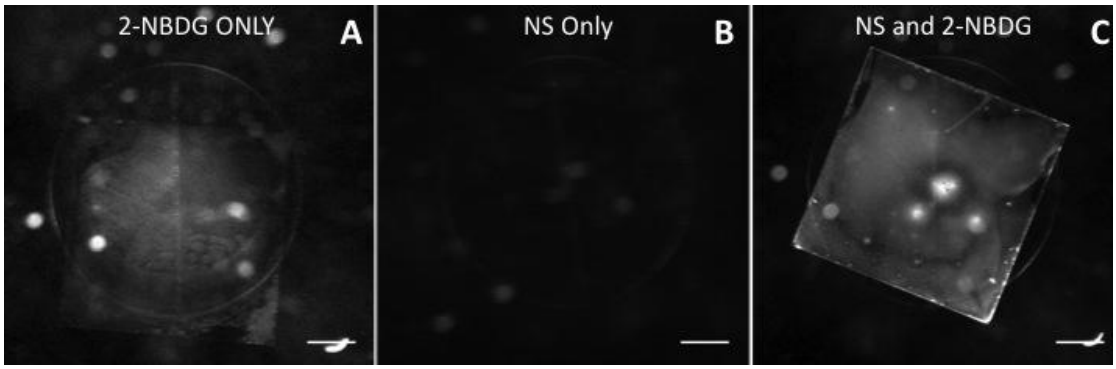

Figure 7.5 Green channel images from Figure 7.4(D-F) that have had contrast enhanced. Images show high signal in the green channel from both cells incubated with 2-NBDG and no signal from cells incubated with anti-HER2 NS only. This confirmed that green signal seen in Figure 7.4 is from the 2-NBDG. Scale bar = 5 mm.

This is an important proof of concept that shows multiple contrast agents can be captured using this system and that these contrast agents can be accurately distinguished. As the green signal from the 2-NBDG only cells was very faint, each blue light image was split into its respective RGB channels and the green channel was used for comparison. The results after enhancing the contrast in each image to further delineate cell signal are shown in Figure 7.5. These results clearly show the 2-NBDG signal in both Figure 7.5(A&C) and no signal from 2-NBDG in cells incubated with NS only. A possible reason for the lower signal from the 2-NBDG only cells is that a limited amount of cells were transferred to the coverslip, lowering the overall signal detected. However, Figure 7.5(C) clearly shows high 2-NBDG signal from cells on the coverslip.

7.4.2. 2-NBDG and anti-HER2 NS in *ex vivo* specimens

Figure 7.6 displays the initial attempt to visualize both 2-NBDG and anti-HER2 NS in *ex vivo* tissue samples. As the tissue was frozen, the signal from 2-NBDG seen in Figure 7.6(E) is from tissue that was not rinsed after incubation as most of the 2-NBDG would have been rinsed away. However, it is important as it illustrates that 2-NBDG

signal on the tissue is much stronger than the autofluorescent signal seen in Figure 7.6(B). These are similar to the images we displayed in chapter 5 which demonstrated the enhanced fluorescent signal after incubation with 2-NBDG. This shows that we are able to use our inexpensive, portable system can create images similar to the expensive Maestro system. Figure 7.6(C&F) show no difference between tissues after anti-HER2 NS incubation NS showing that the system is unable to resolve the NS scattering signal at this low camera exposure time.

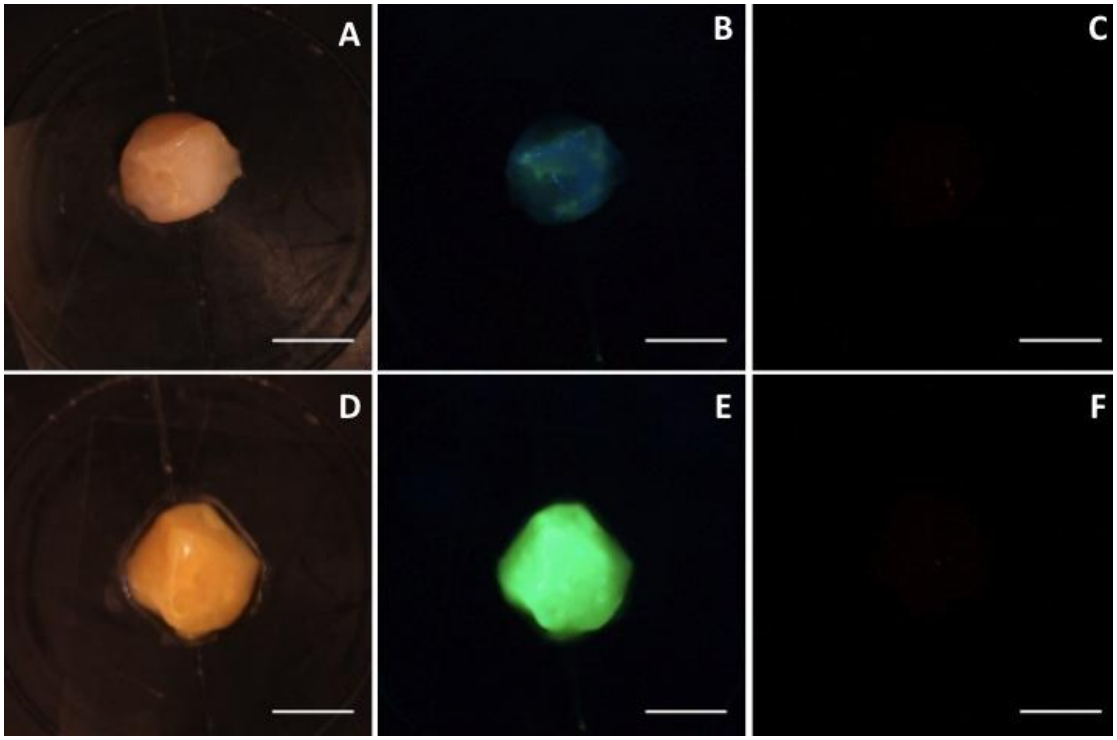

Figure 7.6 Pre (A-C) and post (D-F) incubation images of HER2-positive tissue after incubation with 2-NBDG (B&E) then anti-HER2 NS (C&F). Images display the system's ability to differentiate 2-NBDG signal from autofluorescence. However, anti-HER2 NS binding was not visualized through NIR scattering. Scale bar = 5 mm.

The inability to visualize NS scattering at low exposure settings created a problem as increasing exposure time on the camera not only increased NS scatter but also signal from tissue (Fig. 7.7). At 10 ms exposure with a 720 LP filter, the average signal for HER2-positive tissue was calculated to be (48 (a.u), n=3). Using the graph presented in

Figure 7.3(A), we see that to visualize NS due to their high scattering, we would need approximately 500 million particles to bind in a concentrated area to have enhanced scattering from the tissue. As this high concentration is not feasible, we hypothesized that we could decrease tissue signal through the use of the optical clearing agent, glycerol. Figure 7.8(A&B) demonstrates the reduced signal in tissue after incubation for 10 minutes in glycerol. The 10-minute time point was chosen to minimize incubation time in the glycerol to maintain our goal of developing a system to rapidly differentiate *ex vivo* tissue. However, we were still unable to show increased NIR signal after incubation with anti-HER2 NS (Fig. 7.8(C&D).

7.4.3. Application of FITC-functionalized NS to co-localize NS in tissue

As we were unable to show increased scatter signal after glycerol and NS incubation, we wanted to confirm that the NS were on the tissue. To do this, we back-filled the NS with a fluorescent PEG (FITC-PEG) that could be visualized using the blue imaging settings on the device. We first incubated non-targeted NS (backfilled with either FITC-PEG or non-flourescent PEG) with HER2-negative tissue and imaged the tissues without rinsing the NS. Blue and NIR images comparing the tissues are shown in Figure 7.9(A&B). The FITC labeled NS (F) have a much higher signal in Figure 7.9(A) due to the presence of FITC on the NS incubating the tissue. The NIR images in Figure 7.9(B) show that there is no difference between the tissues' NIR scattering. Due to autofluorescent differences in the tissues, we also calculated the change in green channel intensity for each tissue pre and post NS incubation. The tissue incubated with FITC-NS did have higher autofluorescence; however, the signal difference between the tissues is much higher after incubation with the particles (10 vs. 35). This confirms the NS

location on the surface of the tissue but that we were unable to differentiate their scattering signal from the endogenous tissue signal.

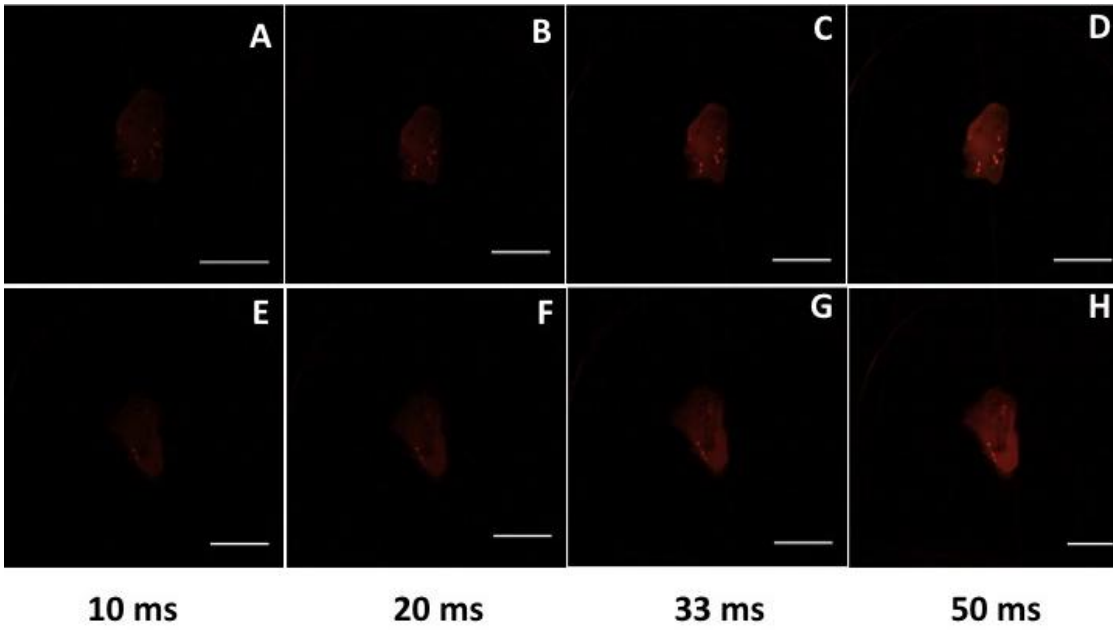

Figure 7.7 HER2-positive tissue pre (A-D) and post (E-H) incubation with anti-HER2 NS at different exposure times for the imaging system. Increasing exposure time increased signal from the tissue and did not improve the scatter signal from the anti-HER2 NS on the tissue. Scale bar = 5 mm

After confirming NS presence via FITC signal, we attempted to use targeted anti-HER2 NS with FITC–PEG to visualize the distribution of targeted NS on tissue. Our goal was to show that even if there was minimal NIR scatter from the NS, we would still be able to demonstrate binding of the NS to tissue through the FITC signal. If we were able to show this, then it would confirm that our optical configuration was not ideal for differentiating the binding of the anti-HER2 NS via their NIR scattering.

Figure 7.10 displays the results from these incubation experiments. As can be seen in the images, the glycerol lowered the NIR signal from the tissue. And as observed in previous experiments, the addition of the anti-HER2 NS failed to increase the NIR signal from the tissue. However, the images that display the green channel of the blue

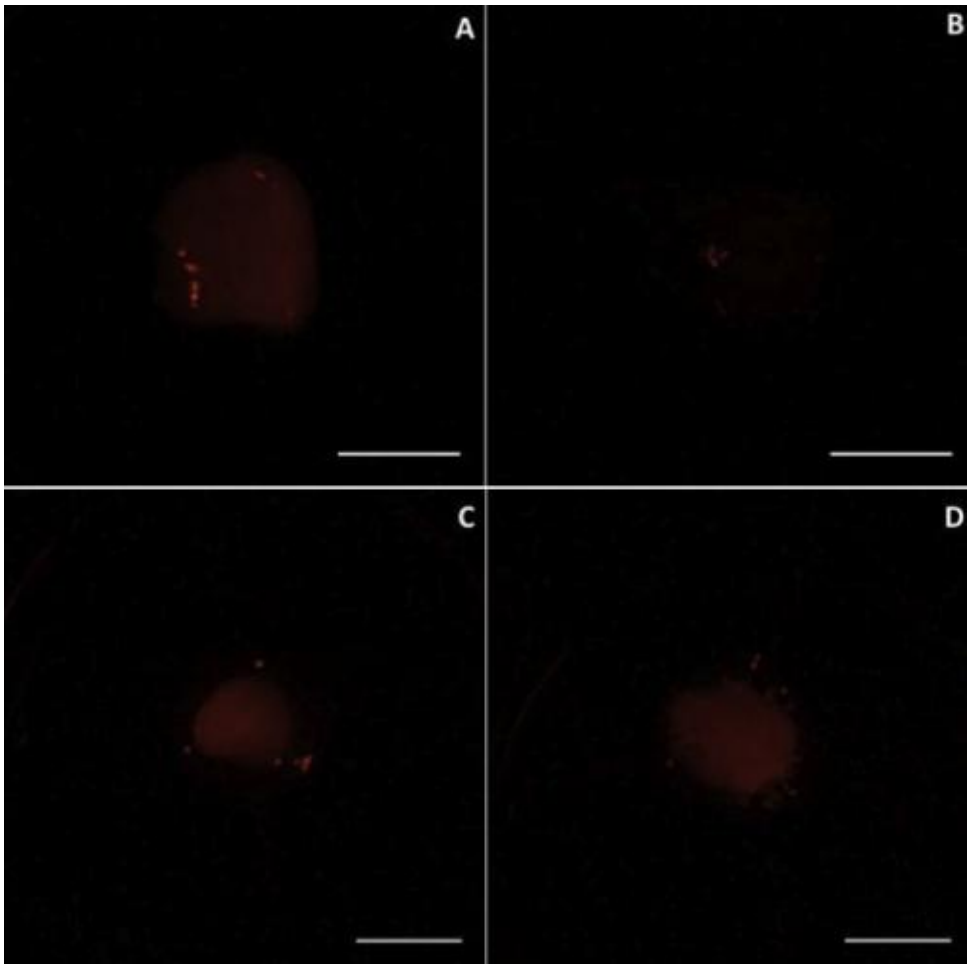

Figure 7.8 Images displaying NIR scatter reduction in HER2-positive tissue after incubation with 99.9% glycerol for 10 minutes. C&D demonstrate that anti-HER2 NS scatter signal could still not be separated from tissue that had been incubated in glycerol (C) and then incubated with anti-HER2 NS (D). Scale bar = 5 mm

imaging settings (Fig 7.10 (C,F,&I)) show increased intensity that is due to the presence of the NS throughout the tissue. Figure 7.10(J) displays the average signal intensity of the tissue in the blue imaging settings during each step of the experiment. As expected, the total signal from the tissue decreases after incubation with glycerol, and there is an increase in signal after the addition of NS but the overall signal intensity is still much less than the normal autofluorescent signal of the tissue. However, this graph shows a sharp increase in green channel intensity that occurs after incubation with FITC-NS. This indicates a presence of NS throughout the tissue that was not visualized through NIR scatter but through FITC signal, confirming our hypothesis that this optical set-up could

not visualize enhanced scattering from targeted silica-gold NS in HER2-positive breast cancer.

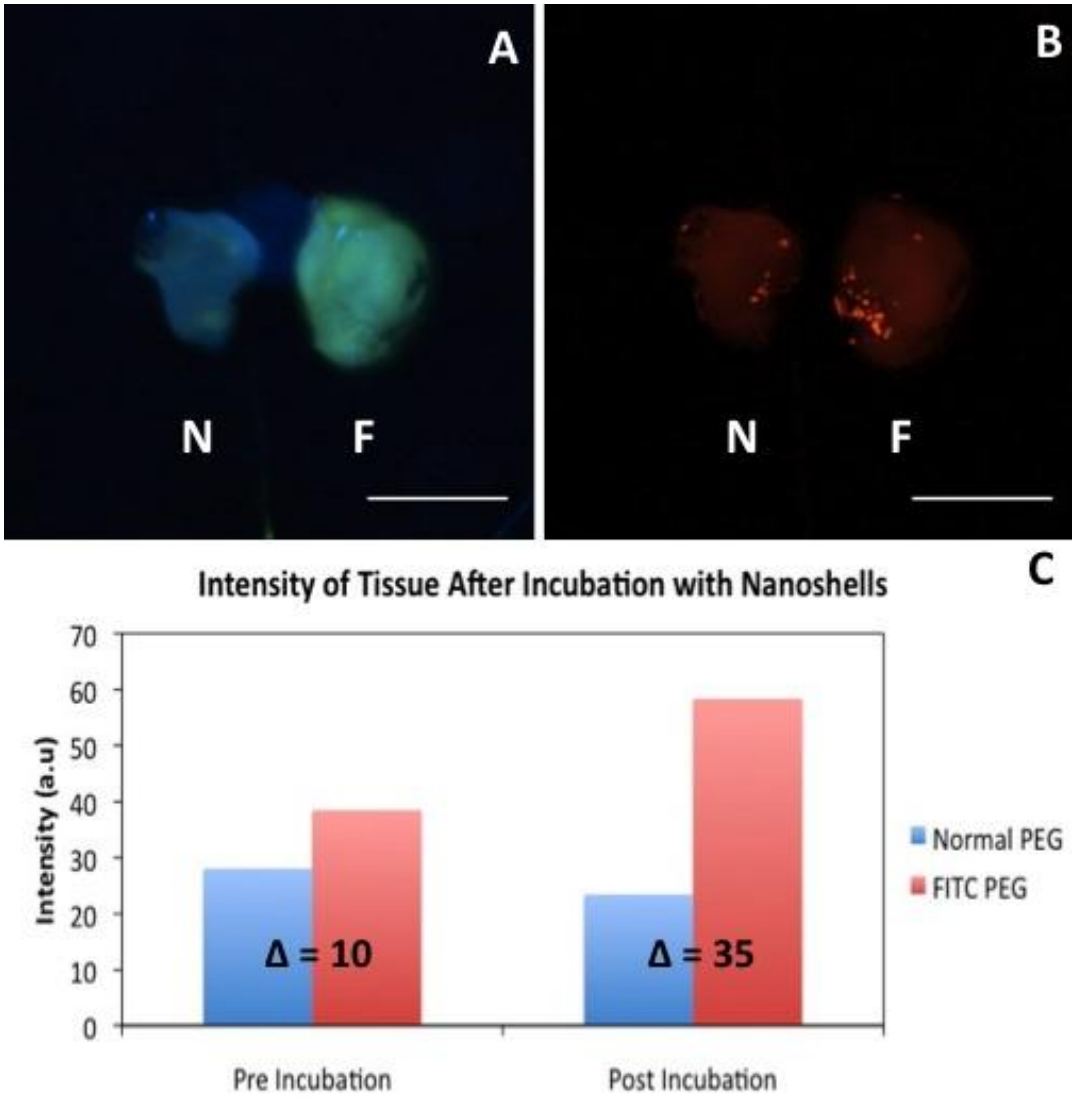

Figure 7.9 NS backfilled with FITC (F) or unmodified (N) PEG on tissue from the same patient. Figure 7.9(A) displays the increased signal from FITC in the blue imaging setup tissue labeled F. However, NIR imaging of the tissues showed minimal difference in scatter from the tissues, demonstrating that increased signal in A is due to FITC. Scale bar = 5 mm. Figure 7.9(C) quantifies the signal difference between the tissues before and after incubation with NS. Increased signal in the FITC NS was due to the presence of FITC on the NS.

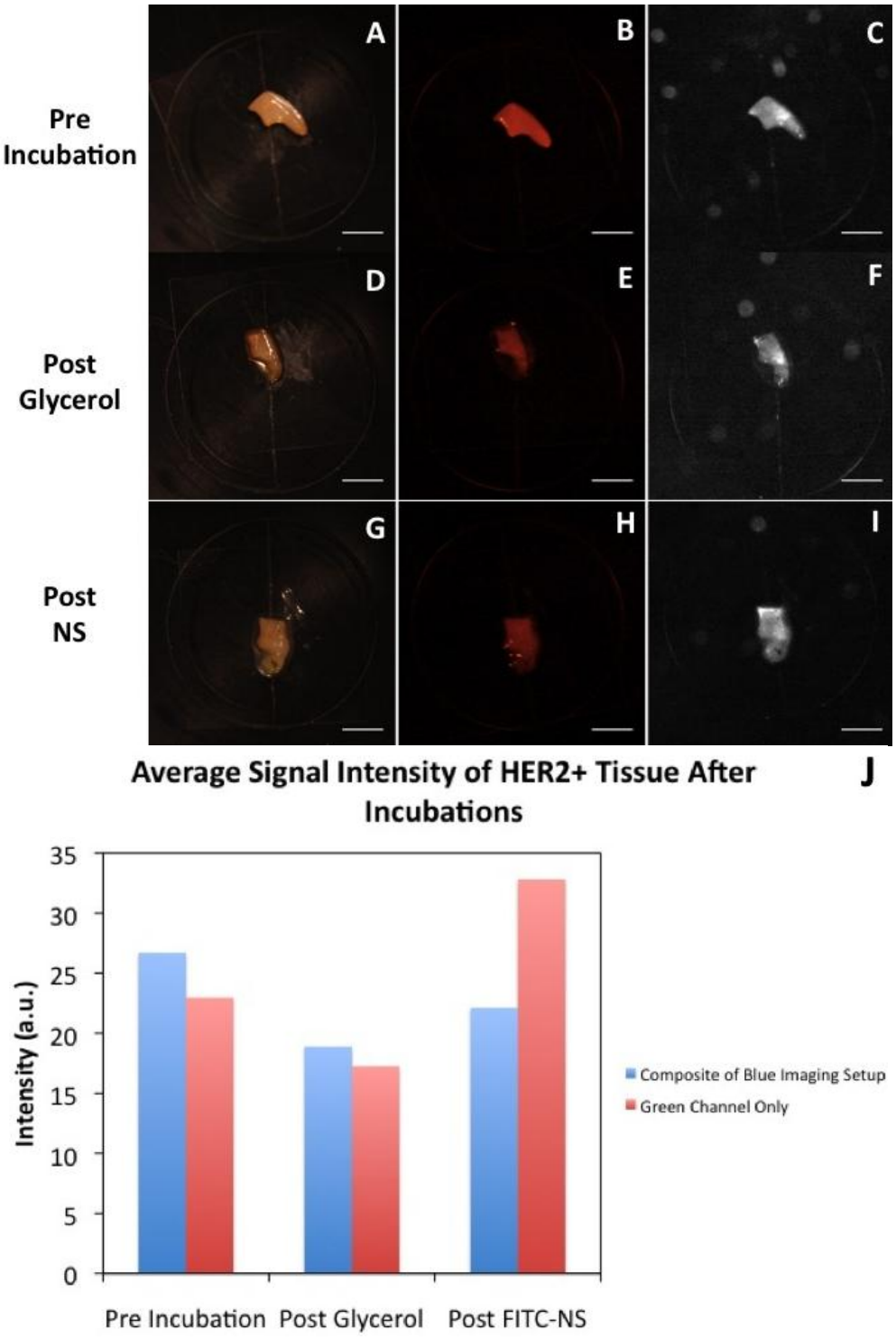

Figure 7.10 Images of HER2-positive tissue after incubation with glycerol (D-F) and anti-HER2 NS backfilled with FITC-PEG. Images demonstrate increased signal from FITC-NS showing distribution throughout the tissue. However, even with widespread tissue distribution, there was little increase in NIR signal from the tissue. Scale bar = 5 mm. Figure 7.10(J) displays intensities from FITC image composites and the green channel. Increased signal is due to FITC presence on the NS distributed throughout the tissue.

Even though we were unable to localize the anti-HER2 NS through NIR scattering, we were able to use white light imaging to visualize small pockets of NS using their absorbance (Fig 7.11). This demonstrates the system's ability to localize contrast agents through white light imaging, as long as the agent can provide ample contrast against the tissue without any special excitation and emission filters. These results are similar to data presented in chapter 6 (Figs. 6.7 & 6.8) that showed absorbance of targeted NS on the surface of HER2-positive tissue.

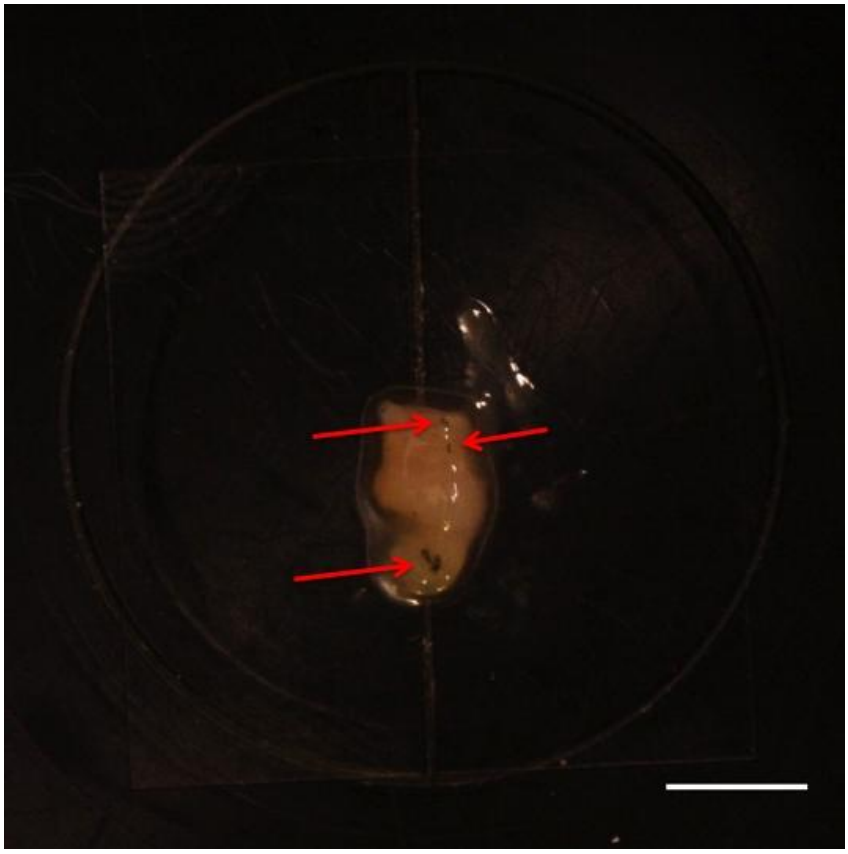

Figure 7.11 White light image of tissue presented in presented in 7.10(G) showing pockets of anti-HER2 NS binding, demonstrating the ability of our system to visualize the absorbance of targeted silica-gold NS in tissue. Scale ber = 5 mm.

To further demonstrate the compatibility of the system with other diagnostic agents, we incubated HER2-positive tissue with an NIR fluorescent dye that stains for EGFR. Recent studies by Xie, Ke, and Kovar et al. have demonstrated the intratumoral

specificity of this dye in EGFR-overexpressing tumor xenografts [27,417,418]. The dye has an excitation maximum of 774 nm and emission maximum of 805 nm [418], allowing us to visualize the fluorophore in our NIR setting with an LP800 filter. In Fgure 7.12, pre (A) and post-incubation (B) results show distinct differences between tissues after incubation with the contrast agent. The blue hue seen in the tissue incubated with the dye is consistent with the signal observed when the fluorophore was suspended in a quartz cuvette (data not shown). This figure demonstrates the proof-of-concept that the imaging system can be used with a contrast agent that is not custom made (as was the case with the NS), but rather a commercially available product that has already demonstrated high specificity *in vivo* [27,417,418].

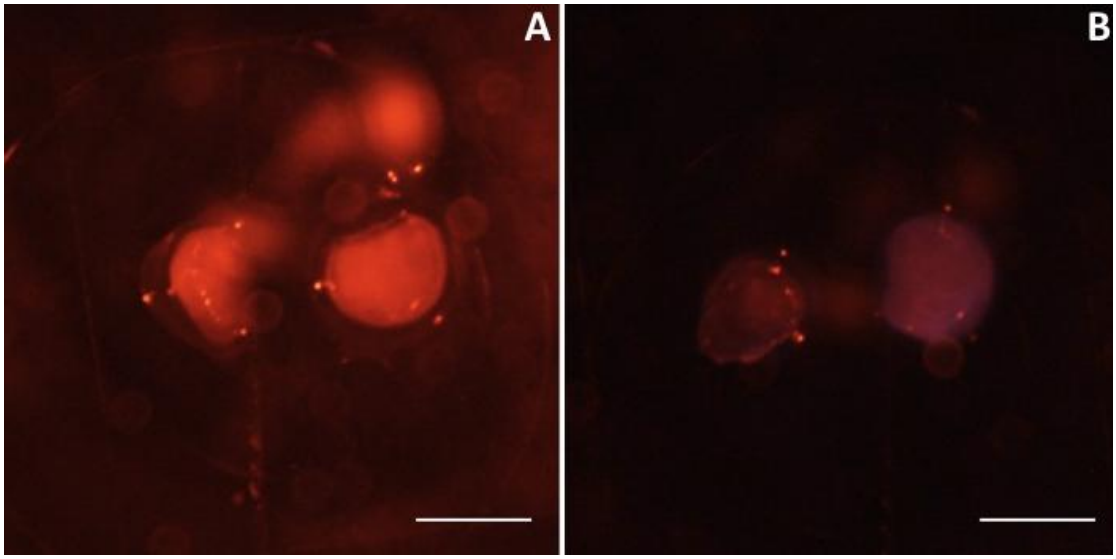

Figure 7.12 HER2-positive tissues before (A) and after (B) incubation with an NIR fluorescent EGFR dye. The tissue on the right of each image was the tissue incubated with the dye and the tissue on the left served as a control. There is a large difference in the tissues after incubation that was not seen in the pre-incubation images. Scale bar = 5 mm.

7.5. Discussion

Our results indicate that we have developed a system that has the ability to image multiple wavelengths and contrast agents on the same tissue. The original design of the system was to visualize 2-NBDG fluorescence and NIR scattering from targeted silica-gold NS. We were unable to develop a method to differentiate NS scatter from tissue scatter; however, we were able to visualize NS absorbance from large aggregates using white light. Even though our system did not differentiate NIR scatter from tissue, we were able to show that we could visualize NIR fluorescence from the optical probe IRDye 800CW EGF. As its excitation and emission maxima are located in the middle of the water window (700-900 nm) [419] , IRDye 800CW is thought to have optimal characteristics for *in vivo* imaging [418]. In addition to imaging EGF, IRDye 800 CW has been conjugated to deoxy-glucose to visualize GLUT1 expression in the same manner as 2-NBDG [27,316,420]. As the system can visualize contrast agents in three different modes (white light and visible/NIR fluorescence), it is conceivable that this system could be used to visualize three separate contrast agents on one tissue. However, this system is designed as a portable device to be used intra-operatively and provide surgeons with rapid visualization of cancerous tissue, so appropriate contrast agents would need to be selected.

One design parameter for the device was to develop the system using inexpensive components with minimum costs for customized parts and contrast agents. The total cost of the materials was $2,954.00. Additionally, two of the contrast agents that we used (2-NBDG and IRDye 800CW EGF) were commercially available products that required only re-suspension in PBS upon receipt, and their cost was $171.00 and $325.00,

respectively. Our silica-gold NS were manufactured by Nanospectra and required functionalization with both an OPSS-PEG-antibody linker and PEG-SH. The integration of inexpensive imaging components with commercially available contrast agents dramatically decreases the overall construction and operation for this system while also providing enhanced visualization of contrast agents in cancerous tissue.

Another positive characteristic of this system is the ability to customize the system to contrast agents by replacing LEDs, excitation filters, and emission filters. As the majority of optical contrast agents have been focused in the NIR range due to their optimal signal-to-background [418,421], one could design the system so that multiple NIR dyes (such as Cy 5.5 and IRDye 800CW) with different molecular targets are imaged using different combinations of NIR LEDs and emission filters.

Finally, the speed with which tissues were incubated and imaged is a promising indication for the future use of this system. The goal of this project was to develop an imaging device that would provide surgeons with a rapid detection method of cancerous tissue using molecular contrast agents as a tool to lower positive margin rates. We do not envision this technology as a replacement for intraoperative pathology, but rather as a tool to help surgeons who do not have any method to visualize microscopic disease.

This device can also be thought of as a tool to supplement intraoperative pathology. As discussed earlier, a recent study by Vosoughhosseini et al. demonstrated that patients diagnosed with negative margins via standard H&E pathology were found to have positive margins when EGFR staining was performed on the same specimens [13]. If the pathologists had a method of visualizing specific receptors in a rapid method, there is a greater possibility that these false negatives would have been avoided. Additionally,

the system could also be used to pre-screen resected specimens by helping the surgical team visualize the specific areas of the margin that need H&E performed and not spend unnecessary resources and time on areas that are benign.

There are system limitations. As it is a wide-field imaging system, there are limitations to the resolution of the system. While we were able to visualize the signal from cells incubated with molecular contrast agents, individual cells could not be resolved. Additionally, this system can only visualize the surface of the tissues. However, this is also a limitation of the anti-HER2 NS, as the contrast agents do not penetrate the surface of the tissue in the limited incubation time [128]. Additionally, the operation of the system is done by hand. The system could be improved by integration with a data acquisition (DAQ) board so that control of the camera and image processing would be performed with a graphical user interface (GUI) that would easily translate clinically. An example of this interface is the MDM created by Roblyer at al [301]. Futhermore, changing the filters between different wavelengths is also done by hand, and the use of a filter wheel to control the filters placement would also improve the translational ability of the system. Finally, we were unable to differentiate the NIR scatter of silica-gold NS from tissue, but we were still able to image the NS via their absorbance after aggregation on the tissue surface. In addition, we were still able to use the system to visualize the NIR fluorescence of a commercially available and highly specific contrast agent that has demonstrated enhanced contrast *in vivo*.

This system is an important first step in development of a translatable device that can be combined with highly specific contrast agents. It demonstrates that readily available components can be engineered to create a system that has the ability to provide

physicians with a tool to visualize molecular expression in resected tissue in a limited amount of time. As it is low-cost and portable, one can imagine this system located in the surgical suite with a technician performing the tissue processing while the surgeon continues operating on the patient. The system can also be customized to visualize different contrast agents for other molecular markers that are more common in other cancers.

7.6. Conclusion

The portable imaging device developed in this chapter was designed for compatibility with contrast agents that were characterized in previous work in our research group [23,128,129,155]. Previously, we had found that optical contrast agents 2-NBDG and anti-HER2 silica-gold NS could differentiate cancerous tissue due to the overexpression of GLUT1 and HER2 proteins. We had also demonstrated that the contrast provided by these agents was done in a rapid manner (≤ 20 minutes), demonstrating possible use as an intraoperative agent. However, previous methods to visualize these agents were performed with non-portable and expensive equipment. Our system was designed to overcome these issues by developing a platform in which these agents could be visualized in tissue using inexpensive and portable components. By using LEDs, a DSLR, and commercially available optical filters, we were able to visualize the enhanced contrast of three different contrast agents, 2-NBDG, anti-HER2 silica-gold NS, and IRDye 800CW.

Chapter 8

Conclusion

The research presented in this thesis demonstrates the utility of using molecularly targeted contrast agents in both cells and tissue specimens to enhance contrast using the overexpression of molecular markers. It also represents the first step in the development of an intraoperative imaging device that is capable of visualizing multiple contrast agents in a single specimen. To simulate intraoperative conditions, contrast agents that require minimal incubation time were chosen; additionally, targeting multiple molecular targets using different agents enhances the specificity of the system as areas without enhanced contrast would have to be negative for multiple molecular markers.

This thesis advances research as it demonstrates the ability of a rapid, portable, and inexpensive system designed to enhance and visualize contrast in breast cancer. We first demonstrated that 2-NBDG enhanced contrast in breast cancer tissues that had a higher metabolic rate than normal tissues from the same patient. A search on SCOPUS and Pubmed for "2-NBDG breast cancer" revealed only seven publications for each

search engine. One of those publications is the work presented by our group in chapter 5. No other research has been published on *ex vivo* fluorescent signal enhancement from 2-NBDG in breast cancer. As well, research presented in chapter 6 presents the novel use of targeted silica-gold nanoshells as rapid contrast agents in whole *ex vivo* tissue specimens, as well as multiple methods to determine the intratumor location of the nanoshells in the tissue. Using data from our first two *ex vivo* experiments, we hypothesized that we could design a device to image both contrast agents in the same tissue via the fluorescence of 2-NBDG and the NIR scatter of the nanoshells. The device was unable to differentiate tissue scatter from nanoshell scatter. However, nanoshell aggregation was still visualized in white light imaging. Additionally, we were able to visualize the NIR fluorescence of IRDye 800CW, demonstrating the ability of the system to visualize three different contrast agents in tissue.

The research presented in this thesis provides the foundation for the development of a device that can supplement surgeons performing BCT with optical information on the molecular expression of tissue. The contrast agents used in this thesis are able to enhance contrast in a rapid fashion to ensure that surgeons are able to probe margin status while the patient is still under anesthesia. Additionally, the low weight and foot-space of the device allows for ease of use during a surgery; a larger piece of equipment does not need to be moved in to facilitate the intraoperative imaging. The system uses contrast agents that are non-ionizing (unlike the handheld PET probes or intraoperative X-rays), limiting the exposure of harmful material to the surgical team. If the surgeon knows the tumor's molecular expression profile prior to surgery (by using the pre-operative biopsy specimen), the system could be prepared to visualize contrast agents different from those

presented in this thesis. For example, if a patient is HER2-negative but ER+, a different cocktail of contrast agents such as a FITC-conjugated antibody to estrogen and IRDye conjugated with 2-deoxyglucose, could be used to enhance visualization during surgery. This system has the potential to improve margin status in patients who do not receive intraoperative pathology by offering physicians an opportunity to visualize molecular expression through contrast agents.

This system is not designed to replace intraoperative pathology at centers like MDACC; it can be used as a supplement for the surgeon and pathologist when determining margin status intraoperatively. As mentioned in chapters 2 and 6, standard H&E does not provide information on the receptor status of tissue at the margins, which could lead to a recurrence in patients. If pathologists had a tool that allowed them to rapidly interrogate receptor status of tissue at the margin, they would be able to make a more informed decision on further re-excision. Providing physicians with additional information regarding receptor status could save a patient from undergoing additional surgeries and enhanced radiation. Again, the size and portability of this system becomes a factor in how this device would work in a pathology suite. If it were large, bulky, and used ionizing radiation, then it would be impractical inside the suite not be beneficial for the pathological team. There is minimal sample preparation, which could potentially interfere with the routine preparation. Finally, this system could even be used to pre-screen resected tissue for the pathological team by allowing the pathologist to focus on areas of the tissue that have enhanced contrast from a contrast agent, rather than processing the entire tissue during the surgery.

Optical contrast agents can provide valuable information about the molecular expression of tissues in a rapid manner. They allow for physicians to visualize cancerous tissue by providing enhanced contrast in areas of high expression. As research becomes more familiar with the application of these agents the benefit they provide to the physicians and patients will only increase.

References

[1] R. Siegel, D. Naishadham, and A. Jemal, "Cancer statistics, 2012.," *CA: a cancer journal for clinicians* **62**, 10–29 [doi:10.3322/caac.20138].

[2] R. G. Pleijhuis, M. Graafland, J. de Vries, J. Bart, J. S. de Jong, and G. M. van Dam, "Obtaining adequate surgical margins in breast-conserving therapy for patients with early-stage breast cancer: current modalities and future directions," *Ann Surg Oncol* **16**, 2009/07/18 ed., 2717–2730 (2009) [doi:10.1245/s10434-009-0609-z].

[3] L. Jacobs, "Positive margins: the challenge continues for breast surgeons," *Ann Surg Oncol* **15**, 2008/03/06 ed., 1271–1272 (2008) [doi:10.1245/s10434-007-9766-0].

[4] B. Fisher, S. Anderson, J. Bryant, R. G. Margolese, M. Deutsch, E. R. Fisher, J.-H. Jeong, and N. Wolmark, "Twenty-year follow-up of a randomized trial comparing total mastectomy, lumpectomy, and lumpectomy plus irradiation for the treatment of invasive breast cancer.," *The New England journal of medicine* **347**, 1233–1241 (2002) [doi:10.1056/NEJMoa022152].

[5] J. A. van Dongen, A. C. Voogd, I. S. Fentiman, C. Legrand, R. J. Sylvester, D. Tong, E. van der Schueren, P. A. Helle, K. van Zijl, et al., "Long-term results of a randomized trial comparing breast-conserving therapy with mastectomy: European Organization for Research and Treatment of Cancer 10801 trial.," *Journal of the National Cancer Institute* **92**, 1143–1150 (2000).

[6] M. Blichert-Toft, M. Nielsen, M. Düring, S. Møller, F. Rank, M. Overgaard, and H. T. Mouridsen, "Long-term results of breast conserving surgery vs. mastectomy for early stage invasive breast cancer: 20-year follow-up of the Danish randomized DBCG-82TM protocol.," *Acta oncologica (Stockholm, Sweden)* **47**, 672–681 (2008) [doi:10.1080/02841860801971439].

[7] L. S. Wilkinson, R. Given-Wilson, T. Hall, H. Potts, A. K. Sharma, and E. Smith, "Increasing the diagnosis of multifocal primary breast cancer by the use of bilateral whole-breast ultrasound.," *Clinical radiology* **60**, 573–578 (2005) [doi:10.1016/j.crad.2004.10.015].

[8] R. Jeevan, D. A. Cromwell, M. Trivella, G. Lawrence, O. Kearins, J. Pereira, C. Sheppard, C. M. Caddy, and J. H. P. van der Meulen, "Reoperation rates after breast conserving surgery for breast cancer among women in England: retrospective study of hospital episode statistics," *BMJ* **345**, e4505–e4505 (2012) [doi:10.1136/bmj.e4505].

[9] A. Munshi, S. Kakkar, R. Bhutani, R. Jalali, A. Budrukkar, and K. A. Dinshaw, "Factors influencing cosmetic outcome in breast conservation.," *Clinical oncology (Royal College of Radiologists (Great Britain))* **21**, 285–293 (2009) [doi:10.1016/j.clon.2009.02.001].

[10] O. Gentillini and J. Gahir, "An urgent need to reduce re-operation rates after breast conserving surgery," *Gland Surgery* **1**, 159–160 (2012) [doi:10.3978/j.issn.2227-684X.2012.10.03].

[11] E. R. Camp, P. F. McAuliffe, J. S. Gilroy, C. G. Morris, D. S. Lind, N. P. Mendenhall, and E. M. Copeland, "Minimizing local recurrence after breast conserving therapy using intraoperative shaved margins to determine pathologic tumor clearance.," *Journal of the American College of Surgeons* **201**, 855–861 (2005) [doi:10.1016/j.jamcollsurg.2005.06.274].

[12] O. Riedl, F. Fitzal, N. Mader, P. Dubsky, M. Rudas, M. Mittlboeck, M. Gnant, and R. Jakesz, "Intraoperative frozen section analysis for breast-conserving therapy in 1016 patients with breast cancer.," *European journal of surgical oncology : the journal of the European Society of Surgical Oncology and the British Association of Surgical Oncology* **35**, 264–270 (2009) [doi:10.1016/j.ejso.2008.05.007].

[13] S. Vosoughhosseini, M. Lotfi, A. Fakhrjou, A. Aghbali, M. Moradzadeh, M. Sina, and P. Emamverdizadeh, "Analysis of epidermal growth factor receptor in histopathologically tumor-free surgical margins in patients with oral squamous cell carcinoma," *African Journal of Biotechnology* **11**, 516–520 (2012) [doi:10.5897/AJB 10.489].

[14] S. Altintas, K. Lambein, M. T. Huizing, G. Braems, F. T. Asjoe, H. Hellemans, E. Van Marck, J. Weyler, M. Praet, et al., "Prognostic significance of oncogenic markers in ductal carcinoma in situ of the breast: a clinicopathologic study.," *The breast journal* **15**, 120–132 (2009) [doi:10.1111/j.1524-4741.2009.00686.x].

[15] A. Laurinavicius, A. Laurinaviciene, V. Ostapenko, D. Dasevicius, S. Jarmalaite, and J. Lazutka, "Immunohistochemistry profiles of breast ductal carcinoma: factor analysis of digital image analysis data.," *Diagnostic pathology* **7**, 27 (2012) [doi:10.1186/1746-1596-7-27].

[16] I. Vanden Bempt, P. Van Loo, M. Drijkoningen, P. Neven, A. Smeets, M.-R. Christiaens, R. Paridaens, and C. De Wolf-Peeters, "Polysomy 17 in breast cancer: clinicopathologic significance and impact on HER-2 testing.," *Journal of clinical oncology : official journal of the American Society of Clinical Oncology* **26**, 4869–4874 (2008) [doi:10.1200/JCO.2007.13.4296].

[17] S. Vranic, O. Tawfik, J. Palazzo, N. Bilalovic, E. Eyzaguirre, L. M. Lee, P. Adegboyega, J. Hagenkord, and Z. Gatalica, "EGFR and HER-2/neu expression in invasive apocrine carcinoma of the breast.," *Modern pathology : an official journal of the United States and Canadian Academy of Pathology, Inc* **23**, 644–653 (2010) [doi:10.1038/modpathol.2010.50].

[18] A. R. Miller, G. Brandao, T. J. Prihoda, C. Hill, A. B. Cruz, and I.-T. Yeh, "Positive margins following surgical resection of breast carcinoma: analysis of pathologic correlates.," *Journal of surgical oncology* **86**, 134–140 (2004) [doi:10.1002/jso.20059].

[19] J. F. Vermeulen, A. S. A. van Brussel, P. van der Groep, F. H. M. Morsink, P. Bult, E. van der Wall, and P. J. van Diest, "Immunophenotyping invasive breast cancer: paving the road for molecular imaging.," *BMC cancer* **12**, 240 (2012) [doi:10.1186/1471-2407-12-240].

[20] R. L. Wahl, R. L. Cody, G. D. Hutchins, and E. E. Mudgett, "Primary and metastatic breast carcinoma: initial clinical evaluation with PET with the radiolabeled glucose analogue 2-[F-18]-fluoro-2-deoxy-D-glucose," *Radiology* **179**, 765–770 (1991).

[21] R. Bos, J. J. M. van der Hoeven, E. van der Wall, P. van Der Groep, P. J. van Diest, E. F. I. Comans, U. Joshi, G. L. Semenza, O. S. Hoekstra, et al., "Biologic Correlates of 18Fluorodeoxyglucose Uptake in Human Breast Cancer Measured by Positron Emission Tomography," *J Clin Oncol* **20**, 379–387 (2002) [doi:10.1200/jco.20.2.379].

[22] H. Cai and F. Peng, "2-NBDG Fluorescence Imaging of Hypermetabolic Circulating Tumor Cells in Mouse Xenograft model of Breast Cancer.," *Journal of fluorescence* (2012) [doi:10.1007/s10895-012-1136-z].

[23] R. J. Langsner, L. P. Middleton, J. Sun, F. Meric-Bernstam, K. K. Hunt, R. A. Drezek, and T. K. Yu, "Wide-field imaging of fluorescent deoxy-glucose in ex vivo malignant and normal breast tissue," *Biomed Opt Express* **2**, 2011/06/24 ed., 1514–1523 (2011) [doi:10.1364/BOE.2.001514 145022 [pii]].

[24] J. Levi, Z. Cheng, O. Gheysens, M. Patel, C. T. Chan, Y. Wang, M. Namavari, and S. S. Gambhir, "Fluorescent fructose derivatives for imaging breast cancer cells.," *Bioconjugate chemistry* **18**, 628–634 (2007) [doi:10.1021/bc060184s].

[25] R. G. O'Neil, L. Wu, N. Mullani, and R. O'Neil, "Uptake of a Fluorescent Deoxyglucose Analog (2-NBDG) in Tumor Cells," *Molecular Imaging and Biology* **7**, 388–392, Springer New York (2005) [doi:10.1007/s11307-005-0011-6].

[26] K. Sano, M. Mitsunaga, T. Nakajima, P. L. Choyke, and H. Kobayashi, "In vivo breast cancer characterization imaging using two monoclonal antibodies activatably labeled with near infrared fluorophores.," *Breast cancer research : BCR* **14**, R61 (2012) [doi:10.1186/bcr3167].

[27] B.-W. Xie, I. M. Mol, S. Keereweer, E. R. van Beek, I. Que, T. J. A. Snoeks, A. Chan, E. L. Kaijzel, and C. W. G. M. Löwik, "Dual-wavelength imaging of tumor progression by activatable and targeting near-infrared fluorescent probes in a bioluminescent breast cancer model.," *PloS one* **7**, e31875 (2012) [doi:10.1371/journal.pone.0031875].

[28] R. Ankri, H. Duadi, M. Motiei, and D. Fixler, "In-vivo Tumor detection using diffusion reflection measurements of targeted gold nanorods - a quantitative study.," *Journal of biophotonics* **5**, 263–273 (2012) [doi:10.1002/jbio.201100120].

[29] C. DeSantis, R. Siegel, P. Bandi, and A. Jemal, "Breast cancer statistics, 2011.," *CA: a cancer journal for clinicians* **61**, 409–418 (2011) [doi:10.3322/caac.20134].

[30] S. C. Lester, "The Breast," in *Pathologic Basis of Disease*, 7th ed., V. Kumar, A. Abbas, and N. Fausto, Eds., pp. 1119–1154, Elsevier Inc., Philadelphia (2004).

[31] F. T. Nguyen, A. M. Zysk, E. J. Chaney, J. G. Kotynek, U. J. Oliphant, F. J. Bellafiore, K. M. Rowland, P. A. Johnson, and S. A. Boppart, "Intraoperative evaluation of breast tumor margins with optical coherence tomography.," *Cancer research* **69**, 8790–8796 (2009) [doi:10.1158/0008-5472.CAN-08-4340].

[32] J. Atkins, F. Al Mushawah, C. M. Appleton, A. E. Cyr, W. E. Gillanders, R. L. Aft, T. J. Eberlein, F. Gao, and J. A. Margenthaler, "Positive margin rates following breast-conserving surgery for stage I-III breast cancer: Palpable versus nonpalpable tumors.," *The Journal of surgical research* (2012) [doi:10.1016/j.jss.2012.03.045].

[33] M. Schelling, N. Avril, J. Nahrig, W. Kuhn, W. Romer, D. Sattler, M. Werner, J. Dose, F. Janicke, et al., "Positron Emission Tomography Using [18F]Fluorodeoxyglucose for Monitoring Primary Chemotherapy in Breast Cancer," *J Clin Oncol* **18**, 1689–1695 (2000).

[34] N. Avril, M. Menzel, M. Schelling, W. Weber, F. Ja, W. Nathrath, and M. Schwaiger, "Glucose Metabolism of Breast Cancer Assessed by 18 F-FDG PET : Histologic and Immunohistochemical Tissue Analysis," *Journal of Nuclear Medicine*, 9–16 (2001).

[35] D. Groheux, S. Giacchetti, J.-L. Moretti, R. Porcher, M. Espié, J. Lehmann-Che, A. de Roquancourt, A.-S. Hamy, C. Cuvier, et al., "Correlation of high 18F-FDG uptake to clinical, pathological and biological prognostic factors in breast cancer.," *European journal of nuclear medicine and molecular imaging* **38**, 426–435 (2011) [doi:10.1007/s00259-010-1640-9].

[36] A. Chung, D. Liou, S. Karlan, A. Waxman, K. Fujimoto, M. Hagiike, and E. H. Phillips, "Preoperative FDG-PET for axillary metastases in patients with breast cancer.," *Archives of surgery (Chicago, Ill. : 1960)* **141**, 783–8; discussion 788–9 (2006) [doi:10.1001/archsurg.141.8.783].

[37] N. Avril, C. a Rosé, M. Schelling, J. Dose, W. Kuhn, S. Bense, W. Weber, S. Ziegler, H. Graeff, et al., "Breast imaging with positron emission tomography and fluorine-18 fluorodeoxyglucose: use and limitations.," *Journal of clinical oncology : official journal of the American Society of Clinical Oncology* **18**, 3495–3502 (2000).

[38] H. S. Lim, W. Yoon, T. W. Chung, J. K. Kim, J. G. Park, H. K. Kang, H. S. Bom, and J. H. Yoon, "FDG PET/CT for the detection and evaluation of breast diseases: usefulness and limitations.," *Radiographics : a review publication of the Radiological Society of North America, Inc* **27 Suppl 1**, S197–213 (2007) [doi:10.1148/rg.27si075507].

[39] G. M. K. Tse, P. C. W. Lui, J. S. L. Vong, K.-M. Lau, T. C. Putti, R. Karim, R. A. Scolyer, C.-S. Lee, A. M. C. Yu, et al., "Increased epidermal growth factor receptor (EGFR) expression in malignant mammary phyllodes tumors.," *Breast cancer research and treatment* **114**, 441–448 (2009) [doi:10.1007/s10549-008-0030-5].

[40] A. J. Lowery, M. R. Kell, R. W. Glynn, M. J. Kerin, and K. J. Sweeney, "Locoregional recurrence after breast cancer surgery: a systematic review by receptor phenotype.," *Breast cancer research and treatment* (2011) [doi:10.1007/s10549-011-1891-6].

[41] R. M. Tamimi, H. J. Baer, J. Marotti, M. Galan, L. Galaburda, Y. Fu, A. C. Deitz, J. L. Connolly, S. J. Schnitt, et al., "Comparison of molecular phenotypes of ductal carcinoma in situ and invasive breast cancer.," *Breast cancer research : BCR* **10**, R67 (2008) [doi:10.1186/bcr2128].

[42] W. Shao and M. Brown, "Advances in estrogen receptor biology: prospects for improvements in targeted breast cancer therapy.," *Breast cancer research : BCR* **6**, 39–52 (2004) [doi:10.1186/bcr742].

[43] S. R. D. Johnston and M. Dowsett, "Aromatase inhibitors for breast cancer: lessons from the laboratory.," *Nature reviews. Cancer* **3**, 821–831 (2003) [doi:10.1038/nrc1211].

[44] L. Rodríguez Lajusticia, M. Martín Jiménez, and S. López-Tarruella Cobo, "Endocrine therapy of metastatic breast cancer.," *Clinical & translational oncology : official publication of the Federation of Spanish Oncology Societies and of the National Cancer Institute of Mexico* **10**, 462–467 (2008).

[45] S.-Y. Wang, T. Shamliyan, B. A. Virnig, and R. Kane, "Tumor characteristics as predictors of local recurrence after treatment of ductal carcinoma in situ: a meta-analysis.," *Breast cancer research and treatment* **127**, 1–14 (2011) [doi:10.1007/s10549-011-1387-4].

[46] M. J. Duffy, P. M. McGowan, and J. Crown, "Targeted therapy for triple-negative breast cancer: where are we?," *International journal of cancer. Journal international du cancer* (2012) [doi:10.1002/ijc.27632].

[47] M. Kaufmann, G. N. Hortobagyi, A. Goldhirsch, S. Scholl, A. Makris, P. Valagussa, J.-U. Blohmer, W. Eiermann, R. Jackesz, et al., "Recommendations from an international expert panel on the use of neoadjuvant (primary) systemic treatment of operable breast cancer: an update.," *Journal of clinical oncology : official journal of the American Society of Clinical Oncology* **24**, 1940–1949 (2006) [doi:10.1200/JCO.2005.02.6187].

[48] J. A. Margenthaler, "Optimizing conservative breast surgery.," *Journal of surgical oncology* **103**, 306–312 (2011) [doi:10.1002/jso.21700].

[49] J. H. Lee and A. Nan, "Combination drug delivery approaches in metastatic breast cancer.," *Journal of drug delivery* **2012**, 915375 (2012) [doi:10.1155/2012/915375].

[50] J. Jassem, T. Pieńkowski, A. Płuzańska, S. Jelic, V. Gorbunova, Z. Mrsic-Krmpotic, J. Berzins, T. Nagykalnai, N. Wigler, et al., "Doxorubicin and paclitaxel versus fluorouracil, doxorubicin, and

cyclophosphamide as first-line therapy for women with metastatic breast cancer: final results of a randomized phase III multicenter trial.," *Journal of clinical oncology : official journal of the American Society of Clinical Oncology* **19**, 1707–1715 (2001).

[51] L. Livi, I. Meattini, C. D. L. Cardillo, M. Mangoni, D. Greto, A. Petrucci, A. Rampini, A. Bruni, A. Galardi, et al., "Non-pegylated liposomal doxorubicin in combination with cyclophosphamide or docetaxel as first-line therapy in metastatic breast cancer: a retrospective analysis.," *Tumori* **95**, 422–426 (2009).

[52] E. Bria, D. Giannarelli, A. Felici, W. P. Peters, C. Nisticò, B. Vanni, F. Cuppone, F. Cognetti, and E. Terzoli, "Taxanes with anthracyclines as first-line chemotherapy for metastatic breast carcinoma.," *Cancer* **103**, 672–679 (2005) [doi:10.1002/cncr.20757].

[53] M. A. Cobleigh, V. K. Langmuir, G. W. Sledge, K. D. Miller, L. Haney, W. F. Novotny, J. D. Reimann, and A. Vassel, "A phase I/II dose-escalation trial of bevacizumab in previously treated metastatic breast cancer.," *Seminars in oncology* **30**, 117–124 (2003).

[54] J. Baselga, J. M. Trigo, J. Bourhis, J. Tortochaux, H. Cortés-Funes, R. Hitt, P. Gascón, N. Amellal, A. Harstrick, et al., "Phase II multicenter study of the antiepidermal growth factor receptor monoclonal antibody cetuximab in combination with platinum-based chemotherapy in patients with platinum-refractory metastatic and/or recurrent squamous cell carcinoma of the head and n," *Journal of clinical oncology : official journal of the American Society of Clinical Oncology* **23**, 5568–5577 (2005) [doi:10.1200/JCO.2005.07.119].

[55] D. Cameron, M. Casey, C. Oliva, B. Newstat, B. Imwalle, and C. E. Geyer, "Lapatinib plus capecitabine in women with HER-2-positive advanced breast cancer: final survival analysis of a phase III randomized trial.," *The oncologist* **15**, 924–934 (2010) [doi:10.1634/theoncologist.2009-0181].

[56] M. Clarke, R. Collins, S. Darby, C. Davies, P. Elphinstone, E. Evans, J. Godwin, R. Gray, C. Hicks, et al., "Effects of radiotherapy and of differences in the extent of surgery for early breast cancer on local recurrence and 15-year survival: an overview of the randomised trials," *Lancet* **366**, 2005/12/20 ed., 2087–2106 (2005) [doi:S0140-6736(05)67887-7 [pii] 10.1016/S0140-6736(05)67887-7].

[57] V. Vinh-Hung and C. Verschraegen, "Breast-conserving surgery with or without radiotherapy: pooled-analysis for risks of ipsilateral breast tumor recurrence and mortality.," *Journal of the National Cancer Institute* **96**, 115–121 (2004).

[58] D. W. Arthur, K. Winter, R. R. Kuske, J. Bolton, R. Rabinovitch, J. White, W. F. Hanson, R. M. Wilenzick, and B. McCormick, "A Phase II trial of brachytherapy alone after lumpectomy for select breast cancer: tumor control and survival outcomes of RTOG 95-17.," *International journal of radiation oncology, biology, physics* **72**, 467–473 (2008) [doi:10.1016/j.ijrobp.2007.12.056].

[59] A. J. Stewart, D. A. O'Farrell, R. A. Cormack, J. L. Hansen, A. J. Khan, S. Mutyala, and P. M. Devlin, "Dose volume histogram analysis of normal structures associated with accelerated partial breast irradiation delivered by high dose rate brachytherapy and comparison with whole breast external beam radiotherapy fields.," *Radiation oncology (London, England)* **3**, 39 (2008) [doi:10.1186/1748-717X-3-39].

[60] L. J. Lee and J. R. Harris, "Innovations in radiation therapy (RT) for breast cancer.," *Breast (Edinburgh, Scotland)* **18 Suppl 3**, S103–11 (2009) [doi:10.1016/S0960-9776(09)70284-X].

[61] F. A. Vicini, V. Remouchamps, M. Wallace, M. Sharpe, J. Fayad, L. Tyburski, N. Letts, L. Kestin, G. Edmundson, et al., "Ongoing clinical experience utilizing 3D conformal external beam radiotherapy to deliver partial-breast irradiation in patients with early-stage breast cancer treated

with breast-conserving therapy.," *International journal of radiation oncology, biology, physics* **57**, 1247–1253 (2003).

[62] J. Yu, F. Al Mushawah, M. E. Taylor, A. E. Cyr, W. E. Gillanders, R. L. Aft, T. J. Eberlein, F. Gao, and J. A. Margenthaler, "Compromised margins following mastectomy for stage I-III invasive breast cancer.," *The Journal of surgical research* (2012) [doi:10.1016/j.jss.2012.03.046].

[63] K. P. McGuire, A. A. Santillan, P. Kaur, T. Meade, J. Parbhoo, M. Mathias, C. Shamehdi, M. Davis, D. Ramos, et al., "Are mastectomies on the rise? A 13-year trend analysis of the selection of mastectomy versus breast conservation therapy in 5865 patients," *Ann Surg Oncol* **16**, 2009/08/05 ed., 2682–2690 (2009) [doi:10.1245/s10434-009-0635-x].

[64] R. A. Audisio and L. S. Chagla, "Oncoplastic fellowship: can we do better?," *Breast (Edinburgh, Scotland)* **16**, 11–12 (2007) [doi:10.1016/j.breast.2006.07.001].

[65] K. B. Clough, G. J. Kaufman, C. Nos, I. Buccimazza, and I. M. Sarfati, "Improving breast cancer surgery: a classification and quadrant per quadrant atlas for oncoplastic surgery.," *Annals of surgical oncology* **17**, 1375–1391 (2010) [doi:10.1245/s10434-009-0792-y].

[66] J. B. Osborn, G. L. Keeney, J. W. Jakub, A. C. Degnim, and J. C. Boughey, "Cost-effectiveness analysis of routine frozen-section analysis of breast margins compared with reoperation for positive margins.," *Annals of surgical oncology* **18**, 3204–3209 (2011) [doi:10.1245/s10434-011-1956-0].

[67] U. Veronesi, N. Cascinelli, L. Mariani, M. Greco, R. Saccozzi, A. Luini, M. Aguilar, and E. Marubini, "Twenty-year follow-up of a randomized study comparing breast-conserving surgery with radical mastectomy for early breast cancer.," *The New England journal of medicine* **347**, 1227–1232 (2002) [doi:10.1056/NEJMoa020989].

[68] U. Mahmood, C. Morris, G. Neuner, M. Koshy, S. Kesmodel, R. Buras, S. Chumsri, T. Bao, K. Tkaczuk, et al., "Similar Survival with Breast Conservation Therapy or Mastectomy in the Management of Young Women with Early-Stage Breast Cancer," *International Journal of Radiation Oncology*Biology*Physics* (2012) [doi:10.1016/j.ijrobp.2011.10.075].

[69] R. C. Miles, R. E. Gullerud, C. M. Lohse, J. W. Jakub, A. C. Degnim, and J. C. Boughey, "Local recurrence after breast-conserving surgery: multivariable analysis of risk factors and the impact of young age.," *Annals of surgical oncology* **19**, 1153–1159 (2012) [doi:10.1245/s10434-011-2084-6].

[70] B. M. Beadle, W. A. Woodward, S. L. Tucker, E. D. Outlaw, P. K. Allen, J. L. Oh, E. A. Strom, G. H. Perkins, W. Tereffe, et al., "Ten-year recurrence rates in young women with breast cancer by locoregional treatment approach.," *International journal of radiation oncology, biology, physics* **73**, 734–744 (2009) [doi:10.1016/j.ijrobp.2008.04.078].

[71] N. Cabioglu, K. K. Hunt, A. A. Sahin, H. M. Kuerer, G. V Babiera, S. E. Singletary, G. J. Whitman, M. I. Ross, F. C. Ames, et al., "Role for intraoperative margin assessment in patients undergoing breast-conserving surgery," *Ann Surg Oncol* **14**, 2007/01/30 ed., 1458–1471 (2007) [doi:10.1245/s10434-006-9236-0].

[72] E. Tanis, C. J. H. van de Velde, H. Bartelink, M. J. van de Vijver, H. Putter, and J. A. van der Hage, "Locoregional recurrence after breast-conserving therapy remains an independent prognostic factor even after an event free interval of 10years in early stage breast cancer.," *European journal of cancer (Oxford, England : 1990)* (2012) [doi:10.1016/j.ejca.2012.02.051].

[73] J. A. Guidroz, G. Larrieux, J. Liao, S. L. Sugg, C. E. H. Scott-Conner, and R. J. Weigel, "Sampling of secondary margins decreases the need for re-excision after partial mastectomy.," *Surgery* **150**, 802–809 (2011) [doi:10.1016/j.surg.2011.07.064].

[74] A. Mannell, "Breast-conserving therapy in breast cancer patients--a 12-year experience.," *South African journal of surgery. Suid-Afrikaanse tydskrif vir chirurgie* **43**, 28–30; discussion 30, 32 (2005).

[75] H.-C. Yang, L. M. Thornton, C. L. Shapiro, and B. L. Andersen, "Surviving recurrence: psychological and quality-of-life recovery.," *Cancer* **112**, 1178–1187 (2008) [doi:10.1002/cncr.23272].

[76] B. Kreike, A. A. M. Hart, T. van de Velde, J. Borger, H. Peterse, E. Rutgers, H. Bartelink, and M. J. van de Vijver, "Continuing risk of ipsilateral breast relapse after breast-conserving therapy at long-term follow-up.," *International journal of radiation oncology, biology, physics* **71**, 1014–1021 (2008) [doi:10.1016/j.ijrobp.2007.11.029].

[77] A. C. Voogd, F. J. van Oost, E. J. T. Rutgers, P. H. M. Elkhuizen, A. N. van Geel, L. J. E. E. Scheijmans, M. J. C. van der Sangen, G. Botke, C. J. Hoekstra, et al., "Long-term prognosis of patients with local recurrence after conservative surgery and radiotherapy for early breast cancer.," *European journal of cancer (Oxford, England : 1990)* **41**, 2637–2644 (2005) [doi:10.1016/j.ejca.2005.04.040].

[78] E. Yildirim, "Locoregional recurrence in breast carcinoma patients.," *European journal of surgical oncology : the journal of the European Society of Surgical Oncology and the British Association of Surgical Oncology* **35**, 258–263 (2009) [doi:10.1016/j.ejso.2008.06.010].

[79] Y. Komoike, F. Akiyama, Y. Iino, T. Ikeda, S. Akashi-Tanaka, S. Ohsumi, M. Kusama, M. Sano, E. Shin, et al., "Ipsilateral breast tumor recurrence (IBTR) after breast-conserving treatment for early breast cancer: risk factors and impact on distant metastases.," *Cancer* **106**, 35–41 (2006) [doi:10.1002/cncr.21551].

[80] M. K. Nottage, K. A. Kopciuk, A. Tzontcheva, I. L. Andrulis, S. B. Bull, and M. E. Blackstein, "Analysis of incidence and prognostic factors for ipsilateral breast tumour recurrence and its impact on disease-specific survival of women with node-negative breast cancer: a prospective cohort study.," *Breast cancer research : BCR* **8**, R44 (2006) [doi:10.1186/bcr1531].

[81] G. A. Cèfaro, D. Genovesi, R. Marchese, L. A. Ursini, E. Cianchetti, E. Ballone, and M. Di Nicola, "Predictors of local recurrence after conservative surgery and whole-breast irradiation.," *Breast cancer research and treatment* **98**, 329–335 (2006) [doi:10.1007/s10549-006-9169-0].

[82] C. Vargas, L. Kestin, N. Go, D. Krauss, P. Chen, N. Goldstein, A. Martinez, and F. A. Vicini, "Factors associated with local recurrence and cause-specific survival in patients with ductal carcinoma in situ of the breast treated with breast-conserving therapy or mastectomy.," *International journal of radiation oncology, biology, physics* **63**, 1514–1521 (2005) [doi:10.1016/j.ijrobp.2005.04.045].

[83] D. Aziz, E. Rawlinson, S. A. Narod, P. Sun, H. L. A. Lickley, D. R. McCready, and C. M. B. Holloway, "The role of reexcision for positive margins in optimizing local disease control after breast-conserving surgery for cancer.," *The breast journal* **12**, 331–337 (2006) [doi:10.1111/j.1075-122X.2006.00271.x].

[84] K. Gülben, U. Berberoğlu, A. Cengiz, and H. Altinyollar, "Prognostic factors affecting locoregional recurrence in patients with stage IIIB noninflammatory breast cancer.," *World journal of surgery* **31**, 1724–1730, Springer New York (2007) [doi:10.1007/s00268-007-9139-7].

[85] T. Karni, I. Pappo, J. Sandbank, O. Lavon, V. Kent, R. Spector, S. Morgenstern, and S. Lelcuk, "A device for real-time, intraoperative margin assessment in breast-conservation surgery," *Am J Surg* **194**, 2007/09/11 ed., 467–473 (2007) [doi:S0002-9610(07)00530-2 [pii] 10.1016/j.amjsurg.2007.06.013].

[86] A. N. Ali, N. Vapiwala, M. Guo, W. T. Hwang, E. E. Harris, and L. J. Solin, "The impact of re-excision and residual disease on local recurrence after breast conservation treatment for patients with early stage breast cancer," *Clin Breast Cancer* **11**, 2011/10/14 ed., 400–405 (2011) [doi:S1526-8209(11)00160-1 [pii] 10.1016/j.clbc.2011.08.003].

[87] N. Houssami, P. Macaskill, M. L. Marinovich, J. M. Dixon, L. Irwig, M. E. Brennan, and L. J. Solin, "Meta-analysis of the impact of surgical margins on local recurrence in women with early-stage invasive breast cancer treated with breast-conserving therapy.," *European journal of cancer (Oxford, England : 1990)* **46**, 3219–3232 (2010) [doi:10.1016/j.ejca.2010.07.043].

[88] G. F. Schwartz, U. Veronesi, K. B. Clough, J. M. Dixon, I. S. Fentiman, S. H. Heywang-Köbrunner, R. Holland, K. S. Hughes, R. E. Mansel, et al., "Consensus conference on breast conservation.," *Journal of the American College of Surgeons* **203**, 198–207 (2006) [doi:10.1016/j.jamcollsurg.2006.04.009].

[89] S. E. Singletary, "Surgical margins in patients with early-stage breast cancer treated with breast conservation therapy," *The American Journal of Surgery* **184**, 383–393 (2002).

[90] R. W. Carlson, D. C. Allred, B. O. Anderson, H. J. Burstein, W. B. Carter, S. B. Edge, J. K. Erban, W. B. Farrar, L. J. Goldstein, et al., "Breast cancer. Clinical practice guidelines in oncology.," *Journal of the National Comprehensive Cancer Network : JNCCN* **7**, 122–192 (2009).

[91] G. Zavagno, E. Goldin, R. Mencarelli, G. Capitanio, P. Del Bianco, R. Marconato, S. Mocellin, G. Marconato, V. Belardinelli, et al., "Role of resection margins in patients treated with breast conservation surgery.," *Cancer* **112**, 1923–1931 (2008) [doi:10.1002/cncr.23383].

[92] S. MacDonald and A. G. Taghian, "Prognostic factors for local control after breast conservation: does margin status still matter?," *Journal of clinical oncology : official journal of the American Society of Clinical Oncology* **27**, 4929–4930 (2009) [doi:10.1200/JCO.2009.23.6679].

[93] A. Luini, J. Rososchansky, G. Gatti, S. Zurrida, P. Caldarella, G. Viale, G. Rosali dos Santos, and A. Frasson, "The surgical margin status after breast-conserving surgery: discussion of an open issue.," *Breast cancer research and treatment* **113**, 397–402 (2009) [doi:10.1007/s10549-008-9929-0].

[94] M. Kaufmann, M. Morrow, G. von Minckwitz, and J. R. Harris, "Locoregional treatment of primary breast cancer: consensus recommendations from an International Expert Panel.," *Cancer* **116**, 1184–1191 (2010) [doi:10.1002/cncr.24874].

[95] "Surgical Margins – How Surgical Margins Affect Treatment Decisions," <http://breastcancer.about.com/od/diagnosis/tp/surgical_margins.htm> (3 June 2012).

[96] J. H. Rowland, K. A. Desmond, B. E. Meyerowitz, T. R. Belin, G. E. Wyatt, and P. A. Ganz, "Role of breast reconstructive surgery in physical and emotional outcomes among breast cancer survivors.," *Journal of the National Cancer Institute* **92**, 1422–1429 (2000).

[97] S. K. Al-Ghazal, L. Fallowfield, and R. W. Blamey, "Comparison of psychological aspects and patient satisfaction following breast conserving surgery, simple mastectomy and breast reconstruction.," *European journal of cancer (Oxford, England : 1990)* **36**, 1938–1943 (2000).

[98] A. Chakravorty, A. K. Shrestha, N. Sanmugalingam, F. Rapisarda, N. Roche, G. Querci Della Rovere, and F. A. Macneill, "How safe is oncoplastic breast conservation? Comparative analysis with standard breast conserving surgery.," *European journal of surgical oncology : the journal of the European Society of Surgical Oncology and the British Association of Surgical Oncology* **38**, 395–398 (2012) [doi:10.1016/j.ejso.2012.02.186].

[99] I. S. Fentiman, "Marginal effect in breast-conserving surgery.," *International journal of clinical practice* **65**, 519–520 (2011) [doi:10.1111/j.1742-1241.2011.02608.x].

[100] K. R. Cho, B. K. Seo, C. H. Kim, K. W. Whang, Y. H. Kim, B. H. Kim, O. H. Woo, Y. H. Lee, and K. B. Chung, "Non-calcified ductal carcinoma in situ: ultrasound and mammographic findings correlated with histological findings.," *Yonsei medical journal* **49**, 103–110 (2008) [doi:10.3349/ymj.2008.49.1.103].

[101] G. H. Rauscher, T. P. Johnson, Y. I. Cho, and J. A. Walk, "Accuracy of self-reported cancer-screening histories: a meta-analysis.," *Cancer epidemiology, biomarkers & prevention : a publication of the American Association for Cancer Research, cosponsored by the American Society of Preventive Oncology* **17**, 748–757 (2008) [doi:10.1158/1055-9965.EPI-07-2629].

[102] D. M. Ikeda, R. L. Birdwell, K. F. O'Shaughnessy, R. J. Brenner, and E. A. Sickles, "Analysis of 172 subtle findings on prior normal mammograms in women with breast cancer detected at follow-up screening.," *Radiology* **226**, 494–503 (2003).

[103] M. Van Goethem, K. Schelfout, E. Kersschot, C. Colpaert, I. Verslegers, I. Biltjes, W. A. Tjalma, A. De Schepper, J. Weyler, et al., "MR mammography is useful in the preoperative locoregional staging of breast carcinomas with extensive intraductal component.," *European journal of radiology* **62**, 273–282 (2007) [doi:10.1016/j.ejrad.2006.12.004].

[104] C. K. Kuhl, S. Schrading, H. B. Bieling, E. Wardelmann, C. C. Leutner, R. Koenig, W. Kuhn, and H. H. Schild, "MRI for diagnosis of pure ductal carcinoma in situ: a prospective observational study.," *Lancet* **370**, 485–492 (2007) [doi:10.1016/S0140-6736(07)61232-X].

[105] N. Houssami, S. Ciatto, P. Macaskill, S. J. Lord, R. M. Warren, J. M. Dixon, and L. Irwig, "Accuracy and surgical impact of magnetic resonance imaging in breast cancer staging: systematic review and meta-analysis in detection of multifocal and multicentric cancer.," *Journal of clinical oncology : official journal of the American Society of Clinical Oncology* **26**, 3248–3258 (2008) [doi:10.1200/JCO.2007.15.2108].

[106] L. J. Solin, S. G. Orel, W.-T. Hwang, E. E. Harris, and M. D. Schnall, "Relationship of breast magnetic resonance imaging to outcome after breast-conservation treatment with radiation for women with early-stage invasive breast carcinoma or ductal carcinoma in situ.," *Journal of clinical oncology : official journal of the American Society of Clinical Oncology* **26**, 386–391 (2008) [doi:10.1200/JCO.2006.09.5448].

[107] K. E. Pengel, C. E. Loo, H. J. Teertstra, S. H. Muller, J. Wesseling, J. L. Peterse, H. Bartelink, E. J. Rutgers, and K. G. A. Gilhuijs, "The impact of preoperative MRI on breast-conserving surgery of invasive cancer: a comparative cohort study.," *Breast cancer research and treatment* **116**, 161–169 (2009) [doi:10.1007/s10549-008-0182-3].

[108] M. Morrow and G. Freedman, "A clinical oncology perspective on the use of breast MR.," *Magnetic resonance imaging clinics of North America* **14**, 363–78, vi (2006) [doi:10.1016/j.mric.2006.07.006].

[109] P. Kelly and E. H. Winslow, "Needle wire localization for nonpalpable breast lesions: sensations, anxiety levels, and informational needs.," *Oncology nursing forum* **23**, 639–645 (1996).

[110] C. R. Thind, S. Desmond, O. Harris, R. Nadeem, L. S. Chagla, and R. A. Audisio, "Radio-guided localization of clinically occult breast lesions (ROLL): a DGH experience.," *Clinical radiology* **60**, 681–686 (2005) [doi:10.1016/j.crad.2004.12.004].

[111] H. C. Burkholder, L. E. Witherspoon, R. P. Burns, J. S. Horn, and M. D. Biderman, "Breast surgery techniques: preoperative bracketing wire localization by surgeons.," *The American surgeon* **73**, 574–8; discussion 578–9 (2007).

[112] H. Medina-Franco, L. Abarca-Pérez, M. N. García-Alvarez, J. L. Ulloa-Gómez, C. Romero-Trejo, and J. Sepúlveda-Méndez, "Radioguided occult lesion localization (ROLL) versus wire-guided lumpectomy for non-palpable breast lesions: a randomized prospective evaluation.," *Journal of surgical oncology* **97**, 108–111 (2008) [doi:10.1002/jso.20880].

[113] I. C. Bennett, J. Greenslade, and H. Chiam, "Intraoperative ultrasound-guided excision of nonpalpable breast lesions.," *World journal of surgery* **29**, 369–374 (2005) [doi:10.1007/s00268-004-7554-6].

[114] C. Ngô, A. G. Pollet, J. Laperrelle, G. Ackerman, S. Gomme, F. Thibault, V. Fourchotte, and R. J. Salmon, "Intraoperative ultrasound localization of nonpalpable breast cancers.," *Annals of surgical oncology* **14**, 2485–2489 (2007) [doi:10.1245/s10434-007-9420-x].

[115] F. D. Rahusen, A. J. A. Bremers, H. F. J. Fabry, A. H. M. T. van Amerongen, R. P. A. Boom, and S. Meijer, "Ultrasound-guided lumpectomy of nonpalpable breast cancer versus wire-guided resection: a randomized clinical trial.," *Annals of surgical oncology* **9**, 994–998 (2002).

[116] M. M. Moore, L. A. Whitney, L. Cerilli, J. Z. Imbrie, M. Bunch, V. B. Simpson, and J. B. Hanks, "Intraoperative ultrasound is associated with clear lumpectomy margins for palpable infiltrating ductal breast cancer.," *Annals of surgery* **233**, 761–768 (2001).

[117] P. T. Huynh, A. M. Jarolimek, and S. Daye, "The false-negative mammogram.," *Radiographics : a review publication of the Radiological Society of North America, Inc* **18**, 1137–54; quiz 1243–4 (1998).

[118] L. Tafra, R. Fine, P. Whitworth, M. Berry, J. Woods, G. Ekbom, J. Gass, P. Beitsch, D. Dodge, et al., "Prospective randomized study comparing cryo-assisted and needle-wire localization of ultrasound-visible breast tumors.," *American journal of surgery* **192**, 462–470 (2006) [doi:10.1016/j.amjsurg.2006.06.012].

[119] J. E. Rusby, N. Paramanathan, S. A. M. Laws, and R. M. Rainsbury, "Immediate latissimus dorsi miniflap volume replacement for partial mastectomy: use of intra-operative frozen sections to confirm negative margins.," *American journal of surgery* **196**, 512–518 (2008) [doi:10.1016/j.amjsurg.2008.06.026].

[120] T. P. Olson, J. Harter, A. Muñoz, D. M. Mahvi, and T. Breslin, "Frozen section analysis for intraoperative margin assessment during breast-conserving surgery results in low rates of re-excision and local recurrence.," *Annals of surgical oncology* **14**, 2953–2960 (2007) [doi:10.1245/s10434-007-9437-1].

[121] J. C. Cendán, D. Coco, and E. M. Copeland, "Accuracy of intraoperative frozen-section analysis of breast cancer lumpectomy-bed margins.," *Journal of the American College of Surgeons* **201**, 194–198 (2005) [doi:10.1016/j.jamcollsurg.2005.03.014].

[122] A. J. Creager, J. A. Shaw, P. R. Young, and K. R. Geisinger, "Intraoperative evaluation of lumpectomy margins by imprint cytology with histologic correlation: a community hospital experience.," *Archives of pathology & laboratory medicine* **126**, 846–848 (2002) [doi:10.1043/0003-9985(2002)126<0846:IEOLMB>2.0.CO;2].

[123] M. Bakhshandeh, S. O. Tutuncuoglu, G. Fischer, and S. Masood, "Use of imprint cytology for assessment of surgical margins in lumpectomy specimens of breast cancer patients.," *Diagnostic*

cytopathology **35**, 656–659, Wiley Subscription Services, Inc., A Wiley Company (2007) [doi:10.1002/dc.20704].

[124] E. K. Valdes, S. K. Boolbol, J.-M. Cohen, and S. M. Feldman, "Intra-operative touch preparation cytology; does it have a role in re-excision lumpectomy?," *Annals of surgical oncology* **14**, 1045–1050 (2007) [doi:10.1245/s10434-006-9263-x].

[125] F. D'Halluin, P. Tas, S. Rouquette, C. Bendavid, F. Foucher, H. Meshba, J. Blanchot, O. Coué, and J. Levêque, "Intra-operative touch preparation cytology following lumpectomy for breast cancer: a series of 400 procedures.," *Breast (Edinburgh, Scotland)* **18**, 248–253 (2009) [doi:10.1016/j.breast.2009.05.002].

[126] E. Weinberg, C. Cox, E. Dupont, L. White, M. Ebert, H. Greenberg, N. Diaz, V. Vercel, B. Centeno, et al., "Local recurrence in lumpectomy patients after imprint cytology margin evaluation.," *American journal of surgery* **188**, 349–354 (2004) [doi:10.1016/j.amjsurg.2004.06.024].

[127] T. M. Bydlon, S. A. Kennedy, L. M. Richards, J. Q. Brown, B. Yu, M. K. Junker, J. Gallagher, J. Geradts, L. G. Wilke, et al., "Performance metrics of an optical spectral imaging system for intra-operative assessment of breast tumor margins.," *Optics express* **18**, 8058–8076 (2010).

[128] L. R. Bickford, R. J. Langsner, J. Chang, L. C. Kennedy, G. D. Agollah, and R. Drezek, "Rapid Stereomicroscopic Imaging of HER2 Overexpression in Ex Vivo Breast Tissue Using Topically Applied Silica-Based Gold Nanoshells," *Journal of Oncology* **2012**, 1–10 (2012) [doi:10.1155/2012/291898].

[129] L. R. Bickford, G. Agollah, R. Drezek, and T.-K. K. Yu, "Silica-gold nanoshells as potential intraoperative molecular probes for HER2-overexpression in ex vivo breast tissue using near-infrared reflectance confocal microscopy," *Breast Cancer Research and Treatment* **120**, 2009/05/07 ed., 1–9, Springer Netherlands (2010) [doi:10.1007/s10549-009-0408-z].

[130] T. M. Allweis, Z. Kaufman, S. Lelcuk, I. Pappo, T. Karni, S. Schneebaum, R. Spector, A. Schindel, D. Hershko, et al., "A prospective, randomized, controlled, multicenter study of a real-time, intraoperative probe for positive margin detection in breast-conserving surgery.," *American journal of surgery* **196**, 483–489 (2008) [doi:10.1016/j.amjsurg.2008.06.024].

[131] F. Pons, J. Duch, and D. Fuster, "Breast cancer therapy: the role of PET-CT in decision making," *Q J Nucl Med Mol Imaging* **53**, 2009/03/19 ed., 210–223 (2009).

[132] A. Kumar, R. Kumar, V. Seenu, S. D. Gupta, M. Chawla, A. Malhotra, and S. N. Mehta, "The role of 18F-FDG PET/CT in evaluation of early response to neoadjuvant chemotherapy in patients with locally advanced breast cancer," *Eur Radiol* **19**, 2009/02/14 ed., 1347–1357 (2009) [doi:10.1007/s00330-009-1303-z].

[133] R. Minamimoto, M. Senda, K. Uno, S. Jinnouchi, T. Iinuma, K. Ito, C. Okuyama, K. Oguchi, M. Kawamoto, et al., "Performance profile of FDG-PET and PET/CT for cancer screening on the basis of a Japanese Nationwide Survey," *Ann Nucl Med* **21**, 2007/11/22 ed., 481–498 (2007) [doi:10.1007/s12149-007-0061-8].

[134] H. Kaida, M. Ishibashi, T. Fuji, S. Kurata, M. Uchida, K. Baba, T. Miyagawa, H. Kaibara, S. Kawamura, et al., "Improved breast cancer detection of prone breast fluorodeoxyglucose-PET in 118 patients.," *Nuclear medicine communications* **29**, 885–893 (2008) [doi:10.1097/MNM.0b013e32830439d9].

[135] S. A. Gulec, F. Daghighian, and R. Essner, "PET-Probe: Evaluation of Technical Performance and Clinical Utility of a Handheld High-Energy Gamma Probe in Oncologic Surgery.," *Annals of surgical oncology* (2006) [doi:10.1245/ASO.2006.05.047].

[136] V. E. Strong, J. Humm, P. Russo, A. Jungbluth, W. D. Wong, F. Daghighian, L. Old, Y. Fong, and S. M. Larson, "A novel method to localize antibody-targeted cancer deposits intraoperatively using handheld PET beta and gamma probes.," *Surgical endoscopy* **22**, 386–391 (2008) [doi:10.1007/s00464-007-9611-3].

[137] D. E. Cohn, N. C. Hall, S. P. Povoski, L. G. Seamon, W. B. Farrar, and E. W. Martin, "Novel perioperative imaging with 18F-FDG PET/CT and intraoperative 18F-FDG detection using a handheld gamma probe in recurrent ovarian cancer.," *Gynecologic oncology* **110**, 152–157 (2008) [doi:10.1016/j.ygyno.2008.04.026].

[138] N. C. Hall, S. P. Povoski, D. A. Murrey, M. V Knopp, and E. W. Martin, "Combined approach of perioperative 18F-FDG PET/CT imaging and intraoperative 18F-FDG handheld gamma probe detection for tumor localization and verification of complete tumor resection in breast cancer.," *World journal of surgical oncology* **5**, 143 (2007) [doi:10.1186/1477-7819-5-143].

[139] E. Heckathorne, C. Dimock, and M. Dahlbom, "Radiation dose to surgical staff from positron-emitter-based localization and radiosurgery of tumors.," *Health physics* **95**, 220–226 (2008) [doi:10.1097/01.HP.0000310962.96089.44].

[140] D. Sarlos, L. D. Frey, H. Haueisen, G. Landmann, L. A. Kots, and G. Schaer, "Radioguided occult lesion localization (ROLL) for treatment and diagnosis of malignant and premalignant breast lesions combined with sentinel node biopsy: a prospective clinical trial with 100 patients.," *European journal of surgical oncology : the journal of the European Society of Surgical Oncology and the British Association of Surgical Oncology* **35**, 403–408 (2009) [doi:10.1016/j.ejso.2008.06.016].

[141] C. De Cicco, M. Pizzamiglio, G. Trifirò, A. Luini, M. Ferrari, G. Prisco, V. Galimberti, E. Cassano, G. Viale, et al., "Radioguided occult lesion localisation (ROLL) and surgical biopsy in breast cancer. Technical aspects.," *The quarterly journal of nuclear medicine : official publication of the Italian Association of Nuclear Medicine (AIMN) [and] the International Association of Radiopharmacology (IAR)* **46**, 145–151 (2002).

[142] R. S. Rampaul, M. Bagnall, H. Burrell, S. E. Pinder, A. J. Evans, and R. D. Macmillan, "Randomized clinical trial comparing radioisotope occult lesion localization and wire-guided excision for biopsy of occult breast lesions.," *The British journal of surgery* **91**, 1575–1577 (2004) [doi:10.1002/bjs.4801].

[143] N. Tagaya, R. Yamazaki, A. Nakagawa, A. Abe, K. Hamada, K. Kubota, and T. Oyama, "Intraoperative identification of sentinel lymph nodes by near-infrared fluorescence imaging in patients with breast cancer.," *American journal of surgery* **195**, 850–853 (2008) [doi:10.1016/j.amjsurg.2007.02.032].

[144] E. M. Sevick-Muraca, R. Sharma, J. C. Rasmussen, M. V Marshall, J. A. Wendt, H. Q. Pham, E. Bonefas, J. P. Houston, L. Sampath, et al., "Imaging of lymph flow in breast cancer patients after microdose administration of a near-infrared fluorophore: feasibility study.," *Radiology* **246**, 734–741 (2008) [doi:10.1148/radiol.2463070962].

[145] Y. Ogasawara, H. Ikeda, M. Takahashi, K. Kawasaki, and H. Doihara, "Evaluation of breast lymphatic pathways with indocyanine green fluorescence imaging in patients with breast cancer.," *World journal of surgery* **32**, 1924–1929 (2008) [doi:10.1007/s00268-008-9519-7].

[146] S. L. Troyan, V. Kianzad, S. L. Gibbs-Strauss, S. Gioux, A. Matsui, R. Oketokoun, L. Ngo, A. Khamene, F. Azar, et al., "The FLARE intraoperative near-infrared fluorescence imaging system: a first-in-human clinical trial in breast cancer sentinel lymph node mapping.," *Annals of surgical oncology* **16**, 2943–2952 (2009) [doi:10.1245/s10434-009-0594-2].

[147] R. G. Pleijhuis, G. C. Langhout, W. Helfrich, G. Themelis, A. Sarantopoulos, L. M. A. Crane, N. J. Harlaar, J. S. de Jong, V. Ntziachristos, et al., "Near-infrared fluorescence (NIRF) imaging in breast-conserving surgery: assessing intraoperative techniques in tissue-simulating breast phantoms.," *European journal of surgical oncology : the journal of the European Society of Surgical Oncology and the British Association of Surgical Oncology* **37**, 32–39 (2011) [doi:10.1016/j.ejso.2010.10.006].

[148] V. J. Pansare, S. Hejazi, W. J. Faenza, and R. K. Prud'homme, "Review of Long-Wavelength Optical and NIR Imaging Materials: Contrast Agents, Fluorophores, and Multifunctional Nano Carriers," *Chemistry of Materials* **24**, 812–827 (2012) [doi:10.1021/cm2028367].

[149] L. G. Wilke, J. Q. Brown, T. M. Bydlon, S. a Kennedy, L. M. Richards, M. K. Junker, J. Gallagher, W. T. Barry, J. Geradts, et al., "Rapid noninvasive optical imaging of tissue composition in breast tumor margins.," *American journal of surgery* **198**, 566–574 (2009) [doi:10.1016/j.amjsurg.2009.06.018].

[150] B. J. Tromberg, B. W. Pogue, K. D. Paulsen, A. G. Yodh, D. A. Boas, and A. E. Cerussi, "Assessing the future of diffuse optical imaging technologies for breast cancer management.," *Medical physics* **35**, 2443–2451 (2008).

[151] H. Soliman, A. Gunasekara, M. Rycroft, J. Zubovits, R. Dent, J. Spayne, M. J. Yaffe, and G. J. Czarnota, "Functional imaging using diffuse optical spectroscopy of neoadjuvant chemotherapy response in women with locally advanced breast cancer.," *Clinical cancer research : an official journal of the American Association for Cancer Research* **16**, 2605–2614 (2010) [doi:10.1158/1078-0432.CCR-09-1510].

[152] B. J. Tromberg and A. E. Cerussi, "Imaging breast cancer chemotherapy response with light. Commentary on Soliman et al., p. 2605.," *Clinical cancer research : an official journal of the American Association for Cancer Research* **16**, 2486–2488 (2010) [doi:10.1158/1078-0432.CCR-10-0397].

[153] S. Kukreti, A. E. Cerussi, W. Tanamai, D. Hsiang, B. J. Tromberg, and E. Gratton, "Characterization of metabolic differences between benign and malignant tumors: high-spectral-resolution diffuse optical spectroscopy.," *Radiology* **254**, 277–284 (2010) [doi:10.1148/radiol.09082134].

[154] L. Bickford, J. Sun, K. Fu, N. Lewinski, V. Nammalvar, J. Chang, and R. Drezek, "Enhanced multi-spectral imaging of live breast cancer cells using immunotargeted gold nanoshells and two-photon excitation microscopy," *Nanotechnology* **19**, - (2008) [doi:Artn 315102 Doi 10.1088/0957-4484/19/31/315102].

[155] L. Bickford, J. Chang, K. Fu, J. Sun, Y. Hu, A. Gobin, T.-K. Yu, and R. Drezek, "Evaluation of Immunotargeted Gold Nanoshells as Rapid Diagnostic Imaging Agents for HER2-Overexpressing Breast Cancer Cells: A Time Based Analysis," *Nanobiotechnology* **4**, 1–8 (2008).

[156] L. B. Carpin, L. R. Bickford, G. Agollah, T. K. Yu, R. Schiff, Y. Li, and R. A. Drezek, "Immunoconjugated gold nanoshell-mediated photothermal ablation of trastuzumab-resistant breast cancer cells," *Breast Cancer Res Treat* **125**, 2010/03/11 ed., 27–34 (2011) [doi:10.1007/s10549-010-0811-5].

[157] T. T. Purmonen, E. Pänkäläinen, J. H. O. Turunen, C. Asseburg, and J. A. Martikainen, "Short-course adjuvant trastuzumab therapy in early stage breast cancer in Finland: cost-effectiveness and value of information analysis based on the 5-year follow-up results of the FinHer Trial.," *Acta oncologica (Stockholm, Sweden)* **50**, 344–352 (2011) [doi:10.3109/0284186X.2011.553841].

[158] I. Smith, M. Procter, R. D. Gelber, S. Guillaume, A. Feyereislova, M. Dowsett, A. Goldhirsch, M. Untch, G. Mariani, et al., "2-year follow-up of trastuzumab after adjuvant chemotherapy in HER2-positive breast cancer: a randomised controlled trial.," *Lancet* **369**, 29–36 (2007) [doi:10.1016/S0140-6736(07)60028-2].

[159] C. E. Geyer, J. Forster, D. Lindquist, S. Chan, C. G. Romieu, T. Pienkowski, A. Jagiello-Gruszfeld, J. Crown, A. Chan, et al., "Lapatinib plus capecitabine for HER2-positive advanced breast cancer.," *The New England journal of medicine* **355**, 2733–2743 (2006) [doi:10.1056/NEJMoa064320].

[160] H. L. Gomez, D. C. Doval, M. A. Chavez, P. C.-S. Ang, Z. Aziz, S. Nag, C. Ng, S. X. Franco, L. W. C. Chow, et al., "Efficacy and safety of lapatinib as first-line therapy for ErbB2-amplified locally advanced or metastatic breast cancer.," *Journal of clinical oncology : official journal of the American Society of Clinical Oncology* **26**, 2999–3005 (2008) [doi:10.1200/JCO.2007.14.0590].

[161] M. S. Moran, Q. Yang, S. Goyal, L. Harris, G. Chung, and B. G. Haffty, "Evaluation of vascular endothelial growth factor as a prognostic marker for local relapse in early-stage breast cancer patients treated with breast-conserving therapy.," *International journal of radiation oncology, biology, physics* **81**, 1236–1243 (2011) [doi:10.1016/j.ijrobp.2010.07.031].

[162] B. Linderholm, B. Tavelin, K. Grankvist, and R. Henriksson, "Does vascular endothelial growth factor (VEGF) predict local relapse and survival in radiotherapy-treated node-negative breast cancer?," *British journal of cancer* **81**, 727–732 (1999) [doi:10.1038/sj.bjc.6690755].

[163] P. Manders, F. C. G. J. Sweep, V. C. G. Tjan-Heijnen, A. Geurts-Moespot, D. T. H. van Tienoven, J. A. Foekens, P. N. Span, J. Bussink, and L. V. A. M. Beex, "Vascular endothelial growth factor independently predicts the efficacy of postoperative radiotherapy in node-negative breast cancer patients.," *Clinical cancer research : an official journal of the American Association for Cancer Research* **9**, 6363–6370 (2003).

[164] M. A. Munirah, M. A. Siti-Aishah, M. Z. Reena, N. A. Sharifah, M. Rohaizak, A. Norlia, M. K. M. Rafie, A. Asmiati, A. Hisham, et al., "Identification of different subtypes of breast cancer using tissue microarray.," *Romanian journal of morphology and embryology = Revue roumaine de morphologie et embryologie* **52**, 669–677 (2011).

[165] M.-J. Kim, J. Y. Ro, S.-H. Ahn, H. H. Kim, S.-B. Kim, and G. Gong, "Clinicopathologic significance of the basal-like subtype of breast cancer: a comparison with hormone receptor and Her2/neu-overexpressing phenotypes.," *Human pathology* **37**, 1217–1226 (2006) [doi:10.1016/j.humpath.2006.04.015].

[166] B. A. Virnig, T. M. Tuttle, T. Shamliyan, and R. L. Kane, "Ductal carcinoma in situ of the breast: a systematic review of incidence, treatment, and outcomes.," *Journal of the National Cancer Institute* **102**, 170–178 (2010) [doi:10.1093/jnci/djp482].

[167] R. Sørum, S. Hofvind, P. Skaane, and T. Haldorsen, "Trends in incidence of ductal carcinoma in situ: the effect of a population-based screening programme.," *Breast (Edinburgh, Scotland)* **19**, 499–505 (2010) [doi:10.1016/j.breast.2010.05.014].

[168] M. A. de Roos, G. H. de Bock, J. de Vries, B. van der Vegt, and J. Wesseling, "p53 overexpression is a predictor of local recurrence after treatment for both in situ and invasive ductal carcinoma of the breast.," *The Journal of surgical research* **140**, 109–114 (2007) [doi:10.1016/j.jss.2006.10.045].

[169] E. Provenzano, J. L. Hopper, G. G. Giles, G. Marr, D. J. Venter, and J. E. Armes, "Biological markers that predict clinical recurrence in ductal carcinoma in situ of the breast.," *European journal of cancer (Oxford, England : 1990)* **39**, 622–630 (2003).

[170] X. R. Yang, M. E. Sherman, D. L. Rimm, J. Lissowska, L. A. Brinton, B. Peplonska, S. M. Hewitt, W. F. Anderson, N. Szeszenia-Dabrowska, et al., "Differences in risk factors for breast cancer molecular subtypes in a population-based study.," *Cancer epidemiology, biomarkers & prevention : a publication of the American Association for Cancer Research, cosponsored by the American Society of Preventive Oncology* **16**, 439–443 (2007) [doi:10.1158/1055-9965.EPI-06-0806].

[171] S. M. Janib, A. S. Moses, and J. A. MacKay, "Imaging and drug delivery using theranostic nanoparticles.," *Advanced drug delivery reviews* **62**, 1052–1063 (2010) [doi:10.1016/j.addr.2010.08.004].

[172] A. Albanese, P. S. Tang, and W. C. W. Chan, "The effect of nanoparticle size, shape, and surface chemistry on biological systems.," *Annual review of biomedical engineering* **14**, 1–16 (2012) [doi:10.1146/annurev-bioeng-071811-150124].

[173] C. Leuschner, C. S. S. R. Kumar, W. Hansel, W. Soboyejo, J. Zhou, and J. Hormes, "LHRH-conjugated magnetic iron oxide nanoparticles for detection of breast cancer metastases.," *Breast cancer research and treatment* **99**, 163–176 (2006) [doi:10.1007/s10549-006-9199-7].

[174] A. Moore, "In Vivo Targeting of Underglycosylated MUC-1 Tumor Antigen Using a Multimodal Imaging Probe," *Cancer Research* **64**, 1821–1827 (2004) [doi:10.1158/0008-5472.CAN-03-3230].

[175] S. Battah, S. Balaratnam, A. Casas, S. O'Neill, C. Edwards, A. Batlle, P. Dobbin, and A. J. MacRobert, "Macromolecular delivery of 5-aminolaevulinic acid for photodynamic therapy using dendrimer conjugates.," *Molecular cancer therapeutics* **6**, 876–885 (2007) [doi:10.1158/1535-7163.MCT-06-0359].

[176] Y. Shan, T. Luo, C. Peng, R. Sheng, A. Cao, X. Cao, M. Shen, R. Guo, H. Tomás, et al., "Gene delivery using dendrimer-entrapped gold nanoparticles as nonviral vectors.," *Biomaterials* **33**, 3025–3035 (2012) [doi:10.1016/j.biomaterials.2011.12.045].

[177] M. Wang and M. Thanou, "Targeting nanoparticles to cancer.," *Pharmacological research : the official journal of the Italian Pharmacological Society* **62**, 90–99 (2010) [doi:10.1016/j.phrs.2010.03.005].

[178] J. Treat, A. Greenspan, D. Forst, J. A. Sanchez, V. J. Ferrans, L. A. Potkul, P. V. Woolley, and A. Rahman, "Antitumor Activity of Liposome-Encapsulated Doxorubicin in Advanced Breast Cancer: Phase II Study," *JNCI Journal of the National Cancer Institute* **82**, 1706–1710 (1990) [doi:10.1093/jnci/82.21.1706].

[179] N. J. Robert, C. L. Vogel, I. C. Henderson, J. A. Sparano, M. R. Moore, P. Silverman, B. A. Overmoyer, C. L. Shapiro, J. W. Park, et al., "The role of the liposomal anthracyclines and other systemic therapies in the management of advanced breast cancer," *Seminars in Oncology* **31**, 106–146 (2004) [doi:10.1053/j.seminoncol.2004.09.018].

[180] N. Desai, V. Trieu, Z. Yao, L. Louie, S. Ci, A. Yang, C. Tao, T. De, B. Beals, et al., "Increased antitumor activity, intratumor paclitaxel concentrations, and endothelial cell transport of cremophor-free, albumin-bound paclitaxel, ABI-007, compared with cremophor-based paclitaxel.," *Clinical cancer research : an official journal of the American Association for Cancer Research* **12**, 1317–1324 (2006) [doi:10.1158/1078-0432.CCR-05-1634].

[181] E. Miele, G. P. Spinelli, E. Miele, F. Tomao, and S. Tomao, "Albumin-bound formulation of paclitaxel (Abraxane ABI-007) in the treatment of breast cancer.," *International journal of nanomedicine* **4**, 99–105 (2009).

[182] M. J. Hawkins, P. Soon-Shiong, and N. Desai, "Protein nanoparticles as drug carriers in clinical medicine.," *Advanced drug delivery reviews* **60**, 876–885 (2008) [doi:10.1016/j.addr.2007.08.044].

[183] R. H. MÜLLER, W. MEHNERT, J.-S. LUCKS, C. SCHWARZ, A. ZUR MÜHLEN, H. MEYHERS, C. FREITAS, and D. RÜHL, "Solid lipid nanoparticles (SLN) : an alternative colloidal carrier system for controlled drug delivery," *European journal of pharmaceutics and biopharmaceutics* **41**, 62–69, Elsevier.

[184] S. A. Wissing, O. Kayser, and R. H. Müller, "Solid lipid nanoparticles for parenteral drug delivery.," *Advanced drug delivery reviews* **56**, 1257–1272 (2004) [doi:10.1016/j.addr.2003.12.002].

[185] H. L. Wong, R. Bendayan, A. M. Rauth, Y. Li, and X. Y. Wu, "Chemotherapy with anticancer drugs encapsulated in solid lipid nanoparticles.," *Advanced drug delivery reviews* **59**, 491–504 (2007) [doi:10.1016/j.addr.2007.04.008].

[186] C. C. Lee, J. A. MacKay, J. M. J. Fréchet, and F. C. Szoka, "Designing dendrimers for biological applications.," *Nature biotechnology* **23**, 1517–1526 (2005) [doi:10.1038/nbt1171].

[187] T. P. Thomas, R. Shukla, A. Kotlyar, J. Kukowska-Latallo, and J. R. Baker, "Dendrimer-based tumor cell targeting of fibroblast growth factor-1.," *Bioorganic & medicinal chemistry letters* **20**, 700–703 (2010) [doi:10.1016/j.bmcl.2009.11.065].

[188] S. K. Choi, T. Thomas, M.-H. Li, A. Kotlyar, A. Desai, and J. R. Baker, "Light-controlled release of caged doxorubicin from folate receptor-targeting PAMAM dendrimer nanoconjugate.," *Chemical communications (Cambridge, England)* **46**, 2632–2634 (2010) [doi:10.1039/b927215c].

[189] V. I. Shubayev, T. R. Pisanic, and S. Jin, "Magnetic nanoparticles for theragnostics.," *Advanced drug delivery reviews* **61**, 467–477 (2009) [doi:10.1016/j.addr.2009.03.007].

[190] Z. Medarova, W. Pham, C. Farrar, V. Petkova, and A. Moore, "In vivo imaging of siRNA delivery and silencing in tumors.," *Nature medicine* **13**, 372–377 (2007) [doi:10.1038/nm1486].

[191] A. Moore and Z. Medarova, "Imaging of siRNA delivery and silencing.," *Methods in molecular biology (Clifton, N.J.)* **487**, 93–110 (2009) [doi:10.1007/978-1-60327-547-7_5].

[192] M. K. Yu, Y. Y. Jeong, J. Park, S. Park, J. W. Kim, J. J. Min, K. Kim, and S. Jon, "Drug-loaded superparamagnetic iron oxide nanoparticles for combined cancer imaging and therapy in vivo.," *Angewandte Chemie (International ed. in English)* **47**, 5362–5365 (2008) [doi:10.1002/anie.200800857].

[193] E. E. Connor, J. Mwamuka, A. Gole, C. J. Murphy, and M. D. Wyatt, "Gold nanoparticles are taken up by human cells but do not cause acute cytotoxicity.," *Small (Weinheim an der Bergstrasse, Germany)* **1**, 325–327 (2005) [doi:10.1002/smll.200400093].

[194] G. Han, P. Ghosh, M. De, and V. M. Rotello, "Drug and Gene Delivery using Gold Nanoparticles," *Nanobiotechnology*, 40–45 (2007) [doi:10.1007/s].

[195] S. Santra and D. Dutta, "Nanoparticles for Optical Imaging," in *Nanomaterials For Cancer Diagnosis*, C. Kumar, Ed., pp. 46–85, Wiley Subscription Services, Inc., A Wiley Company (2007).

[196] S. Santra, J. Xu, K. Wang, and W. Tand, "Luminescent Nanoparticle Probes for Bioimaging," *Journal of Nanoscience and Nanotechnology* **4**, 590–599 (2004) [doi:10.1166/jnn.2004.017].

[197] U. Kreibig and L. Genzel, "Optical absorption of small metallic particles," *Surface Science* **156**, 678–700 (1985) [doi:10.1016/0039-6028(85)90239-0].

[198] K. Sokolov, J. Aaron, B. Hsu, D. Nida, A. Gillenwater, M. Follen, C. MacAulay, K. Adler-Storthz, B. Korgel, et al., "Optical systems for in vivo molecular imaging of cancer.," *Technology in cancer research & treatment* **2**, 491–504 (2003).

[199] C. J. J. Murphy and N. R. R. Jana, "Controlling the aspect ratio of inorganic nanorods and nanowires," *Adv. Mater.* **14**, 80 (2002) [doi:10.1002/1521-4095(20020104)14:1<80::AID-ADMA80>3.0.CO;2-#].

[200] I. H. El-Sayed, X. Huang, and M. A. El-Sayed, "Surface plasmon resonance scattering and absorption of anti-EGFR antibody conjugated gold nanoparticles in cancer diagnostics: applications in oral cancer.," *Nano letters* **5**, 2005/05/12 ed., 829–834 (2005) [doi:10.1021/nl050074e].

[201] K. Sokolov, M. Follen, J. Aaron, I. Pavlova, A. Malpica, R. Lotan, R. Richards-Kortum, and F. M. Sokolov K, Aaron J, Pavlova I, Malpica A, Lotan R, "Real-time vital optical imaging of precancer using anti-epidermal growth factor receptor antibodies conjugated to gold nanoparticles.," *Cancer research* **63**, 1999–2004 (2003).

[202] J. F. Hainfeld, D. N. Slatkin, T. M. Focella, and H. M. Smilowitz, "Gold nanoparticles: a new X-ray contrast agent.," *The British journal of radiology* **79**, 248–253 (2006) [doi:10.1259/bjr/13169882].

[203] D. Kim, S. Park, J. H. Lee, Y. Y. Jeong, and S. Jon, "Antibiofouling polymer-coated gold nanoparticles as a contrast agent for in vivo X-ray computed tomography imaging.," *Journal of the American Chemical Society* **129**, 7661–7665 (2007) [doi:10.1021/ja071471p].

[204] F. Geng, K. Song, J. Z. Xing, C. Yuan, S. Yan, Q. Yang, J. Chen, and B. Kong, "Thio-glucose bound gold nanoparticles enhance radio-cytotoxic targeting of ovarian cancer.," *Nanotechnology* **22**, 285101 (2011) [doi:10.1088/0957-4484/22/28/285101].

[205] X. Zhang, J. Z. Xing, J. Chen, L. Ko, J. Amanie, S. Gulavita, N. Pervez, D. Yee, R. Moore, et al., "Enhanced radiation sensitivity in prostate cancer by gold-nanoparticles.," *Clinical and investigative medicine. Médecine clinique et experimentale* **31**, E160–7 (2008).

[206] G. Han, C. T. Martin, and V. M. Rotello, "Stability of gold nanoparticle-bound DNA toward biological, physical, and chemical agents.," *Chemical biology & drug design* **67**, 78–82 (2006) [doi:10.1111/j.1747-0285.2005.00324.x].

[207] S. J. Oldenburg, R. D. Averitt, S. L. Westcott, and N. J. Halas, "Nanoengineering of optical resonances," *Chemical Physics Letters* **288**, 243–247 (1998).

[208] D. P. O'Neal, L. R. Hirsch, N. J. Halas, J. D. Payne, and J. L. West, "Photo-thermal tumor ablation in mice using near infrared-absorbing nanoparticles.," *Cancer letters* **209**, 171–176 (2004) [doi:10.1016/j.canlet.2004.02.004].

[209] H. Maeda, "The enhanced permeability and retention (EPR) effect in tumor vasculature: the key role of tumor-selective macromolecular drug targeting," *Advances in Enzyme Regulation* **41**, 189–207 (2001) [doi:10.1016/S0065-2571(00)00013-3].

[210] H. Maeda, J. Fang, T. Inutsuka, and Y. Kitamoto, "Vascular permeability enhancement in solid tumor: various factors, mechanisms involved and its implications.," *International immunopharmacology* **3**, 319–328 (2003) [doi:10.1016/S1567-5769(02)00271-0].

[211] J. A. Schwartz, A. M. Shetty, R. E. Price, R. J. Stafford, J. C. Wang, R. K. Uthamanthil, K. Pham, R. J. McNichols, C. L. Coleman, et al., "Feasibility study of particle-assisted laser ablation of brain tumors in orthotopic canine model.," *Cancer research* **69**, 1659–1667 (2009) [doi:10.1158/0008-5472.CAN-08-2535].

[212] E. Day, L. Bickfrod, J. Slater, N. Riggall, R. Drezek, and J. West, "Antibody-conjugated gold-gold sulfide nanoparticles as multifunctional agents for imaging and therapy of breast cancer," *International Journal of Nanomedicine*, 445 (2010) [doi:10.2147/IJN.S10881].

[213] C. Loo, A. Lin, L. Hirsch, M. H. Lee, J. Barton, N. Halas, J. West, and R. Drezek, "Nanoshell-enabled photonics-based imaging and therapy of cancer," *Technol Cancer Res Treat* **3**, 2004/01/31 ed., 33–40 (2004) [doi:d=3018&c=4130&p=12032&do=detail [pii]].

[214] J. Funkhouser, "Reinventing pharma: The theranostic revolution," *Current Drug Discovery*, 17–19 (2002).

[215] J. V Jokerst and S. S. Gambhir, "Molecular imaging with theranostic nanoparticles.," *Accounts of chemical research* **44**, 1050–1060 (2011) [doi:10.1021/ar200106e].

[216] M. E. R. O'Brien, "Reduced cardiotoxicity and comparable efficacy in a phase III trial of pegylated liposomal doxorubicin HCl (CAELYXTM/Doxil") versus conventional doxorubicin for first-line treatment of metastatic breast cancer," *Annals of Oncology* **15**, 440–449 (2004) [doi:10.1093/annonc/mdh097].

[217] X. Michalet, F. F. Pinaud, L. A. Bentolila, J. M. Tsay, S. Doose, J. J. Li, G. Sundaresan, A. M. Wu, S. S. Gambhir, et al., "Quantum dots for live cells, in vivo imaging, and diagnostics.," *Science (New York, N.Y.)* **307**, 538–544 (2005) [doi:10.1126/science.1104274].

[218] C. G. Hadjipanayis, R. Machaidze, M. Kaluzova, L. Wang, A. J. Schuette, H. Chen, X. Wu, and H. Mao, "EGFRvIII antibody-conjugated iron oxide nanoparticles for magnetic resonance imaging-guided convection-enhanced delivery and targeted therapy of glioblastoma.," *Cancer research* **70**, 6303–6312 (2010) [doi:10.1158/0008-5472.CAN-10-1022].

[219] E. Pollert, P. Veverka, M. Veverka, O. Kaman, K. Závěta, S. Vasseur, R. Epherre, G. Goglio, and E. Duguet, "Search of new core materials for magnetic fluid hyperthermia: Preliminary chemical and physical issues," *Progress in Solid State Chemistry* **37**, 1–14 (2009) [doi:10.1016/j.progsolidstchem.2009.02.001].

[220] B. Chertok, A. E. David, and V. C. Yang, "Polyethyleneimine-modified iron oxide nanoparticles for brain tumor drug delivery using magnetic targeting and intra-carotid administration.," *Biomaterials* **31**, 6317–6324 (2010) [doi:10.1016/j.biomaterials.2010.04.043].

[221] K. D. Watson, C.-Y. Lai, S. Qin, D. E. Kruse, Y.-C. Lin, J. W. Seo, R. D. Cardiff, L. M. Mahakian, J. Beegle, et al., "Ultrasound increases nanoparticle delivery by reducing intratumoral pressure and increasing transport in epithelial and epithelial-mesenchymal transition tumors.," *Cancer research* **72**, 1485–1493 (2012) [doi:10.1158/0008-5472.CAN-11-3232].

[222] A. J. Cole, V. C. Yang, and A. E. David, "Cancer theranostics: the rise of targeted magnetic nanoparticles.," *Trends in biotechnology* **29**, 323–332 (2011) [doi:10.1016/j.tibtech.2011.03.001].

[223] J. P. M. Almeida, A. L. Chen, A. Foster, and R. Drezek, "In vivo biodistribution of nanoparticles.," *Nanomedicine (London, England)* **6**, 815–835 (2011) [doi:10.2217/nnm.11.79].

[224] T. Cedervall, I. Lynch, S. Lindman, T. Berggård, E. Thulin, H. Nilsson, K. A. Dawson, and S. Linse, "Understanding the nanoparticle-protein corona using methods to quantify exchange rates and affinities of proteins for nanoparticles.," *Proceedings of the National Academy of Sciences of the United States of America* **104**, 2050–2055 (2007) [doi:10.1073/pnas.0608582104].

[225] I. Lynch and K. A. Dawson, "Protein-nanoparticle interactions," *Nano Today* **3**, 40–47 (2008) [doi:10.1016/S1748-0132(08)70014-8].

[226] M. A. Dobrovolskaia and S. E. McNeil, "Immunological properties of engineered nanomaterials.," *Nature nanotechnology* **2**, 469–478 (2007) [doi:10.1038/nnano.2007.223].

[227] M. A. Dobrovolskaia, P. Aggarwal, J. B. Hall, and S. E. McNeil, "Preclinical studies to understand nanoparticle interaction with the immune system and its potential effects on nanoparticle biodistribution.," *Molecular pharmaceutics* **5**, 487–495 [doi:10.1021/mp800032f].

[228] I. Slowing, B. G. Trewyn, and V. S.-Y. Lin, "Effect of surface functionalization of MCM-41-type mesoporous silica nanoparticles on the endocytosis by human cancer cells.," *Journal of the American Chemical Society* **128**, 14792–14793 (2006) [doi:10.1021/ja0645943].

[229] D. L. J. Thorek and A. Tsourkas, "Size, charge and concentration dependent uptake of iron oxide particles by non-phagocytic cells.," *Biomaterials* **29**, 3583–3590 (2008) [doi:10.1016/j.biomaterials.2008.05.015].

[230] S. M. Moghimi, A. C. Hunter, and J. C. Murray, "Long-circulating and target-specific nanoparticles: theory to practice.," *Pharmacological reviews* **53**, 283–318 (2001).

[231] F. Alexis, E. Pridgen, L. K. Molnar, and O. C. Farokhzad, "Factors affecting the clearance and biodistribution of polymeric nanoparticles.," *Molecular pharmaceutics* **5**, 505–515 [doi:10.1021/mp800051m].

[232] S. D. Perrault, C. Walkey, T. Jennings, H. C. Fischer, and W. C. W. Chan, "Mediating tumor targeting efficiency of nanoparticles through design.," *Nano letters* **9**, 1909–1915 (2009) [doi:10.1021/nl900031y].

[233] G. Zhang, Z. Yang, W. Lu, R. Zhang, Q. Huang, M. Tian, L. Li, D. Liang, and C. Li, "Influence of anchoring ligands and particle size on the colloidal stability and in vivo biodistribution of polyethylene glycol-coated gold nanoparticles in tumor-xenografted mice.," *Biomaterials* **30**, 1928–1936 (2009) [doi:10.1016/j.biomaterials.2008.12.038].

[234] T. Liu and B. Thierry, "A Solution to the PEG Dilemma: Efficient Bioconjugation of Large Gold Nanoparticles for Biodiagnostic Applications using Mixed Layers.," *Langmuir : the ACS journal of surfaces and colloids* (2012) [doi:10.1021/la301390u].

[235] P. Bourrinet, H. H. Bengele, B. Bonnemain, A. Dencausse, J.-M. Idee, P. M. Jacobs, and J. M. Lewis, "Preclinical safety and pharmacokinetic profile of ferumoxtran-10, an ultrasmall superparamagnetic iron oxide magnetic resonance contrast agent.," *Investigative radiology* **41**, 313–324 (2006) [doi:10.1097/01.rli.0000197669.80475.dd].

[236] R. Lawaczeck, H. Bauer, T. Frenzel, M. Hasegawa, Y. Ito, K. Kito, N. Miwa, H. Tsutsui, H. Vogler, et al., "Magnetic Iron Oxide Particles Coated with Carboxydextran for Parenteral Administration and Liver Contrasting," *Acta Radiologica* **38**, 584–597 (1997) [doi:10.1080/02841859709174391].

[237] H. Chen, L. Wang, J. Yeh, X. Wu, Z. Cao, Y. A. Wang, M. Zhang, L. Yang, and H. Mao, "Reducing non-specific binding and uptake of nanoparticles and improving cell targeting with an

antifouling PEO-b-PgammaMPS copolymer coating.," *Biomaterials* **31**, 5397–5407 (2010) [doi:10.1016/j.biomaterials.2010.03.036].

[238] C. H. J. Choi, C. A. Alabi, P. Webster, and M. E. Davis, "Mechanism of active targeting in solid tumors with transferrin-containing gold nanoparticles.," *Proceedings of the National Academy of Sciences of the United States of America* **107**, 1235–1240 (2010) [doi:10.1073/pnas.0914140107].

[239] F. M. Kievit, Z. R. Stephen, O. Veiseh, H. Arami, T. Wang, V. P. Lai, J. O. Park, R. G. Ellenbogen, M. L. Disis, et al., "Targeting of primary breast cancers and metastases in a transgenic mouse model using rationally designed multifunctional SPIONs.," *ACS nano* **6**, 2591–2601 (2012) [doi:10.1021/nn205070h].

[240] R. Goel, N. Shah, R. Visaria, G. F. Paciotti, and J. C. Bischof, "Biodistribution of TNF-alpha-coated gold nanoparticles in an in vivo model system.," *Nanomedicine (London, England)* **4**, 401–410 (2009) [doi:10.2217/nnm.09.21].

[241] K. Fu, J. Sun, L. R. Bickford, A. W. H. Lin, N. J. Halas, T.-K. Yu, and R. a Drezek, "Measurement of immunotargeted plasmonic nanoparticles' cellular binding: a key factor in optimizing diagnostic efficacy," *Nanotechnology* **19**, 045103 (2008) [doi:10.1088/0957-4484/19/04/045103].

[242] W. Jiang, B. Y. S. Kim, J. T. Rutka, and W. C. W. Chan, "Nanoparticle-mediated cellular response is size-dependent.," *Nature nanotechnology* **3**, 145–150 (2008) [doi:10.1038/nnano.2008.30].

[243] V. Sée, P. Free, Y. Cesbron, P. Nativo, U. Shaheen, D. J. Rigden, D. G. Spiller, D. G. Fernig, M. R. H. White, et al., "Cathepsin L digestion of nanobioconjugates upon endocytosis.," *ACS nano* **3**, 2461–2468 (2009) [doi:10.1021/nn9006994].

[244] P. Rees, M. R. Brown, H. D. Summers, M. D. Holton, R. J. Errington, S. C. Chappell, and P. J. Smith, "A transfer function approach to measuring cell inheritance.," *BMC systems biology* **5**, 31 (2011) [doi:10.1186/1752-0509-5-31].

[245] Y. Williams, A. Sukhanova, M. Nowostawska, A. M. Davies, S. Mitchell, V. Oleinikov, Y. Gun'ko, I. Nabiev, D. Kelleher, et al., "Probing cell-type-specific intracellular nanoscale barriers using size-tuned quantum dots.," *Small (Weinheim an der Bergstrasse, Germany)* **5**, 2581–2588 (2009) [doi:10.1002/smll.200900744].

[246] P. V AshaRani, G. Low Kah Mun, M. P. Hande, and S. Valiyaveettil, "Cytotoxicity and genotoxicity of silver nanoparticles in human cells.," *ACS nano* **3**, 279–290 (2009) [doi:10.1021/nn800596w].

[247] B. Kang, M. a Mackey, and M. A. El-Sayed, "Nuclear targeting of gold nanoparticles in cancer cells induces DNA damage, causing cytokinesis arrest and apoptosis.," *Journal of the American Chemical Society* **132**, 1517–1519 (2010) [doi:10.1021/ja9102698].

[248] Y. Pan, S. Neuss, A. Leifert, M. Fischler, F. Wen, U. Simon, G. Schmid, W. Brandau, and W. Jahnen-Dechent, "Size-dependent cytotoxicity of gold nanoparticles.," *Small (Weinheim an der Bergstrasse, Germany)* **3**, 1941–1949 (2007) [doi:10.1002/smll.200700378].

[249] Y. Pan, A. Leifert, D. Ruau, S. Neuss, J. Bornemann, G. Schmid, W. Brandau, U. Simon, and W. Jahnen-Dechent, "Gold nanoparticles of diameter 1.4 nm trigger necrosis by oxidative stress and mitochondrial damage.," *Small (Weinheim an der Bergstrasse, Germany)* **5**, 2067–2076 (2009) [doi:10.1002/smll.200900466].

[250] C. M. Goodman, C. D. McCusker, T. Yilmaz, and V. M. Rotello, "Toxicity of gold nanoparticles functionalized with cationic and anionic side chains.," *Bioconjugate chemistry* **15**, 897–900 [doi:10.1021/bc049951i].

[251] R. R. Arvizo, O. R. Miranda, M. A. Thompson, C. M. Pabelick, R. Bhattacharya, J. D. Robertson, V. M. Rotello, Y. S. Prakash, and P. Mukherjee, "Effect of nanoparticle surface charge at the plasma membrane and beyond.," *Nano letters* **10**, 2543–2548 (2010) [doi:10.1021/nl101140t].

[252] H. S. Choi, W. Liu, P. Misra, E. Tanaka, J. P. Zimmer, B. Itty Ipe, M. G. Bawendi, and J. V Frangioni, "Renal clearance of quantum dots.," *Nature biotechnology* **25**, 1165–1170 (2007) [doi:10.1038/nbt1340].

[253] B. Ballou, B. C. Lagerholm, L. A. Ernst, M. P. Bruchez, and A. S. Waggoner, "Noninvasive imaging of quantum dots in mice.," *Bioconjugate chemistry* **15**, 79–86 [doi:10.1021/bc034153y].

[254] W. H. De Jong, W. I. Hagens, P. Krystek, M. C. Burger, A. J. A. M. Sips, and R. E. Geertsma, "Particle size-dependent organ distribution of gold nanoparticles after intravenous administration.," *Biomaterials* **29**, 1912–1919 (2008) [doi:10.1016/j.biomaterials.2007.12.037].

[255] G. Sonavane, K. Tomoda, and K. Makino, "Biodistribution of colloidal gold nanoparticles after intravenous administration: effect of particle size.," *Colloids and surfaces. B, Biointerfaces* **66**, 274–280 (2008) [doi:10.1016/j.colsurfb.2008.07.004].

[256] S. Hirn, M. Semmler-Behnke, C. Schleh, A. Wenk, J. Lipka, M. Schäffler, S. Takenaka, W. Möller, G. Schmid, et al., "Particle size-dependent and surface charge-dependent biodistribution of gold nanoparticles after intravenous administration.," *European journal of pharmaceutics and biopharmaceutics : official journal of Arbeitsgemeinschaft für Pharmazeutische Verfahrenstechnik e.V* **77**, 407–416 (2011) [doi:10.1016/j.ejpb.2010.12.029].

[257] X.-D. Zhang, D. Wu, X. Shen, P.-X. Liu, N. Yang, B. Zhao, H. Zhang, Y.-M. Sun, L.-A. Zhang, et al., "Size-dependent in vivo toxicity of PEG-coated gold nanoparticles.," *International journal of nanomedicine* **6**, 2071–2081 (2011) [doi:10.2147/IJN.S21657].

[258] S. E. A. Gratton, P. A. Ropp, P. D. Pohlhaus, J. C. Luft, V. J. Madden, M. E. Napier, and J. M. DeSimone, "The effect of particle design on cellular internalization pathways.," *Proceedings of the National Academy of Sciences of the United States of America* **105**, 11613–11618 (2008) [doi:10.1073/pnas.0801763105].

[259] B. D. Chithrani, A. A. Ghazani, and W. C. W. Chan, "Determining the size and shape dependence of gold nanoparticle uptake into mammalian cells.," *Nano letters* **6**, 662–668 (2006) [doi:10.1021/nl052396o].

[260] B. D. Chithrani and W. C. W. Chan, "Elucidating the mechanism of cellular uptake and removal of protein-coated gold nanoparticles of different sizes and shapes.," *Nano letters* **7**, 1542–1550 (2007) [doi:10.1021/nl070363y].

[261] Arnida, M. M. Janát-Amsbury, A. Ray, C. M. Peterson, and H. Ghandehari, "Geometry and surface characteristics of gold nanoparticles influence their biodistribution and uptake by macrophages.," *European journal of pharmaceutics and biopharmaceutics : official journal of Arbeitsgemeinschaft für Pharmazeutische Verfahrenstechnik e.V* **77**, 417–423 (2011) [doi:10.1016/j.ejpb.2010.11.010].

[262] Y.-N. Sun, C.-D. Wang, X.-M. Zhang, L. Ren, and X.-H. Tian, "Shape dependence of gold nanoparticles on in vivo acute toxicological effects and biodistribution.," *Journal of nanoscience and nanotechnology* **11**, 1210–1216 (2011).

[263] K. Yu, K. L. Kelly, N. Sakai, and T. Tatsuma, "Morphologies and surface plasmon resonance properties of monodisperse bumpy gold nanoparticles.," *Langmuir : the ACS journal of surfaces and colloids* **24**, 5849–5854 (2008) [doi:10.1021/la703903b].

[264] O. M. Bakr, B. H. Wunsch, and F. Stellacci, "High-Yield Synthesis of Multi-Branched Urchin-Like Gold Nanoparticles," *Chemistry of Materials* **18**, 3297–3301 (2006) [doi:10.1021/cm060681i].

[265] E. Hutter, S. Boridy, S. Labrecque, M. Lalancette-Hébert, J. Kriz, F. M. Winnik, and D. Maysinger, "Microglial response to gold nanoparticles.," *ACS nano* **4**, 2595–2606 (2010) [doi:10.1021/nn901869f].

[266] P. Senthil Kumar, I. Pastoriza-Santos, B. Rodríguez-González, F. Javier García de Abajo, and L. M. Liz-Marzán, "High-yield synthesis and optical response of gold nanostars.," *Nanotechnology* **19**, 015606 (2008) [doi:10.1088/0957-4484/19/01/015606].

[267] A. Hellebust and R. Richards-Kortum, "Advances in molecular imaging: targeted optical contrast agents for cancer diagnostics.," *Nanomedicine (London, England)* **7**, 429–445 (2012) [doi:10.2217/nnm.12.12].

[268] K. Glunde, A. P. Pathak, and Z. M. Bhujwalla, "Molecular-functional imaging of cancer: to image and imagine.," *Trends in molecular medicine* **13**, 287–297 (2007) [doi:10.1016/j.molmed.2007.05.002].

[269] D. Hanahan and R. A. Weinberg, "The hallmarks of cancer.," *Cell* **100**, 57–70 (2000).

[270] D. A. Hamstra, M. S. Bhojani, L. B. Griffin, B. Laxman, B. D. Ross, and A. Rehemtulla, "Real-time evaluation of p53 oscillatory behavior in vivo using bioluminescent imaging.," *Cancer research* **66**, 7482–7489 (2006) [doi:10.1158/0008-5472.CAN-06-1405].

[271] W. Wang, S.-H. Kim, and W. S. El-Deiry, "Small-molecule modulators of p53 family signaling and antitumor effects in p53-deficient human colon tumor xenografts.," *Proceedings of the National Academy of Sciences of the United States of America* **103**, 11003–11008 (2006) [doi:10.1073/pnas.0604507103].

[272] A. J. Beer, R. Haubner, M. Sarbia, M. Goebel, S. Luderschmidt, A. L. Grosu, O. Schnell, M. Niemeyer, H. Kessler, et al., "Positron emission tomography using [18F]Galacto-RGD identifies the level of integrin alpha(v)beta3 expression in man.," *Clinical cancer research : an official journal of the American Association for Cancer Research* **12**, 3942–3949 (2006) [doi:10.1158/1078-0432.CCR-06-0266].

[273] R. Haubner, W. A. Weber, A. J. Beer, E. Vabuliene, D. Reim, M. Sarbia, K.-F. Becker, M. Goebel, R. Hein, et al., "Noninvasive visualization of the activated alphavbeta3 integrin in cancer patients by positron emission tomography and [18F]Galacto-RGD.," *PLoS medicine* **2**, e70 (2005) [doi:10.1371/journal.pmed.0020070].

[274] B. B. Koolen, M. J. T. F. D. Vrancken Peeters, J. Wesseling, E. H. Lips, W. V Vogel, T. S. Aukema, E. van Werkhoven, K. G. A. Gilhuijs, S. Rodenhuis, et al., "Association of primary tumour FDG uptake with clinical, histopathological and molecular characteristics in breast cancer patients scheduled for neoadjuvant chemotherapy.," *European journal of nuclear medicine and molecular imaging* (2012) [doi:10.1007/s00259-012-2211-z].

[275] T. S. Aukema, E. J. T. Rutgers, W. V Vogel, H. J. Teertstra, H. S. Oldenburg, M. T. F. D. Vrancken Peeters, J. Wesseling, N. S. Russell, and R. A. Valdés Olmos, "The role of FDG PET/CT in patients with locoregional breast cancer recurrence: a comparison to conventional imaging techniques.," *European journal of surgical oncology : the journal of the European Society of Surgical Oncology and the British Association of Surgical Oncology* **36**, 387–392 (2010) [doi:10.1016/j.ejso.2009.11.009].

[276] W. L. Lu, L. Jansen, W. J. Post, J. Bonnema, J. C. Van de Velde, and G. H. De Bock, "Impact on survival of early detection of isolated breast recurrences after the primary treatment for breast

cancer: a meta-analysis.," *Breast cancer research and treatment* **114**, 403–412 (2009) [doi:10.1007/s10549-008-0023-4].

[277] M. C. Pierce, D. J. Javier, and R. Richards-Kortum, "Optical contrast agents and imaging systems for detection and diagnosis of cancer.," *International journal of cancer. Journal international du cancer* **123**, 1979–1990 (2008) [doi:10.1002/ijc.23858].

[278] J. V Frangioni, "New technologies for human cancer imaging.," *Journal of clinical oncology : official journal of the American Society of Clinical Oncology* **26**, 4012–4021 (2008) [doi:10.1200/JCO.2007.14.3065].

[279] S. Luo, E. Zhang, Y. Su, T. Cheng, and C. Shi, "A review of NIR dyes in cancer targeting and imaging.," *Biomaterials* **32**, 7127–7138 (2011) [doi:10.1016/j.biomaterials.2011.06.024].

[280] A. T. Yeh, B. Choi, J. S. Nelson, and B. J. Tromberg, "Reversible dissociation of collagen in tissues.," *The Journal of investigative dermatology* **121**, 1332–1335 (2003) [doi:10.1046/j.1523-1747.2003.12634.x].

[281] O. Vargas, E. K. Chan, J. K. Barton, H. G. Rylander, and A. J. Welch, "Use of an agent to reduce scattering in skin," *Lasers in Surgery and Medicine* **24**, 133–141 (1999).

[282] G. Strangman, D. A. Boas, and J. P. Sutton, "Non-invasive neuroimaging using near-infrared light.," *Biological psychiatry* **52**, 679–693 (2002).

[283] R. Weissleder, "A clearer vision for in vivo imaging.," *Nature biotechnology* **19**, 316–317 (2001) [doi:10.1038/86684].

[284] M. S. Mathews and M. E. Linskey, "Neuroendovascular Optical Coherence Tomography Imaging for Cerebrovascular Disease: Current Concepts and Clinical Potential.," *Current cardiology reports* (2012) [doi:10.1007/s11886-012-0310-x].

[285] A. E. Cerussi, V. W. Tanamai, D. Hsiang, J. Butler, R. S. Mehta, and B. J. Tromberg, "Diffuse optical spectroscopic imaging correlates with final pathological response in breast cancer neoadjuvant chemotherapy.," *Philosophical transactions. Series A, Mathematical, physical, and engineering sciences* **369**, 4512–4530 (2011) [doi:10.1098/rsta.2011.0279].

[286] M. Herranz and A. Ruibal, "Optical Imaging in Breast Cancer Diagnosis: The Next Evolution," *Journal of Oncology* **2012**, 1–10 (2012) [doi:10.1155/2012/863747].

[287] B. Chance, S. Nioka, J. Zhang, E. F. Conant, E. Hwang, S. Briest, S. G. Orel, M. D. Schnall, and B. J. Czerniecki, "Breast cancer detection based on incremental biochemical and physiological properties of breast cancers: a six-year, two-site study.," *Academic radiology* **12**, 925–933 (2005) [doi:10.1016/j.acra.2005.04.016].

[288] D. Hanahan and R. A. Weinberg, "Hallmarks of cancer: the next generation.," *Cell* **144**, 646–674 (2011) [doi:10.1016/j.cell.2011.02.013].

[289] D. Floery, T. H. Helbich, C. C. Riedl, S. Jaromi, M. Weber, S. Leodolter, and M. H. Fuchsjaeger, "Characterization of benign and malignant breast lesions with computed tomography laser mammography (CTLM): initial experience.," *Investigative radiology* **40**, 328–335 (2005).

[290] B. J. Tromberg, A. Cerussi, N. Shah, M. Compton, A. Durkin, D. Hsiang, J. Butler, and R. Mehta, "Imaging in breast cancer: diffuse optics in breast cancer: detecting tumors in pre-menopausal women and monitoring neoadjuvant chemotherapy.," *Breast cancer research : BCR* **7**, 279–285 (2005) [doi:10.1186/bcr1358].

[291] Q. Zhu, E. B. Cronin, A. A. Currier, H. S. Vine, M. Huang, N. Chen, and C. Xu, "Benign versus malignant breast masses: optical differentiation with US-guided optical imaging reconstruction.," *Radiology* **237**, 57–66 (2005) [doi:10.1148/radiol.2371041236].

[292] D. R. Leff, O. J. Warren, L. C. Enfield, A. Gibson, T. Athanasiou, D. K. Patten, J. Hebden, G. Z. Yang, and A. Darzi, "Diffuse optical imaging of the healthy and diseased breast: a systematic review.," *Breast cancer research and treatment* **108**, 9–22 (2008) [doi:10.1007/s10549-007-9582-z].

[293] A. E. Cerussi, A. J. Berger, F. Bevilacqua, N. Shah, D. Jakubowski, J. Butler, R. F. Holcombe, and B. J. Tromberg, "Sources of absorption and scattering contrast for near-infrared optical mammography.," *Academic radiology* **8**, 211–218 (2001) [doi:10.1016/S1076-6332(03)80529-9].

[294] B. W. Pogue, S. Jiang, H. Dehghani, C. Kogel, S. Soho, S. Srinivasan, X. Song, T. D. Tosteson, S. P. Poplack, et al., "Characterization of hemoglobin, water, and NIR scattering in breast tissue: analysis of intersubject variability and menstrual cycle changes.," *Journal of biomedical optics* **9**, 541–552 [doi:10.1117/1.1691028].

[295] R. Cubeddu, C. D'Andrea, A. Pifferi, P. Taroni, A. Torricelli, and G. Valentini, "Effects of the menstrual cycle on the red and near-infrared optical properties of the human breast.," *Photochemistry and photobiology* **72**, 383–391 (2000).

[296] S. Fantini and A. Sassaroli, "Near-infrared optical mammography for breast cancer detection with intrinsic contrast.," *Annals of biomedical engineering* **40**, 398–407 (2012) [doi:10.1007/s10439-011-0404-4].

[297] L. C. Enfield, A. P. Gibson, J. C. Hebden, and M. Douek, "Optical tomography of breast cancer-monitoring response to primary medical therapy.," *Targeted oncology* **4**, 219–233 (2009) [doi:10.1007/s11523-009-0115-z].

[298] M. E. Straver, T. S. Aukema, R. A. V. Olmos, E. J. T. Rutgers, K. G. A. Gilhuijs, M. E. Schot, W. V Vogel, and M.-J. T. F. D. V. Peeters, "Feasibility of FDG PET/CT to monitor the response of axillary lymph node metastases to neoadjuvant chemotherapy in breast cancer patients.," *European journal of nuclear medicine and molecular imaging* **37**, 1069–1076 (2010) [doi:10.1007/s00259-009-1343-2].

[299] S. Leide-Svegborn, "Radiation exposure of patients and personnel from a PET/CT procedure with 18F-FDG.," *Radiation protection dosimetry* **139**, 208–213 [doi:10.1093/rpd/ncq026].

[300] P. M. Lane, T. Gilhuly, P. Whitehead, H. Zeng, C. F. Poh, S. Ng, P. M. Williams, L. Zhang, M. P. Rosin, et al., "Simple device for the direct visualization of oral-cavity tissue fluorescence.," *Journal of biomedical optics* **11**, 024006, SPIE (2006) [doi:10.1117/1.2193157].

[301] D. Roblyer, R. Richards-Kortum, K. Sokolov, A. K. El-Naggar, M. D. Williams, A. M. Gillenwater, and C. Kurachi, "Multispectral optical imaging device for in vivo detection of oral neoplasia," *Journal of Biomedical Optics* **13**, 2008/05/10 ed., 1–11 (2008) [doi:10.1117/1.2904658].

[302] D. Roblyer, C. Kurachi, V. Stepanek, M. D. Williams, A. K. El-Naggar, J. J. Lee, A. M. Gillenwater, and R. Richards-Kortum, "Objective detection and delineation of oral neoplasia using autofluorescence imaging," *Cancer Prev Res (Phila Pa)* **2**, 2009/04/30 ed., 423–431 (2009) [doi:1940-6207.CAPR-08-0229 [pii] 10.1158/1940-6207.CAPR-08-0229].

[303] S. Y. Park, M. Follen, A. Milbourne, H. Rhodes, A. Malpica, N. MacKinnon, C. MacAulay, M. K. Markey, and R. Richards-Kortum, "Automated image analysis of digital colposcopy for the

detection of cervical neoplasia.," *Journal of biomedical optics* **13**, 014029 [doi:10.1117/1.2830654].

[304] S. Lam, C. MacAulay, J. C. LeRiche, and B. Palcic, "Detection and localization of early lung cancer by fluorescence bronchoscopy.," *Cancer* **89**, 2468–2473 (2000).

[305] W. L. Curvers, R. Singh, L.-M. W.-K. Song, H. C. Wolfsen, K. Ragunath, K. Wang, M. B. Wallace, P. Fockens, and J. J. G. H. M. Bergman, "Endoscopic tri-modal imaging for detection of early neoplasia in Barrett's oesophagus: a multi-centre feasibility study using high-resolution endoscopy, autofluorescence imaging and narrow band imaging incorporated in one endoscopy system.," *Gut* **57**, 167–172 (2008) [doi:10.1136/gut.2007.134213].

[306] J. E. East, N. Suzuki, and B. P. Saunders, "Comparison of magnified pit pattern interpretation with narrow band imaging versus chromoendoscopy for diminutive colonic polyps: a pilot study.," *Gastrointestinal endoscopy* **66**, 310–316 (2007) [doi:10.1016/j.gie.2007.02.026].

[307] H. Suzuki and Y. Saito, "Autofluorescence and narrow-band imaging endoscopy for detecting early-staged cancer in Barrett's esophagus: a case report.," *Japanese journal of clinical oncology* **38**, 871 (2008) [doi:10.1093/jjco/hyn137].

[308] F. J. C. van den Broek, P. Fockens, S. van Eeden, J. B. Reitsma, J. C. H. Hardwick, P. C. F. Stokkers, and E. Dekker, "Endoscopic tri-modal imaging for surveillance in ulcerative colitis: randomised comparison of high-resolution endoscopy and autofluorescence imaging for neoplasia detection; and evaluation of narrow-band imaging for classification of lesions.," *Gut* **57**, 1083–1089 (2008) [doi:10.1136/gut.2007.144097].

[309] C. Loo, A. Lowery, N. Halas, J. West, and R. Drezek, "Immunotargeted nanoshells for integrated cancer imaging and therapy.," *Nano letters* **5**, 2005/04/14 ed., 709–711 (2005) [doi:10.1021/nl050127s].

[310] M. Wuest, B. J. Trayner, T. N. Grant, H.-S. Jans, J. R. Mercer, D. Murray, F. G. West, A. J. B. McEwan, F. Wuest, et al., "Radiopharmacological evaluation of 6-deoxy-6-[18F]fluoro-D-fructose as a radiotracer for PET imaging of GLUT5 in breast cancer.," *Nuclear medicine and biology* **38**, 461–475 (2011) [doi:10.1016/j.nucmedbio.2010.11.004].

[311] R. S. Haber, A. Rathan, K. R. Weiser, A. Pritsker, S. H. Itzkowitz, C. Bodian, G. Slater, A. Weiss, and D. E. Burstein, "GLUT1 glucose transporter expression in colorectal carcinoma: a marker for poor prognosis.," *Cancer* **83**, 34–40 (1998).

[312] S. Fukuda and L. M. Pelus, "Survivin, a cancer target with an emerging role in normal adult tissues.," *Molecular cancer therapeutics* **5**, 1087–1098 (2006) [doi:10.1158/1535-7163.MCT-05-0375].

[313] R. Redmond, "Introduction to Fluorescence and Photophysics," in *Handbook of Biomedical Fluorescence*, M.-A. Mycek and B. Pogue, Eds., pp. 1–28, New York, New York (2003).

[314] N. Nitin, K. J. Rosbach, A. El-naggar, M. Williams, A. Gillenwater, and R. R. Richards-Kortum, "Optical Molecular Imaging of Epidermal Growth Factor Receptor Expression to Improve Detection of Oral Neoplasia," *Neoplasia* **11**, 2009/06/02 ed., 542–551 (2009) [doi:10.1593/neo.09188].

[315] K. E. Adams, S. Ke, S. Kwon, F. Liang, Z. Fan, Y. Lu, K. Hirschi, M. E. Mawad, M. A. Barry, et al., "Comparison of visible and near-infrared wavelength-excitable fluorescent dyes for molecular imaging of cancer.," *Journal of biomedical optics* **12**, 024017 [doi:10.1117/1.2717137].

[316] J. L. Kovar, W. Volcheck, E. Sevick-Muraca, M. a Simpson, and D. M. Olive, "Characterization and performance of a near-infrared 2-deoxyglucose optical imaging agent for mouse cancer models.," *Analytical biochemistry* **384**, 254–262, Elsevier Inc. (2009) [doi:10.1016/j.ab.2008.09.050].

[317] E. M. Sevick-Muraca, J. P. Houston, and M. Gurfinkel, "Fluorescence-enhanced, near infrared diagnostic imaging with contrast agents," *Current Opinion in Chemical Biology* **6**, 642–650 (2002) [doi:10.1016/S1367-5931(02)00356-3].

[318] R. E. Bailey and S. Nie, "Alloyed semiconductor quantum dots: tuning the optical properties without changing the particle size.," *Journal of the American Chemical Society* **125**, 7100–7106 (2003) [doi:10.1021/ja035000o].

[319] X. Wu, H. Liu, J. Liu, K. N. Haley, J. A. Treadway, J. P. Larson, N. Ge, F. Peale, and M. P. Bruchez, "Immunofluorescent labeling of cancer marker Her2 and other cellular targets with semiconductor quantum dots.," *Nature biotechnology* **21**, 41–46 (2003) [doi:10.1038/nbt764].

[320] N. Lewinski, "Biodistribution of Cd/Se/ZnS Quantum Dots in Aquatic Organisms," Rice University (2011).

[321] M. E. Akerman, W. C. W. Chan, P. Laakkonen, S. N. Bhatia, and E. Ruoslahti, "Nanocrystal targeting in vivo.," *Proceedings of the National Academy of Sciences of the United States of America* **99**, 12617–12621 (2002) [doi:10.1073/pnas.152463399].

[322] A. M. Derfus, W. C. W. Chan, and S. N. Bhatia, "Probing the Cytotoxicity of Semiconductor Quantum Dots," *Nano Letters* **4**, 11–18 (2004) [doi:10.1021/nl0347334].

[323] R. Kumar, M. Nyk, T. Y. Ohulchanskyy, C. A. Flask, and P. N. Prasad, "Combined Optical and MR Bioimaging Using Rare Earth Ion Doped NaYF 4 Nanocrystals," *Advanced Functional Materials* **19**, 853–859 (2009) [doi:10.1002/adfm.200800765].

[324] S. Setua, D. Menon, A. Asok, S. Nair, and M. Koyakutty, "Folate receptor targeted, rare-earth oxide nanocrystals for bi-modal fluorescence and magnetic imaging of cancer cells.," *Biomaterials* **31**, 714–729 (2010) [doi:10.1016/j.biomaterials.2009.09.090].

[325] L. R. Ferguson and W. A. Denny, "Genotoxicity of non-covalent interactions: DNA intercalators.," *Mutation research* **623**, 14–23 (2007) [doi:10.1016/j.mrfmmm.2007.03.014].

[326] T. J. Muldoon, D. Roblyer, M. D. Williams, V. M. T. Stepanek, R. Richards-Kortum, and A. M. Gillenwater, "Noninvasive imaging of oral neoplasia with a high-resolution fiber-optic microendoscope.," *Head & neck* **34**, 305–312 (2012) [doi:10.1002/hed.21735].

[327] P. A. Janssen, B. L. Selwood, S. R. Dobson, D. Peacock, and P. N. Thiessen, "To Dye or Not to Dye: A Randomized, Clinical Trial of a Triple Dye/Alcohol Regime Versus Dry Cord Care," *PEDIATRICS* **111**, 15–20 (2003) [doi:10.1542/peds.111.1.15].

[328] A. L. Polglase, W. J. McLaren, S. A. Skinner, R. Kiesslich, M. F. Neurath, and P. M. Delaney, "A fluorescence confocal endomicroscope for in vivo microscopy of the upper- and the lower-GI tract.," *Gastrointestinal endoscopy* **62**, 686–695 (2005) [doi:10.1016/j.gie.2005.05.021].

[329] R. Kiesslich, M. Goetz, J. Burg, M. Stolte, E. Siegel, M. J. Maeurer, S. Thomas, D. Strand, P. R. Galle, et al., "Diagnosing Helicobacter pylori In Vivo by Confocal Laser Endoscopy," *Gastroenterology* **128**, 2119–2123 (2005) [doi:10.1053/j.gastro.2004.12.035].

[330] R. Cao, H. Ji, N. Feng, Y. Zhang, X. Yang, P. Andersson, Y. Sun, K. Tritsaris, A. J. Hansen, et al., "Collaborative interplay between FGF-2 and VEGF-C promotes lymphangiogenesis and

metastasis.," *Proceedings of the National Academy of Sciences of the United States of America* **109**, 15894–15899 (2012) [doi:10.1073/pnas.1208324109].

[331] N. Belugali Nataraj and B. P. Salimath, "Crosstalk between VEGF and novel angiogenic protein regulates tumor angiogenesis and contributes to aggressiveness of breast carcinoma.," *Cellular signalling* **25**, 277–294 (2013) [doi:10.1016/j.cellsig.2012.09.013].

[332] J. J. Laskin and A. B. Sandler, "Epidermal growth factor receptor: a promising target in solid tumours.," *Cancer treatment reviews* **30**, 1–17 (2004) [doi:10.1016/j.ctrv.2003.10.002].

[333] I. Kallel, M. Rebai, A. Khabir, N. R. Farid, and A. Rebaï, "Genetic polymorphisms in the EGFR (R521K) and estrogen receptor (T594T) genes, EGFR and ErbB-2 protein expression, and breast cancer risk in Tunisia.," *Journal of biomedicine & biotechnology* **2009**, 753683 (2009) [doi:10.1155/2009/753683].

[334] S. Han, Y. Mu, Q. Zhu, Y. Gao, Z. Li, Q. Jin, and W. Jin, "Au:CdHgTe quantum dots for in vivo tumor-targeted multispectral fluorescence imaging.," *Analytical and bioanalytical chemistry* **403**, 1343–1352 (2012) [doi:10.1007/s00216-012-5921-y].

[335] W.-J. Hsieh, C.-J. Liang, J.-J. Chieh, S.-H. Wang, I.-R. Lai, J.-H. Chen, F.-H. Chang, W.-K. Tseng, S.-Y. Yang, et al., "In vivo tumor targeting and imaging with anti-vascular endothelial growth factor antibody-conjugated dextran-coated iron oxide nanoparticles.," *International journal of nanomedicine* **7**, 2833–2842 (2012) [doi:10.2147/IJN.S32154].

[336] S. K. Chang, I. Rizvi, N. Solban, and T. Hasan, "In vivo optical molecular imaging of vascular endothelial growth factor for monitoring cancer treatment.," *Clinical cancer research : an official journal of the American Association for Cancer Research* **14**, 4146–4153 (2008) [doi:10.1158/1078-0432.CCR-07-4536].

[337] I. Hilger, Y. Leistner, A. Berndt, C. Fritsche, K. M. Haas, H. Kosmehl, and W. A. Kaiser, "Near-infrared fluorescence imaging of HER-2 protein over-expression in tumour cells.," *European radiology* **14**, 1124–1129 (2004) [doi:10.1007/s00330-004-2257-9].

[338] P. J. Hudson and C. Souriau, "Engineered antibodies.," *Nature medicine* **9**, 129–134 (2003) [doi:10.1038/nm0103-129].

[339] W. Y. K. Hwang and J. Foote, "Immunogenicity of engineered antibodies.," *Methods (San Diego, Calif.)* **36**, 3–10 (2005) [doi:10.1016/j.ymeth.2005.01.001].

[340] P. Holliger and P. J. Hudson, "Engineered antibody fragments and the rise of single domains.," *Nature biotechnology* **23**, 1126–1136 (2005) [doi:10.1038/nbt1142].

[341] T. Sawada, T. Nishihara, A. Yamamoto, H. Teraoka, Y. Yamashita, T. Okamura, H. Ochi, J. J. L. Ho, Y.-S. Kim, et al., "Preoperative Clinical Radioimmunodetection of Pancreatic Cancer by 111In-labeled Chimeric Monoclonal Antibody Nd2," *Cancer Science* **90**, 1179–1186 (1999) [doi:10.1111/j.1349-7006.1999.tb00693.x].

[342] D. R. Colnot, J. C. Roos, R. de Bree, A. J. Wilhelm, J. A. Kummer, G. Hanft, K.-H. Heider, G. Stehle, G. B. Snow, et al., "Safety, biodistribution, pharmacokinetics, and immunogenicity of 99mTc-labeled humanized monoclonal antibody BIWA 4 (bivatuzumab) in patients with squamous cell carcinoma of the head and neck.," *Cancer immunology, immunotherapy : CII* **52**, 576–582 (2003) [doi:10.1007/s00262-003-0396-5].

[343] P. K. E. Börjesson, E. J. Postema, J. C. Roos, D. R. Colnot, H. A. M. Marres, M. H. van Schie, G. Stehle, R. de Bree, G. B. Snow, et al., "Phase I therapy study with (186)Re-labeled humanized monoclonal antibody BIWA 4 (bivatuzumab) in patients with head and neck squamous cell

carcinoma.," *Clinical cancer research : an official journal of the American Association for Cancer Research* **9**, 3961S–72S (2003).

[344] N. K. Navani and Y. Li, "Nucleic acid aptamers and enzymes as sensors.," *Current opinion in chemical biology* **10**, 272–281 (2006) [doi:10.1016/j.cbpa.2006.04.003].

[345] W. Kusser, "Chemically modified nucleic acid aptamers for in vitro selections: evolving evolution," *Reviews in Molecular Biotechnology* **74**, 27–38 (2000) [doi:10.1016/S1389-0352(99)00002-1].

[346] E. N. Brody and L. Gold, "Aptamers as therapeutic and diagnostic agents," *Reviews in Molecular Biotechnology* **74**, 5–13 (2000) [doi:10.1016/S1389-0352(99)00004-5].

[347] B. Glick and J. Pasternack, "Molecular Diagnostics," in *Molecular Biotechnology*, 3rd ed., B. Glick and J. Pasternack, Eds., pp. 227–255 (2003).

[348] M. Miura, H. Zhu, R. Rotello, E. A. Hartwieg, and J. Yuan, "Induction of apoptosis in fibroblasts by IL-1 beta-converting enzyme, a mammalian homolog of the C. elegans cell death gene ced-3.," *Cell* **75**, 653–660 (1993).

[349] J. Grimm, D. G. Kirsch, S. D. Windsor, C. F. B. Kim, P. M. Santiago, V. Ntziachristos, T. Jacks, and R. Weissleder, "Use of gene expression profiling to direct in vivo molecular imaging of lung cancer.," *Proceedings of the National Academy of Sciences of the United States of America* **102**, 14404–14409 (2005) [doi:10.1073/pnas.0503920102].

[350] A. L. van de Ven, K. Adler-Storthz, and R. Richards-Kortum, "Delivery of optical contrast agents using Triton-X100, part 2: enhanced mucosal permeation for the detection of cancer biomarkers.," *Journal of biomedical optics* **14**, 021013 (2009) [doi:10.1117/1.3090437].

[351] L. P. Adler, P. F. Faulhaber, K. C. Schnur, N. L. Al-Kasi, R. R. Shenk, and C. Schnur, "Axillary Lymph Node Metastases: Screening with [F-18]2-deoxy-2-fluoro-D-glucose (FDG) PET," *Radiology* **203**, 323–327 (1997).

[352] O. Warburg Wind, F., Negelein, E.,, "The Metabolism of Tumors in the Body," *The Journal of General Physiology*, 519–530 (1930).

[353] L. P. Adler, J. P. Crowe, N. K. Al-Kaisi, and J. L. Sunshine, "Evaluation of breast masses and axillary lymph nodes with [F-18] 2-deoxy-2-fluoro-D-glucose PET.," *Radiology* **187**, 743–750 (1993).

[354] R. S. Brown, J. Y. Leung, P. V Kison, K. R. Zasadny, A. Flint, and R. L. Wahl, "Glucose transporters and FDG uptake in untreated primary human non-small cell lung cancer.," *Journal of nuclear medicine : official publication, Society of Nuclear Medicine* **40**, 556–565 (1999).

[355] R. S. Brown and R. L. Wahl, "Overexpression of Glut-1 glucose transporter in human breast cancer. An immunohistochemical study.," *Cancer* **72**, 2979–2985 (1993).

[356] G. Weber and A. Cantero, "Glucose-6-phosphatase Activity in Normal, Precancerous, and Neoplastic Tissues," *Cancer Res* **15**, 105–108 (1955).

[357] K. Yu, S. J. Schomisch, V. Chandramouli, and Z. Lee, "Hexokinase and glucose-6-phosphatase activity in woodchuck model of hepatitis virus-induced hepatocellular carcinoma," *Comparative Biochemistry and Physiology Part C: Toxicology & Pharmacology* **143**, 225–231 (2006).

[358] K. Yamada, M. Nakata, N. Horimoto, M. Saito, H. Matsuoka, and N. Inagaki, "Measurement of glucose uptake and intracellular calcium concentration in single, living pancreatic beta-cells.," *The Journal of biological chemistry* **275**, 22278–22283 (2000) [doi:10.1074/jbc.M908048199].

[359] N. Nitin, L. C. Alicia, M. Tim, K. E.-N. Adel, G. Ann, R.-K. Rebecca, A. L. Carlson, T. Muldoon, A. K. El-Naggar, et al., "Molecular imaging of glucose uptake in oral neoplasia following topical application of fluorescently labeled deoxy-glucose," *International Journal of Cancer* **124**, 2634–2642 (2009) [doi:10.1002/ijc.24222].

[360] D. Vercauteren, R. E. Vandenbroucke, A. T. Jones, J. Rejman, J. Demeester, S. C. De Smedt, N. N. Sanders, and K. Braeckmans, "The use of inhibitors to study endocytic pathways of gene carriers: optimization and pitfalls.," *Molecular therapy : the journal of the American Society of Gene Therapy* **18**, 561–569 (2010) [doi:10.1038/mt.2009.281].

[361] T. Kong, J. Zeng, X. Wang, X. Yang, J. Yang, S. McQuarrie, A. McEwan, W. Roa, J. Chen, et al., "Enhancement of radiation cytotoxicity in breast-cancer cells by localized attachment of gold nanoparticles," *Small* **4**, 2008/08/21 ed., 1537–1543 (2008) [doi:10.1002/smll.200700794].

[362] A. Salas-Burgos, P. Iserovich, F. Zuniga, J. C. Vera, and J. Fischbarg, "Predicting the three-dimensional structure of the human facilitative glucose transporter glut1 by a novel evolutionary homology strategy: insights on the molecular mechanism of substrate migration, and binding sites for glucose and inhibitory molecules.," *Biophysical journal* **87**, 2990–2999, Elsevier (2004) [doi:10.1529/biophysj.104.047886].

[363] J. J. Li, D. Hartono, C.-N. Ong, B.-H. Bay, and L.-Y. L. Yung, "Autophagy and oxidative stress associated with gold nanoparticles.," *Biomaterials* **31**, 5996–6003 (2010) [doi:10.1016/j.biomaterials.2010.04.014].

[364] E. C. Dreaden, A. M. Alkilany, X. Huang, C. J. Murphy, and M. A. El-Sayed, "The golden age: gold nanoparticles for biomedicine.," *Chemical Society reviews* **41**, 2740–2779 (2012) [doi:10.1039/c1cs15237h].

[365] A. M. Alkilany and C. J. Murphy, "Toxicity and cellular uptake of gold nanoparticles: what we have learned so far?," *Journal of nanoparticle research : an interdisciplinary forum for nanoscale science and technology* **12**, 2313–2333 (2010) [doi:10.1007/s11051-010-9911-8].

[366] M. Turner, V. B. Golovko, O. P. H. Vaughan, P. Abdulkin, A. Berenguer-Murcia, M. S. Tikhov, B. F. G. Johnson, and R. M. Lambert, "Selective oxidation with dioxygen by gold nanoparticle catalysts derived from 55-atom clusters.," *Nature* **454**, 981–983 (2008) [doi:10.1038/nature07194].

[367] M. Tsoli, H. Kuhn, W. Brandau, H. Esche, and G. Schmid, "Cellular uptake and toxicity of Au55 clusters.," *Small (Weinheim an der Bergstrasse, Germany)* **1**, 841–844 (2005) [doi:10.1002/smll.200500104].

[368] A. Fourquet, F. Campana, B. Zafrani, Vè. Mosseri, P. Vielh, J.-C. Durand, and J. R. Vilcoq, "Prognostic factors of breast recurrence in the conservative management of early breast cancer: A 25-year follow-up," *International Journal of Radiation Oncology*Biology*Physics* **17**, 719–725 (1989).

[369] M. C. Smitt, K. Nowels, R. W. Carlson, and S. S. Jeffrey, "Predictors of reexcision findings and recurrence after breast conservation," *International Journal of Radiation Oncology*Biology*Physics* **57**, 979–985 (2003).

[370] S. C. Renton, J. C. Gazet, H. T. Ford, C. Corbishley, and R. Sutcliffe, "The importance of the resection margin in conservative surgery for breast cancer," *European Journal of Surgical Oncology* **22**, 17–22 (1996).

[371] C. A. Perez, "Conservation therapy in t1-t2 breast cancer: past, current issues, and future challenges and opportunities," *Cancer Journal* **9**, 442–453 (2003).

[372] M. E. Peterson, D. J. Schultz, C. Reynolds, and L. J. Solin, "Outcomes in breast cancer patients relative to margin status after treatment with breast-conserving surgery and radiation therapy: the University of Pennsylvania experience.," *International journal of radiation oncology, biology, physics* **43**, 1029–1035 (1999).

[373] R. Heimann, C. Powers, H. J. Halpern, A. G. Michel, C. A. Ewing, B. Wyman, W. Recant, and R. R. Weichselbaum, "Breast preservation in stage I and II carcinoma of the breast: The University of Chicago experience," *Cancer* **78**, 1722–1730 (1996).

[374] N. Y. Tse, C. K. Hoh, R. A. Hawkins, et al., M. J. Zinner, M. Dahlbom, Y. Choi, J. Maddahi, F. C. Brunicardi, et al., "The application of positron emission tomographic imaging with fluorodeoxyglucose to the evaluation of breast disease," *Ann Surg* **216**, 1992/07/01 ed., 27–34 (1992).

[375] A. M. Byrne, A. D. K. Hill, S. J. Skehan, E. W. McDermott, and N. J. O'Higgins, "Positron emission tomography in the staging and management of breast cancer," *British Journal of Surgery* **91**, 1398–1409 (2004).

[376] O. E. Nieweg, E. E. Kim, W. H. Wong, et al., W. F. Broussard, S. E. Singletary, G. N. Hortobagyi, and R. S. Tilbury, "Positron emission tomography with fluorine-18-deoxyglucose in the detection and staging of breast cancer," *Cancer* **71**, 1993/06/15 ed., 3920–3925 (1993).

[377] L. Arnould, M. Gelly, F. Penault-Llorca, L. Benoit, F. Bonnetain, C. Migeon, V. Cabaret, V. Fermeaux, P. Bertheau, et al., "Trastuzumab-based treatment of HER2-positive breast cancer: an antibody-dependent cellular cytotoxicity mechanism?," *British Journal of Cancer* **94**, 259–267, Nature Publishing Group (2006) [doi:10.1038/sj.bjc.6602930].

[378] S. F. Dent, S. Verma, K. I. Pritchard, J. Latreille, D. Rayson, M. Clemons, J. R. Mackey, L. Provencher, S. Verma, et al., *The Role of HER2-targeted Therapies in Women with HER2-Overexpressing Metastatic Breast Cancer*, in *2009* (2009).

[379] M. Moros, B. Hernáez, E. Garet, J. T. Dias, B. Sáez, V. Grazú, A. González-Fernández, C. Alonso, and J. M. de la Fuente, "Monosaccharides versus PEG-functionalized NPs: influence in the cellular uptake.," *ACS nano* **6**, 1565–1577 (2012) [doi:10.1021/nn204543c].

[380] L. M. Bareford and P. W. Swaan, "Endocytic mechanisms for targeted drug delivery.," *Advanced drug delivery reviews* **59**, 748–758 (2007) [doi:10.1016/j.addr.2007.06.008].

[381] X. Ma, Y. Wu, S. Jin, Y. Tian, X. Zhang, Y. Zhao, L. Yu, and X.-J. Liang, "Gold nanoparticles induce autophagosome accumulation through size-dependent nanoparticle uptake and lysosome impairment.," *ACS nano* **5**, 8629–8639 (2011) [doi:10.1021/nn202155y].

[382] X. Wang, C. O. Eno, B. J. Altman, Y. Zhu, G. Zhao, K. E. Olberding, J. C. Rathmell, and C. Li, "ER stress modulates cellular metabolism.," *The Biochemical journal* **435**, 285–296 (2011) [doi:10.1042/BJ20101864].

[383] A. C. Society, "Breast Cancer Facts and Figures 2005-2006," *American Cancer Society, Inc*, <http://www.cancer.org/Research/CancerFactsFigures/BreastCancerFactsFigures/breast-cancer-facts--figures-2005-2006> (11 May 2010).

[384] R. G. Steen, *A Conspiracy of Cells*., Plenum Press, New York (1993).

[385] C. M. Mojica, R. Bastani, W. J. Boscardin, and N. A. Ponce, "Low-income women with breast abnormalities: system predictors of timely diagnostic resolution," *Cancer Control* **14**, 2007/03/28 ed., 176–182 (2007).

[386] A. Oouchi, K. Sakata, H. Masuoka, M. Tamakawa, H. Nagakura, M. Someya, K. Nakata, K. Asaishi, M. Okazaki, et al., "The treatment outcome of patients undergoing breast-conserving therapy: the clinical role of postoperative radiotherapy," *Breast Cancer* **16**, 49–57, Springer Japan (2009) [doi:10.1007/s12282-008-0079-3].

[387] C. S. Melanie, W. N. Kent, J. Z. Mark, J. Stefanie, W. C. Robert, E. S. Frank, R. G. Don, M. C. Smitt, K. W. Nowels, et al., "The importance of the lumpectomy surgical margin status in long term results of breast conservation," *Cancer* **76**, 259–267 (1995).

[388] R. A. Graham, M. J. Homer, C. J. Sigler, H. Safaii, C. H. Schmid, D. J. Marchant, and T. J. Smith, "The efficacy of specimen radiography in evaluating the surgical margins of impalpable breast carcinoma," *AJR Am J Roentgenol* **162**, 1994/01/01 ed., 33–36 (1994).

[389] X. Liu, Q. Dai, L. Austin, J. Coutts, G. Knowles, J. Zou, H. Chen, and Q. Huo, "A One-Step Homogeneous Immunoassay for Cancer Biomarker Detection Using Gold Nanoparticle Probes Coupled with Dynamic Light Scattering," *Journal of the American Chemical Society* **130**, 2780–2782, American Chemical Society (2008) [doi:10.1021/ja711298b].

[390] R. Nahta, D. Yu, M. C. Hung, G. N. Hortobagyi, and F. J. Esteva, "Mechanisms of disease: understanding resistance to HER2-targeted therapy in human breast cancer," *Nat Clin Pract Oncol* **3**, 2006/05/10 ed., 269–280 (2006) [doi:ncponc0509 [pii] 10.1038/ncponc0509].

[391] D. J. Slamon, G. M. Clark, S. G. Wong, W. J. Levin, A. Ullrich, and W. L. McGuire, "Human breast cancer: correlation of relapse and survival with amplification of the HER-2/neu oncogene," *Science* **235**, 1987/01/09 ed., 177–182 (1987).

[392] D. G. Hicks and S. Kulkarni, "HER2+ Breast Cancer," *American Journal of Clinical Pathology* **129**, 263–273 (2008) [doi:10.1309/99ae032r9fm8wnd1].

[393] C. Loo, L. Hirsch, M. H. Lee, E. Chang, J. West, N. Halas, and R. Drezek, "Gold nanoshell bioconjugates for molecular imaging in living cells," *Opt Lett* **30**, 2005/05/24 ed., 1012–1014 (2005).

[394] W. Stober, A. Fink, and E. Bohn, "Controlled Growth of Monodisperse Silica Spheres in Micron Size Range," *Journal of Colloid and Interface Science* **26**, 62–& (1968).

[395] D. G. Duff, A. Baiker, and P. P. Edwards, "A new hydrosol of gold clusters. 1. Formation and particle size variation," *Langmuir* **9**, 2301–2309, American Chemical Society (1993) [doi:10.1021/la00033a010].

[396] T. Magalhães, A. von Bohlen, M. L. Carvalho, and M. Becker, "Trace elements in human cancerous and healthy tissues from the same individual: A comparative study by TXRF and EDXRF," *Spectrochimica Acta Part B: Atomic Spectroscopy* **61**, 1185–1193 (2006) [doi:10.1016/j.sab.2006.06.002].

[397] J. Qian, X. Li, M. Wei, X. Gao, Z. Xu, and S. He, "Bio-molecule-conjugated fluorescent organically modified silica nanoparticles as optical probes for cancer cell imaging.," *Optics express* **16**, 19568–19578 (2008).

[398] D. E. Owens and N. A. Peppas, "Opsonization, biodistribution, and pharmacokinetics of polymeric nanoparticles.," *International journal of pharmaceutics* **307**, 93–102 (2006) [doi:10.1016/j.ijpharm.2005.10.010].

[399] S. A. Rasbridge, C. E. Gillett, A. M. Seymour, K. Patel, M. A. Richards, R. D. Rubens, and R. R. Millis, "The effects of chemotherapy on morphology, cellular proliferation, apoptosis and oncoprotein expression in primary breast carcinoma," *Br J Cancer* **70**, 1994/08/01 ed., 335–341 (1994).

[400] A. Haid, M. Knauer, S. Dunzinger, Z. Jasarevic, R. Köberle-Wührer, A. Schuster, M. Toeppker, B. Haid, E. Wenzl, et al., "Intra-operative Sonography: A Valuable Aid During Breast-Conserving Surgery for Occult Breast Cancer," *Annals of Surgical Oncology* **14**, 3090–3101, Springer New York (2007) [doi:10.1245/s10434-007-9490-9].

[401] J. Aaron, N. Nitin, K. Travis, S. Kumar, T. Collier, S. Y. Park, M. Jose-Yacaman, L. Coghlan, M. Follen, et al., "Plasmon resonance coupling of metal nanoparticles for molecular imaging of carcinogenesis in vivo," *Journal of Biomedical Optics* **12**, 34007–34011, SPIE (2007).

[402] A. L. van de Ven, K. Adler-Storthz, and R. Richards-Kortum, "Delivery of optical contrast agents using Triton-X100, part 1: reversible permeabilization of live cells for intracellular labeling.," *Journal of biomedical optics* **14**, 021012 (2009) [doi:10.1117/1.3090448].

[403] J. Baeten, J. Haller, H. Shih, and V. Ntziachristos, "In vivo investigation of breast cancer progression by use of an internal control.," *Neoplasia (New York, N.Y.)* **11**, 220–227 (2009).

[404] X. Montet, J.-L. Figueiredo, H. Alencar, V. Ntziachristos, U. Mahmood, and R. Weissleder, "Tomographic fluorescence imaging of tumor vascular volume in mice.," *Radiology* **242**, 751–758 (2007) [doi:10.1148/radiol.2423052065].

[405] N. Nitin, D. J. Javier, D. M. Roblyer, and R. Richards-Kortum, "Widefield and high-resolution reflectance imaging of gold and silver nanospheres.," *Journal of biomedical optics* **12**, 051505 (2010) [doi:10.1117/1.2800314].

[406] N. Bedard, M. Pierce, A. El-Nagger, S. Anandasabapathy, A. Gillenwater, and R. Richards-Kortum, "Emerging roles for multimodal optical imaging in early cancer detection: a global challenge.," *Technology in cancer research & treatment* **9**, 211–217 (2010).

[407] T. J. Muldoon, M. C. Pierce, D. L. Nida, M. D. Williams, A. Gillenwater, and R. Richards-Kortum, "Subcellular-resolution molecular imaging within living tissue by fiber microendoscopy.," *Optics express* **15**, 16413–16423 (2007).

[408] S. Lam, B. Standish, C. Baldwin, A. McWilliams, J. LeRiche, A. Gazdar, A. I. Vitkin, V. Yang, N. Ikeda, et al., "In vivo optical coherence tomography imaging of preinvasive bronchial lesions.," *Clinical cancer research : an official journal of the American Association for Cancer Research* **14**, 2006–2011 (2008) [doi:10.1158/1078-0432.CCR-07-4418].

[409] R. Patel, A. Khan, D. Wirth, M. Kamionek, D. Kandil, R. Quinlan, and A. N. Yaroslavsky, "Multimodal optical imaging for detecting breast cancer.," *Journal of biomedical optics* **17**, 066008 (2012) [doi:10.1117/1.JBO.17.6.066008].

[410] M. Shipitsin, L. L. Campbell, P. Argani, S. Weremowicz, N. Bloushtain-Qimron, J. Yao, T. Nikolskaya, T. Serebryiskaya, R. Beroukhim, et al., "Molecular definition of breast tumor heterogeneity.," *Cancer cell* **11**, 259–273 (2007) [doi:10.1016/j.ccr.2007.01.013].

[411] L. Liotta and E. Petricoin, "Molecular profiling of human cancer.," *Nature reviews. Genetics* **1**, 48–56 (2000) [doi:10.1038/35049567].

[412] L. Milas and W. N. Hittelman, "Cancer stem cells and tumor response to therapy: current problems and future prospects.," *Seminars in radiation oncology* **19**, 96–105 (2009) [doi:10.1016/j.semradonc.2008.11.004].

[413] C. G. Rylander, O. F. Stumpp, T. E. Milner, N. J. Kemp, J. M. Mendenhall, K. R. Diller, and A. J. Welch, "Dehydration mechanism of optical clearing in tissue.," *Journal of biomedical optics* **11**, 041117 [doi:10.1117/1.2343208].

[414] E. A. Genina, A. N. Bashkatov, A. A. Korobko, E. A. Zubkova, V. V Tuchin, I. Yaroslavsky, and G. B. Altshuler, "Optical clearing of human skin: comparative study of permeability and dehydration of intact and photothermally perforated skin.," *Journal of biomedical optics* **13**, 021102 [doi:10.1117/1.2899149].

[415] E. A. Genina, A. N. Bashkatov, Y. P. Sinichkin, and V. V. Tuchin, "Optical clearing of skin under action of glycerol: Ex vivo and in vivo investigations," *Optics and Spectroscopy* **109**, 225–231 (2010) [doi:10.1134/S0030400X10080126].

[416] J. Hirshburg, B. Choi, J. S. Nelson, and A. T. Yeh, "Collagen solubility correlates with skin optical clearing.," *Journal of biomedical optics* **11**, 040501 [doi:10.1117/1.2220527].

[417] S. Ke, X. Wen, M. Gurfinkel, C. Charnsangavej, S. Wallace, E. M. Sevick-Muraca, and C. Li, "Near-infrared optical imaging of epidermal growth factor receptor in breast cancer xenografts.," *Cancer research* **63**, 7870–7875 (2003).

[418] J. L. Kovar, M. A. Simpson, A. Schutz-Geschwender, and D. M. Olive, "A systematic approach to the development of fluorescent contrast agents for optical imaging of mouse cancer models.," *Analytical biochemistry* **367**, 1–12 (2007) [doi:10.1016/j.ab.2007.04.011].

[419] K. R. Bhushan, P. Misra, F. Liu, S. Mathur, R. E. Lenkinski, and J. V Frangioni, "Detection of breast cancer microcalcifications using a dual-modality SPECT/NIR fluorescent probe.," *Journal of the American Chemical Society* **130**, 17648–17649 (2008) [doi:10.1021/ja807099s].

[420] M. R. Chatni, J. Xia, R. Sohn, K. Maslov, Z. Guo, Y. Zhang, K. Wang, Y. Xia, M. Anastasio, et al., "Tumor glucose metabolism imaged in vivo in small animals with whole-body photoacoustic computed tomography.," *Journal of biomedical optics* **17**, 076012 (2012) [doi:10.1117/1.JBO.17.7.076012].

[421] H. Kobayashi, M. Ogawa, R. Alford, P. L. Choyke, and Y. Urano, "New strategies for fluorescent probe design in medical diagnostic imaging.," *Chemical reviews* **110**, 2620–2640 (2010) [doi:10.1021/cr900263j].